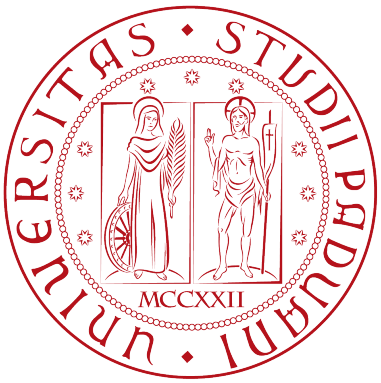

HEAD OFFICE:
UNIVERSITÀ DEGLI STUDI DI PADOVA
DEPARTMENT OF PHYSICS AND ASTRONOMY "G. GALILEI"

Ph.D. COURSE IN ASTRONOMY
SERIES XXXIV

GALACTIC ARCHAEOLOGY. FROM MULTIPLE STELLAR POPULATIONS IN STAR CLUSTERS TO EXTREMELY METAL-POOR STARS

Thesis written with the financial contribution of the European Research Council (ERC) under the European Union's Horizon 2020 research innovation programme (grant Agreement ERC-StG 2016, No. 716082 "GALFOR," PI: Milone)

Coordinator
Prof. Giovanni Carraro

Supervisor
Prof. Antonino P. Milone

Co-supervisor
Dr. Edoardo P. Lagioia

***Ph.D.* candidate**
Giacomo Cordoni

Contents

Abstract

Galactic archaeology aims at uncovering the history of the nearby universe, with a special focus on our own Galaxy, the Milky Way (MW). Just like classical archaeologists study fossils to unveil the history of mankind, Galactic archaeologists sift through and examine the most ancient structures observable today, i.e. the stellar fossils, to shed light on the earliest phases of our Universe. Among the oldest objects in our Galaxy, old Galactic Globular Clusters (GCs), which formed around 13 Gyr ago, and Extremely Metal-Poor stars, i.e. the progenies of population-III stars, provide the unique opportunity to trace the formation of the Milky Way.

Specifically, nearly all ancient Galactic Globular Clusters are known to harbor multiple stellar populations with different chemical composition, and, possibly age. Despite the efforts of the astronomical community, the origin of these stellar populations, and therefore of GCs, remains one of the greatest mysteries of modern stellar astrophysics.

While most literature works rely on photometry and spectroscopy, recent theoretical and numerical works suggest that the present-day dynamics of stars belonging to different stellar populations can provide a unique window into the formation of these objects, thus shedding some light on the Early Universe. Specifically, the kinematics and morphology of multiple stellar populations can yield fundamental insights into the cluster's environment at the time of formation, thus discriminating between different formation scenarios.
In my work, I combine ground- and space-based photometry with Gaia Data Release 2 (DR2) and Hubble Space Telescope (HST) astrometry and proper motions to explore the still quite uncharted internal dynamics of multiple stellar populations. I investigated a sample of 9 Galactic GCs, ranging from one of the least massive clusters, i.e. NGC 6838, to the most massive one, ω Centauri.
I find that in some of these GCs multiple stellar populations are dynamically and spatially mixed, while in some other clusters first- and second-population stars exhibit a different overall dynamics, with, for instance, the second population

showing a stronger anisotropy with respect to the first-population. Furthermore, we detect morphological differences often associated with the observed dynamical differences.
Altogether, my work provides new observational evidence to constrain the formation scenario of multiple stellar populations in Galactic GCs.
Further increasing the complexity of the puzzle, recent Hubble Space Telescope observations revealed that the Color-Magnitude Diagrams (CMDs) of Magellanic Clouds (MC) younger than 2 Gyr exhibit features that are not consistent with the presence of simple stellar populations, e.g. split Main-Sequences (MS) and extended Main-Sequence Turn-Offs (eMSTO).
Moreover, exploiting the exquisite dataset of Gaia DR2, we discovered that split-MSs and eMSTOs are not a peculiarity of young MC clusters, but are also common features of Galactic Open Clusters (OC) in the same age range, i.e. younger than 2 Gyr.
In this framework, young and intermediate-age Magellanic Clouds (MC) clusters, would offer the unique opportunity to address this phenomenon whilst taking place, or right after it happened.
To shed light on the nature of multiple stellar populations in young star clusters I analyzed 12 Galactic OCs comparing photometry and astrometry from Gaia DR2 with theoretical models. As a result, I identified stellar rotation as the main driver of the observed features observed in the CMDs of young Galactic OCs and Magellanic Clouds as well. Furthermore, while confirming the central role of stellar rotation, the analysis carried out on Galactic OCs and young Magellanic Clouds clusters does not provide enough accuracy to exclude the presence of residual age differences among cluster stars.
To exclude, or support, the presence of a residual age spread among stars in these young stellar systems, I made use of deep HST observations collected as part of the observing campaign GO-15495 (P.I. Cordoni). Specifically, I introduced a novel approach that overcomes the degeneracy between age and stellar rotations, making use of the Main-Sequence Turn-On, i.e. the point where pre-Main-Sequence (pre-MS) stars join the MS. Indeed, the luminosity of such a feature is strongly dependent on the age of the cluster, while poorly affected by stellar rotation. The analysis of the 40-Myr clusters NGC 1818 revealed a Star Formation History (SFH) characterized by a single star formation episode, which lasted, at most, 8 Myr, therefore excluding, once and for all, age as the responsible of the observed features in young Magellanic Clouds clusters.

While the light coming from ancient Galactic GCs bears fundamental constraints into the early life of our Galaxy, it is not the only source of information that we have. Indeed, in the same way, the lowest metallicity stars observable at the present-day can yield priceless clues into the formation process of the Milky Way. As a matter of fact, these stars formed from gas enriched with the nucleosynthetic products from the first generation metal-free stars, the so-called Population-III stars. Moreover, the kinematics of such stars can supply much information on the events that occurred during the formation of the Milky Way, which is believed

to include both *in-situ* star formation and the accretion of lower-mass galaxies. Together, the abundances and kinematics of these low metallicity stars offer a distinct perspective on the earliest stages of the formation and evolution of the Milky Way, and by implication, of galaxies in general. Under these circumstances, I determined and analyzed the kinematics of a sample of 475 metal-poor stars, with metallicity ranging from -6.5 to -2.05 dex.
Exploiting their orbital properties, such as the integral of motions, I identify 16 and 40 stars dynamically consistent with the recently discovered remnants of the *Gaia Sausage* and *Gaia Sequoia* accretion events, uncovering the metal-poor tail of such remnants.
Remarkably, I find that 53 of the analyzed stars ($\sim$ 11% of the total) exhibit orbits confined within 3 kpc from the Galactic plane, and dynamical properties consistent with the definition of thick disk stars. This sub-sample is best interpreted as the very low-metallicity tail of the metal-weak thick disc population, thus hindering the accepted interpretation of the thick disc as the one of the younger component of our Galaxy.

List of papers

In the following you can find the complete list of the papers I published during my PhD Thesis, with first author paper first. Moreover, I published a total of 21 refereed articles with > 350 citations, including 4 first author papers, 1 first author paper submitted to Nature Communications, and 16 co-authored papers. The complete list of both refereed and non refereed papers (including conference proceedings) is available at Nasa Ads.
The present thesis is mostly based on first author papers.

21 – Cordoni et al. 2021, *Submitted to Nature Communications, The Turn-On of NGC1818 unveils the origin of Multiple Stellar Populations in Magellanic Cloud clusters.*

20 – Cordoni et al. 2021, *MNRAS, Exploring the Galaxy's halo and very metal-weak thick disk with SkyMapper and Gaia DR2*
https://ui.adsabs.harvard.edu/abs/2021MNRAS.503.2539C/abstract
DOI: 10.1093/mnras/staa3417

19 – Cordoni et al. 2020b, *ApJ, Gaia and Hubble unveil the kinematics of stellar populations in the Type II globular clusters ω Centauri and M 22.*
https://ui.adsabs.harvard.edu/abs/2020ApJ...898..147C/abstract
DOI: 10.3847/1538-4357/aba04b

18 – Cordoni et al. 2020a, *ApJ, Three-Component Kinematics of Multiple Stellar Populations in Globular Clusters with Gaia and VLT*
https://ui.adsabs.harvard.edu/abs/2020ApJ...889...18C/abstract
DOI: 10.3847/1538-4357/ab5aee

17 – Cordoni et al. 2018, *ApJ, Extended Main-sequence Turnoff as a Common Feature of Milky Way Open Clusters*

https://ui.adsabs.harvard.edu/abs/2018ApJ...869..139C/abstract
DOI: 10.3847/1538-4357/aaedc1

16 – Jang et al. 2021 *Submitted to ApJ, Integrated photometry of multiple stellar populations in Globular Clusters*

15 – Tailo et al. 2021 *ApJ, Mass-loss law for red giant stars in simple population globular clusters*
https://ui.adsabs.harvard.edu/abs/2021MNRAS.503..694T/abstract
DOI: 10.1093/mnras/stab568

14 – Lagioia et al. 2021 *ApJ, Multiple stellar populations in Asymptotic Giant Branch stars of Galactic Globular Clusters*
https://ui.adsabs.harvard.edu/abs/2021ApJ...910....6L/abstract
DOI: 10.3847/1538-4357/abdfcf

13 – Dondoglio et al. 2021 *ApJ, Multiple Stellar Populations along the Red Horizontal Branch and Red Clump of Globular Clusters*
https://ui.adsabs.harvard.edu/abs/2021ApJ...906...76D/abstract
DOI: 10.3847/1538-4357/abc882

12 – Tailo et al. 2020 *MNRAS, Mass loss along the red giant branch in 46 Globular Clusters and their multiple populations*
https://ui.adsabs.harvard.edu/abs/2020MNRAS.498.5745T/abstract
DOI: 10.1093/mnras/staa2639

11 – Milone et al. 2020 *MNRAS, A chromosome map to unveil stellar populations with different magnesium abundances. The case of Omega Centauri*
https://ui.adsabs.harvard.edu/abs/2020MNRAS.497.3846M/abstract
DOI: 10.1093/mnras/staa2119

10 – Milone et al. 2020 *MNRAS, Multiple populations in globular clusters and their parent galaxies*
https://ui.adsabs.harvard.edu/abs/2020MNRAS.491..515M/abstract
DOI: 10.1093/mnras/stz2999

9 – Milone et al. 2020 *MNRAS, The Hubble Space Telescope UV Legacy Survey of Galactic Globular Clusters. - XXI. Binaries among multiple stellar populations*
https://ui.adsabs.harvard.edu/abs/2020MNRAS.492.5457M/abstract
DOI: 10.1093/mnras/stz3629

8 – Lagioia et al. 2019, *AJ, The Role of Cluster Mass in the Multiple Populations of Galactic and Extragalactic Globular Clusters*
https://ui.adsabs.harvard.edu/abs/2019AJ....158..202L/abstract

DOI: 10.3847/1538-3881/ab45f2

7 – Marino et al. 2019, *ApJ, Chemical abundances along the 1G sequence of the chromosome maps: The Globular Cluster NGC 3201*
https://ui.adsabs.harvard.edu/abs/2019ApJ...887...91M/abstract
DOI: 10.3847/1538-4357/ab53d9

6 – Marino et al. 2019, *MNRAS, The Hubble Space Telescope UV Legacy Survey of Galactic Globular Clusters. XVIII. A Chemical Tagging of the Multiple Stellar Populations along the chromosome maps*
https://ui.adsabs.harvard.edu/abs/2019MNRAS.487.3815M/abstract
DOI: 10.1093/mnras/stz1415

5 – Zennaro et al. 2019, *MNRAS, Four stellar populations and extreme helium variation in the massive outer-halo globular cluster NGC 2419*
https://ui.adsabs.harvard.edu/abs/2019MNRAS.487.3239Z/abstract
DOI: 10.1093/mnras/stz1477

4 – Tailo et al. 2019, *MNRAS, Is helium the key parameter in the extended color spread of the first generation stars in M3?*
https://ui.adsabs.harvard.edu/abs/2019MNRAS.486.5895T/abstract
DOI: 10.1093/mnras/stz1273

3 – Li et al. 2019, *ApJ, Extended main-sequence turnoffs in the double cluster h and χ Persei: The complex role of stellar rotation*
https://ui.adsabs.harvard.edu/abs/2019ApJ...876...65L/abstract
DOI: 10.3847/1538-4357/ab15d2

2 – Tailo et al. 2019, *ApJ, Mass loss of different stellar populations in Globular Clusters: the case of M4*
https://ui.adsabs.harvard.edu/abs/2019ApJ...873..123T/abstract
DOI: 10.3847/1538-4357/ab05cc

1 – Milone et al. 2018, *ApJ, The Hubble Space Telescope UV Legacy Survey of Galactic Globular Clusters. XVI. The helium abundance of multiple populations*
http://adsabs.harvard.edu/abs/2018ApJ...869..139C
DOI: 10.1093/mnras/sty2573

CHAPTER

1 Introduction

The understanding of the physical properties of the Early Universe and its components can be considered as the holy grail of modern astronomy and astrophysics. Moreover, the comprehension of the physical phenomena that took place in the infant Cosmos and that, consequently, shaped what we observe today would represent a milestone in our knowledge. To uncover how the Universe formed, we must investigate its fundamental components and shed light on their genesis. Like traditional archaeologists who study the history of the Earth by exploiting the present-day fossils, Galactic archaeologists trace the history and formation of the Milky Way investigating the stellar fossils that can be observed with modern facilities. Galactic archaeologists thus focus on the oldest objects in the nearby Universe, e.g. the "first" stars and star clusters, to uncover the processes that lead to the formation of our Galaxy and, finally, of the Universe. Among the oldest objects in the Milky Way, Galactic GCs and the first stars, i.e. namely population-III stars represent, in different ways, the best possibility to perform this task. As a matter of fact, the light coming from these ancient stars and clusters can reveal their properties, and, more importantly, the properties of their progenitors and of the surrounding Interstellar Medium (ISM) at the time and place of their location. Even though the study of these two classes of objects serves slightly different purposes, and comes with different challenges, both can help us to answer to some of the fundamental questions of modern astrophysics.

How did the Milky Way formed?
How did stars in the Galaxy formed?
How did star clusters assembled?
What is the contribution of stars and star clusters to the re-ionization of the Universe?

1.1 Galactic archaeology through star clusters

Old Galactic Globular clusters, objects for which reliable ages can be obtained, have been intensively studied during the course of the last century. Indeed, their nature and their physical properties make them the perfect laboratories to test stellar evolution models, and improve our understanding of star formation and stellar evolution. Being very dense, up to tens of hundreds of thousands of stars compressed in few cubic parsecs, and very close to us, they represent the perfect opportunity to study a large number of stars likely sharing the same physical properties, e.g. distance and possibly chemical composition and age.
Supported by countless photometric observations, GCs were considered the prototype of Simple Stellar populations (SSPs), where stars formed from the same molecular cloud in the same star formation episode, so that age and chemical composition are common to all stars belonging to the cluster.
The advent of the Hubble Space Telescope (*HST*) completely shattered this picture, revealing the much much more complex, and interesting, nature of Galactic GCs. Indeed, among the recent discoveries of modern astronomy and astrophysics, the presence of Multiple Stellar populations (MPs) in ancient Galactic GCs is undoubtedly one the greatest and most fascinating ones. The idea that globular clusters host chemically homogeneous stars definitely crushed under the increasing evidence revealing the ubiquitous nature of Multiple Stellar populations.

As previously mentioned, the physical properties of stellar populations that form these ancient stellar systems provide important insights into the Early Universe, and, specifically, into the pre-enrichment of the interstellar medium by the first stars and the role of first galaxies in the assembly of the halo.
Despite of the combined efforts of theory and observations, all the proposed models fail to fulfill the observational constraints, and thus the origin of multiple stellar populations in globular clusters remains a mystery of modern stellar astrophysics.
In the attempt to shed light on this puzzling phenomenon, detailed *HST* observations of young and intermediate-age Magellanic Clouds (MC) globular clusters revealed unexpected features not consistent with the presence of SSP, thus demonstrating that MPs may not be a peculiarity of old Galactic GCs. We still discuss in detail the multipopulation phenomenon in young star clusters in Section 1.1.4.

1.1.1 Old Galactic Globular clusters

The presence of MPs in old GCs have been confirmed by countless observations, both spectroscopic and photometric. Moreover, photometric diagrams with appropriate combinations of ultraviolet, optical and near-infrared filters are highly-efficient tools to characterize MPs in GCs. As an example, the F814W, F275W,

F336W, F438W filters can be exploited to build CMDs and pseudo-CMDs where the presence of multiple populations along the Red Giant Branch (RGB), Sub Giant Branch (RGB) and MS becomes evident. Specifically, the $\Delta_{CF275W,F336W,F438W}$ vs. $\Delta_{F275W,F814W}$ pseudo two-colors diagram, or "Chromosome Map" is the most efficient tool to separate stellar populations, as clearly discussed in Milone et al. (2017a) where a detailed description of the procedure adopted to derive such diagram is provided. As an example, Figure 1.1 shows two CMDs and the ChM of the Globular NGC2808. A visual inspection immediately reveals the presence of multiple sequences in the bottom CMDs, ranging from the bottom of the Main Sequence to the tip of the RGB. Particularly evident is the separation in the bottom left panel, where the pseudo color is defined as follows:

$$C_{\mathrm{F438W,F336W,F275W}} = (m_{\mathrm{F275W}} - m_{\mathrm{F336W}}) - (m_{\mathrm{F336W}} - m_{\mathrm{F438W}})$$

Furthermore, the ChM in the top panel highlights the distribution of stars in different clumps, which corresponds to multiple stellar populations.
The reason behind the power of such tool is to be found in the chemical composition of the different stellar populations. Indeed, the magnitude derived through specific filters reflects the chemical composition of the star by selecting specific features of the stellar spectra. As a result, the position of each star in these color-magnitude diagrams can be considered as a proxy of its chemical composition, allowing us to simultaneously identify and study the chemical properties of tens of thousands of stars.
Moreover, detailed spectroscopical studies confirmed the complex chemical nature of Galactic GCs, revealing unexpected chemical patterns common to most GCs. Specifically, a first group of stars exhibits a chemical composition consistent with the cloud from which the cluster has formed. Beside this first group, all clusters host a second group of stars that displays a different chemical composition, being depleted in Carbon (C) and Oxygen (O), and enriched in Sodium (Na), Nitrogen (N) and Helium (He). Furthermore, such chemical differences are neither random nor continuous, but rather define correlations and anti-correlations and discrete patterns that are ubiquitous among the analyzed clusters. As an example, in Figure 1.2 we display Na-O anti-correlations in NGC 2808 and NGC 5904, from left to right, respectively, where the loci of first generation stars are highlighted with the red shading. We refer to Marino et al. (2019b) for a detailed description of the chemical properties of MPs in Galactic GCs.

As aforementioned, while our knowledge of multiple stellar populations in GCs keeps improving, their origin remains one of the greatest open questions of modern stellar astrophysics, and many scenarios have been proposed trying explain the observations. In the following I will highlight the main known features of multiple stellar populations and the relation with the proposed scenarios.
In the last decades, the "*Hubble Space Telescope UV Legacy Survey of Galactic Globular Cluster* (GO-13297, PI: G.Piotto, Piotto et al. (2012, and series)) has demonstrated that multiple stellar populations are a common feature in nearly all GCs,

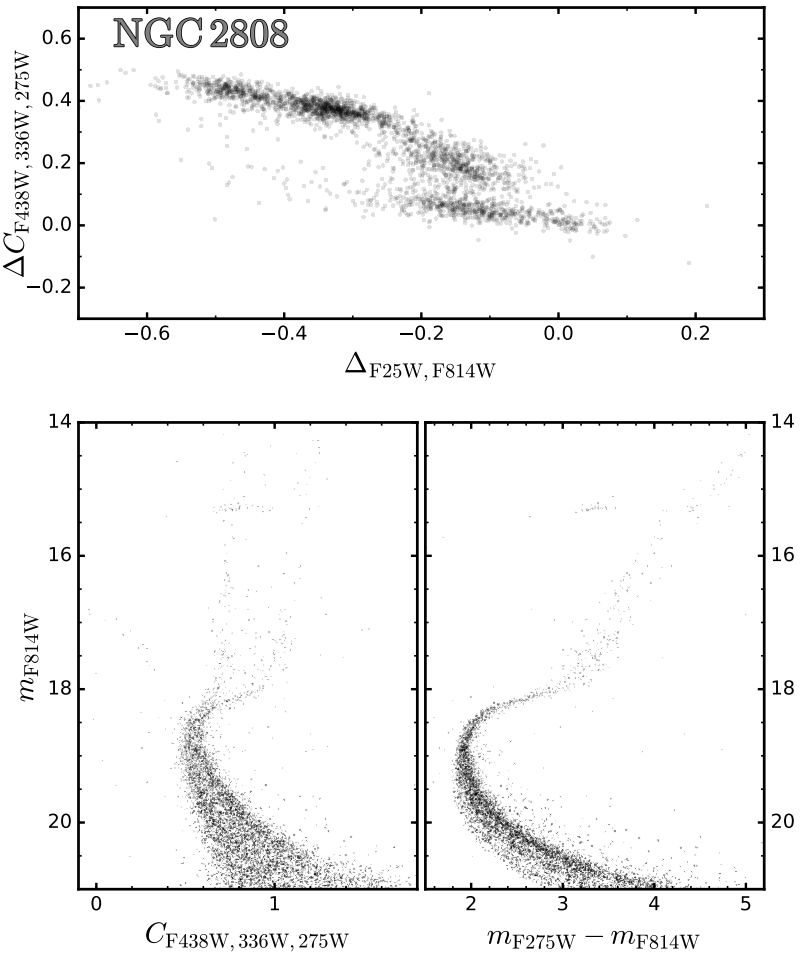

Figure 1.1. *Top panel.* Chromosome Map of Red Giant Branch stars in NGC 2808. *Bottom panels.* m_{F814W} vs. $m_{\mathrm{F275W}} - m_{\mathrm{F814W}}$ and $C_{\mathrm{F438W,F336W,F275W}}$ shown respectively in the left and right panel. The latter quantity is defined in the text as $C_{\mathrm{F438W,F336W,F275W}} = (m_{\mathrm{F275W}} - m_{\mathrm{F336W}}) - (m_{\mathrm{F336W}} - m_{\mathrm{F438W}})$

adding observational and theoretical constraints. Furthermore, Milone et al. (2015, 2018b), compiled an atlas of MPs in 57 GCs, analyzing the relation between the host cluster and the observed features of MPs.
Following Renzini et al. (2015), the main properties and constraints that concern multiple stellar populations in GCs are:

- **GC Specificity** The presence of 2G stars with peculiar chemical composition, common to nearly all GCs, is very rare in the Milky Way field, thus suggesting an *in-situ* origin. Consequently, every possible scenario for the formation of multiple stellar populations has to account for the rarity of 2G-like stars in the field, being specific to GC.

- **Ubiquity** As discussed in the previous paragraphs, multiple stellar popula-

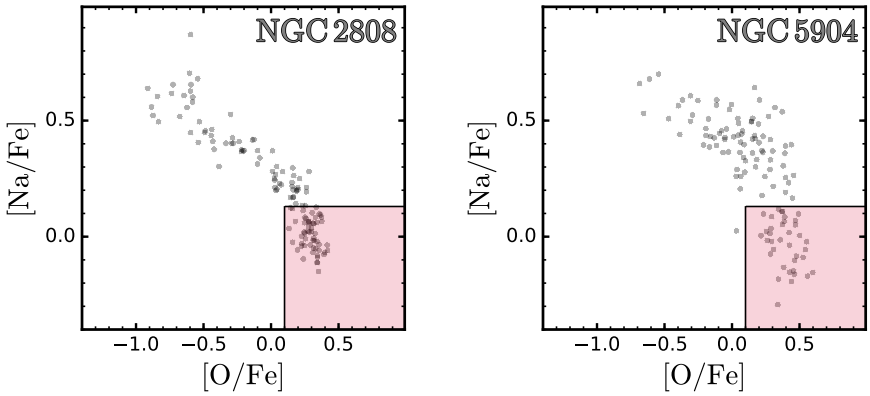

Figure 1.2. Sodium-Oxygen anti-correlation in NGC 2808, left panel, and NGC 5904, right panel. The red shaded regions highlights the location of first generation stars

tions are observed in almost every analyzed GC. Therefore, in the environment typical of a GC, the formation of 2G stars is a direct consequence of the cluster physical conditions.

- **Variety** While MPs are a common feature among GCs, their properties are case dependent. Indeed, the number of observed populations ranges from a minimum of 2, up to a maximum of 17 and possibly more as in the case of ω Centauri. The same variety is still observable in the specific chemical composition of each sub-populations.

- **Predominance** As clearly shown in Milone et al. (2018b), 2G stars are, in most GCs, the dominant population, account up-to more than the 50% of the totality of cluster stars.

- **Discreteness** As already noted, the appropriate combinations of filters allows to separate multiple populations distinct sequences or group in CMDs and/or in two-color diagram, and these groups reflect the different chemical composition of the population. Such discreteness in chemical composition has been demonstrated, for the first time, in Marino et al. (2008) and Yong et al. (2005) using high resolution data.

- **Supernova avoidance** Although present in all GC, the appearance and properties of multiple stellar populations differs from cluster to cluster. Specifically, Milone et al. (2018b) and Marino et al. (2019b) identified two distinct classes of GCs, based on the morphology of the chromosome map, i.e. on the chemical compositions of MPs. While stars in the majority of Type I Galactic GCs exhibit homogeneous abundances of heavy elements (e.g. Carretta et al., 2009), a small but significant number of 'anomalous' clusters (Type II GCs) show internal variations in metallicity and in those

elements that are associated to *s* processes (e.g. Yong & Grundahl, 2008; Da Costa et al., 2009; Yong et al., 2014; Marino et al., 2015; Johnson et al., 2015; Marino et al., 2019b). This second class accounts for ∼ 17% of the total analyzed clusters, and, among these ω Centauri and $M22$ are probably the most studied examples.
As a possible interpretation, these GCs would have retained a small fraction of Supernovae (SN) products, thus modifying the chemical composition of 2G stars with heavy-elements.

- **Hot CNO and Ne-Na processing** A distinctive feature of 2G stars is the chemical composition resulting from CNO-cycling and p-capture processes at high temperatures. Every scenario should therefore account for the variety of chemical patterns exhibited by 2G stars in the analyzed GCs.

- **Helium enrichment** Almost every studied GC presents He-enriched 2G stars, as quantified in Milone et al. (2018b). Hence, 1G donors have to account for the production of helium-rich material.

- **Mass Budget** One of the main challenges for every scenario, so far, is the predominance of 2G stars. Indeed, only a small fraction of initial 1G stars mass, ejected during their life, has the required chemical composition, so that it gets difficult, if not impossible, to explain the dominance of 2G stars over their progenitors. A possible solution is the assumption that GC were much more massive at birth, with respect to what is observed today. Specifically, GC progenitors would have lost 80-90% of their initial masses. This would have important consequences in our understanding of the re-ionization of the Universe, and of the early formation and evolution of the host galaxies, i.e., where are those stars now?.

1.1.2 Formation of Multiple Populations

As the properties of multiple stellar populations have been, and are still being, investigated, it is natural to propose scenarios and models that aim at explaining the formation of such intriguing stellar populations. Specifically, two classes of scenarios have been hypothesized: the multi-generations and single-generation scenarios. In the former case, some stars, namely 1G stars, act as polluters of the intra-cluster medium, and the ejecta of such stars get incorporated in subsequent generations of stars, i.e. 2G stars.
On the other hand, in the latter class of scenarios, variations in light-elements abundance are a consequence of early-disk accretion in pre-main sequence binaries. In light of this, the observed multiple stellar populations would be coeval, belonging to the same stellar generation.
Each scenarios having its pros and con's, none have been able to fulfill the observational constraints discussed above.
In the following paragraphs I will examine, in more detail, these two classes of

scenarios, highlighting their successes and limitations. In the context of multiple stellar generations, each scenarios differ based on the nature of the proposed polluters.

- **Asymptotic Giant Branch stars (AGB)** were originally proposed in Cottrell & Da Costa (1981) and later developed and implemented by D'Ercole et al. (2010a) and Ventura et al. (2001a). Intermediate mass AGB stars (4-5 $\lesssim M/M_{\odot} \lesssim$ 8) are characterized by peculiar nucleosynthesis processes, such as slow neutron capture (s-processes) and hot-bottom burning (HBB), which allows efficient p-capture nuclear processing. The elements produced in these processes are then injected in the ISM by stellar winds and subsequent evolutionary phases.
  The fact that stars in a wide range of stellar masses contribute to the pollution of the cluster environment, translates into a wide range of temperatures for p-processes. Specifically sodium is mostly provided by less massive stars while and oxygen-depleted material come from more massive ones.
  Accordingly, this model predicts a first episode of star formation forming the first generations of stars, i.e. 1G, followed by a second star burst that takes place when enough polluted material has accumulated in the potential well of the cluster. The timescale for this collapse is, roughly, a few hundred Myrs. Then, evolving, the cluster loses most of its 1G stars via tidal interaction with the environment of the Milky Way.
  This model succeed in partially reproducing the chemical patterns observed in the analyzed GCs, while, it fails to reproduce that Na-O anti-correlation.

- **Fast rotating massive stars** ($20M_{\odot}$ and $\sim 100M_{\odot}$) (Decressin et al., 2007b; Krause et al., 2013). As a consequence of rapid stellar rotation, the nuclear burning products gets mixed from the core to the envelope, and then get ejected in the ISM at a later stage. This polluting material then falls toward the cluster center, as in the AGB scenario, when the density is high enough, a second star formation episode incorporates this enriched material in 2G stars. Consequently, the age resulting stellar populations would differ for a few tens of Myrs. As an alternative hypothesis, Krause et al. (2013) proposed that 2G stars may form in the stellar discs of fast rotating massive stars.
  However, as rotating stars are not a peculiarity of GCs, this scenario fails to match the GC specificity constraint. However, 2G-like stars are not observed in the Milky Way halo, thus hindering this model.
  Furthermore, the physical processes responsible for the chemical enrichment of the ISM would produce continuous distribution of the chemical abundances, which would not result in multiple stellar population with discrete chemical variations, as instead is observed.
  Moreover, Decressin et al. (2007a) showed that in order to correctly repro-

duce the lowest abundances of magnesium (Mg), the $^{24}Mg(p,\gamma)^{25}$ nuclear reaction rate needs to be increase with respect to the literature value.

- **Super massive stars (SMS)** Described in Denissenkov & Hartwick (2013) and Denissenkov et al. (2015), this scenario relies on the idea that stars in the center of the cluster can sink together and form SMS of hundreds of solar masses (up to $\sim 10^4 M_\odot$). A star this massive would theoretically be fully convective, and it would lose mass at a really high rate, enriching the ISM on a short timescale. Convection would in turn homogenize the interior of the star, while stellar wind would continuously enrich the ISM with helium CNO cycling and p-capture products, creating the chemical composition observed in 2G stars. Although appealing, this model fails to fulfill many of the observational requirements, as for example SN avoidance, mass budget and Helium enrichment. Specifically, in order to reproduce the maximum Helium abundance observed in GCs, the model needs to be fine tuned.

These are the possible producers of polluted material in the context of multiple stellar generations scenarios. On the other hand, in the case of single star-formation episode, Massive Interacting Binaries (MIB) represent potential donors. Precisely, in a binary system, the primary star envelope rotation would cause chemical mixing, which, when reaching down to the hydrogen-burning shell, would result in CNO and p-capture processing of the material in the whole envelope, hence leading to helium enhancement, oxygen depletion, etc. Next, the processed envelope enrich the ISM in the subsequent common-envelope phase of the MIBs. Within this scenario, 2G stars can form directly out of the MIB ejecta (De Mink et al., 2009) without the need for multiple star formation episodes, as the ejecta can be accreted onto circumstellar disks of young low mass stars.
This model, as the ones previously presented, is not completely consistent with the observations. Moreover, while GCs specificity is fulfilled, and variety might be, populations discreteness is a major problem, because large and random star-to-star differences in the amount of swept/accreted material is expected, thus preventing the formation of discrete populations. Also SN avoidance is an unfulfilled constraint.

1.1.3 A new perspective: Internal dynamics of cluster stars

As we struggle to comprehend the evermore puzzling multi-populations phenomenon, new and more observational constraints are likely the key to the final solution. While, numerous spectroscopic and photometric studies keep providing priceless insights into the chemistry of multiple stellar populations, the spatial morphology, as well as the internal dynamics of cluster stars is still an uncharted territory. This lack of data can be attributed to the challenges that come with this kind of study. As an example, the analysis of the internal dynamics of cluster stars, requires, first of all, the correct identification of different stellar populations over the investigated field of view, and, at the same time, the accurate

knowledge of the proper motions and/or the radial velocities of the very same stars. While the former can be accomplished with great accuracy with the use of the chromosome maps made with *HST* data, the latter presents more complications that have, so far, hindered our path.
For instance, while HST provides very exquisite astrometric measurements, as undoubtedly demonstrated by Bellini and collaborators, it is limited to small field of view and to relative measurements (Bellini et al., 2011, 2015).
Nonetheless, recent theoretical and numerical works (e.g. Vesperini et al., 2013, 2018, 2021; Mastrobuono-Battisti & Perets, 2013, 2016; Sollima, 2021) have shown that the internal dynamics of multiple stellar populations represents a unique opportunity to understand the origin of these populations. Indeed, in the framework of multi-generations scenarios, if second star formation episodes take place in the potential well of the host cluster, the resulting stellar generations would form in a more centrally concentrated environment, with respect to their progenitors. N-body simulations (e.g. Mastrobuono-Battisti & Perets, 2013, 2016; Vesperini et al., 2013; Hénault-Brunet et al., 2015; Tiongco et al., 2019) in turn demonstrate that, in this case, the dynamical evolution of second-generation stars should be significantly different from that of the first generation, and the signature of the different initial conditions could be detected in present-day GC kinematics of GCs, if stars are not fully mixed yet, i.e. if the cluster have yet to completely relax. Precisely, the more centrally concentrated populations would tend to mix with the older populations, displaying a stronger rotation, and a more radially anisotropic motion.
Hence, the present-day dynamics of stellar populations with different metallicities and light-element abundances provide a unique window into the origin of multiple populations in Type-I and type-II GCs.

In the past decade, nearly all works on the internal kinematics of GCs were based on radial velocities of a relatively-small sample of stars (e. g. Norris et al., 1997; Bellazzini et al., 2012; Marino et al., 2014; Cordero et al., 2014) with the study of 650 stars of NGC 5139 (ω Centauri) by Pancino et al. (2007), being a remarkable exception.

More recently, as aforementioned, *HST* provided high-precision relative proper motions of a small but increasing number of clusters, namely NGC 0104 (47 Tucanae), NGC 0362, NGC 2808, NGC 5139 and NGC 6352 that allowed the investigation of the kinematics of multiple populations in the plane of the sky Richer et al. (2013); Bellini et al. (2015, 2018); Libralato et al. (2018, 2019). In all the studies the authors concluded that 2P stars show a more-radially anisotropic velocity distribution. While these works are based on high-precision relative proper motions of thousands of stars, the small field of view of *HST* does not allow the study of the entire cluster.

To overcome this shortcoming and study the kinematics of multiple stellar populations over a large field of view, we started a project based on Gaia Data Release 2

(DR2[1], Gaia Collaboration et al., 2018a) accurate proper motions and multi-band wide-field ground-based photometry. In the pilot paper of this project, we investigated for the first time the kinematics of 1P and 2P stars of NGC 0104 over a wide field of view, up to ~18 arcmin from the cluster center (corresponding to ~ 22 pc, Milone et al., 2018b). During my *Ph.D.* I extended the project investigating the spatial distributions and the 3D kinematics of 7 type-I GCs, namely NGC 0104 and other six GCs, namely NGC 0288, NGC 5904 (M 5), NGC 6121 (M 4), NGC 6254 (M 10), NGC 6752 and NGC 6838 (M 71), and 2 type-II cluster, ω Centauri and M 22, whose physical parameters are listed in Table 2.1 and 2.5.
Section 2.1 and 2.2 describe in detail the results obtained in Cordoni et al. (2020a) and Cordoni et al. (2020b).

1.1.4 Back in time: young globular clusters in Magellanic Clouds

As thoroughly discussed in the previous sections, while observational and theoretical evidence of multiple stellar populations in old galactic GCs keep piling up, their origin still eludes the astronomical community. How can we then solve this puzzle? One possibility is to exploit new data and new techniques to study Galactic GCs, as, for instance, the internal dynamics. Alternatively, young globular clusters could provide priceless clues into the early life of star clusters, and, consequently, into the formation of MPs.
Indeed, at the luminosities of stars belonging to star cluster as old as a few tens or hundreds of Myr, *HST* photometry allows us to exploit the Turn-Off point (TOff) in the CMD to disentangle MPs with a few tens of Myr of difference, thus possibly confirming or excluding different scenarios.
Moreover, while the Milky Way is poor in young globular clusters, the Magellanic Clouds host a vast population of clusters younger than 2 Gyr, with physical properties consistent with old galactic GCs. Much like Milky Way GCs, young star clusters were once considered the prototype of SSP. Surprisingly, *HST* observations revealed the presence of photometrical features not consistent with the presence of a simple stellar populations, immediately shattering the simplistic view of these objects. Specifically, Milone et al. (2009, and series) showed that Magellanic Clouds clusters younger than 2 Gyr exhibit extended Main-Sequence Turn-Offs (eMSTO) and/or split or broad Main-Sequences in their CMD, beyond what is expected from observational uncertainties, reddening effects, field and binary stars contamination. Figure 1.3 displays a collection of CMDs, with clusters ordered based on their ages, from the youngest to the oldest.

As a straightforward interpretation, many authors proposed a prolonged star formation of a few hundreds of Myrs as the likely cause of the observed eMSTOs and split or broad MSs in Magellanic Clouds clusters (Bertelli et al., 2003; Mackey & Broby Nielsen, 2007a; Baume et al., 2007), thus suggesting that young clusters

[1] https://gea.esac.esa.int/archive/

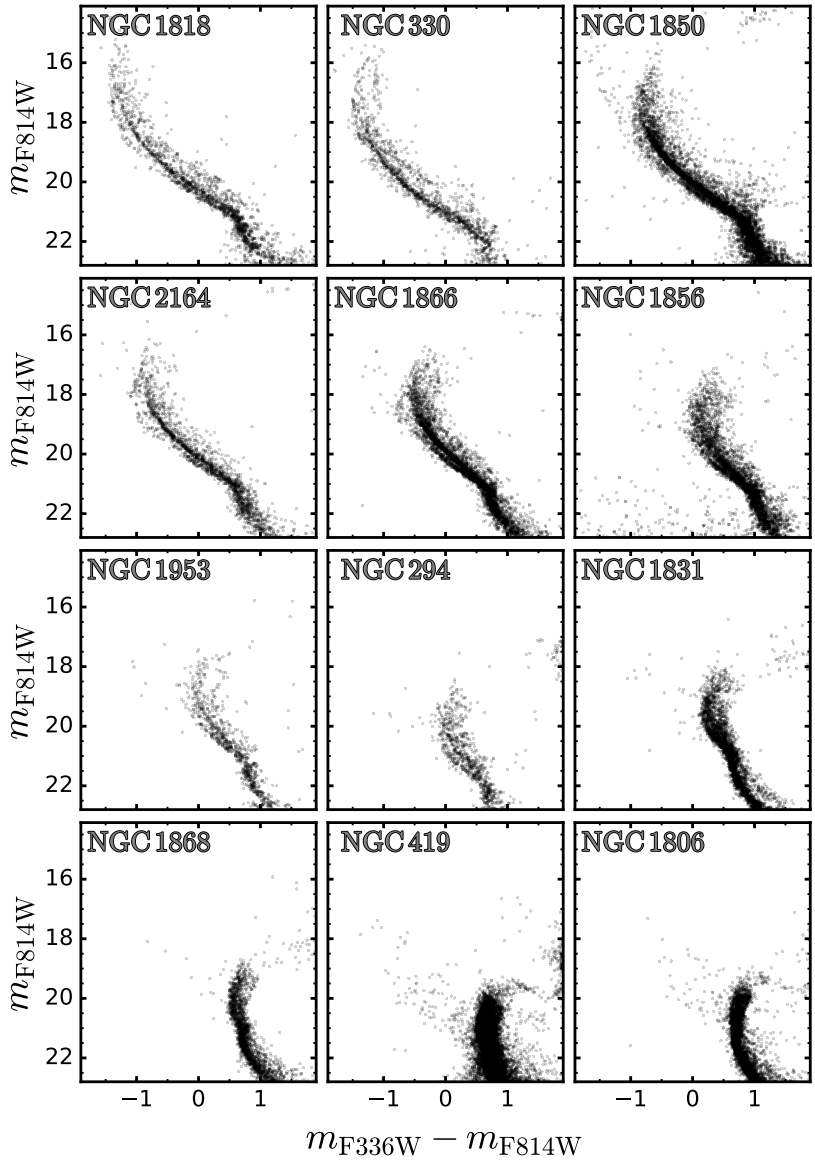

Figure 1.3. $m_{\rm F814W}$ vs. $m_{\rm F336W} - m_{\rm F814W}$ CMDs of NGC 1818, NGC 330, NGC 330, NGC 1850, NGC 2164, NGC 1866, NGC 1856, NGC 1953, NGC 294, NGC 1831, NGC 1868, NGC 419, NGC 1806. The cluster are ordered from the youngest, namely NGC 1818 with an age of 37 Myr, to the oldest, i.e. NGC1806 with 1.750 Gyr.

in the Magellanic Clouds represent the younger counterpart of old galactic GCs. The left panel of Figure 1.4 shows the observed CMD of the ~ 40 Myr old cluster NGC 1818, superimposed with theoretical isochrones which differ only in their

age. m_{F814W} vs. $m_{F336W} - m_{F814W}$ CMD, with two isochrones which only differ for their age, as indicated in the bottom left legend. Clearly, a visual inspection reveals that an age difference of roughly 40 Myr is able to explain the observed spread in the TOff region.
In the following I will refer to this possibility as the "Age spread" scenario. If confirmed, young MC clusters would allow us to study the early life of MPs, possibly leading to the understanding of this phenomenon.

Nonetheless, while MPs in old GCs are characterized by the presence of light-elements variations, no evidence of chemical differences have been detected in stars belonging to these young stellar systems (Mucciarelli et al., 2011; Martocchia et al., 2018), thus casting some shadows on the connection between young and old clusters.
Following an alternative hypothesis, eMSTOs and split or broad MSs would represent the result of the presence of stars with different rotational velocities. Indeed, depending on the initial mass, rotational velocity, and chemical composition of the star, the centrifugal acceleration may either reduce the effective gravity causing a decrease in both temperature and luminosity, or it may induce internal mixing, which can lead to an increase in both temperature and luminosity. Furthermore, the temperature becomes a function of the viewing angle, which again can create an intrinsic color extension. Such effects can therefore explain the morphology of the observed CMDs, without the need of the presence of multiple stellar generations.
Specifically, it seems that a fast-rotating stellar population, beside a non-rotating one, are required to reproduce the observed red and blue MS, respectively (Milone et al., 2016b, 2018b). The right panel of Figure 1.4 shows the CMD of NGC 1818, with superimposed rotating and non-rotating isochrones, shown with dashed and solid lines, respectively.
Clearly, both the age spread and the rotational scenario are able to reproduce the color extension in the TOff region, and, such degeneracy between age and rotation makes it virtually impossible to discern between the two models.

During my master thesis, I analyzed 27 Magellanic Clouds clusters younger than 2 Gyr to disentangle between the two possible interpretation here depicted. My analysis suggested that, while rotation is likely the main driver of MPs in Magellanic Clouds clusters, a residual age spread of a few tens of Myr could still be needed to match the observed color extension. The same conclusion was previously reached by Milone and collaborators (Milone et al., 2017b) analyzing NGC 1866.
Figure 1.5 shows the observed age spread against the age of the host cluster with filled gray circles, while the trend expected in the case of differently rotating stellar populations is represented with a filled orange stars. Only clusters younger than 1.5 Gyr are shown in Figure 1.5 because of the lack of rotating models of older stellar populations at the time of the study. From a visual inspection, it is clear that the observed age spread agrees with the predictions of the rota-

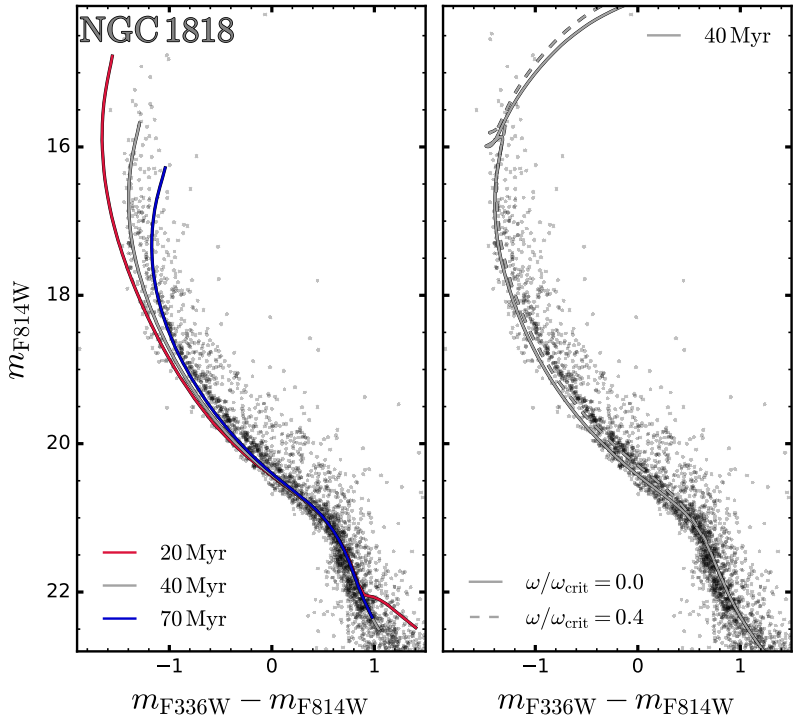

Figure 1.4. *Left panel.* $m_{\rm F814W}$ vs. $m_{\rm F336W} - m_{\rm F814W}$ CMD of NGC 1818 with isochrones from the Padova models (Marigo et al., 2017) computed for different ages, namely 20, 40 and 70 Myr. *Right panel.* The same CMD is shown in the left panel, together with isochrones with rotation rate, namely $\omega/\omega_{\rm crit}$ = 0., 0.4, computed with the MIST models (Dotter, 2016).

tional model, thus confirming the key role of stellar rotation. Nonetheless, an age spread of a few tens of Myr still cannot be excluded, as some clusters exhibit a spread larger than the predicted one. I refer to Section 3.2 for a detailed description of the procedure used to infer such results[2].
Furthermore, confirming the central role of stellar rotation, Marino et al. (2018a) found, for the first time, direct spectroscopic evidence of the alleged spread in stellar rotation among stars in NGC 1818.

Quite interestingly, while our Galaxy contains virtually no GC younger than a few Gyr, that is not the case for Open clusters (OCs). As a matter of fact, the Milky Way hosts a large population of OCs, many of which are younger than 1-2, hence being consistent with their Magellanic Clouds "counterpart". Considering that OCs and GCs are very different objects, the comparison between OCs and GCs in the same age range can provide fundamental clues on the nature of the physical processes happening in young star clusters. For instance, are these phenomena linked to the particular age of the cluster, i.e. to the physical properties of stars

[2]The procedure described in Section 3.2 is however applied to Galactic Open clusters, but has been developed in the context of my master thesis on Magellanic Clouds clusters.

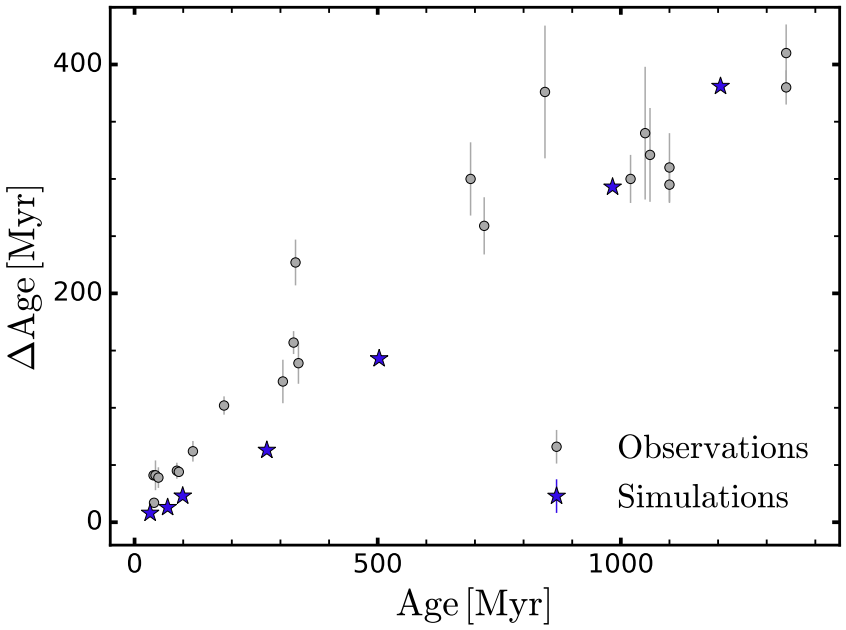

Figure 1.5. ΔAge vs. Age relation for 22 Magellanic Clouds clusters younger than 1.5 Gyr, marked with gray filled circles. Orange stars indicate the expected age spread in the context of the rotational scenario, discussed in the previous paragraphs, derived with Geneva SYCLIST models. These data are the results of the work carried out in the context of my master thesis, which is publicly available at http://tesi.cab.unipd.it/61306/1/Tesi_Giacomo_CORDONI.pdf

in that age range? Or are they link to the properties of the host cluster, being therefore specific to GCs?

In the last years, Gaia Data Release 2 (DR2 Gaia Collaboration et al., 2016), and now GAIA early DR3 (eDR3 Gaia Collaboration et al., 2021), revolutionized the field of Galactic astronomy with accurate photometric and astrometric data for nearly 1.5 billions of stars in the Milky Way. Hence, the Gaia dataset represents the perfect "tool' to answer our questions[3]. My analysis (Cordoni et al., 2018), discussed in detail in Section 3.2, revealed that eMSTOs and split or broad-MSs are a common feature among Galactic OCs younger than 1-2 Gyr. The CMDs of the 12 analyzed Galactic OCs present the very same features observed in young Magellanic Clouds clusters with the alleged age spread correlating with cluster age, in the same fashion as Magellanic Clouds clusters (see Figure 1.5, following the trend expected in the framework of the rotational scenario.

These results suggest that the peculiar features observed in both young Magellanic Clouds cluster and young Open clusters in the Milky Way could be linked to evolutionary phases of the host clusters and its stars. It remains unclear, if, beside this "rotational" multiple stellar populations, Magellanic Clouds clusters

[3]At the time of the analysis Gaia DR2 was the up to date data release

also host multiple stellar generations, as discussed in Milone et al. (2017b) and D'Antona et al. (2017). Indeed, in order to reproduce the brighter portion of the TOff, it seems that the presence of a younger non-rotating population would be required. As an alternative hypothesis, D'Antona et al. (2017) suggested that these brighter, non rotating and allegedly younger stars would be stars that were initially rotating, but then braked as a consequence of some physical mechanism. In this case, these stars would be in a younger evolutionary state, thus only mimicking younger stars.
So, in order to settle the debate on the presence of a residual age spread, I proposed a new approach which makes use of the Main-Sequence Turn-On as an unbiased clock to date the cluster and its multiple stellar populations, if present, exploiting deep *HST* observations of which I am Principal Investigator (Cordoni et al., 2019). Such method allows us to fully discriminate between age and stellar rotation effects, concluding, once and for all, the controversy on whether stellar rotation alone can explain the observations of young Magellanic Clouds clusters. Section 3.1 explain in detail the adopted procedure.
Indeed, as the magnitude of Main-Sequence Turn-On is uniquely determined, in first approximation, by the age of the stellar population, the presence of multiple stellar generations would be revealed by the presence of multiple or extended Main-Sequence Turn-On. On the other hand, rotation has no, or negligible, effect on the luminosity, so that there is no degeneracy between the rotation and age difference.

1.2 Galactic archaeology through "the First stars"

As discussed in the first paragraph, galactic archaeologists exploit the fossils spread in our neighbourhood to shed light on the early Universe, and, in Section 1.1 we discussed ancient Galactic GCs as possible fossils. However, much information can be gained studying "simpler" and yet very intriguing objects: the "First star". These stars, the so-called population-III stars, (pop-III) provide a fundamental window into the first phases of our Cosmos, allowing us to study, for instance, the pristine chemical composition of the ISM. As these stars would form just a few hundred Myr after the Big Bang, their chemical composition would reflect that of the surrounding Universe: Hydrogen, Helium and small amount of Lithium.
Hence, these stars would exhibit a metal-free chemical composition, and, theoretically, they would be hundreds of times more massive than our Sun, with a lifetime of a few Myrs. Given their mass, these stars would then enrich the interstellar medium with the products of their nucleosynthetic processes, i.e. elements heavier than Helium such as metals, either by means of stellar winds, or exploding as Supernovae.
Such enriched material would then be incorporated by the direct progenies of pop-III, and the subsequent generations of stars. It is clear that, in this model, the older a star, the more metal-poor it is, and viceversa, the more metal-rich a star is, the younger it is. In other words, the metal content of a star can be considered as a proxy of its age.
As aforementioned, pop-III stars are characterized by large masses and short lifetimes, so that their direct observation is incredibly challenging. Indeed, despite our efforts, no pop-III has been detected so far. On the other hand, stars born out of the ejecta of the first stars, i.e. the most metal-poor stars, despite being very rare, are observable today, and their detailed chemical studies can reveal fundamental insights into the properties of the notorious pop-III stars.

In the last decade, the astronomical community has experienced a renewal of interest in the properties of low-metallicity stars, particularly those with [Fe/H] < -2 dex[4]. Motivated by the successful surveys of Beers et al. (1992) and Christlieb et al. (2008), in recent years numerous spectroscopic (e.g., SDSS, SEGUE, LAMOST, APOGEE; York et al., 2000; Yanny et al., 2009; Cui et al., 2012; Zhao et al., 2012; Majewski et al., 2017) and photometric (e.g., Pristine, SkyMapper; Starkenburg et al., 2017; Wolf et al., 2018) surveys have been commissioned, scanning extensive sky-areas for these very rare and key objects. We refer to Da Costa et al. (2019, their Section 1) for a more complete list of spectro-photometric surveys targeting low-metallicity stars. Not surprisingly, the underlying scientific motive is the understanding of the formation of our Galaxy, as well as other galaxies in the Universe.

[4]We will generally endeavour to follow the convention of Beers & Christlieb (2005) in that the terminology 'very', 'extremely', 'ultra', etc, metal-poor indicates [Fe/H] < –2.0, –3.0 and –4.0, respectively.

Specifically, the lowest metallicity stars observable at the present-day formed from gas enriched with the nucleosynthetic products from first generation metal-free stars, the so-called Population-III stars. Studies of abundances and abundance ratios in ultra- and extremely metal-poor stars can then yield constraints on the properties of the Pop III stars, such as their masses, and on star formation processes at the earliest times (e.g., Frebel & Norris, 2015). Moreover, the kinematics of these stars can also provide much information on the events that occurred during the formation of the Milky Way (MW), which is believed to include both star formation in-situ and the accretion of lower-mass galaxies. Indeed, together the abundances and kinematics of the lowest metallicity stars offer a distinct perspective on the earliest stages of the formation and evolution of the Milky Way, and by implication, of galaxies in general.

In terms of the formation of the MW, the most common scenario predicts that the most metal-poor stars will be found mainly in the Galactic halo and Bulge, as these components likely formed in the earliest stages of the MW's evolution (e.g. White & Springel, 2000; Brook et al., 2007; Tumlinson, 2010; El-Badry et al., 2018). In such a scenario relatively few, if any, very metal-poor stars are expected to lie in the MW disk as it formed at a later epoch after the settling into the plane of gas enriched by multiple generations of star formation (e.g. Bland-Hawthorn & Gerhard, 2016). However, recent kinematic results from surveys for the most metal-poor stars have cast doubt on this scenario, altering our understanding of the formation of the Milky Way. For example, the recent studies of Sestito et al. (2019, 2020b), Di Matteo et al. (2020) and Venn et al. (2020) have revealed a new scenario where $\sim$ 20 % of very metal-poor stars have orbits that are confined to within 3 kpc of the MW plane; evidently the majority of these stars are not Galactic halo objects despite their low metallicities.

In particular, Sestito et al. (2019) compiled a catalogue of 42 ultra metal-poor ([Fe/H] $\leq$ –4.0) stars from the literature and analyzed their orbital properties making use of Gaia DR2 proper motions (Gaia Collaboration et al., 2018b). They found that 11 out of 42 stars have prograde orbits that are confined to within 3 kpc of the Milky Way disk. Moreover, two of these MW-planar stars are found to be on nearly circular prograde orbits, and one is the star with the lowest overall metal content currently known (Caffau et al., 2011). In the same fashion, Di Matteo et al. (2020) investigated the kinematics of a sample of coincidentally the same number of low-metallicity stars drawn from the ESO Large Program "First stars – First nucleosynthesis" (Cayrel et al., 2004). Their analysis also finds that $\sim$ 20% of the stars show disk-like kinematics. They went on to consider a larger sample of stars covering a wider metallicity range and found consistent results. Di Matteo et al. (2020) then postulated the existence of an "ultra-metal poor thick disk" that is an extension to low metallicities of the Galaxy's thick disk population.

Sestito et al. (2020b) carried out a similar kinematic analysis on a substantially larger sample, consisting of 1027 very metal-poor stars with [Fe/H] $\leq$ –2.5 selected from the Pristine (Starkenburg et al., 2017; Aguado et al., 2019) and LAMOST (Cui et al., 2012; Li et al., 2018) surveys. Again they find that almost 1/3rd of the stars in the sample have orbits that do not deviate significantly from the

disk plane of the Galaxy. They suggest that this implies that a significant fraction of the MW's metal-poor stars formed with the Milky Way (thick) disk. Moreover, they note that as a consequence, the history of the disk must have been sufficiently quiescent that (presumably old) metal-poor stars were able to retain their disk-like orbits to the present-day (Sestito et al., 2020b).
Venn et al. (2020) have also investigated the kinematics of metal-poor stars using a sample of 115 objects chosen from the Pristine survey (Starkenburg et al., 2017) that have been observed at high dispersion. They find 16, out of 70, metal-poor stars whose orbits are confined to the vicinity of the Galactic plane, together with small numbers of stars that may have unbound orbits. They also identify stars whose orbital characteristics/actions are consistent with an origin in the *Gaia Enceladus* (Helmi et al., 2018) accretion event.
These somewhat unexpected results support the idea that the metallicity distribution of the Galaxy's thick disk does indeed possess a low metallicity tail, as first advocated by Norris et al. (1985) and Morrison et al. (1990). Moreover, the proposed low metallicity tail would extend to lower metallicities than those authors suggested (see also Chiba & Beers, 2000; Beers et al., 2014).
The origin(s) of these metal-poor thick disk stars is, however, still uncertain, though the implications of their existence for the formation and evolution of the MW, and disk galaxies in general, are likely significant. A number of different possibilities have been discussed (e.g. Sestito et al., 2019, 2020b; Di Matteo et al., 2020) including that the stars were accreted from small satellites once the MW disk had already formed, or that they represent low metallicity stars formed in the gas-rich building-blocks that came together to form the main body of the Galaxy's disk (see also the theoretical simulations presented in Sestito et al., 2020a).
In my work, presented in Section 4.1, I conducted a similar study to those mentioned above by exploiting the metallicity determinations from the *SkyMapper Survey for extremely metal-poor stars* (see Da Costa et al., 2019), together with Gaia DR2 astrometry (Gaia Collaboration et al., 2018b), to investigate the dynamics of 475 very metal-poor ([Fe/H] < -2) stars in the southern sky. The wide extension in metallicity space, together with the relatively large number of stars, provide us with a detailed view of the kinematic properties of these objects. We also consider the potential connection of any of the stars in our sample with the MW accretion events, such as those designated *Gaia Enceladus, Gaia Sausage* and *Gaia Sequoia* that have been recently discovered in large scale analyses of Gaia DR2 data (e.g. Helmi et al., 2018; Belokurov et al., 2018; Myeong et al., 2019; Mackereth et al., 2019). Such a connection has also been pursued in Monty et al. (2020).
The detailed results are discussed in Section 4.1

1.2.1 Thesis layout

The present thesis is structured as follows: Chapter 1 presents an overview of the literature framework, while in Section 2.1 and 2.2 I discuss the results concerning the dynamical properties of multiple stellar populations in Type I and Type II

Galactic Globular clusters, respectively. The multipopulation phenomenon in Young Galactic Open clusters and Young Magellanic Clouds clusters is addressed in Section 3.1 and 3.2, and in Chapter 4 I investigate the kinematics of Extremely Metal-Poor stars. Finally, the conclusion of my *Ph.D.* project are presented in Chapter 5.

CHAPTER

2 Multiple Stellar populations in Globular Clusters. A dynamical perspective

2.1 Three-Component Kinematics of Multiple Stellar Populations in Globular Clusters with Gaia and VLT.

This Section is taken from Cordoni et al. (2020a).

Abstract

The internal dynamics of multiple stellar populations in Globular Clusters (GCs) provides unique constraints on the physical processes responsible for their formation. Specifically, the present-day kinematics of cluster stars, such as rotation and velocity-dispersion, could be related to the initial configuration of the system. In recent work, we provided the first study of the kinematics of different stellar populations in NGC0104 over a large field of view in the plane of the sky, exploiting Gaia Data Release 2 (DR2) proper motions combined with multi-band ground-based photometry.
In this paper, we combine Gaia DR2 proper motions with Very Large Telescope radial velocities to investigate the kinematics along the line of sight and in the plane of the sky of multiple populations in seven GCs, namely NGC0104, NGC0288, NGC5904, NGC6121, NGC6254, NGC6752 and NGC6838. Among the analyzed clusters only NGC0104 and NGC5904 show significant rotation.
Separating our sample into two groups of first- and second-population stars (1P and 2P) we find that overall these two populations exhibit a similar rotation pattern in NGC0104. However, some hints of different rotation are observed in the external regions of this cluster. Interestingly, 1P and 2P stars in NGC5904 show different rotation curves, with distinct phases and such difference is significant at the ~2.5-σ level. The analysis of the velocity-dispersion profiles of multiple

populations confirms that 2P stars of NGC 0104 show stronger anisotropy than the 1P.

2.1.1 Introduction

Studies based on *Hubble Space Telescope* (*HST*) images revealed that the photometric diagrams of nearly all GCs are composed of two main groups of first- and second-population stars (1P, 2P, e.g. Milone et al., 2017a) with different chemical compositions (e.g. Marino et al., 2019b). Many efforts have been made to understand their origin, but, so far, none of the proposed scenarios have been able to reach a satisfactory agreement with observations (e.g. Renzini et al., 2015).
According to many of these scenarios, 2P stars formed out of the ejecta of 1P more-massive stars (e.g. Ventura et al., 2001b; Decressin et al., 2007a; D'Ercole et al., 2010b; Denissenkov & Hartwick, 2014) after the segregation of the gas in the cluster center. As a consequence, 2P stars may have formed in a more centrally-concentrated environment.
As an alternative hypothesis, GCs host a single stellar generation and stars with different chemical composition are the product of exotic physical phenomena specific of proto-GCs (e.g. de Mink et al., 2009; Bastian et al., 2013; Gieles et al., 2018).
An important signature of the physical processes responsible for the formation of multiple populations is the kinematics of cluster stars. Specifically, N-body simulations suggest that the dynamical evolution of more centrally-concentrated 2P stars should be significantly different from that of 1P stars, and such difference could still be observable in present-day GC kinematics (e. g. Vesperini et al., 2013; Mastrobuono-Battisti & Perets, 2013, 2016; Hénault-Brunet et al., 2015; Tiongco et al., 2019).
In the past decade, nearly all works on the internal kinematics of GCs were based on radial velocities of a relatively-small sample of stars (e. g. Norris et al., 1997; Bellazzini et al., 2012; Marino et al., 2014; Cordero et al., 2014) with the study of 650 stars of NGC 5139 (ω Centauri) by Pancino et al. (2007), being a remarkable exception.
More recently, *HST* provided high-precision relative proper motions of a small but increasing number of clusters, namely NGC 0104 (47 Tucanae), NGC 0362, NGC 2808, NGC 5139 and NGC 6352 that allowed the investigation of the kinematics of multiple populations in the plane of the sky Richer et al. (2013); Bellini et al. (2015, 2018); Libralato et al. (2018, 2019). In all the studies the authors concluded that 2P stars show a more-radially anisotropic velocity distribution. While these works are based on high-precision relative proper motions of thousands of stars, the small field of view of *HST* does not allow the study of the entire cluster.
To overcome this shortcoming and study the kinematics of multiple stellar populations over a large field of view, we started a project based on Gaia Data Release 2 (DR2[1], Gaia Collaboration et al., 2018a) accurate proper motions and multi-

[1] https://gea.esac.esa.int/archive/

band wide-field ground-based photometry. In the pilot paper of this project, we investigated for the first time the kinematics of 1P and 2P stars of NGC 0104 over a wide field of view, up to ~18 arcmin from the cluster center (corresponding to ~ 22 pc, Milone et al., 2018b). In the present work, we analyse the spatial distributions and the 3D kinematics of NGC 0104 and other six GCs, namely NGC 0288, NGC 5904 (M 5), NGC 6121 (M 4), NGC 6254 (M 10), NGC 6752 and NGC 6838 (M 71), whose physical parameters are listed in Table 2.1.
The paper is organized as follows: in Section 2.1.2 we introduce the dataset and present the photometric diagrams of the analyzed clusters. In Section 2.1.3 we analyze the spatial distribution of multiple stellar populations. The 3D rotation of 1P and 2P stars and their velocity dispersion are investigated in Sections 2.1.4 and 2.1.5, respectively. Finally, Section 2.1.6 provides the summary and the discussion of the results.

2.1.2 Data and data analysis

To investigate the internal kinematics of multiple stellar populations in each GC, we combined ground-based wide-field photometry, proper motions from Gaia DR2 and high-precision radial velocities provided by Baumgardt & Hilker (2018) and derived from archival ESO/VLT and Keck spectra together with published radial velocities from the literature.
Photometry in U, B, V, I bands has been derived by Peter Stetson from images collected with various facilities and by using the methods and the computer programs by Stetson (2005) and Stetson et al. (2019). Photometry has been calibrated on the reference system by Landolt (1992). Details on the dataset and on the data reduction are provided by Monelli et al. (2013) and Stetson et al. (2019). The photometric catalogs by Stetson and collaborators have been widely used to investigate multiple populations in GCs (e.,g. Monelli et al., 2013; Marino et al., 2016, 2017; Milone et al., 2012b, 2018b; Stetson et al., 2019). Most of these works are based on the pseudo color $C_{\rm U,B,I} = (U-B)-(B-I)$, which is an efficient tool to identify stellar populations with different light-element abundance along the RGB and will be used in the following to identify 1P and 2P stars. We corrected proper motions for the perspective expansion/contraction due to the bulk motion of the GC by means of Equation 6 in van de Ven et al. (2006).
As well established in the literature, Gaia DR2 proper motions suffer from systematic errors that mostly depend on stellar colors and positions (e.g. Gaia Collaboration et al., 2018a; Bianchini et al., 2018; Lindegren et al., 2018; Sollima et al., 2019; Vasiliev, 2019a,b). In this work we are interested in the relative motions of groups of 1P and 2P stars that are almost indistinguishable to the eye of Gaia, as they have similar colors and magnitudes and, to a first approximation, share the same spatial distributions. As a consequence, the systematic errors associated with the motions of both populations are similar and their effects on the relative motions of 1P and 2P stars may be cancelled out when infinite amounts of 1P and 2P stars are available. However, in the case of finite numbers of stars the effect of systematics on the relative proper motions of the two populations may not en-

tirely cancel out. In this work, we used a conservative approach and followed the recipe described in (Vasiliev, 2019b)[2] to entirely account for systematic errors in our analysis of 1P and 2P stars. Since we are considering relative motions, our error estimates would overestimate the true uncertainties.

Selection of cluster members

To study the kinematics of stellar populations in GCs we need accurate stellar proper motions. To identify a sample of RGB stars with high-quality astrometric measurements we exploited the method used by Milone et al. (2018b) and Cordoni et al. (2018), which is illustrated in Figure 2.1 for NGC 6838, and exploits the parameters provided by the Gaia DR2.
In a nutshell, we first selected a sample of stars with high-accuracy proper motions, by using the `astrometric_gof_al` (`As_gof_al`) parameter, indicative of the goodness of fit statistics of the astrometric solution for the source in the along-scan direction (see Gaia Collaboration et al., 2018a, for details), and the renormalized unit weight error Lindegren et al. (2018). To do this, we divided the $G_{\rm RP}$-magnitude range between 11.0 and 18.5 into bins of 0.5 mag. We calculated the median magnitude ($G_{\rm RP,i}$), the median `As_gof_al` value ($\texttt{As\_gof\_al}_{\rm i}$) and the corresponding random mean scatter ($\sigma_{\rm i}$) for stars in each magnitude bin (i). We associated the values of $G_{\rm RP,i}$ and $\texttt{As\_gof\_al}_{\rm i} + 4\,\sigma_{\rm i}$ and linearly interpolated these points to derive the green line of Figure 2.1a. We considered those stars that lie on the left side of the green line as well measured. Moreover, only stars with proper motion uncertainties smaller than 0.35 mas/yr have been included in our analysis.
We determined cluster membership of each star using the same procedure described in (Cordoni et al., 2018, see their Section 2). Briefly, we analyzed the proper motion vector-point diagram (VPD) shown in panel d of Figure 2.1, and derived by eye a circle enclosing most cluster stars. Then, we calculated the proper motion of each star relative to the cluster mean motion ($\mu_{\rm R}$). We plotted $\mu_{\rm R}$ against the $G_{\rm RP}$-magnitude and selected only stars with dispersion lower than 4σ from the mean relation. We then repeated the same procedure for the parallax, π. This procedure has been iterated three times. We verified that the sample of cluster stars identified from the criteria described above is nearly coincident with that obtained by following the method by Vasiliev (2019a), which is based on Gaussian mixture models. When we adopt the latter stellar sample the conclusions of the paper remain unchanged.
As a final step, the U, B, V, I photometry of cluster members has been corrected for differential reddening using the method described in (Milone et al., 2012a, see their Section 3.1). In a nutshell, we first derived the fiducial line of MS and SGB stars in the I vs. $(B-I)$ plane, where 1P/2P stars are almost indistinguishable, and we calculated the residuals from this line. Then we selected 35 neighbors MS and SGB bright cluster members and computed the median of

[2] code publicly available at https://github.com/GalacticDynamics-Oxford/GaiaTools

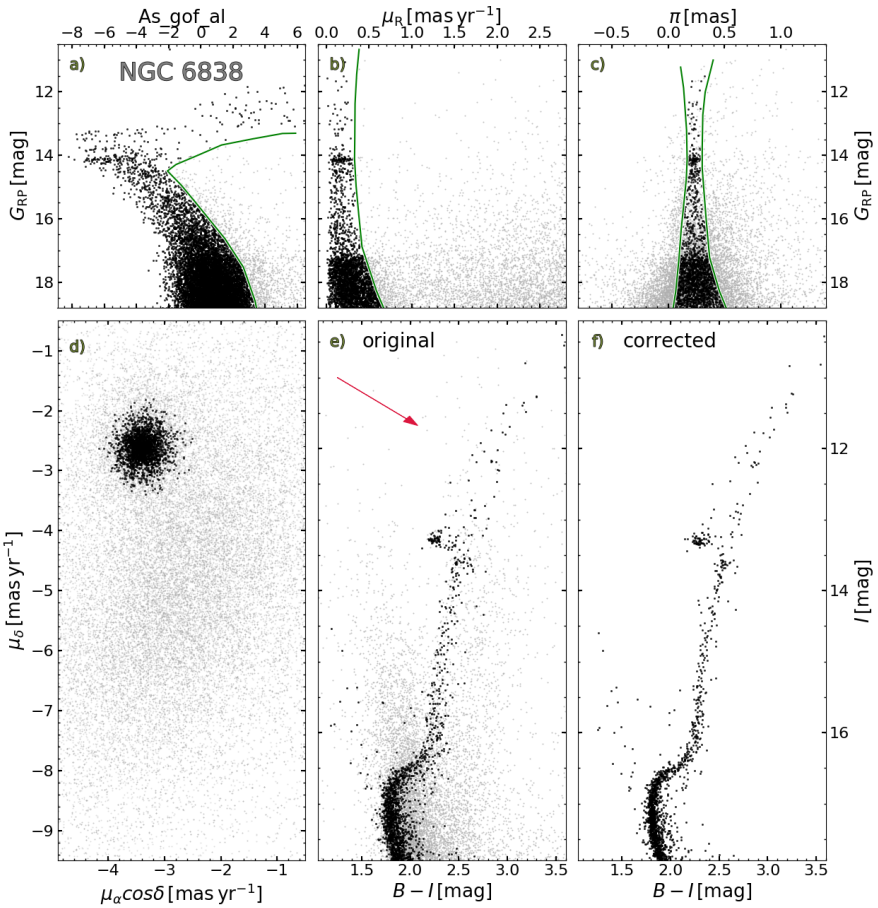

Figure 2.1. Illustration of the procedure to select stars with high-quality proper motions and to determine the *bona-fide* cluster members of NGC 6838. Panels a, b, and c show the G_{RP} magnitude from Gaia DR2 against the `As_gof_al` parameter, stellar proper motions relative to the cluster mean motion, μ_R, and parallax, π, respectively. The green lines separate cluster members (black points) from field stars (gray points). The proper motion vector-point diagram is plotted in panel d. Panels e and f compare the original I vs. $B-I$ CMD of cluster members with the CMD corrected for differential reddening. The red arrow in panel e represents the reddening vector and corresponds to a reddening variation of E($B-V$)=0.3. See text for details.

the color-residuals, calculated along the reddening direction, as our differential-reddening estimate. In panels e and f of Figure 2.1 we compare the original I vs. $(B-I)$ CMD of NGC 6838 members and the corresponding CMD corrected for differential reddening. Clearly, the comparison between the original and the differential-reddening free CMD suggests that our correction provides much narrower photometric sequences, demonstrating the goodness of our procedure.

Multiple populations along the color-magnitude diagrams

To distinguish 2P from 1P stars we exploit photometric diagrams based on the $C_{\rm U,B,I}$ index. Indeed, a visual inspection of our V vs. $C_{\rm U,B,I}$ diagrams of cluster members, reveals that 1P and 2P stars of the analyzed GCs define two distinct RGBs (see also Monelli et al., 2013; Marino et al., 2016, 2017; Milone et al., 2012b, 2018b).

The procedure that we used to identify the sample of 1P and 2P stars is illustrated in Figure 2.2 for NGC 6838 and is based on the V vs. $C_{\rm U,B,I}$ diagram plotted in panel a. The red and blue lines superimposed on the diagram correspond to the RGB boundaries and are derived as in (Milone et al., 2017a, see their Section 3). In the case of NGC 6838 we only used stars in the magnitude interval between V=12.0 and V=17.5, where the RGB split is clearly visible. In a nutshell, we first divided the magnitude interval between V=14.0 and V=17.5 into a series of bins of size dV = 0.9 mag. The bins are defined over a grid of points separated by 0.3 mag. For each bin we calculated the average V magnitude and associate its value to the $4^{\rm th}$ and the $96^{\rm th}$ percentile of the $C_{\rm U,B,I}$ distribution of RGB stars. We smoothed these points by using boxcar averaging, where we substituted each point with the average of its three adjacent points. Due to the small number of stars brighter than V = 14.0, the fiducial points of the portion of the RGB with $12.0 \lesssim V \lesssim 14.0$ are drawn by eye.

The fiducial lines are verticalized as in (Milone et al., 2015, see their Section 3.1) to derive the V vs. $\Delta C_{\rm U,B,I}$ diagram plotted in panel b. Panel c of Figure 2.2 shows the histogram and the kernel-density distribution of the $\Delta C_{\rm U,B,I}$ for RGB stars with $12.0 < V < 17.5$. Clearly, the $\Delta C_{\rm U,B,I}$ distribution represented in panels b and c allows us to distinguish 1P stars (represented with red circles) from 2P stars (blue triangles), based on the vertical dashed line.

The same procedure illustrated for NGC 6838 has been applied to the other six clusters that we have analyzed. Figure 2.3 shows the V vs. $C_{\rm U,B,I}$ diagrams and the corresponding $\Delta C_{\rm U,B,I}$ histograms and kernel-density distributions of RGB stars for NGC 0104, NGC 0288, NGC 5904, NGC 6121, NGC 6254 and NGC 6752. The RGB of each cluster defines two distinct sequences and allows us to select the groups of 1P (red dots) and 2P stars (blue triangles). Only the selected 1P and 2P RGB stars will be used to explore the kinematics of multiple populations in each GC. In NGC 0104 and NGC 6838, we included in the analysis 1P and 2P HB stars that we selected from the $U-B$ vs. $B-I$ two-color diagram as in Milone et al. (2012b).

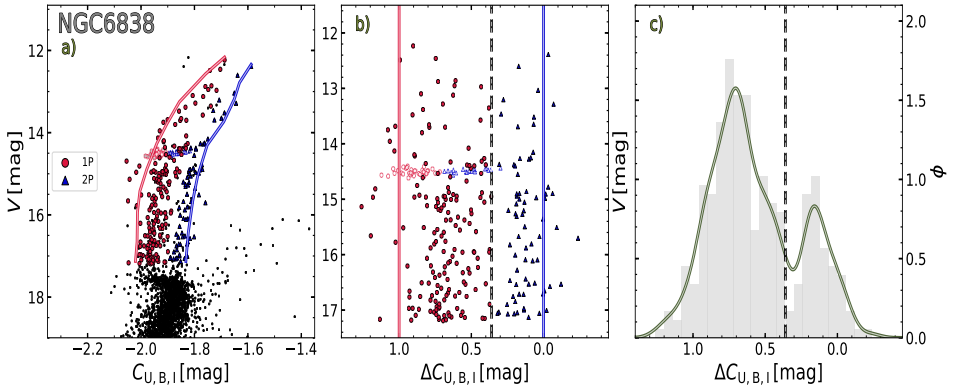

Figure 2.2. This figure illustrates the procedure to select 1P and 2P stars along the RGB of NGC 6838. Panel a shows the V vs. $C_{\rm U,B,I}$ diagram for cluster members, while the verticalized V vs. $\Delta C_{\rm U,B,I}$ diagram for RGB stars and the corresponding $\Delta C_{\rm U,B,I}$ histogram distribution are plotted in panel b and c, respectively. The red and blue continuous lines mark the boundaries of the RGB, while the dashed gray vertical line is used to separate 1P (red circles) stars from 2P stars (blue triangles). HB stars are marked with empty symbols. The continuous line superimposed on the histogram represents the $\Delta C_{\rm U,B,I}$ kernel-density distribution of RGB stars. See text for details.

ID	RA (J2000)[3]	DEC (J2000)[a]	mass[b] [$M_\odot$]	$d_{\rm sun}$[4] [kpc]	$R^{\rm a}_{\rm Gal}$ [kpc]	$R^{\rm b}_{\rm c}$ [arcmin]	$R^{\rm b}_{\rm h}$ [arcmin]	$\bar{V}^{\rm b}_{\rm LoS}$ [km/s]	$\log\tau^{\rm b}_{\rm RH}$ yr
NGC 0104	00 24 05.67	−72 04 52.6	7.79×10^5	4.41	7.40	0.38	2.78	-17.20	9.58
NGC 0288	00 52 45.24	−26 34 57.4	1.16×10^5	9.80	12.0	1.67	2.45	-44.83	9.58
NGC 5904	15 18 33.22	+02 04 51.7	3.72×10^5	7.50	6.20	0.55	1.65	53.70	9.45
NGC 6121	16 23 35.22	−26 31 32.7	9.69×10^4	2.14	5.90	1.06	4.53	71.05	8.99
NGC 6254	16 57 09.05	−04 06 01.1	1.84×10^5	4.71	4.60	0.59	2.03	74.02	9.15
NGC 6752	19 10 52.11	−59 59 04.4	2.39×10^5	4.30	5.20	0.15	1.92	-26.28	9.16
NGC 6838	19 53 46.49	+18 46 45.1	4.91×10^4	3.86	6.70	0.46	2.63	-22.27	8.90

Table 2.1. Identification, positional data and adopted structural parameters for the analyzed clusters. For each cluster we list position (RA, DEC), distance from the Sun, galactocentric radius ($R_{\rm Gal}$), mass, core radius ($R_{\rm c}$), half-light radius ($R_{\rm h}$), line-of-sight mean velocity ($\bar{V}_{\rm LoS}$) and half-mass relaxation time ($\log\tau_{\rm RH}$).

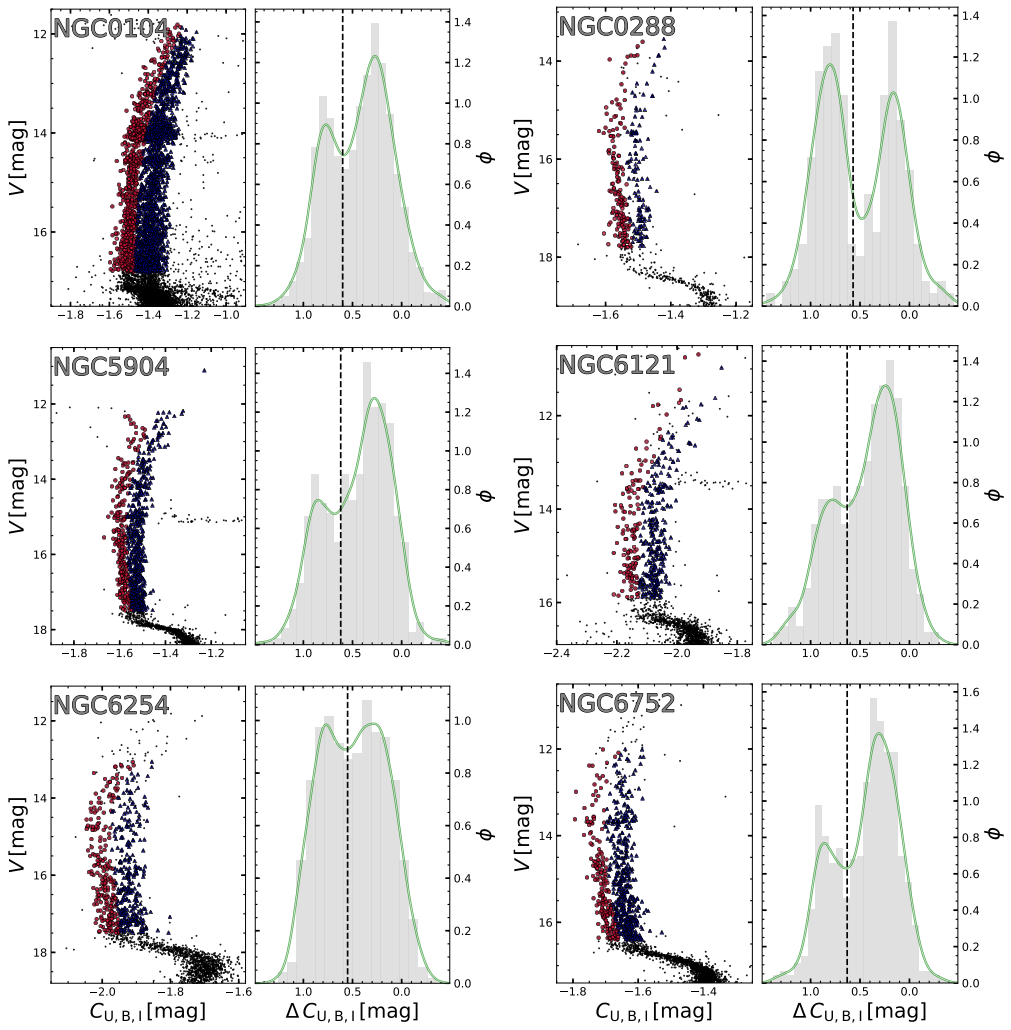

Figure 2.3. V vs. $C_{U,B,I}$ diagrams for the selected cluster members of NGC 0104, NGC 0288, NGC 5904, NGC 6121, NGC 6254 and NGC 6752 (left panels). The panels on the right show the histogram and the kernel-density $\Delta C_{U,B,I}$ distributions for the RGB stars that we used to investigate the internal kinematics of stellar populations. The vertical dashed lines separate the selected 1P and 2P stars that are colored red and blue, respectively, in the left-panel diagrams.

2.1.3 Spatial distribution

In the following, we analyze the spatial distribution of the two groups of 1P and 2P stars that we identified in the previous section for the seven analyzed clusters. To do this, we used a procedure, which is based on the 2D Binned Kernel Density Estimate[5], illustrated in the left and right panels of Figure 2.4 for the first and second population of NGC 5904, respectively. The levels of red and blue in the upper panels are indicative of the density of 1P and 2P stars in a reference frame where the origin corresponds to the cluster center and the X and Y axes point towards the directions of increasing RA and DEC.
We calculated six and nine iso-density contour lines for 1P and 2P respectively, spaced by 0.001 in normalized density unit (black lines in the upper panel). We used the algorithm by Halir & Flusser (1998) to fit each contour line with an ellipse by means of least-squares and plot the best-fit ellipses in the bottom-left panel of Figure 2.4, where we also show the corresponding directions of the major axes. A visual inspection of Figure 2.4 suggests that 2P stars exhibit more-elongated distributions than the 1P. To quantify this fact, we define the ellipticity as $e = 1 - b/a$ where a, b are respectively the semi-major and semi-minor axis of the interpolated ellipses.
The ellipticity radial profile is presented in Figure 2.5. The uncertainty associated with each ellipticity measurement is determined by means of bootstrapping 1,000 times with replacement. Clearly, 2P stars exhibit larger values of e than the 1P, as previously found in Lee (2017). The ellipticity difference between 2P and 1P decreases from $\Delta(e) \sim 0.1$, at a radial distance of about 1 arcmin (~0.61 $R_{\rm h}$, ~2 pc) from the cluster center, to ~0.02 for $a \sim 8$ arcmin (~4.7 $R_{\rm h}$, ~17 pc).
To estimate the statistical significance of $\Delta(e)$ we sampled the observed radial profile of the cluster to create a catalog of 100,000 stars with a radial distribution similar to the observed ones and with ellipticity $e = 0$. We selected two stellar groups with the same number of stars as observed for the 1P and the 2P, derived their ellipticity at different radial distances from the center and calculated $\Delta e_{\rm sim}$ in close analogy with what we did for the observed stars. Finally, we computed the ratio between the number of simulations where $\Delta e_{\rm sim} \geq \Delta e$ and the total number of simulations. This quantity corresponds to the probability that the observed ellipticity difference between 2P and 1P stars is not due to observational uncertainties. As shown in the inset of Figure 2.5, where we plot Δe against the semi-major axis of the corresponding the best-fit ellipse, the significance of the ellipticity difference between the stellar populations of NGC 5904 ranges from more than 90% in the innermost regions, to ~60% for $a \sim 8$ arcmin.
Results for the other clusters are shown in Figure 2.6. We find significant differences in the spatial distribution of 1P and 2P stars in NGC 0104, NGC 5904 and NGC 6254. The remaining clusters do not show hints of different distribution between both populations. It is worth mentioning that while NGC 5904 and NGC 6254 are consistent with a more elliptical 2P, NGC 0104 shows the opposite trend, with a more elliptical 1P.

[5] https://cran.r-project.org/web/packages/KernSmooth/index.html

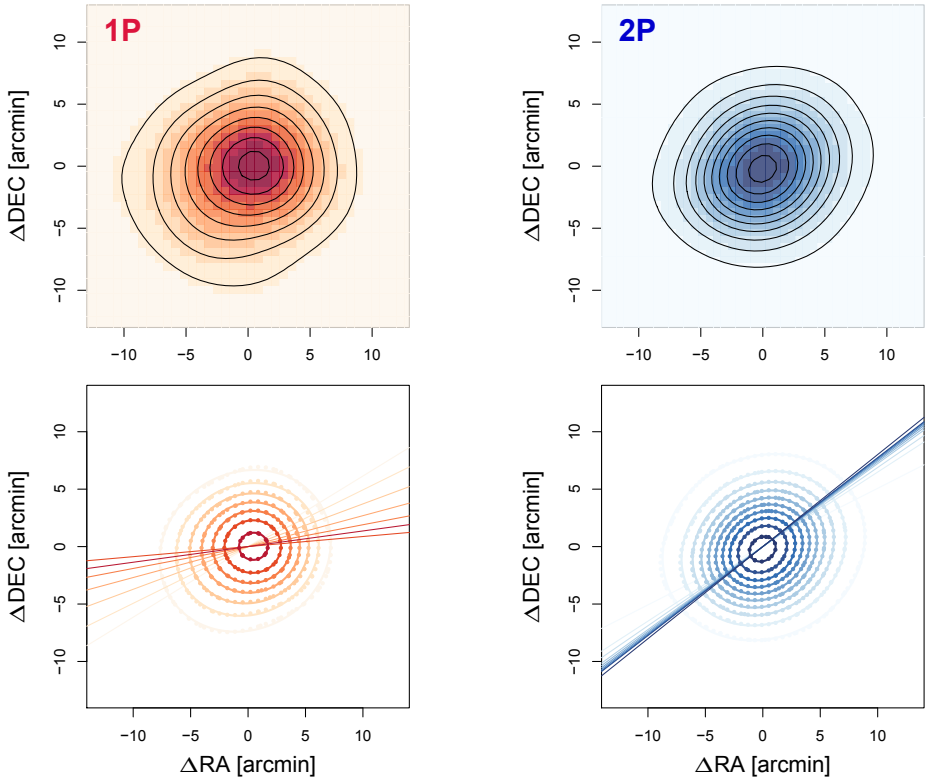

Figure 2.4. Spatial distribution of multiple stellar populations in NGC 5904. *Top panels.* 2D Binned Kernel Density Estimate with iso-density contour lines. *Bottom panels.* Least squares fit ellipses to the iso-density contours. The ellipses have been interpolated using the algorithm described in Halir & Flusser (1998).

2.1.4 Rotation of multiple populations.

In the following, we investigate the rotation in the plane of the sky and along the line-of-sight (LoS) for the selected 1P and 2P stars by using the procedure illustrated in Figure 2.7 for NGC 5904. We applied the orthographic projection of the celestial coordinates and converted proper motions by using Equation 2 from (Gaia Collaboration et al., 2018c).

In the left panel of Figure 2.7 we plotted the positions of the selected 1P and 2P stars relative to the cluster center and defined the angle θ. In the right panels of the same figure we show the density diagrams of the proper-motion and LoS velocity components ($\mu_\alpha \cos\delta, \mu_\delta, V_{\rm LoS}$) of each population against θ. We divided the field of view in sixteen circular sectors with arc length of 45° by using a method based on the naive estimator Silverman (1986). Specifically, we defined a series of points separated by arc length of $l = 45°$. The circular sectors are defined over a grid of points that are separated by steps of $l/2$ in arc length. We calculated the median proper motions and angular positions of stars in each circular sector. The median values are superimposed on the density plots in the right panels of

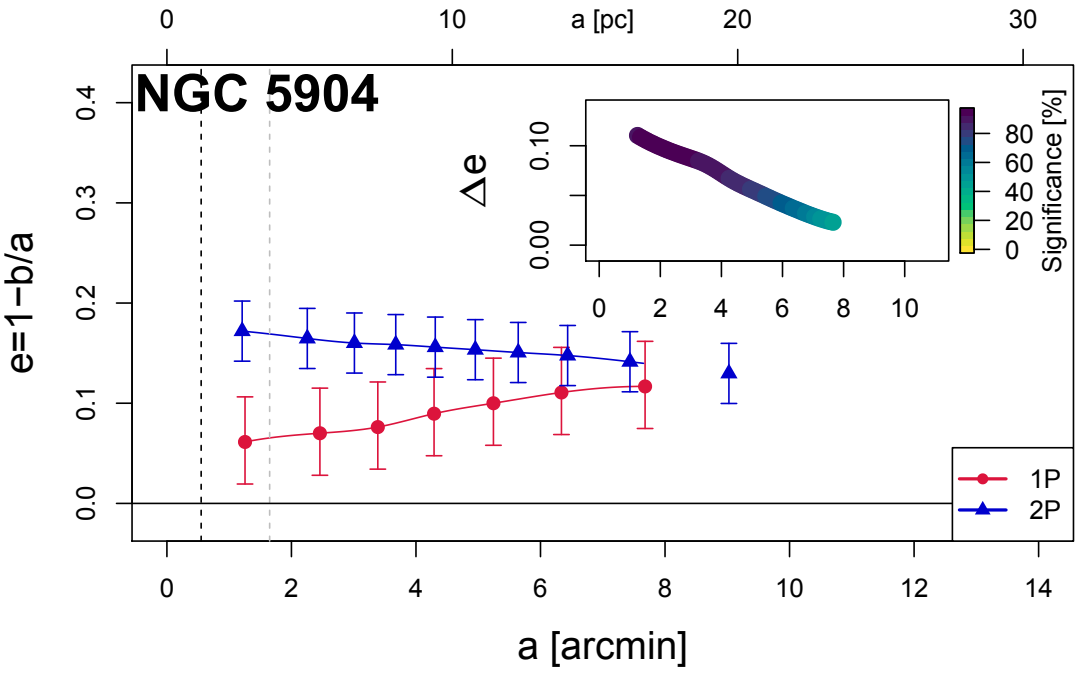

Figure 2.5. Ellipticity, e, of 1P and 2P (color coded in red and blue respectively) as a function of the semi-major axis, a. Black and gray dashed lines indicate the core radius (R_c) and the half-light radius (R_h), respectively. The inset shows the ellipticity difference between 2P and 1P stars, Δe against a. The colors indicate the significance of such difference, as indicated in the colorbar on the right. See text for details.

Figure 2.7.

A visual inspection of this figure reveals that the proper motions of both 1P and 2P stars of NGC 5904 exhibit sinusoidal patterns, thus suggesting that both populations are rotating.

To investigate the rotation of 1P and 2P stars of all the GCs, we calculated the quantities $\Delta\mu_\alpha cos\delta$, $\Delta\mu_\delta$ and ΔV_{LoS} respectively corresponding to the difference between the $\mu_\alpha cos\delta$, μ_δ and V_{LoS} of each star, and the cluster median motion. Results are shown in Figure 2.8 where we plot for each cluster the median values of $\Delta\mu_\alpha cos\delta$, $\Delta\mu_\delta$ and ΔV_{LoS} calculated in sixteen circular sectors as a function of θ. This analysis suggests that NGC 0104 and NGC 5904 are the only two clusters with clear evidence of rotation among both 1P and 2P stars. Remarkably, 1P and 2P stars follow the same random pattern in all the clusters with the possible exception of NGC 5904[6].

[6]Work based on N-body simulations (e.g. Vesperini et al., 2013; Mastrobuono-Battisti & Perets, 2016; Tiongco et al., 2019) suggest that the force of rotation should vary within the cluster field, as a function of radial distance. Due to the small number of available 1P and 2P stars in each GC, we performed a global analysis that is based on the rotation of stars at different radial distances from the cluster center. NGC 0104 is the only cluster that contains a sufficient number of stars to study rotation in different radial bins, as discussed in Section 2.1.4.

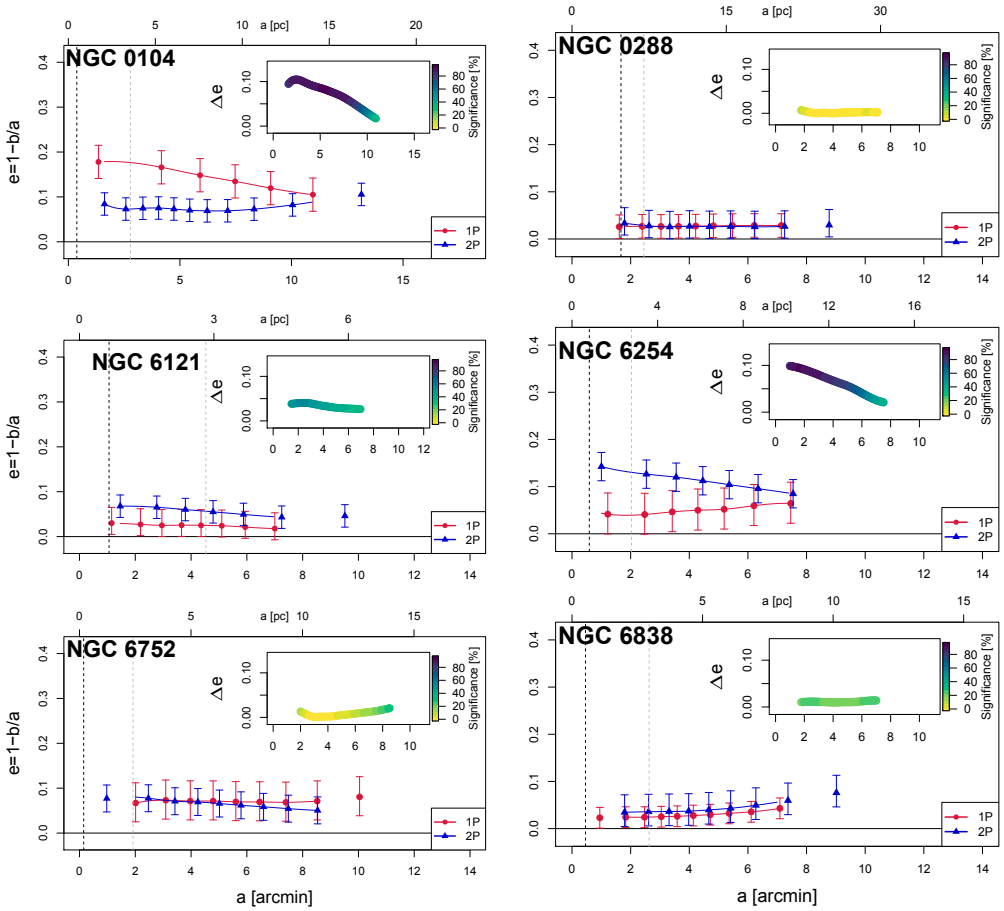

Figure 2.6. Same as Figure 2.5 for NGC 0104, NGC 0288, NGC 6121, NGC 6254, NGC 6752 and NGC 6838.

To quantify the rotation of each population of NGC 0104 and NGC 5904 and estimate its amplitude, A, and phase, ϕ, we performed least-squares fitting to all 1P and 2P stars of the function:

$$f(\theta) = M + A \cdot \sin(F \cdot \theta + \phi) \tag{2.1}$$

where M is the zero point of the sine function and F is the frequency. We exploit the r^2 parameter (Glantz et al., 1990) to estimate the statistical significance of the fit:

$$r^2 = 1 - \frac{\sum_i (y_i - f(\theta, i))^2}{\sum_i (f(\theta, i) - \bar{y})^2} \tag{2.2}$$

where y_i is the value of $\mu_\alpha \cos\delta(\mu_\delta)$ for each star, i, θ is the corresponding position angle, $\bar{y}$ is the average value of y, and f is the best-fit function. This parameter quantifies the goodness of the fit of a linear function, with the perfect match corresponding to $r^2 = 1$. We then eye-checked every cluster for consistency between the interpolation and the value of r^2.
The values of r^2 for NGC 0288, NGC 6121, NGC 6254, NGC 6752 and NGC 6838 are smaller than 0.5 thus demonstrating that the observations are poorly reproduced

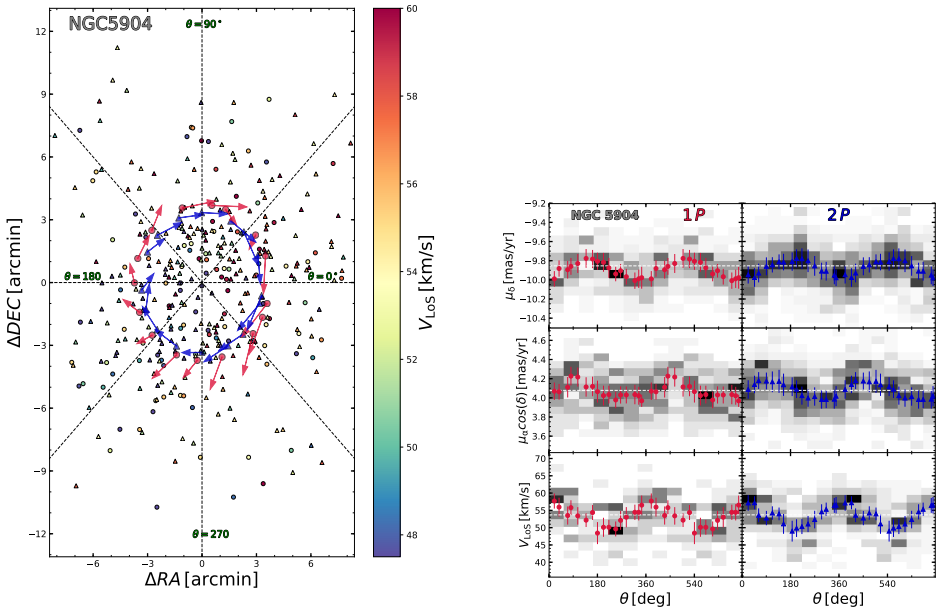

Figure 2.7. *Left.*Relative position of the analyzed RGB stars of NGC 5904 with respect to the cluster center. 1P and 2P stars are shown with circles and triangles, while the color is representative of the LoS velocity as shown in the colorbar. The red and blue arrows indicate the average rotation field, in the plane of the sky, of 1P stars and 2P stars for the 16 analyzed circular sectors. *Right.* $\mu_\alpha \cos\delta$, μ_δ and $V_{\rm LoS}$ as a function of the position angle, θ, for 1P and 2P stars of NGC 5904. The gray levels are indicative of the density of stars. The red dots and the blue triangles represent the average motions of 1P and 2P stars in angular sectors.

by Equation 2.1. Hence, there is no evidence for rotation among 1P and 2P stars of these clusters.

In contrast, NGC 0104 and NGC 5904 exhibit a reliable match between the function of Equation 2.1 for both populations. The obtained r^2 values for 1P and 2P stars are listed in the bottom right insets of Figure 2.8 and are larger than 0.6. The best-fit functions to all 1P and 2P stars for these two clusters are shown in Figure 2.8.

Once established that 1P and 2P stars of NGC 0104 and NGC 5904 rotate, we can further explore the rotation pattern of different stellar populations in these two clusters.

The values of A and ϕ that provide the best-fit to the observations of NGC 0104 and NGC 5904 are listed in Table 2.2. In both GCs the zero point, M, is consistent with zero within 0.01 (mas/yr for the proper motion components and km/s for the LoS velocity) and the frequency F is consistent with 1.00 within 0.01 as expected for stellar rotation in GCs.

To estimate the uncertainties on the amplitude and the phase of the sine function that best reproduces the distribution of 1P (2P) stars of each cluster in both

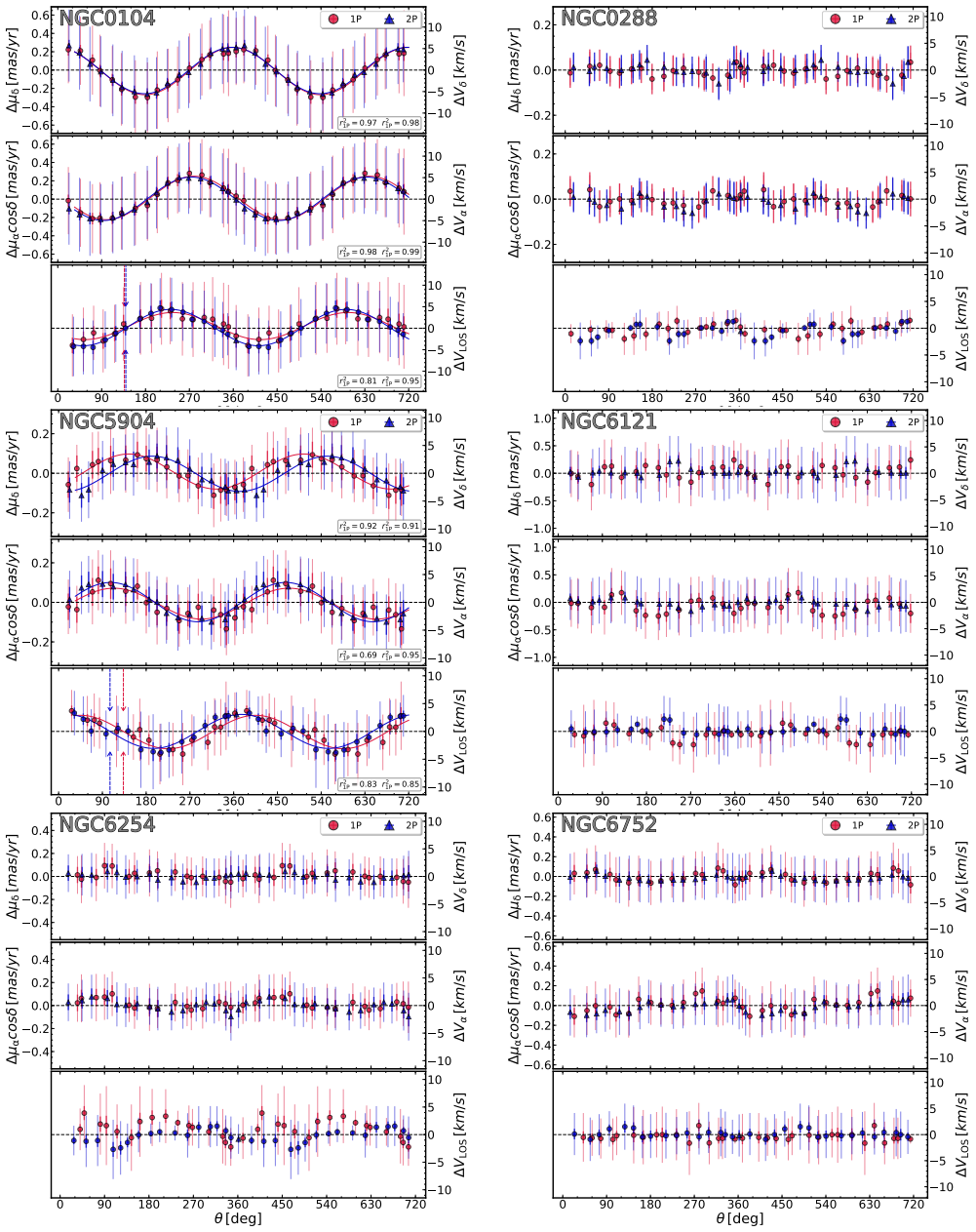

Figure 2.8. Average proper motions (top and middle panels) and LoS velocities (bottom panels) of 1P (red circles) and 2P stars (blue triangles) as a function of the position angle for 1P and 2P stars of NGC 0104, NGC 0288, NCG 5904, NGC 6121, NGC 6254 and NGC 6752. Thin and thick error bars indicate the uncertainties associated with the average motions and the dispersions, respectively. The red and blue lines superimposed on the plots of NGC 0104 and NGC 5904 are the least-squares best-fit functions of 1P and 2P stars, respectively. The vertical red/blue arrows plotted in the bottom panels highlight the PA of the rotation axis of 1P and 2P stars, determined as the zero of the rotation curve.

ID		field	motion component	ϕ (PA) rad	A mas/yr (km/s)
NGC 0104	1P	all	$\mu_\alpha \cos\delta$	2.96±0.06	0.237±0.007
			μ_δ	1.54±0.07	0.257±0.008
			$V_{\rm LoS}$	5.53±0.30	3.35±0.35
	2P		$\mu_\alpha \cos\delta$	3.13±0.04	0.236±0.005
			μ_δ	1.61±0.05	0.253±0.006
			$V_{\rm LoS}$	5.50±0.16	4.23±0.18
NGC 5904	1P	all	$\mu_\alpha \cos\delta$	2.691±0.24	0.078±0.010
			μ_δ	2.254±0.11	0.089±0.007
			$V_{\rm LoS}$	2.44±0.33	2.69±0.40
	2P		$\mu_\alpha \cos\delta$	2.91±0.11	0.099±0.007
			μ_δ	1.38±0.13	0.089±0.006
			$V_{\rm LoS}$	1.90±0.19	3.20±0.27
NGC 0104	1P	inner	$\mu_\alpha \cos\delta$	3.10±0.08	0.288±0.013
			μ_δ	1.50±0.14	0.265±0.021
			$V_{\rm LoS}$	4.40±0.39	4.29±0.57
	2P		$\mu_\alpha \cos\delta$	3.18±0.05	0.289±0.009
			μ_δ	1.60±0.07	0.282±0.008
			$V_{\rm LoS}$	5.50±0.15	4.70±0.24
NGC 0104	1P	outer	$\mu_\alpha \cos\delta$	2.86±0.08	0.221±0.009
			μ_δ	1.58±0.07	0.285±0.009
			$V_{\rm LoS}$	5.84±0.45	2.71±0.58
	2P		$\mu_\alpha \cos\delta$	2.92±0.09	0.205±0.008
			μ_δ	1.69±0.08	0.240±0.007
			$V_{\rm LoS}$	5.34±0.16	3.86±0.20

Table 2.2. Amplitudes and phases (Position Angle in the case of the line-of-sight component) of the best-fit functions (Equation 2.1) describing the observations of 1P and 2P stars in the $\mu_\alpha cos\delta$ vs. θ, μ_δ vs. θ planes and $V_{\rm LoS}$ vs. θ. The upper twelve lines in the Table refer to the entire sample of analyzed 1P and 2P stars of NGC 0104 and NGC 5904, while in the lower twelve lines we consider 1P and 2P stars in the inner and outer fields of NGC 0104.

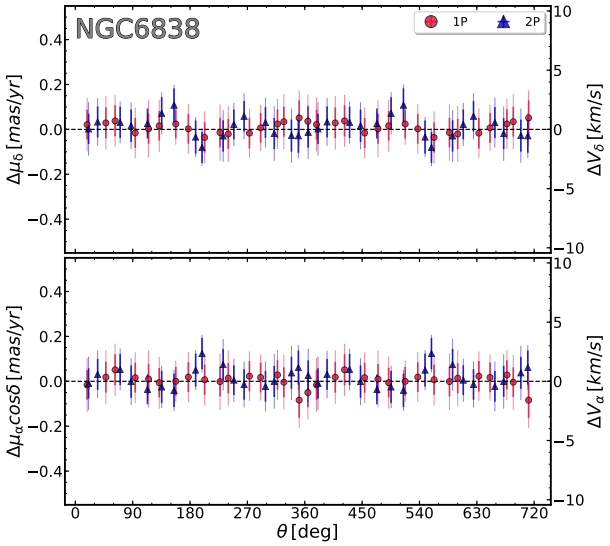

Figure 2.9. Same as Figure 2.8 for NGC 6838. LoS velocities are not available for NGC 6838.

proper motions components, we adopted a procedure based on 1,000 Monte Carlo simulations. In each simulation, we generated a sample of N stars with the same θ distribution of the observed 1P (2P) stars. Here N is the number of analyzed 1P (2P) stars.

We used Equation 2.1 to calculate the value of $f(\theta_i)$ that corresponds to each simulated star, i, by assuming the values of A and ϕ listed in Table 2.2. Then, we added to $f(\theta_i)$ the same uncertainties that we inferred from the observations, and interpolated the simulated distribution of stars in $\Delta\mu_\delta$ vs. θ ($\Delta\mu_\alpha \cos\delta$ vs. θ, $\Delta V_{\rm LoS}$ vs. θ) with Equation 2.1 by means of least-squares, thus estimating the values of A and ϕ.

We calculated the differences between the 1,000 determinations of A and the true value and assumed the 68.27$^{\rm th}$ percentile of the distribution of the absolute values of these differences as the uncertainty on the determination of A. Similarly, we defined the error associated with the best-fit phase. To further compare the distributions of 1P and 2P stars in the $\Delta\mu_\alpha \cos\delta$ vs. θ and $\Delta\mu_\delta$ vs. θ planes we used the k-sample Anderson-Darling test Scholz & Stephens (1987), which provides the probability of two populations to belong to the same parent distribution. In NGC 0104, NGC 0288, NGC 6121, NGC 6254, NGC 6752 and NGC 6838, 1P and 2P stars have probability p$\gtrsim$0.15 to come from the same parent distribution. Hence, we conclude that there is no significant difference between the distributions of stellar populations of these clusters. NGC 5904 represents a remarkable exception. Indeed the k-sample Anderson-Darling test provides probabilities of 0.05, 0.03 and 0.16 that the distributions of 1P and 2P stars in the $\Delta\mu_\alpha \cos\delta$ vs. θ, $\Delta\mu_\delta$ vs. θ and $\Delta V_{\rm LoS}$ vs. θ planes are drawn from the same distribution. Noticeably, the large difference between the phases of the curves that best-fit 1P and 2P stars

in the $\Delta\mu_\delta$ vs. θ plane suggests that the two populations of this cluster exhibit different rotation patterns.
We finally determined the PA of the rotation axis of NGC 0104 and NGC 5904 from the line-of-sight velocity curves as the angle corresponding to a zero LoS velocity. The PAs of the 1P and 2P, marked with red and blue arrows respectively, are shown in the bottom panels of Figure 2.8 and their values are listed in Table 2.2. Our results suggest that multiple stellar populations in NGC 5904 do not share the same rotation axis, with the PA of the 1P differing from that of the 2P by $31° \pm 12°$. On the other hand, NGC 0104 does not show significant differences in the rotation curves of 1P and 2P stars.

Comparing the rotation of first- and second-population stars in NGC 5904 and NGC 0104

To further investigate whether the difference in the rotation patterns of 1P and 2P stars of NGC 5904 is significant or not, we analyzed 1,000 Monte Carlo realizations, for both 1P and 2P stars. First, we assumed that both populations follow the same proper-motion and LoS-velocity distribution, and estimate the probability that the observed phase and amplitude differences between the corresponding rotation curves is entirely due to observational errors. We simulated two samples of stars with the same angular distribution and the same number of stars as the observed 1P and 2P stars. We associated to each star the value of $\Delta\mu_\alpha \cos\delta$ ($\Delta\mu_\delta$, ΔV_{LoS}) corresponding to the sine function that provides the best fit with the observations of 2P stars, $f(\theta_i)$ (see Table 2.2). This procedure ensures that, by construction, the simulated 1P and 2P stars belong to the same parent distribution. Finally, we added the corresponding observational errors to the simulated proper motions of each star, and fitted the resulting distributions of 1P and 2P stars with the function provided by Equation 2.1. We calculated the difference between the phases ($\Delta\phi$) and the amplitudes (ΔA) derived for 2P and 1P stars and analyzed the distributions of the corresponding absolute values. Results are summarized in Table 2.3.
We find that the fraction of simulations where the value of $|\Delta\phi|$ obtained from the $\Delta\mu_\delta$ vs. θ plane is equal or larger than the observed phase difference between 2P and 1P stars is 0.008 Hence, the observed phase difference between the curves of the two stellar populations of NGC 5904 is significant at the $\sim 2.6\sigma$ level. In the ΔV_{LoS} vs. θ plane the phase difference has significance of $\sim 2.3\ \sigma$. On the other hand, we did not detect any significant difference between the amplitudes of the curves of the two populations in the $\Delta\mu_\alpha \cos\delta$ vs. θ plane.
Furthermore, 1P and 2P stars in NGC 5904 are reproduced by sine functions with the same amplitudes. For completeness, we extended the same analysis to NGC 0104 and find no significant difference between the rotation curves of its 1P and 2P stars.
The large number of stars that are available in this cluster allows us to investigate rotation of 1P and 2P stars at different radial distances from the cluster center.

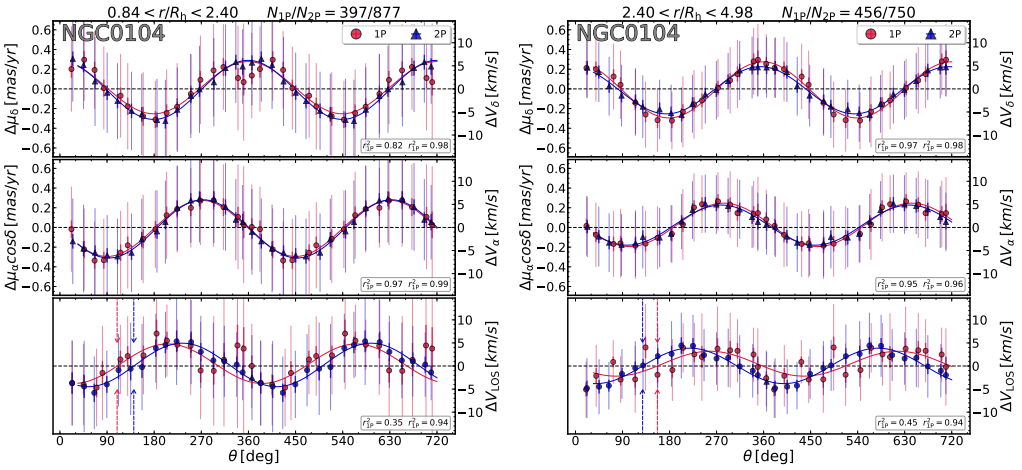

Figure 2.10. Same as Figure 2.8 for stars in the inner (left panel) and outer (right panel) regions of NGC 0104. The curves are the best-fit sine functions. Red and blue colors refer to 1P and 2P stars, respectively. See text for details.

We selected two regions with approximately the same number of stars, namely an inner annulus between $\sim 0.8\,R_{\rm h}$ and $\sim 2.4\,R_{\rm h}$ (2.3 to 6.6 arcmin), and an outer annulus that goes from $\sim 2.4\,R_{\rm h}$ to $\sim 5.0\,R_{\rm h}$ (6.6 to 14.0 arcmin), with $R_{\rm h}$ being the half-light radius listed in Table 2.1. The inner and outer annulus contain respectively 397/877 and 456/750 1P/2P stars. As expected, the star counts are consistent with a more centrally-concentrated 2P ((as previously noticed by Milone et al., 2012a) and Cordero et al. (2014)).

To investigate the rotation of 1P and 2P stars in the inner and outer region we applied the same method described in Section 2.1.4 for all 1P and 2P stars. The average motions of stars in the inner and outer region are shown in Figure 2.10, while the values of A and ϕ of the best-fit sine functions of 1P and 2P stars are listed in Table 2.2. We find that in the inner region the two populations are consistent with the same rotation. On the other hand, in the outer region we detect both an amplitude difference ($\Delta A = 1.150$ km/s) and a phase difference ($\Delta\phi = 0.500$ rad), between the curves that fit the observations of 1P and 2P stars in the $V_{\rm LOS}$ vs. θ plane. Only 1%/4% of our simulations produce an amplitude/phase difference greater than the observed one. The observed differences are therefore significant to the $\sim 2.3/\sim 2\,\sigma$ level.
However, due to the lower number of stars with LoS velocity measurements, we obtain poor quality for the interpolation between the sine function and the observations along the LoS for 1P stars in the inner and outer regions of NCG 0104, as shown by the values of r^2, listed in the bottom right insets of Figure 2.8.

ID	field	motion component	A-D	p-val	ΔA^{obs} mas/yr (km/s)	$\Delta\phi^{obs}$ rad	$P(\lvert\Delta A^{sim}\rvert \geq \lvert\Delta A^{obs}\rvert)$	$P(\lvert\Delta\phi^{sim}\rvert \geq \lvert\Delta\phi^{obs}\rvert)$
NGC 0104	all	$\mu_\alpha cos\delta$	1.53	0.17	0.001 ± 0.020	0.160 ± 0.090	0.960	0.083
		μ_δ	1.59	0.16	0.004 ± 0.022	0.070 ± 0.080	0.104	0.460
		V_{LoS}	1.59	0.16	0.88 ± 0.40	0.030 ± 0.280	0.390	0.281
NGC 5904	all	$\mu_\alpha cos\delta$	2.62	0.05	0.020 ± 0.020	0.224 ± 0.195	0.260	0.170
		μ_δ	3.00	0.03	0.000 ± 0.018	0.870 ± 0.224	0.951	0.008
		V_{LoS}	1.59	0.16	0.51 ± 0.48	0.541 ± 0.200	0.453	0.021
NGC 0104	inner	$\mu_\alpha cos\delta$	1.44	0.20	0.001 ± 0.038	0.080 ± 0.134	0.980	0.503
		μ_δ	0.59	0.66	0.017 ± 0.039	0.100 ± 0.125	0.422	0.434
		V_{LoS}	1.59	0.16	0.41 ± 0.50	0.533 ± 0.410	0.550	0.062
NGC 0104	outer	$\mu_\alpha cos\delta$	2.54	0.05	0.016 ± 0.026	0.060 ± 0.121	0.532	0.593
		μ_δ	1.98	0.10	0.044 ± 0.028	0.110 ± 0.103	0.100	0.402
		V_{LoS}	1.59	0.16	1.15 ± 0.62	0.500 ± 0.500	0.010	0.041

Table 2.3. Comparison of the rotation curves in the $\mu_\alpha cos\delta$ vs. θ, μ_δ vs. θ and V_{LoS} vs. θ planes of 1P and 2P stars in the entire field of view of NGC 0104 and NGC 5904 and in the inner and outer region of NGC 0104. We provide the A-D values from the Anderson-Darling test and the corresponding probability that 1P and 2P stars comes from the same parent distribution (p-val). We list the amplitude (ΔA^{obs}) and phase differences ($\Delta\phi^{obs}$) of the curves that provide the best-fit with 2P and 1P stars and the probability that the observed difference in phase and amplitude are due to observational errors as inferred from Monte-Carlo simulations.

Comparison with theory

Figure 2.8 suggests that the rotation curves of 1P and 2P stars of NGC 5904 exhibit different phases in the μ_δ vs. θ plane and along the line of sight. On the contrary, the two populations seem to share the same rotation pattern when we consider the $\mu_\alpha \cos\delta$ component of the motion. To shed light on this phenomenon, we further investigate the rotation curves of 1P and 2P stars in NGC 5904 by qualitatively comparing the observations with mock simulated stars. Specifically, we generated two stellar populations composed of 50,000 stars each, by extracting their positions and velocities from a King (1966) model with maxwellian velocity distributions. We then added to the motions of each population a specific rotation pattern characterized by the same amplitude A, and different inclination of the rotation axis with respect to the line-of-sight, i, and position angle θ_0, (as in Sollima et al., 2019, their Equation A1).

We compared the rotation curves of pairs of mock stellar populations with different rotation patters along the three space directions X, Y and Z. We find that stellar populations with the same amplitudes but different inclinations and phases qualitatively reproduce the observations of NGC 5904. As an example, we show in Figure 2.11 that two stellar populations with amplitude ($A = 0.4$) inclinations ($i = 80°$ and $120°$) and phases ($\phi_0 = 15°$ and $0°$) qualitatively reproduce the observed pattern. Indeed the simulated rotation curves along the direction X and Y exhibit different phases, while sharing nearly the same phase along the Z direction.

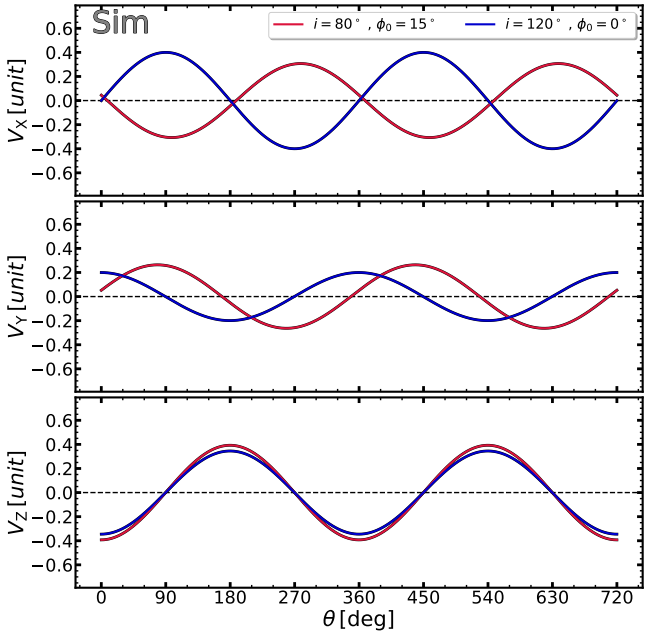

Figure 2.11. Projected motions along three space directions, X, Y and Z, of two simulated stellar populations with different rotation patterns. See text for details.

Line of sight velocity map

For completeness we compare in Figure 2.12 the LoS velocity map with the spatial distribution of 1P and 2P stars in NGC 5904. The four panels show the smoothed LoS velocity map, color coded as indicated by the colorbar. The black dashed lines represent the PA of the rotation axis, derived from the rotation curves as explained in Section 2.1.4, while the black solid lines are the same isodensity contour lines derived in Section 2.1.3. Clearly, the rotation axis is consistent with the minor axis of the best-fit ellipses, as expected for oblate rotators. This agreement is even more important since these quantities, i.e. the PA of the rotation axis and the major/minor axis of the best-fit ellipses, are determined with independent techniques.

2.1.5 Velocity profiles

To study the internal motion of stars as a function of the radial distance from the cluster center we divided the cluster field into different circular annuli, that are determined with the naive estimator method Silverman (1986).
For each annulus we computed the systematics-corrected median values of the radial ($\Delta\mu_{\rm RAD}$) and tangential ($\Delta\mu_{\rm TAN}$) components of proper motions for 1P and 2P stars relative to the corresponding median proper motion components of all

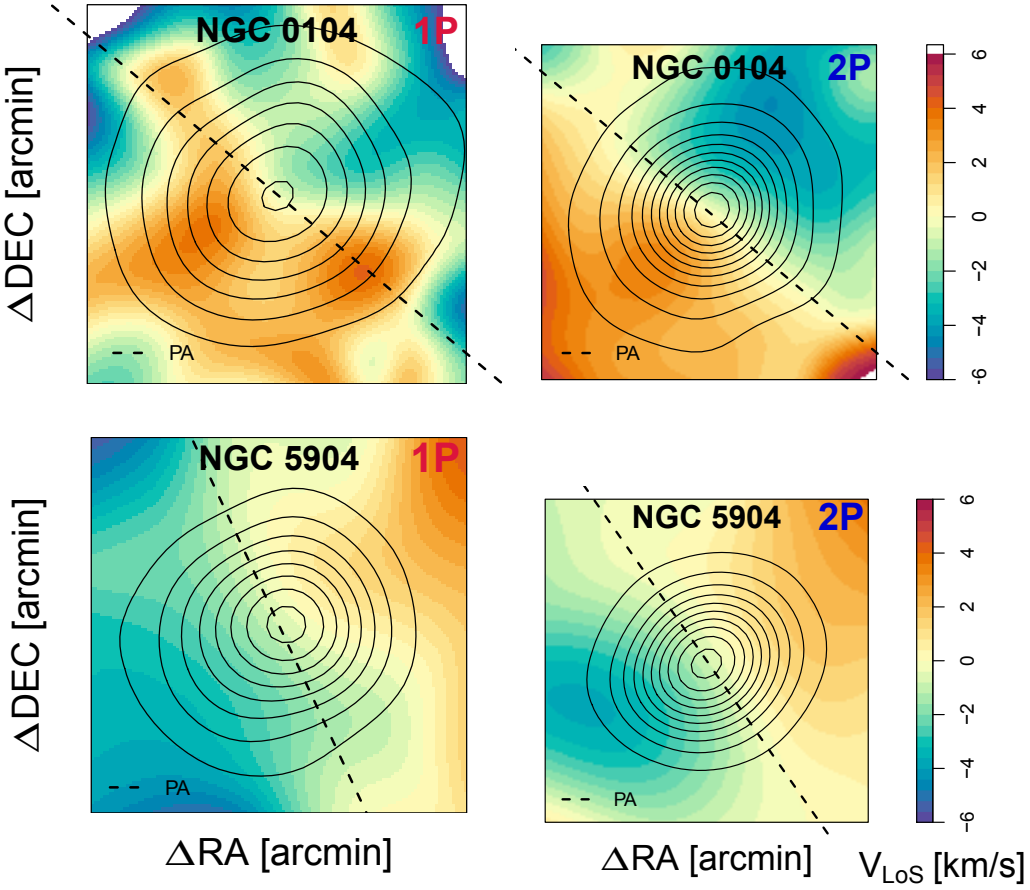

Figure 2.12. Line-of-sight velocity map of different stellar populations in NGC 0104, top panels, and NGC 5904, bottom panels. Superimposed are the isodensity contour lines, derived in Section 2.1.3. The thick black dashed line represents the position angle of the rotation axis, as determined in Section 2.1.4. The colorbars on the right indicate the LoS velocity in km/s.

stars.

These proper motions have been converted into velocities, $\Delta V_{\rm RAD}$ and $\Delta V_{\rm TAN}$, by assuming for each cluster the distances listed in Table 2.1, from Baumgardt & Hilker (2018).

Figure 2.13 shows the velocity profiles of the analyzed clusters as a function of the radial distance from the cluster center. To better compare the various clusters we normalized the radial distance from the cluster center to the value of its half-light radius provided by Baumgardt & Hilker (2018) and converted the radial distances from angular to physical units by means of the distances provided in Table 2.1.

The two populations of most GCs share similar velocity profiles and any difference between the velocities of 1P and 2P stars is smaller than ~1 km/s. These conclusions are corroborated by the Anderson-Darling test, which provides the

probabilities for 1P and 2P stars to be drawn from the same parent distribution that are quoted in the insets of Figure 2.13. As a further determination of the statistical significance of the differences between the velocity profiles of 2P and 1P stars we used the following procedure. We computed the $\chi^2_{\rm obs}$ between the observed profiles of the 1P and 2P. We then simulated 1,000 profiles for 1P and 2P, where we assumed that the two populations have the same distribution, and we scattered each star according to its observed uncertainty. For each simulation we computed the $\chi^2_{\rm sim}$ between 1P and 2P profiles, and we counted the number of realizations for which $\chi^2_{\rm sim} \gtrsim \chi^2_{\rm obs}$, (N^*). The ratio between (N^*) and the total number of realizations, $(N_{\rm sim})$ is indicative of the significance, and it is quoted in the bottom-right corner of each panel in Figure 2.13.
NGC 5904 seems a remarkable exception. Indeed, in the radial interval between ~2 to ~5 half-light radii from the center, 1P stars exhibit higher radial motions than 2P stars.
However, such difference would be attributed to systematics as suggested by the high ratio $N^*/N_{\rm sim} = 0.21$. Improved proper motions, as those from next GAIA data releases, are mandatory to understand whether the observed difference is real or not.

Velocity dispersions of 1P and 2P stars

To derive the velocity dispersion of 1P and 2P stars in each annulus we followed the procedure described in Mackey et al. (2013) and Marino et al. (2014). Briefly we considered the negative log-likelihood function:

$$\lambda = \prod_{i=1}^{N} p(v_i, \epsilon_i)$$

with the probability of finding a star with velocity v_i and uncertainty ϵ_i given by:

$$p(v_i, \epsilon) = \frac{1}{2\pi\sqrt{(\sigma^2 + \epsilon_i^2)}} \exp\left(-\frac{(v_i - v)^2}{2(\sigma^2 + \epsilon_i^2)}\right)$$

and we found the intrinsic dispersion by maximizing the likelihood. Again, the uncertainties associated with each point are determined by bootstrapping with replacements performed 1,000 times. Figure 2.14 shows the velocity dispersion profile for the studied clusters, where the radial coordinated has been normalized to the half-light radius from Baumgardt & Hilker (2018).
We computed the quantity $\sigma_{\rm TAN}/\sigma_{\rm RAD} - 1$, which is indicative of the anisotropy of the internal motion, and show its radial profile in Figure 2.15. The horizontal lines in the plots correspond to isotropic stellar systems. As a global and independent measure of the degree of anisotropy, we determined, for each population, the ratio between the radial kinetic energy and the total kinetic energy, $k = \epsilon_{\rm RAD}/(\epsilon_{\rm TAN} + \epsilon_{\rm RAD})$. The results are listed in bottom-right corners of Figure 2.15. As expected, non rotating clusters are characterized by a value of k close

to $k = 0.5$, expected for isotropic stellar systems. On the other hand, NGC 0104 and NGC 5904 show a higher degree of tangential anisotrpy, as a consequence of the non-zero tangential velocity. We confirm that NGC 0104 exhibits strong differences in the degree of anisotropy of the two populations, with the 2P being more radially anisotropic than the 1P. The external region of NGC 5904 shows hints of a more radially anisotropic 2P, but the large uncertainties prevent us from any further discussion.
The remaining clusters are consistent with being isotropic stellar systems. Concerning the LoS velocity dispersion profile we find some differences in NGC 0104, in the outermost part of NGC 5904 and also in NGC 6254.

2.1.6 Summary and discussion

We exploited Gaia DR2 proper motions and parallaxes of stars in the field of view of seven GCs, namely NGC 0104, NGC 0288, NGC 5904, NGC 6121, NGC 6254, NGC 6752 and NGC 6838 to separate cluster members from field stars. We analyzed the V vs. $C_{U,B,I}$ diagrams corrected for differential reddening of clusters members to identify 1P and 2P stars along the RGB and study their spatial distributions and internal kinematics by using Gaia DR2 stellar positions and proper motions and ESO/VLT and Keck LoS velocities. To our knowledge, this is the first homogeneous study of the three velocity component internal kinematics of distinct stellar populations in a large sample of GCs over a wide field of view.
We find that 1P and 2P stars of NGC 0104, NGC 5904 and NGC 6254 exhibit different spatial distributions. Specifically, in NGC 5904 and NGC 6254 2P stars exhibit higher ellipticities than the 1P, while NGC 0104 seems consistent with a more-elliptical 1P. The two populations of the other clusters share the same spatial distribution. The entire sample of analyzed 1P and 2P stars of NGC 0104 share similar rotation patterns and that 2P stars show stronger anisotropies than the 1P stars thus corroborating previous findings from our group Milone et al. (2018b). When we divide stars of NGC 0104 into two annuli with different radial distances, we find that the sine functions that best reproduce the rotation curves 1P and 2P exhibit different phases and amplitudes in the LoS component. However, such difference is significant at 2-σ level only.
We confirm that NGC 0104 and NGC 5904 exhibit strong rotation both in the plane of the sky Anderson & King (2003); Bianchini et al. (2018); Milone et al. (2018b); Sollima et al. (2019) and along the line-of-sight Kamann et al. (2018); Lanzoni et al. (2018).
Lee (2017) studied multiple populations in NGC 5904 by using ground-based on Ca-CN photometry. He separated 1P and 2P along the RGB by using the V vs. cn_{JWL} diagram, which is a powerful tool to identify stellar populations with different nitrogen abundances along the RGB. Lee used the radial velocities of 100 stars by Carretta et al. (2009) to investigate the projected rotations of the two populations identified photometrically. He found that 2P has a substantial net projected rotation whereas there is no evidence for any net projected rotation of 1P stars.

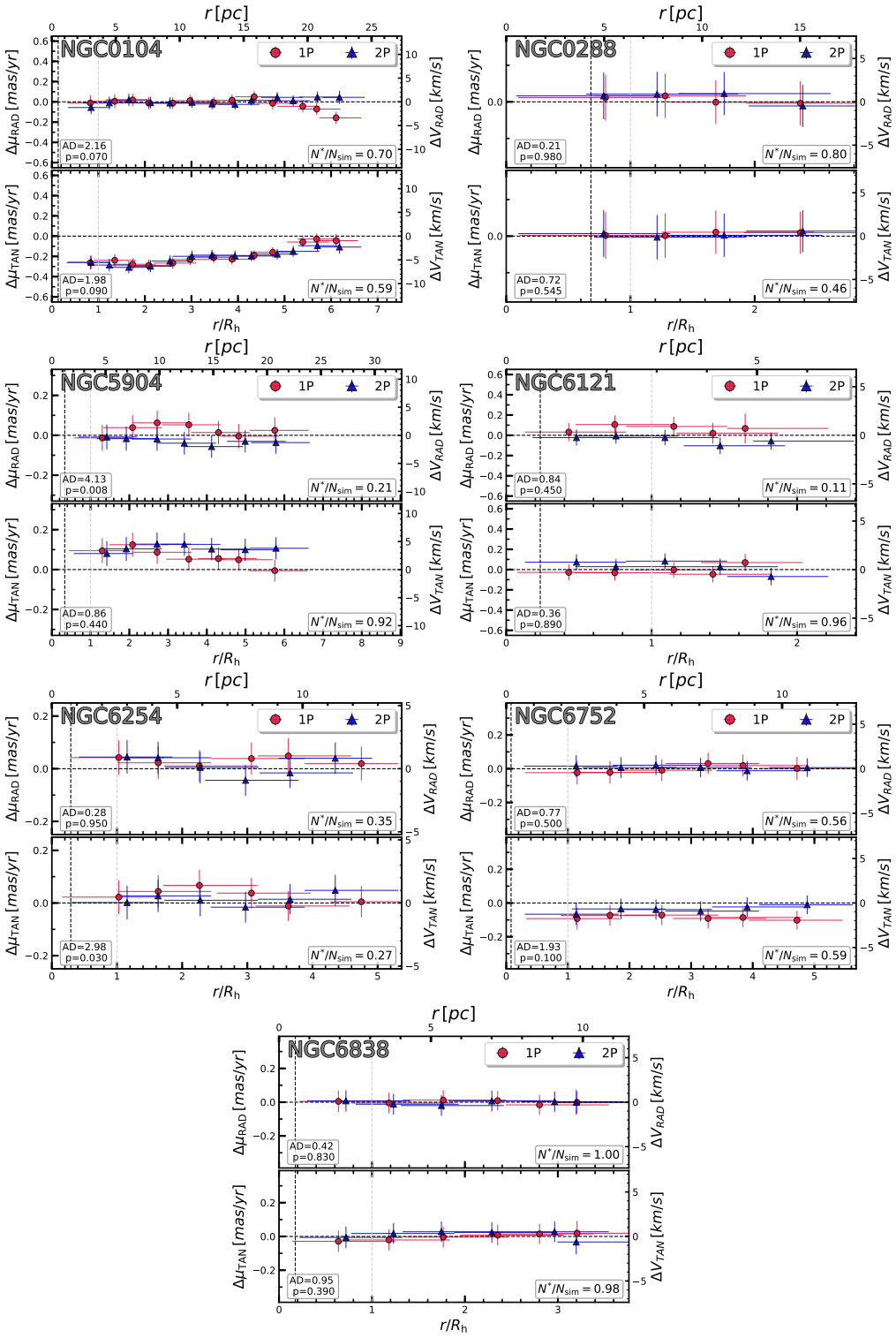

Figure 2.13. Average tangential and radial motions for NGC 0104, NGC 0288, NGC 5904, NGC 6121, NGC 6254, NGC 6752 and NGC 6838 as a function of the radial distance from the cluster center. The radial coordinate is normalized to the half-light radius from Baumgardt & Hilker (2018). Horizontal lines mark the radial extension of the radial bins. The black and gray dashed lines indicate the core and the half-light radius, respectively. We quote for each cluster the probability, p, of the velocity distribution of 1P and 2P stars to be drawn from the same parent distribution according to the Anderson-Darling test (AD, Scholz & Stephens, 1987). In the bottom-right corner of each panel is shown the significance of the differences between the median profile of 1P and 2P, computed as explained in the text.

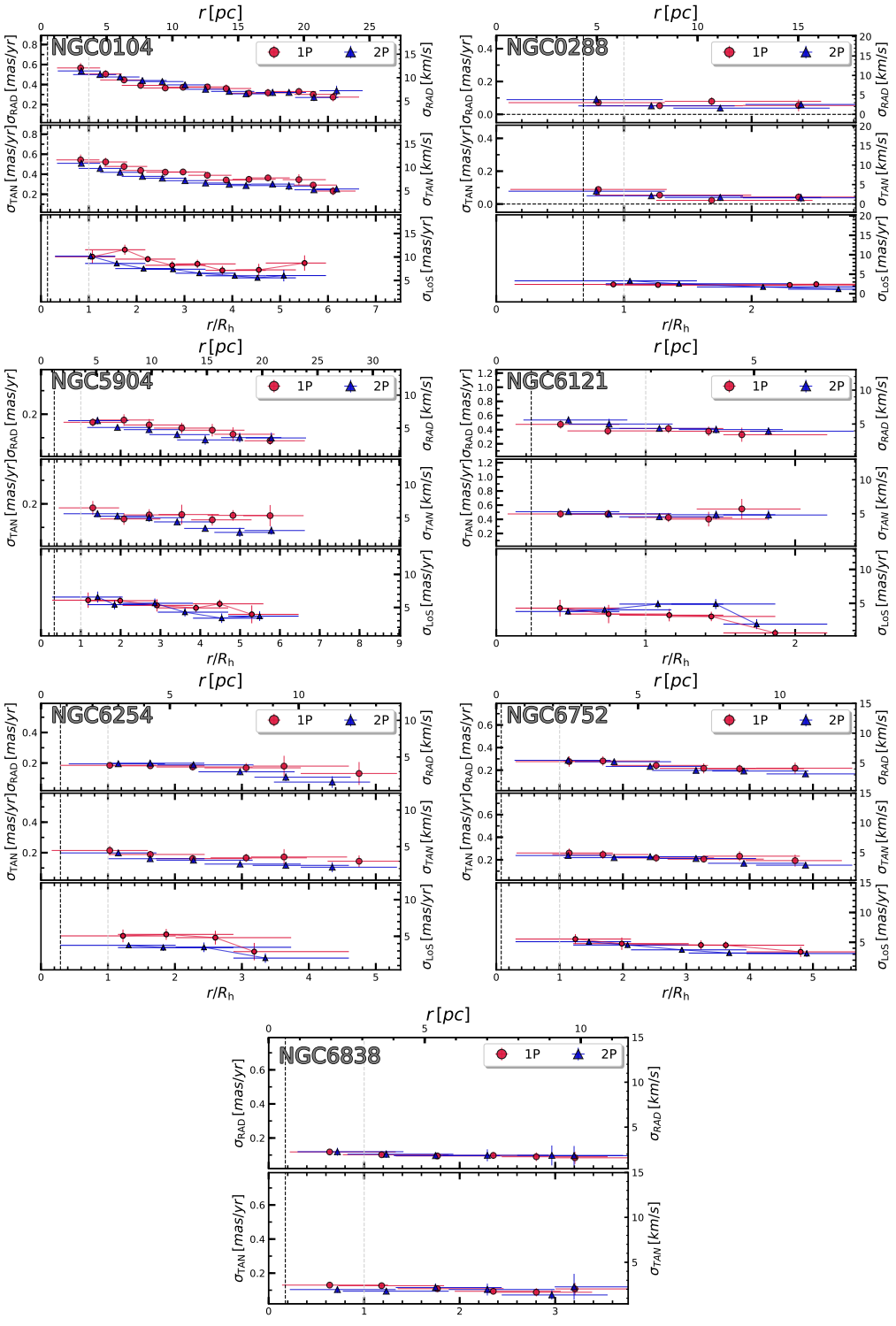

Figure 2.14. Velocity dispersion profiles for the radial, tangential and LoS velocity, for the analyzed GCs, except NGC 6838 for which LoS velocities are not available. As in Figure 2.13, the radial coordinates have been normalized to the half-light radius. Black and gray dashed lines mark the core and the half-light radius, respectively.

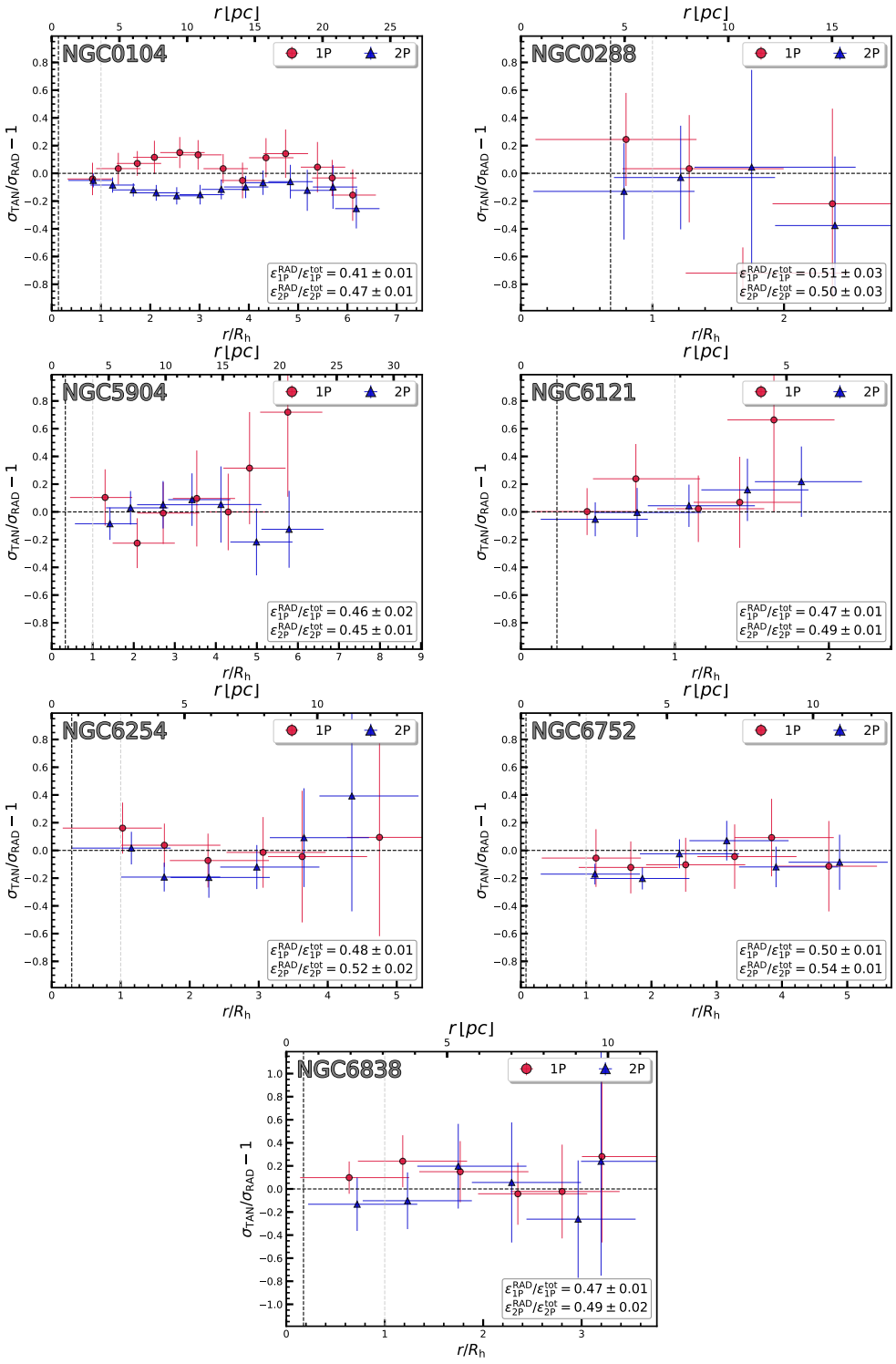

Figure 2.15. Anisotropy profiles for the analyzed clusters. The radial coordinate is normalized to the half-light radius from (Baumgardt & Hilker, 2018). Black and gray dashed lines represent the core- and the half-light radius.

Our results, based on Gaia DR2 proper motions of 263 1P and 535 2P stars and Eso/VLT LoS velocities of 106 and 238 1P/2P stars, show that both populations exhibit significant rotation along the plane of the sky and the line of sight. The sine functions that describe rotation of 2P and 1P stars exhibit different phases in the $\Delta\mu_\delta$ vs. θ and in the $V_{\rm LoS}$ vs. θ planes and such differences are significant at the ~2.6-σ and ~2.3-σ level, respectively. The two populations exhibit the same phase when we consider the rotation in the $\Delta\mu_\alpha cos\delta$ vs. θ plane. Such rotation pattern is qualitatively consistent with different position angles and inclinations of the rotation axis.

Our analysis confirms no evidence of rotation in NGC 0288, NGC 6121, NGC 6254 and NGC 6838 (e.g. Bianchini et al., 2018; Sollima et al., 2019). On the other hand, our results are in apparent disagreement with the conclusion by Bianchini and collaborators who detected a significant rotation of NGC 6752 stars in the plane of the sky. We attribute the discrepancy to the small sample of 1P and 2P NGC 6752 stars studied in our paper. We verified that, when we extend our analysis to all the stars of NGC 6752 as done by Bianchini et al. (2018) and Sollima et al. (2019) we confirm previous evidence of rotation.

There is no significant difference between the tangential and radial motions of 1P and 2P stars in the analyzed clusters. 1P stars of NGC 5904 seem to exhibit, on average, larger motions in the radial direction than 2P stars in the region between ~2 and 5 half-light radii from the cluster center but such difference is not statistically significant when we account for systematic errors in Gaia DR2 proper motions.

We investigate the velocity-dispersion profile of multiple populations in all the GCs and confirm that 2P stars of NGC 0104 show significant anisotropy with respect to the 1P. In the other clusters there is no evidence for strong anisotropy among 1P and 2P stars, with NGC 6121 being a possible exception.

To summarize our results, we find significant kinematical differences in NGC 0104 and NGC 5904, while the remaining clusters are consistent with the presence of multiple stellar populations sharing the same internal dynamic. It is worth mentioning that these two clusters have the highest values for the half-mass relaxation time in our sample (listed in Table 2.1), with the exception of NGC 0288. Finally, these results are consistent with the criterion in Hénault-Brunet et al. (2015). According to the authors, multiple stellar populations are not expected to be fully mixed if the relation in Equation 2.3 is satisfied.

$$M \gtrsim 10^5 M_\odot \cdot \left(\frac{4\,kpc}{R_{\rm G}}\right) \tag{2.3}$$

where $R_{\rm G}$ is the Galactocentric radius, listed in Table 2.1. Among the clusters in our sample, only NGC 6121 and NGC 6838 do not fulfill Equation 2.3, and indeed we do not find significant dynamical differences between the 1P and 2P in these two clusters.

All our findings constitute strong constraints for existing and future multiple population scenarios. Self-enrichment scenarios, and in particular the AGB scenario,

seem to be able to produce different spatial distributions and kinematics between the first and second generation. This scenario, which is the one that has been studied more in detail in terms of dynamics, predicts a higher central concentration for the 2P with respect to 1P stars. 1P stars have a higher velocity dispersion compared to 2P stars and they show a smaller amount of radial anisotropy. If the 1P cluster is initially rotating, the 2P will form in a centrally concentrated disc and will initially rotate faster than 1P stars. All these signatures are washed out by the two-body relaxation of the clusters. Rotational difference could therefore be absent due to the relaxation process in the velocity space.
Further tests and dynamical models exploring a larger phase-space of the parameters are necessary to understand if the AGB scenario, or any of the other proposed 2P formation mechanisms, are able to reproduce simultaneously all the observed features.

2.2 Gaia and Hubble unveil the kinematics of stellar populations in the Type II globular clusters ω Centauri and M 22.

This Section is taken from Cordoni et al. (2020b).

Abstract

The origin of multiple stellar populations in Globular Clusters (GCs) is one of the greatest mysteries of modern stellar astrophysics. *N*-body simulations suggest that the present-day dynamics of GC stars can constrain the events that occurred at high redshift and led to the formation of multiple populations. Here, we combine multi-band photometry from the *Hubble Space Telescope* (*HST*) and ground-based facilities with *HST* and Gaia Data Release 2 proper motions to investigate the spatial distributions and the motions in the plane of the sky of multiple populations in the type II GCs NGC 5139 (ω Centauri) and NGC 6656 (M 22). We first analyzed stellar populations with different metallicities. Fe-poor and Fe-rich stars in M 22 share similar spatial distributions and rotation patterns and exhibit similar isotropic motions. Similarly, the two main populations with different iron abundance in ω Centauri share similar ellipticities and rotation patterns. When analyzing different radial regions, we find that the rotation amplitude decreases from the center towards the external regions. Fe-poor and Fe-rich stars of ω Centauri are radially anisotropic in the central region and show similar degrees of anisotropy. We also investigate the stellar populations with different light-element abundances and find that their N-rich stars exhibit higher ellipticity than N-poor stars. In ω Centauri both stellar groups are radially anisotropic. Interestingly, N-rich, Fe-rich stars exhibit different rotation patterns than N-poor stars with similar metallicities. The stellar populations with different nitrogen of M 22 exhibit similar rotation patterns and isotropic motions. We discuss these findings in the context of the formation of multiple populations.

Introduction

An increasing amount of research is providing evidence for the presence of two main classes of GCs (e.g. Marino et al., 2009, 2019b; Milone et al., 2017a). While stars in the majority of Type I Galactic GCs exhibit homogeneous abundances of heavy elements (e.g. Carretta et al., 2009), a small but significant number of 'anomalous' clusters (Type II GCs) show internal variations in metallicity and in those elements that are associated to *s* processes (e.g. Yong & Grundahl, 2008; Da Costa et al., 2009; Yong et al., 2014; Marino et al., 2015; Johnson et al., 2015; Marino et al., 2019b).
Type II GCs exhibit distinctive photometric features, including multimodal subgiant branches (SGBs) in Color-Magnitude Diagrams (CMDs) made with optical filters (e.g. Milone et al., 2008; Marino et al., 2009; Piotto et al., 2012), and

multimodal red-giant branches (RGBs) and SGBs in the I vs. $U-I$ or V vs. $U-V$ CMDs, with metal-rich stars populating red RGBs and faint SGBs (e.g. Marino et al., 2011; Lee, 2015, 2020).
Based on multi-band photometry of 58 GCs, Milone et al. (2017a) find that Type II GCs make up 17% of the studied clusters. The fact that Type II clusters exhibit star-to-star metallicity variation, suggests that they have been able to retain a small amount of the material ejected by supernovae. In this respect, they differ from Type I GCs, where supernova yields seem to have no effect on the chemical composition of second-population stars.
Due to their large total masses and the complexity of their stellar populations, it has been suggested that Type II GCs formed in the environment of dwarf galaxies, e.g. in their nucleus.
These galaxies are then tidally destroyed by the interaction with the Milky Way. This possibility is supported by the observation that the Type II GC M 54 lies in the nucleus of the Sagittarius dwarf galaxy (Bellazzini et al., 2008) and by the fact that the class of Type II GC includes NGC 5139 (ω Centauri), which is often considered the remnant of a dwarf (e.g. Bekki & Freeman, 2003). Moreover, based on the integrals of motion of their orbits, at least half of the known Type II GCs (seven out thirteen clusters) are associated with the Enceladus Galaxy thus demonstrating their extragalactic origin (Milone et al., 2020).
Remarkably, the evidence that both metal-rich and metal-poor stars of most Type II GCs host stellar populations with different light-element abundances (e.g. Marino et al., 2009, 2011), indicates that independent processes are responsible for the heavy-element enrichment and for the variation of light elements. Insights on the formation processes can be gained via the study of the kinematics of stellar populations with different chemical compositions.
Indeed, the various scenarios on the formation of multiple populations in GCs, suggest that second-generation stars are born in the cluster center, in a high density subsystem embedded in a more-extended first generation (D'Ercole et al., 2008; Calura et al., 2019, and references therein). N-body simulations (e.g. Mastrobuono-Battisti & Perets, 2013, 2016; Vesperini et al., 2013; Hénault-Brunet et al., 2015; Tiongco et al., 2019) demonstrate that the dynamical evolution of second-generation stars should be significantly different from that of the first generation and the signature of the different initial conditions could be detected in present-day GC kinematics of GCs where the stars are not fully mixed. Hence, the present-day dynamics of stellar populations with different metallicities and light-element abundances provide a unique window into the origin of multiple populations in Type II GCs.

In recent papers, we exploited Gaia Data Release 2 (DR2, Gaia Collaboration et al., 2018a) proper motions to investigate the kinematics of stellar populations with different light-element abundances of Type I GCs (Milone et al., 2018b; Cordoni et al., 2020a). We find that multiple stellar populations of various GCs, NGC 0288, NGC 6121, NGC 6752 and NGC 6838, share similar internal kinematics and morphology, in contrast with what is observed in NGC 104, NGC 5904 and NGC 6254.

Indeed, when we select the main groups of N-poor and N-rich stars (called first and second population, respectively) we find that both populations of NGC 104 share similar rotation patterns in the central region and hints of different rotation in the cluster outskirts (Figure 10 in Cordoni et al., 2020a). Moreover, N-rich stars of NGC 104 exhibit show stronger radial anisotropies than the first population (Milone et al., 2018b; Cordoni et al., 2020a, see their Figure 5 and 10, respectively). The rotation curves of N-poor and N-rich stars of NGC 5904 seem to exhibit different phases with a statistical significance of $\sim 2.5\sigma$ (Cordoni et al., 2020a, see their Figure 8) and N-rich stars of NGC 5904 and exhibit higher ellipticy than N-poor ones, in close analogy with what is observed in NGC 6254 (Cordoni et al., 2020a, Figure 5 and 6).

Here, we extend the analysis to the Type II GCs ω Centauri, and NGC 6656 (M 22), to study the internal kinematics of stellar populations with different metallicities and light-element abundances. The main physical parameters of these two clusters, which share similar nucleosynthetic enrichment processes despite their different masses (e.g. Da Costa & Marino, 2011), are listed in Table 2.1. In particular, we note that the long half-mass relaxation time of ω Centauri, which exceeds the Hubble time (Baumgardt & Hilker, 2018), makes this cluster an ideal target to infer the initial configuration of multiple stellar populations. On the contrary, The half-mass relaxation time is shorter in M 22 ($t_{\rm h} \sim 3$ Gyr, e.g. Baumgardt & Hilker, 2018).

The paper is organized as follows. In Section 2.2 we introduce the dataset and describe the method to select stars with high-precision proper motions and in Section 2.2 we identify multiple stellar populations along the CMDs. We discuss the properties of multiple populations with different iron content in Section 2.2.1, such as their spatial distributions, rotation and velocity profiles. In Section 2.2.2 we extend the analysis to the stellar populations with different light-element abundances. Finally, the summary and the discussion of the results are provided in Section 2.2.3.

Data and data analysis

To investigate the kinematics and the spatial distributions of stellar populations in M 22 and ω Centauri, we combined the exquisite catalogues of proper motions and stellar positions provided by Gaia DR2, with multi-band wide-field photometry from Stetson et al. (2019). Photometry and proper motions are available for stars of M 22 and ω Centauri with radial distances smaller than ~8.4 and ~28.5 arcmin from the center, respectively. Most stars within ~1.7 arcmin from the center of M 22 and within ~2.5 arcmin from the center of ω Centauri have poor-quality Gaia DR2 proper motions because of crowding. Hence, for the stars in these central regions we used multi-band photometry and relative proper motions from *HST* images.

Gaia DR2 proper motions are affected by systematic errors that depend on the positions and the colors of the stars (e.g. Lindegren et al., 2018). We followed the method by Vasiliev (2019a), which accounts for systematic errors by enlarging the

uncertainties associated with proper-motion determinations. As a consequence, as discussed by Cordoni et al. (2020a), the error bars provided in this work overestimate the true errors. Indeed, our main focus is the relative motion of the multiple stellar populations in ω Centauri and M 22, which share similar colors in the Gaia passbands and have, in first approximation, similar spatial distributions. Hence, the effect systematic errors on the relative motions of the distinct population may be partially cancelling out. In the following, we provide details for the data from ground-based facilities and *HST*.

Ground-based dataset

We used the catalogues obtained by Stetson et al. (2019), which provide high-precision photometry of stars in the U, B, V and I bands over a wide field of view. Details on the dataset and on the data reduction are provided by Stetson (2005); Monelli et al. (2013); Stetson et al. (2019). U-band photometry of M 22 is taken from Marino et al. (2015) and was derived from images collected with the Wide Field Imager of the ESO/MPI telescope at Cerro Tololo Inter-American Observatory (WFI@2.2m). We refer to the paper by Marino and collaborators for details on their photometric catalogue. The photometry is calibrated on the photometric system by Landolt (1992).

Bellini et al. (2009) used multi-epoch data acquired by WFI@2.2m to derive proper motions of stars in the field of view of ω Centauri, which are suitable to separate field stars from cluster members. Due to crowding, stellar proper motions from GAIA DR2 are not available for most of the stars in the central region of ω Centauri. To increase the sample size, we identified the stars without Gaia DR2 proper motions that according to Bellini et al. (2009) have membership probabilities larger than 90 % and included these stars in the analysis of the spatial distribution of multiple stellar populations of ω Centauri.
We emphasize that proper motions from Bellini and collaborators are not included in our study on the kinematics of ω Centauri. Instead, as we will widely discuss in the next sections, the internal kinematics of multiple stellar populations in ω Centauri and M 22 are investigated by using high-precision proper motions from *HST* images and from Gaia DR2 alone.

HST **dataset**

HST photometry and relative proper motions are used to investigate stellar populations of M 22 and ω Centauri with radial distances smaller than ~1.7 and ~2.5 arcmin, respectively.
To identify the stellar populations along the RGB of M 22 and ω Centauri, we used the catalogues by Milone et al. (2017a) and Milone et al. (2018b), which include photometry collected through the F275W, F336W, F438W and F814W bands of the Ultraviolet and Visual Channel of the Wide Field Camera 3 (UVIS/WFC3).

The main properties of the images that we used to derive relative stellar proper motions are summarized in Table 2.4. To derive the photometry and the astrometry of all the stars we used the FORTRAN software package KS2 developed by Jay Anderson, (see, e.g. Anderson et al., 2008; Sabbi et al., 2016, for details). Since we are interested in proper motion determination, we reduced the images collected in different epochs independently, and measured the position of stars at each epoch. Stellar positions have been corrected for geometrical distortion by using of the solutions provided by Bellini & Bedin (2009); Bellini et al. (2011). We measured proper motions as in Piotto et al. (2012, see their Section 4) by comparing the distortion-corrected stellar positions at different epochs. To derive the proper motion of each star and minimize the effect of any residual distortion, we used the sample of 45 nearest cluster members as reference stars to fix the zero point of the motion. Hence, our measurements from *HST* data provide proper motions relative to the average local cluster motion.

Selection of cluster members

To explore the internal kinematics of the stellar populations from Gaia DR2 data we identified the sample of stars with accurate astro-photometric measurements following the method described in our previous papers (Milone et al., 2018b; Cordoni et al., 2018, 2020a). In a nutshell, we first selected only stars with accurate proper motions measurements, by using both the `astrometric_gof_al` (`As_gof_al`) and the Renormalized Unit Weight Error (RUWE) parameters (see Lindegren et al., 2018). We then selected cluster members from the proper motion vector-point diagram (VPD). We refer to Cordoni et al. (2020a) for a detailed description of the procedure. Finally, we corrected the photometry of cluster members for differential reddening using the method in (Milone et al., 2012a, see their Section 3.1). The final CMDs are shown in the left panels of Figure 2.1.
In the case of the *HST* dataset, the photometric catalogues by Milone et al. (2017a, 2018b) already distinguished cluster members and field stars, based on stellar proper motions. Hence, we included in the analysis only those stars that, according to Milone and collaborators, belong to M 22 and ω Centauri.

Multiple populations along the color-magnitude diagrams

As shown in Marino et al. (2019b), Type II GCs exhibit multimodal SGBs and RGBs in the photometric diagrams made with $U-V$ and $U-I$ colors that correspond to stellar populations with different metallicities. Hence, we exploit the I vs. $U-I$ CMD of ω Centauri and the V vs. $U-V$ CMD of M 22 to separate the stellar populations with low content of iron and s-process elements (Fe-poor) from the chemically enriched ones (Fe-rich).
The main procedure (I) to identify Fe-poor and Fe-rich stars is similar to that used in Cordoni et al. (2020a, see their Figure 2). Briefly, we determined the RGB boundaries as the 4^{th} and 96^{th} percentile of the color distributions, and we verticalized the CMD following the procedure described in Milone et al. (2017a, see

Table 2.4. Description of the *HST* images used in the paper to derive stellar proper motions.

CAMERA	FILTER	DATE	N×EXPTIME	PROGRAM	PI
			M 22		
ACS/WFC	F606W	Jul 01 2006	3s+4×55s	10775	A. Sarajedini
ACS/WFC	F814W	Jul 01 2006	3s+4×65s	10775	A. Sarajedini
WFC3/UVIS	F814W	Sep 23 2010	2×50s	12311	G. Piotto
WFC3/UVIS	F814W	Mar 17-18 2011	2×50s	12311	G. Piotto
WFC3/UVIS	F395N	May 18 2011	2×631s+2×697s	12193	J.-W. Lee
WFC3/UVIS	F467M	May 18 2011	2×361s+2×367s	12193	J.-W. Lee
WFC3/UVIS	F547M	May 18 2011	74s+3×75s	12193	J.-W. Lee
WFC3/UVIS	F438W	Jul 17 2014	2×141s	13297	G. Piotto
			ω Centauri		
ACS/WFC	F435W	Jun 27 2002	12s+3×340s	9442	A. Cool
WFC3/UVIS	F438W	Jul 15 2009	35s	11452	J. Kim Quijano
WFC3/UVIS	F814W	Jul 15 2009	35s	11452	J. Kim Quijano
WFC3/UVIS	F814W	Jan 12 2010	8×40s	11911	E. Sabbi
WFC3/UVIS	F438W	Jan 14 2010	9×350s	11911	E. Sabbi
WFC3/UVIS	F814W	Jan 14 2010	40s	11911	E. Sabbi
WFC3/UVIS	F438W	Apr 29 2010	7×350s	11911	E. Sabbi
WFC3/UVIS	F814W	Apr 29 2010	9×40s	11911	E. Sabbi
WFC3/UVIS	F438W	Jun 30 2010	9×350s	11911	E. Sabbi
WFC3/UVIS	F814W	Jun 30 2010	4×40s	11911	E. Sabbi
WFC3/UVIS	F438W	Jul 04 2010	350s	11911	E. Sabbi
WFC3/UVIS	F814W	Jul 04 2010	5×40s	11911	E. Sabbi
WFC3/UVIS	F438W	Feb 15 2011	350s	12339	E. Sabbi
WFC3/UVIS	F438W	Mar 24 2011	8×350s	12339	E. Sabbi
ACS/WFC	F435W	Aug 18 2012	9×6s+9×339s	13066	L. J. Smith
ACS/WFC	F435W	Aug 27 2019	42s+3×647s	15594	V. Kozhurina-Platais

their Section 3). Finally, we derived the kernel-density distributions of stars in the verticalized I vs $\Delta(U-I)$ CMDs (red lines in the right panels of Figure 2.1) and identified by eye the groups of Fe-poor (orange dots) and Fe-rich (cyan triangles) RGB stars, which are located on the left and right side of the vertical dashed line, respectively. In the case of ω Centauri we adopted an intermediate step, before identifying Fe-poor and Fe-rich stars in the *HST* inner field. Specifically, to ensure consistency between the two fields and data sets, we converted the m_{F336W} and m_{F814W} magnitudes into U and I magnitudes. The same process was redundant in the simpler case of M 22, as revealed by the right panels of Figure 2.1.
To verify the impact of the adopted selection of ω Centauri stars with different metallicities on the conclusions of the paper, we adopted two additional procedures (II and III). Procedure II consists of excluding stars with $U-I$ colors within $\pm$0.03 mag from vertical dashed line from the metal-poor and metal-rich sample

ID	RA (J2000)[7]	DEC (J2000)[a]	mass[b] [$M_\odot$]	d_{sun}[8] [kpc]	R^a_{Gal} [kpc]	R^b_c [kpc]	R^b_h [arcmin]	R^a_t [arcmin
ω Centauri	13 26 47.24	−47 28 46.5	3.36×10^6	5.2	6.40	2.37	5.00	48.4
M 22	18 36 23.94	−23 54 17.1	4.16×10^5	3.2	4.90	1.33	3.36	31.9

Table 2.5. Identification, positional data and adopted structural parameters for the analyzed type-II clusters. For each cluster we list position (RA, DEC), mass, distance from the Sun, galactocentric radius (R_{Gal}), core radius (R_c), half-light radius (R_h), tidal radius (R_t), logarithm of the half-mass relaxation time (t_h), line-of-sight mean velocity ($\bar{V}_{LoS}$).

defined above. Procedure III is based on the Monte-Carlo method for selection of metal-rich and metal-poor stars. We fitted the $\Delta(U-I)$ distributions of stars with $\Delta(U-I) > 0.85$ with a Gaussian function by means of least squares (orange transparent line in the top-left panel of Figure 2.1). Then, we randomly associated each star with a probability to belong to the metal-poor and metal-rich sample based on ratio between the value of the best-fit Gaussian and the histogram distribution corresponding to its $\Delta(U-I)$ value. In the following, we present results based on the selection from procedure I, while in Section 2.2.3 we compare the results from the procedures I, II and III to demonstrate that the conclusions of the paper do not depend on the selection criterion.

Multiple populations with different light-element abundances in ω Centauri

Work based on high-resolution spectroscopy reveals that stellar groups in different metallicity bins of ω Centauri host sub populations with different light-element abundances (e.g. Marino et al., 2010, 2011; Johnson & Pilachowski, 2010). An efficient tool to disentangle the distinct populations in GCs is provided by the pseudo two-color diagram called chromosome map, which revealed that ω Centauri hosts at least 16 sup-populations (ChM, Milone et al., 2015, 2017a). Based on multi-band *HST* photometry of ω Centauri, Marino et al. (2019b) identified three main groups of stars that define distinct streams in the ChM. The stars of each stream span similar intervals of [Fe/H] but different content of He, C, N, O and Na. Specifically, the upper stream is composed of stars with extreme nitrogen abundances (hereafter N-rich sample), while middle- and the lower-stream stars have low and intermediate [N/Fe], respectively and will be called N-poor sample in the following. N-rich and N-poor stars are represented with blue and red points, respectively, in the chromosome map of ω Centauri plotted in the upper panel of Figure 2.2.

Unfortunately, the *HST* photometry required to build the ChM is only available for stars with radial distances smaller than ~2.5 arcmin. Hence, alternative photometric diagrams are needed to disentangle N-rich and N-poor stars in the external region of ω Centauri.

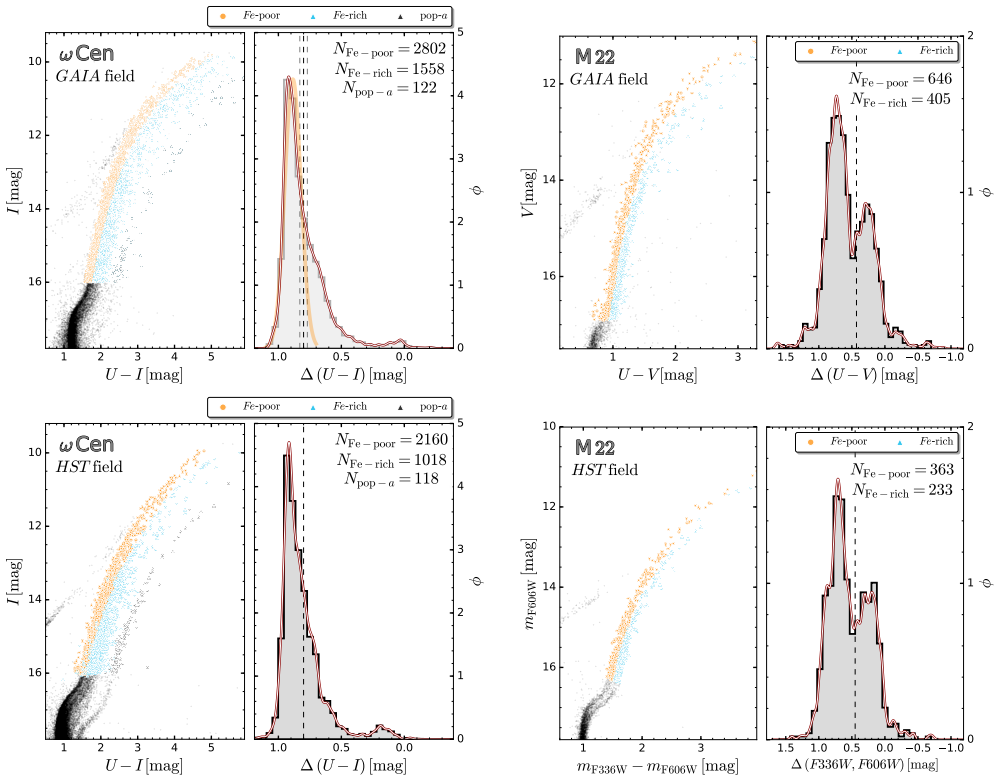

Figure 2.1. I vs. $U - I$ and V vs. $U - V$ diagrams for the selected cluster members of ω Centauri (upper-left) and M 22 (upper-right) from ground-based photometry (upper panels). We also show the histogram and the kernel-density distributions of $\Delta(U - I)$ and $\Delta(U - V)$ for the selected RGB stars of ω Centauri and M 22, respectively. The vertical black dashed lines are used to select Fe-poor and Fe-rich stars in the procedure I, marked with orange circles and cyan triangles, respectively. The orange Gaussian and the gray dashed lines in the top-left panels are adopted to identify alternative groups of stars with different metallicities of ω Centauri from procedures II and III. See text for details. Lower panels show the corresponding diagrams from *HST* photometry of stars in the internal fields. To ensure consistency between the selection of Fe-poor/rich stars in the two fields of ω Centauri, we converted *HST* magnitudes $m_{\rm F336W}$ and $m_{\rm F814W}$ into U and I magnitudes of the photometric system by Landolt (1992).

As shown in the middle panels of Figure 2.2, Fe-rich and Fe-poor stellar populations with different nitrogen abundances also populate different RGB regions in the m_{F814W} vs. $C_{F336W,F438W,F814W}$=$(m_{F336W}-m_{F438W})-(m_{F438W}-m_{F814W})$ pseudo-CMD. Specifically, N-poor stars exhibit lower $C_{F336W,F438W,F814W}$ values than N-rich stars with the same luminosity.
The lower panels of Figure 2.2, show the I vs. $C_{U,B,I} = (U-B)-(B-I)$ pseudo CMD for stars with radial distances larger than ~ 2.5 arcmin, from ground-based photometry. Since the F336W, F438W and F814W filters are the *HST*-analogous of U, B and I, the $C_{F336W,F438W,F814W}$ and $C_{U,B,I}$ have similar sensitivity to stellar populations with different chemical composition, we exploited *HST* photometry to disentangle stellar populations with different nitrogen abundances, and then translated the separation into ground-based photometry.
The black solid lines superimposed on the m_{F814W} vs. $C_{F336W,F438W,F814W}$ and the I vs. $C_{U,B,I}$ diagrams are derived as in Section 2.2 and mark the bluest boundary of the RGBs. We determined the gray lines in the the m_{F814W} vs. $C_{F336W,F438W,F814W}$ diagrams with the criteria to separate most of N-poor stars from N-rich stars, as selected in the ChM shown in the top panel.
To separate the bulk of N-rich and N-poor stars in the ground-based CMD we first estimated the $C_{F336W,F438W,F814W}$ distance between the gray and black fiducials of each CMD for stars with different luminosities ($\Delta C_{F336W,F438W,F814W}$). We then determined the bluest RGB boundaries in the I vs. $C_{U,B,I}$ for both Fe-poor and Fe-rich stars (lower panels). Finally, we shifted these fiducial lines by a certain amount, $\Delta C_{U,B,I}$ that corresponds to the $\Delta C_{F336W,F438W,F814W}$ quantity derived from *HST* photometry.
The selected N-poor and N-rich stars are shown with red and blue circles and triangles, respectively, for both metal-poor and metal-rich stars.
ω Centauri hosts a sample of metal-rich stars ([Fe/H]$\gtrsim -0.9$) that are called population-a stars and define a distinct RGB sequence, on the red side of the bulk of RGB stars (e.g. Lee et al., 1999; Pancino et al., 2000). In the left panels of Figure 2.1 we identified population-a stars in the I vs. $U-I$ (lower-left panel) and I vs. $U-I$ CMDs (lower-right panel). The position of population-a stars in the ChM (see upper panel of Figure 2.2) corroborate previous conclusion by Marino et al. (2011, 2019b) that the majority of population-a stars belong to the N-rich sample, and a small group of population-a stars are N-poor. Specifically, $\sim 92\%$ of population-a are enhanced in nitrogen, while only $\sim 8\%$ are N-poor.
We find that all the aforementioned stellar populations exhibit average proper motions consistent with each other within 1σ.

2.2.1 Kinematics of stellar populations with different metallicities

Spatial distribution of Multiple Populations

In the following, we extend to the sample of Fe-poor and Fe-rich stars of ω Centauri and M 22 the procedure based on the two-dimensional Binned Kernel Density

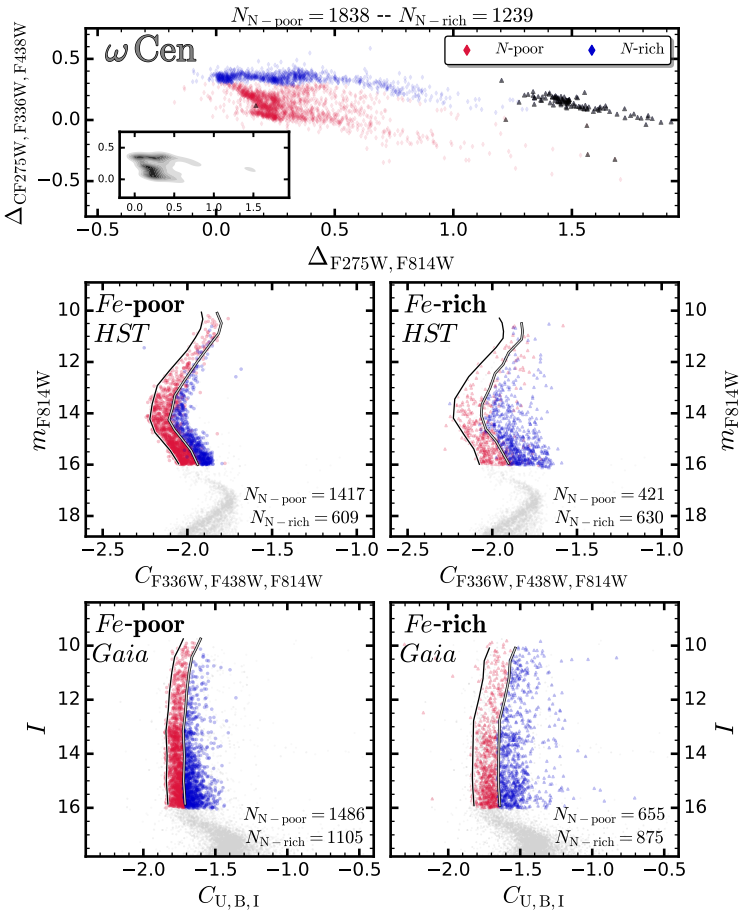

Figure 2.2. *Top panel.* Pseudo two-color diagram, i.e. the Chromosome Map (ChM) of ω Centauri. We adopted the selection criteria of Marino et al. (2019b) to identify stars with different nitrogen abundances. Specifically, N-poor stars (lower and middle stream) are represented with red diamonds, while N-rich stars (upper stream) are marked with blue diamonds. pop-*a* stars are marked with solid black triangles. The bottom-left inset shows the 2D-KDE of the same ChM. *Middle panels.* $m_{\rm F814W}$ vs. $C_{\rm F336W,F438W,F814W}$ for Fe-poor (left) and Fe-rich (right) stars as selected in Section 2.2. The fiducial lines in the CMDs are derived with the purpose of disentangling stellar populations with different nitrogen abundances among stars with different iron. *Lower panels.* I vs. $C_{\rm U,B,I}$ again for metal-poor (left) and metal-rich stars (right). The separation among N-poor and N-rich stars is derived shifting the bluest RGBs from the quantity derived in the *HST* CMDs, as discussed in Section 2.2.2.

Estimate (Wand et al., 2015) used by Cordoni et al. (2020a) to analyse the spatial distributions of stellar populations in seven Type I GCs.

Due to crowding, stellar proper motions from GAIA DR2 are not available for most of the stars in the central regions of ω Centauri. To increase the number of studied stars of ω Centauri cluster members, we included in the analysis those

stars that have membership probabilities larger than 90% according to Bellini et al. (2009).

Results for ω Centauri are illustrated in the upper panels of Figure 2.3 where we show the density plots of the Fe-poor (left) and Fe-rich (right) stars by using orange and blue colors, respectively. The contours are determined by smoothing the data-points with a Gaussian kernel of fixed size. The size is chosen with the criterion of minimizing the small scale structure without loosing the information on the global spatial distribution. To properly compare the results, we adopted the same kernel size for all the populations of both clusters.

We calculated six iso-density contours for each population and used the least square method to fit each contour with an ellipse as in Halir & Flusser (1998). The directions of the resulting minor and major axes are plotted in each panel. The resulting ellipticity, e, is plotted as a function of the semi-major axis, a in Figure 2.4.

We confirm that ω Centauri has an elliptical shape (e.g. Harris, 1996).

The ellipticity of Fe-poor and Fe-rich stars slightly increases from e∼0.05 to 0.07 and from e∼0.06 to 0.08, respectively, when moving from $a \sim 3$ arcmin to 15 arcmin. As a consequence, the ellipticity difference is $\Delta e \sim 0.015$ with statistical significance of $\sim 1\sigma$%.

The major axis of the best-fit ellipses are coincident within one-sigma in both populations.

In the case of M 22, both Fe-poor and Fe-rich stars have similar ellipticities ($e \simeq 0.1$) over the entire analyzed field of view and their major axis have similar directions.

Finally, as expected for oblate rotators, we find that the rotation axis (from Sollima et al., 2019, solid black-gray line in Figure 2.3) is coincident with the semi-minor axis of the best fit-ellipses, i.e. perpendicular to the semi-major axis plotted in Figure 2.3.

Rotation in the plane of the sky

Rotation profile

In this subsection, we analyze the average internal motions of Fe-poor and Fe-rich stars as a function of the radial distance from the cluster center. As a first step, we converted the $\mu_\alpha \cos\delta$ and μ_δ components of proper motions into a radial ($\mu_{\rm RAD}$) and a tangential ($\mu_{\rm TAN}$) motions on the plane of the sky, correcting for the effect of perspective expansion/contraction as in van de Ven et al. (2006). We divided the cluster fields of ω Centauri and M 22 into 17 and 6 circular annulii, respectively, determined with the naive estimator method (Silverman, 1986). To account for the different star densities at different distances from the cluster center we used wider bins in the outskirt of the cluster (in the case of ω Centauri: 5 arcmin for the innermost bin, 3.3 arcmin for $1.2R_{\rm h} < r < 3.2R_{\rm h}$, and 4.2 arcmin for $3.2R_{\rm h} < r < 4.2R_{\rm h}$ and 5.9 arcmin for $r > 4.2R_{\rm h}$).

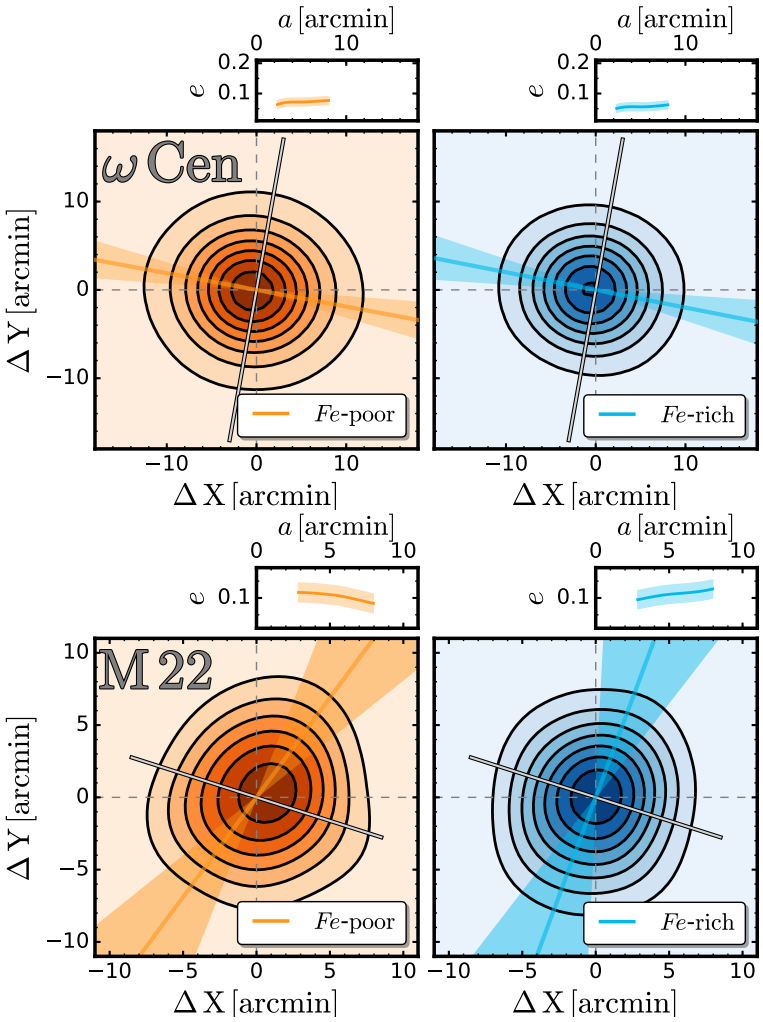

Figure 2.3. Density maps of metal-rich and metal-poor populations in ω Centauri (top panels) and M 22 (bottom panels). The quantities on the abscissa and ordinate are the projected stellar coordinates relative to the cluster center. The color levels are indicative of stellar density and are based on the 2D Binned Kernel Density Estimate Wand et al. (2015). The iso-density contours are shown in each panel together with the rotation axis as determined in Sollima et al. (2019) (solid black-grey line). Red and blue lines in the top-insets show the ellipticity against the major axis, while the shaded regions represent the 1-σ confidence bands.

For each annulus, we used the routines provided by Vasiliev (2019a) to compute the median radial ($\Delta\mu_{\rm RAD}$) and tangential ($\Delta\mu_{\rm TAN}$) motions, thus accounting for systematic errors in Gaia DR2 proper motions. Furthermore, *Gaia* DR2 uncertainties on proper motion are underestimated by a factor of $\sim 10\%$ and $\sim 30\%$ for stars with magnitude $G > 16$ and $G < 13$, respectively.
We therefore artificially increased the observed uncertainties on the proper motions as in Bianchini et al. (2019).

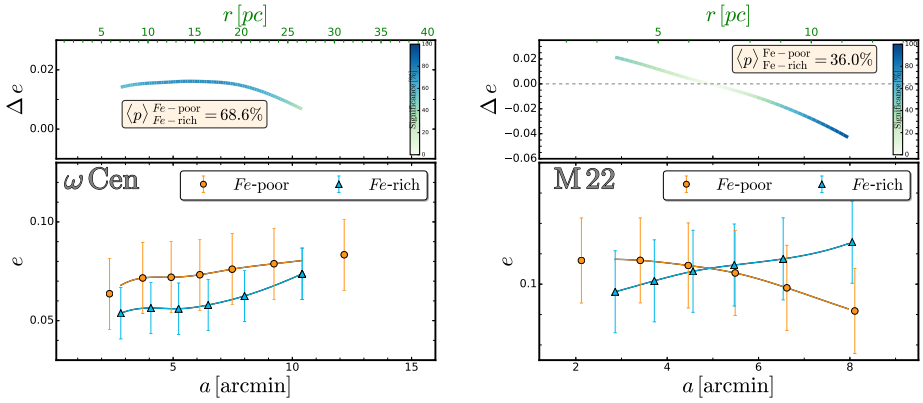

Figure 2.4. Ellipticity, e, of ellipses that best fit the spatial distribution of the different stellar populations of ω Centauri (left) and M 22 (right) against the semi-major axis, a (lower panels). Upper panels show the difference between the ellipticity profiles as a function of a. The level of colors indicate the statistical significance of the difference, as indicated by the colorbar. See text for details.

We then estimated the uncertainty relative to each point by bootstrapping with replacements performed 1,000 times.
The radial and tangential proper motions have been converted from mas/yr to km/s, ($\Delta V_{\rm RAD}$ and $\Delta V_{\rm TAN}$) adopting the distances listed in Table 2.5, derived in Baumgardt & Hilker (2018). The radial and tangential velocity vs. the distance from the cluster center are shown in Figure 2.5. The radial coordinate has been normalized to the half-light radius, from Baumgardt & Hilker (2018) (see Table 2.5).
A visual inspection of Figure 2.5 reveals that the radial profiles of ω Centauri and M 22 are consistent with a zero-velocity up to at least ~4 and ~2 $R_{\rm h}$ respectively. A possible exception is provided by the Fe-rich population of ω Centauri, which seems to exhibit larger radial velocities for distances greater than 4 $R_{\rm h}$.
Concerning the tangential profiles, we find positive values of $\Delta V_{\rm TAN}$ over the entire analyzed radial interval, thus favouring rotation among all the studied populations of ω Centauri and M 22. The tangential profiles of Fe-poor and Fe-rich stars in ω Centauri exhibit their maximum amplitudes of about 6 km s^{-1} at radial distances of about one half-light radii and steadily decrease towards larger distances from the cluster center. In the case of M 22 both populations are consistent with a flat tangential profile in the analyzed radial interval. Our data do not allow to determine whether the rotation pattern of M 22 strongly differs from that of ω Centauri, or if the apparent flat rotation of M 22 is due to the lack of observations in the external regions.
To compare the average velocity profiles of stellar populations we used the same procedure described in Cordoni et al. (2020a, see their Section 5). We first used the Anderson-Darling (A-D) test to estimate the probability, p, that the tangential and radial motions of Fe-poor and Fe-rich stars are drawn from the same parent population. Furthermore, we compared the observed velocity profiles of Fe-poor and Fe-rich stars with $N_{\rm sim}$ = 1000 velocity profiles of simulated Fe-poor and Fe-

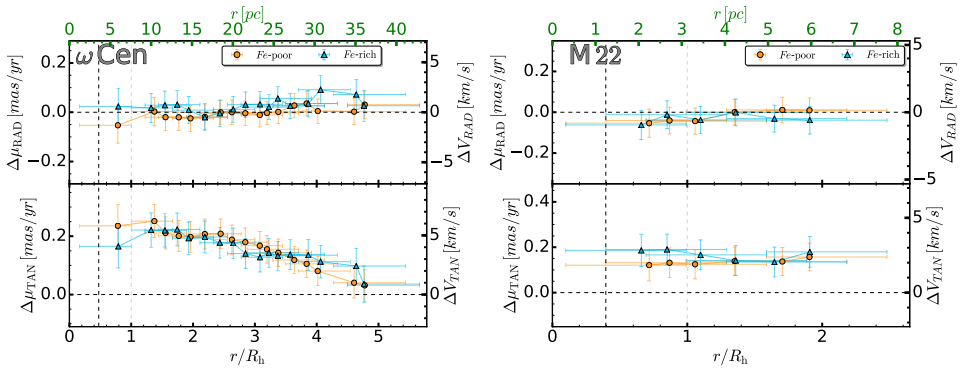

Figure 2.5. Average radial and tangential profile as a function of the radial distance from the cluster centers, for ω Centauri (left) and M 22 (right). The radial quantity is normalized over the half-light radius from Baumgardt & Hilker (2018). Orange circles and cyan triangles represents Fe-poor and Fe-rich stars, respectively.

rich stars. We assumed that the simulated stellar populations share the same velocity profiles and exhibit the same errors as the observed stars. For each bin we calculated the observed difference and counted the number of simulations that resulted in a difference greater than the observed one.

The fraction of simulations, $N^*/N_{\rm sim}$, where $\Delta_{\rm chi} \geq \Delta_{\rm obs}$ is indicative of the significance of the difference of the observed profiles. To quantify the global significance we computed the median of the significance of each bin, as well as the maximum and minimum values along the observed profiles. The results are listed in Table 2.6 for each pair of velocity profiles.

The results from the Anderson-Darling test and the values of $N_{\rm sim}$ are listed in Table 2.6 and reveal that we find no differences between observed velocity profiles of Fe-poor and Fe-rich stars, neither in ω Centauri nor in M 22.

Global rotation

To further quantify the rotation in the plane of the sky of both clusters we adopted the procedure described in Cordoni et al. (2020a, see their Section 3).

Briefly, we divided the field of view of each cluster into 30 circular sectors with an arc length of 45°. We computed the median $\mu_\alpha \cos\delta$ and μ_δ motions for Fe-poor and Fe-rich stars in each sector, and then subtracted the cluster median motion. As previously done for the radial and tangential velocity profiles, we account for Gaia systematic errors as in Vasiliev (2019a).

The resulting quantities, $\Delta\mu_\alpha \cos\delta$ and $\Delta\mu_\delta$, are shown in the bottom panels of Figure 2.6 as a function of the position angle θ, defined counter-clockwise from the east. A visual inspection of this figure suggests that, consistently with the previous method, both populations of ω Centauri and M 22 rotate in the plane of the sky. This result is illustrated in the top panels of Figure 2.6, where we show the positions of the stars relative to the cluster center, together with the vectors

that indicate the median motions of Fe-poor and Fe-rich stars computed in each circular sector.
As in Cordoni et al. (2020a), we used the least-squares technique to fit the sine function defined in Equation 2.1 to all Fe-poor and Fe-rich stars in ω Centauri and M 22. The best fit functions to Fe-poor and Fe-rich stars are represented with orange and azure lines, respectively, in the bottom panels of Figure 2.6. We estimate the goodness of the fit by means of the r^2 parameter described by Equation 2.2 where y_i is the value of $\mu_\alpha \cos\delta (\mu_\delta)$ for each star, i, θ is the corresponding position angle, $\bar{y}$ is the average value of y, and f is the best-fit function. The r^2 values for Fe-poor and Fe-rich are listed in bottom left insets of Figure 2.6. The fact that the motions of ω Centauri and M 22 provide a good match between the data and the sine interpolation ($r^2 > 0.7$), confirms the visual impression that both populations rotate in the plane of the sky.
Figure 2.6 shows that the sine functions that provide the best fit of Fe-poor and Fe-rich stars exhibit slight different rotation patterns. To investigate whether these differences are significant or not, we followed the procedure introduced by Cordoni et al. (2020a, see their Section 4.1). Specifically, we ran 1,000 Monte Carlo simulations of Fe-poor and Fe-rich stars where we assumed that the two populations exhibit the same proper motion distribution corresponding to the sine function that best fits the observed Fe-poor stars. We assumed that the two populations host the same number of stars as the observed Fe-rich and Fe-poor stars and added the corresponding observational errors to the simulated proper motions of each star. We used Equation 2 to fit the proper motion distributions of Fe-poor and Fe-rich stars and calculated the difference between their phases ($\Delta\phi^{\rm abs}$) and amplitudes ($\Delta A^{\rm abs}$). The number of simulations where ($|\Delta {\rm A}^{\rm sim}| \geq |\Delta {\rm A}^{\rm obs}|$) and ($|\Delta\phi^{\rm sim}| \geq |\Delta\phi^{\rm obs}|$) are indicative of the probability that the observed phase and amplitude differences between the corresponding rotation curves is due to observational errors alone. Results are listed in Table 3 and show that there is no evidence for significant differences between the amplitudes and phases of the sine functions that best matches the proper motion distributions of Fe-poor and Fe-rich stars of ω Centauri and M 22.
For completeness, we plot in Figure 2.6 the values of $\mu_\alpha \cos\delta$ and μ_δ inferred for population-a stars against θ. The small sample of population-a stars does not allow to properly fit the data with a sine function ($r^2 = 0.35$) and to understand whether this population shares the same rotation pattern as the bulk of ω Centauri stars or not.

Rotation of stellar populations in ω Centauri as a function of radial distance

The large number of stars available in ω Centauri, together with the wide field of view where Gaia DR2 and UBI ground based photometry from Stetson et al. (2019) offer us the opportunity to investigate the rotation of Fe-poor and Fe-rich stars at different radial distances from the cluster center. We therefore exploit the median tangential velocity profile, re-proposed in the top panel of Figure 2.7 to select three circular annuli (R_1–R_3 in Figure 2.7) with significantly different values

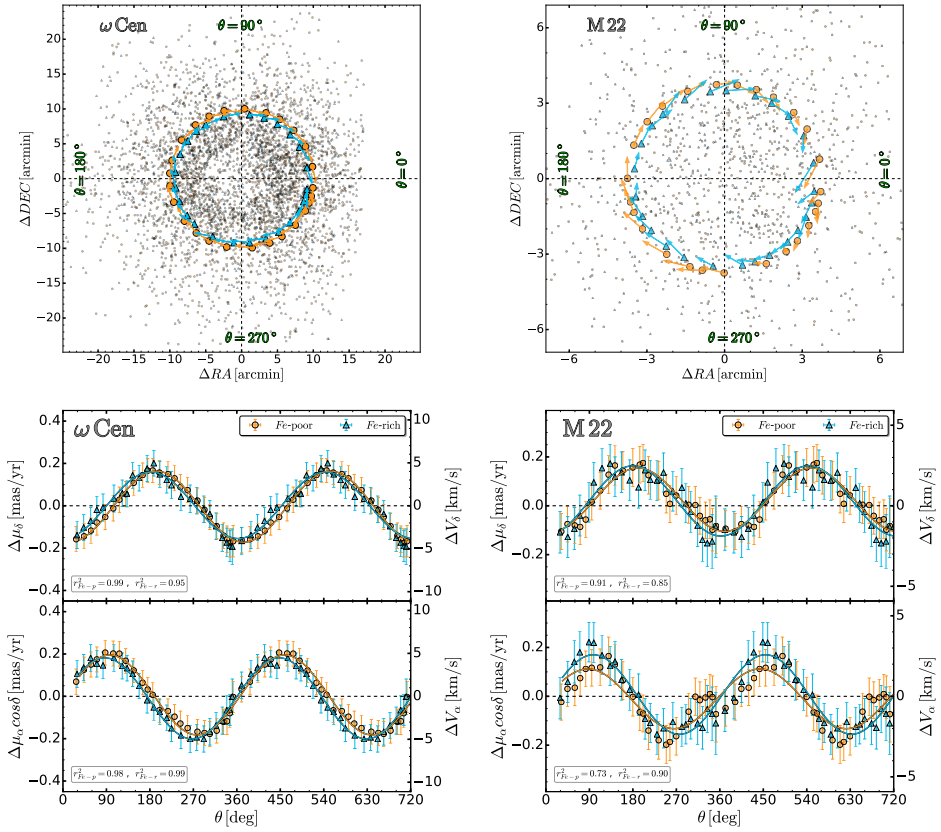

Figure 2.6. *Top panels.* Relative positions of Fe-poor and Fe-rich RGB stars in ω Centauri and M 22 with respect to the cluster center. Orange and cyan arrows indicate the average motion computed in each circular sector, as described in Section 2.2.1, scaled by a factor of 5 for a better visual impact. The radial distances of the arrows correspond to the median radius of stars in each population. *Bottom panels.* $\Delta\mu_\alpha \cos\delta$ and $\Delta\mu_\delta$ as a function of θ for the two analyzed clusters. The bottom-left insets show the value of the r^2 parameter, indicative of the quality of the fit.

of $\Delta\mu_{\rm TAN}$. The three regions are selected so that they contain comparable number of stars. The individual numbers of Fe-poor and Fe-rich stars is indicated in the insets of the lower panels of Figure 2.7.

We'd like to point out that the ratio between Fe-poor and Fe-rich stars increases from the innermost region to the middle region, and remains almost constant between the middle region and the outermost one. Thus confirms previous findings by Bellini et al. (2009).

Concerning the rotation in the plane of the sky, we find that the amplitudes of the best fit sinusoidal functions for both Fe-poor and Fe-rich populations decrease from about six to three km s^{-1} when moving from $r \sim 1\,R_{\rm h}$ to $r \sim 4\,R_{\rm h}$.

The sine functions that provide the least-squares best fit with the observed proper motion distributions of Fe-poor and Fe-rich stars have slightly different values of amplitude A and phase ϕ. We followed the procedure introduced by Cordoni

ID		Region	motion component	ΔA^{obs} mas/yr	$\Delta\phi^{obs}$ rad	$P(\lvert\Delta A^{sim}\rvert \geq \lvert\Delta A^{obs}\rvert)$	$P(\lvert\Delta\phi^{sim}\rvert \geq \lvert\Delta\phi^{obs}\rvert)$
ω Centauri	Fe-poor – Fe-rich	all	$\mu_\alpha \cos\delta$	0.006 ± 0.020	0.179 ± 0.090	0.756	0.403
			μ_δ	0.019 ± 0.022	0.192 ± 0.103	0.333	0.145
		R_1	$\mu_\alpha \cos\delta$	0.026 ± 0.038	0.113 ± 0.134	0.501	0.507
			μ_δ	0.055 ± 0.039	0.047 ± 0.125	0.193	0.845
		R_2	$\mu_\alpha \cos\delta$	0.006 ± 0.026	0.010 ± 0.121	0.848	0.941
			μ_δ	0.032 ± 0.028	0.261 ± 0.133	0.312	0.176
		R_3	$\mu_\alpha \cos\delta$	0.004 ± 0.026	0.399 ± 0.121	0.899	0.112
			μ_δ	0.004 ± 0.028	0.203 ± 0.129	0.916	0.454
	N-poor – N-rich	all	$\mu_\alpha \cos\delta$	0.044 ± 0.019	0.031 ± 0.092	0.878	0.795
			μ_δ	0.004 ± 0.018	0.051 ± 0.110	0.898	0.741
Fe-poor	N-poor – N-rich	all	$\mu_\alpha \cos\delta$	0.008 ± 0.023	0.038 ± 0.155	0.986	0.733
			μ_δ	0.015 ± 0.025	0.114 ± 0.180	0.541	0.147
Fe-rich	N-poor – N-rich	all	$\mu_\alpha \cos\delta$	0.023 ± 0.025	0.107 ± 0.101	0.538	0.655
			μ_δ	0.041 ± 0.024	0.112 ± 0.140	0.196	0.670
		R_1	$\mu_\alpha \cos\delta$	0.102 ± 0.035	0.111 ± 0.168	0.004	0.585
			μ_δ	0.093 ± 0.042	0.127 ± 0.118	0.009	0.477
		R_2	$\mu_\alpha \cos\delta$	0.030 ± 0.025	0.164 ± 0.186	0.451	0.569
			μ_δ	0.043 ± 0.024	0.067 ± 0.195	0.233	0.854
M 22	Fe-poor – Fe-rich	all	$\mu_\alpha \cos\delta$	0.041 ± 0.020	0.210 ± 0.195	0.345	0.379
			μ_δ	0.014 ± 0.018	0.219 ± 0.224	0.745	0.231
	N-poor – N-rich	all	$\mu_\alpha \cos\delta$	0.067 ± 0.020	0.273 ± 0.153	0.077	0.396
			μ_δ	0.041 ± 0.022	0.024 ± 0.143	0.344	0.930

Table 2.6. Comparison of the rotation curves in the $\mu_\alpha cos\delta$ vs. θ, μ_δ vs. θ vs. θ planes of metal-poor and metal-rich stars in the entire field of view of M 22 and ω Centauri and in the analyzed three sub-regions, R_1, R_2, and R_3 of the ω Centauri field of view. We provide the A-D values from the Anderson-Darling test and the corresponding probability that metal-poor and metal-rich stars come from the same parent distribution (p-val). We list the amplitude ($\Delta A^{\rm obs}$) and phase differences ($\Delta\phi^{obs}$) of the curves that provide the best-fit with metal-poor and metal-rich stars and the probability that the observed difference in phase and amplitude are due to observational errors as inferred from Monte-Carlo simulations.

et al. (2020a, see their Section 4.1) and described above to quantify the statistical significance of the observed phase and amplitude differences. Results are listed in Table 2.6 and show that Fe-poor and Fe-rich stars are consistent with sharing the same rotation pattern in the three analyzed regions.

Velocity dispersion profiles

To estimate the radial and tangential velocity dispersion profiles of Fe-poor and Fe-rich stars of ω Centauri and M 22 we followed the procedure described in Mackey et al. (2013); Marino et al. (2014) and Bianchini et al. (2018). Briefly, we maximized the likelihood function

$$\lambda = \prod_{\rm i=1}^{N} p(v_{\rm i}, \epsilon_{\rm i})$$

with the probability of finding a star with velocity $v_{\rm i}$ and uncertainty $\epsilon_{\rm i}$ defined by Equation 2.4. The corresponding uncertainties have been computed by boot-

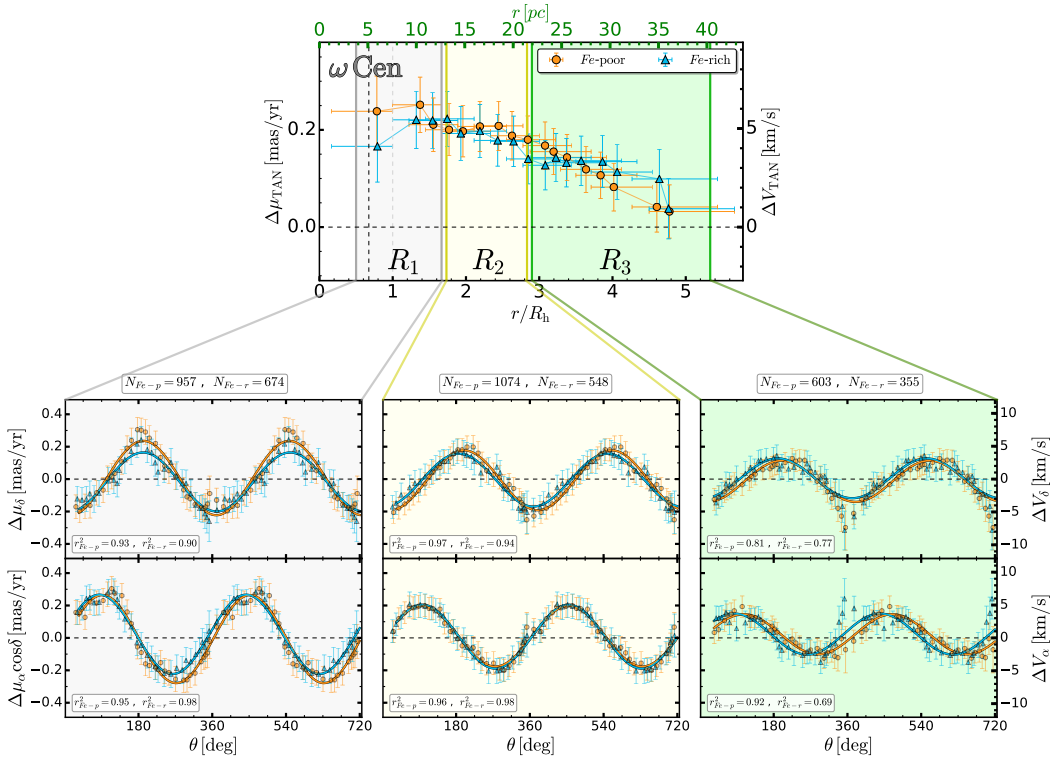

Figure 2.7. *Top panel.* Reproduction of the $\Delta\mu_{\rm TAN}$ vs. r/$R_{\rm h}$ diagram of Fe-poor and Fe-rich stars in ω Centauri plotted in Figure 2.5. *Bottom panels.* $\Delta\mu_\alpha \cos\delta$ and $\Delta\mu_\delta$ against the position angle θ for stars in regions R_1–R_3 defined in the upper panel. The sine functions that provide the best fit with the observations of Fe-poor and Fe-rich stars are represented with orange and azure lines, respectively.

strapping with replacement a 1000 times.

$$p(v_i,\epsilon) = \frac{1}{2\pi\sqrt{(\sigma^2+\epsilon_{\rm i}^2)}} \exp\left(-\frac{(v_{\rm i}-v)^2}{2(\sigma^2+\epsilon_{\rm i}^2)}\right) \tag{2.4}$$

The radial and tangential velocity dispersion profiles as a function of the radial distance from the cluster center are plotted in the upper panels of Figure 2.8, where we used filled and open symbols to represent results from Gaia DR2 and *HST* proper motions, respectively.
The velocity dispersions of ω Centauri and M 22 reach their maximum values of ~18 km s^{-1} and ~9 km s^{-1}, respectively, in the innermost analyzed regions and decline to ~7 and ~6 km s^{-1}, respectively, in the cluster outskirts.
We quantified the anisotropy of cluster stars as $\beta = \sigma_{\rm TAN}/\sigma_{\rm RAD} - 1$, with $\beta < 0$ indicating radial anisotropy and $\beta > 0$ tangential anisotropy. $\beta = 0$ is characteristic of an isotropic stellar system.
β is plotted as a function of the radial distance from the cluster center in the bottom panels of Figure 2.8. Finally, we assessed the statistical significance of the ob-

served differences in the kinematical profiles with the same procedure described in Cordoni et al. (2020a). The average "p-value", together with the its maximum and minimum are listed in Table 2.7 for all the analyzed populations and sub-populations.
Our results show that the studied populations of ω Centauri are radially anisotropic in the central regions, with the Fe-rich population being more radially anisotropic than the Fe-poor ones. In the outermost region of the cluster both populations are consistent with an isotropic system. Furthermore, the p-values listed in Table 2.7 show that the observed differences are statistically not significant.

In M 22 the radial profiles of β for Fe-poor and Fe-rich stars are consistent with each other and are both approximately isotropic.

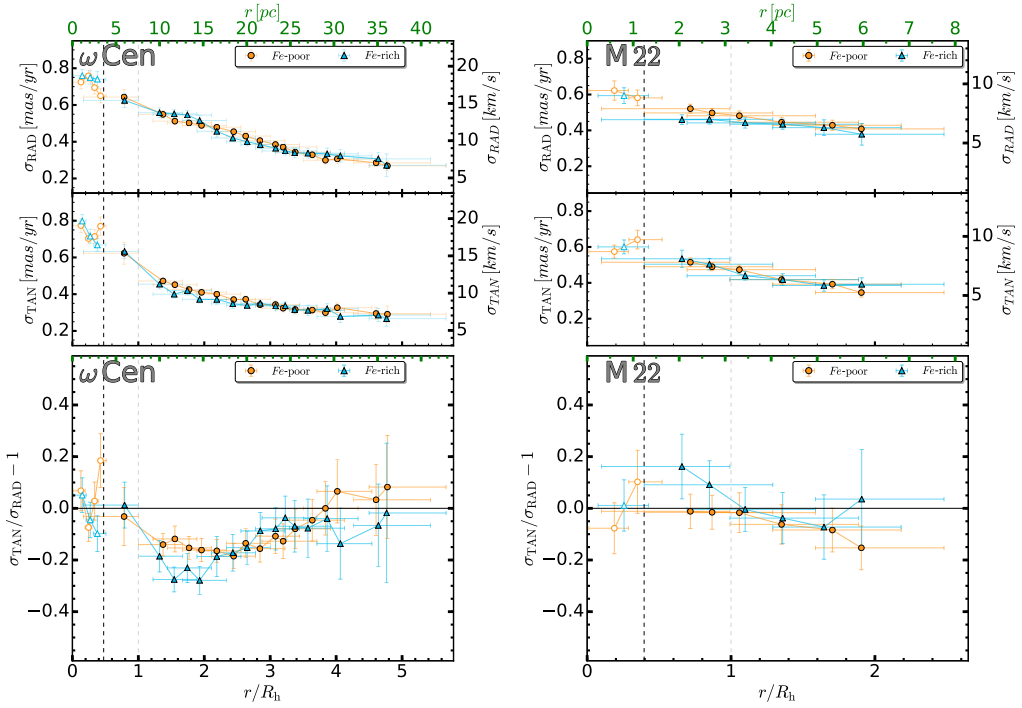

Figure 2.8. Velocity dispersion profiles for ω Centauri (top-left) and M 22 (top-right). Empty markers are *HST* results, while filled markers correspond to Gaia DR2 proper motions. Bottom panels show the corresponding anisotropy radial profiles. The horizontal lines plotted in the bottom panels correspond to isotropic stellar systems. Orange circles and cyan triangles represent Fe-poor and Fe-rich stars, respectively. The black and gray vertical dashed lines highlight the core radii and the half-light radii of each cluster from Baumgardt & Hilker (2018). The radial quantity is normalized over the half-light radius.

Cluster		$\Delta\mu_{RAD}$ A-D	$\Delta\mu_{TAN}$ A-D	$\Delta\mu_{RAD}$ P	$\Delta\mu_{TAN}$ P	$\Delta\sigma_{RAD}$ P	$\Delta\sigma_{TAN}$ P	$\Delta\beta$ P
ω Centauri	Fe-poor – Fe-rich	0.100	0.110	$0.690^{0.230}_{0.999}$	$0.750^{0.660}_{0.949}$	$0.230^{0.026}_{0.989}$	$0.449^{0.012}_{0.946}$	$0.600^{0.030}_{0.923}$
	N-poor – N-rich	0.120	0.090	$0.619^{0.172}_{0.945}$	$0.866^{0.583}_{0.995}$	$0.412^{0.011}_{0.977}$	$0.151^{0.007}_{0.927}$	$0.555^{0.065}_{0.988}$
Fe-poor	N-poor – N-rich	0.180	0.130	$0.600^{0.186}_{0.970}$	$0.745^{0.237}_{0.980}$	$0.478^{0.004}_{0.957}$	$0.132^{0.021}_{0.909}$	$0.638^{0.040}_{0.979}$
Fe-rich	N-poor – N-rich	0.160	0.060	$0.378^{0.003}_{0.970}$	$0.186^{0.000}_{0.825}$	$0.400^{0.005}_{0.959}$	$0.280^{0.012}_{0.874}$	$0.514^{0.043}_{0.998}$
	N-poor – pop-a	0.023	0.020	$0.600^{0.416}_{0.884}$	$0.144^{0.066}_{0.809}$	$0.295^{0.216}_{0.447}$	$0.428^{0.026}_{0.385}$	$0.682^{0.346}_{0.976}$
	N-rich – pop-a	0.014	0.040	$0.650^{0.472}_{0.802}$	$0.201^{0.064}_{0.472}$	$0.850^{0.778}_{0.959}$	$0.446^{0.290}_{0.697}$	$0.388^{0.058}_{0.680}$
M 22	Fe-poor – Fe-rich	0.201	0.015	$0.810^{0.587}_{0.988}$	$0.749^{0.509}_{0.976}$	$0.312^{0.009}_{0.644}$	$0.501^{0.104}_{0.997}$	$0.609^{0.231}_{0.920}$
	N-poor – N-rich	0.250	0.026	$0.772^{0.387}_{0.953}$	$0.709^{0.536}_{0.896}$	$0.460^{0.059}_{0.963}$	$0.504^{0.240}_{0.863}$	$0.587^{0.177}_{0.999}$

Table 2.7. Third and fourth columns indicate the probability (p-value) that the two populations come from the same parent distribution, according to the Anderson-Darling (A-D) test. We considered the radial distributions of the quantities listed in the first line: $\Delta\mu_{RAD}$, $\Delta\mu_{TAN}$, $\Delta\sigma_{RAD}$, $\Delta\sigma_{TAN}$ and $\Delta\beta$. The test has been carried out independently in the radial and tangential component. The remaining columns list the probability, P, that the velocity distributions come from the same parent distribution ($P = 1$) or not ($P = 0$), determined as described in Section 2.2.1. We provide the average value of P and the minimum and maximum P values.

2.2.2 Multiple stellar populations with different light-element abundances

In this section, we investigate the stellar populations of ω Centauri and M 22 selected on the basis of their content of light elements. In ω Centauri, we analyzed the entire groups of N-rich and N-poor stars identified in Figure 2.2. Moreover, we separately compared the spatial distributions and the kinematics of the sub-sample of N-poor and N-rich stars that belong to the Fe-poor population alone and of the sub-sample of N-poor, N-rich and population-a stars among Fe-rich stars. In M 22, which has a smaller number of RGB stars than ω Centauri, we limited the analysis to entire sample of N-rich and N-poor stars. The spatial distributions of the stellar populations with different light-elements of both M 22 and ω Centauri are analyzed in Section 2.2.2, while Section 2.2.2 is focused on their internal kinematics.

Spatial distribution of N-rich and N-poor populations

To investigate the spatial distributions of stellar populations with different nitrogen content, we extended the analysis introduced in Sections 2.2.1 to the selected groups of N-rich and N-poor stars. Results on ω Centauri are illustrated in Figures 2.9 and 2.10.

The upper panels of Figure 2.9 compare the density contours of the overall N-poor and N-rich samples. Clearly, N-rich stars, which have average ellipticity, $e \sim 0.13$, exhibit more elliptical distributions than N-poor stars ($e \sim 0.05$).

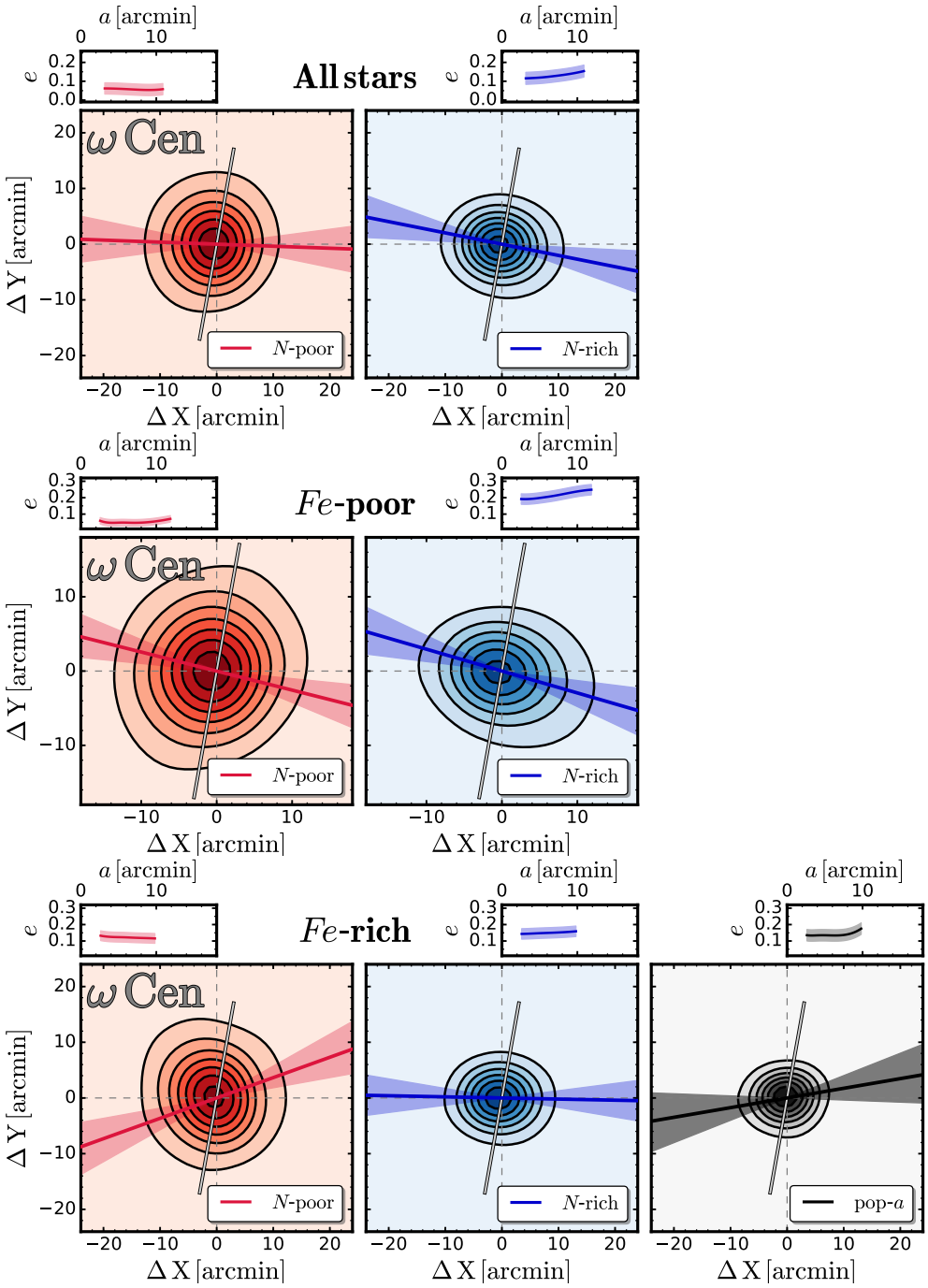

Figure 2.9. Density maps of stellar populations of ω Centauri with different nitrogen abundances and of population-a stars. Top and center rows refer to Fe-poor and Fe-rich stars, respectively, while the bottom panels show the spatial distribution of the entire sample of N-poor and N-rich stars. The ellipticities of the isodensity contours are plotted as a function of the semi-major axis.

The ellipticity difference between the spatial distributions of N-rich and N-poor stars is larger when we limit the analysis to the Fe-poor stars as shown in the mid-

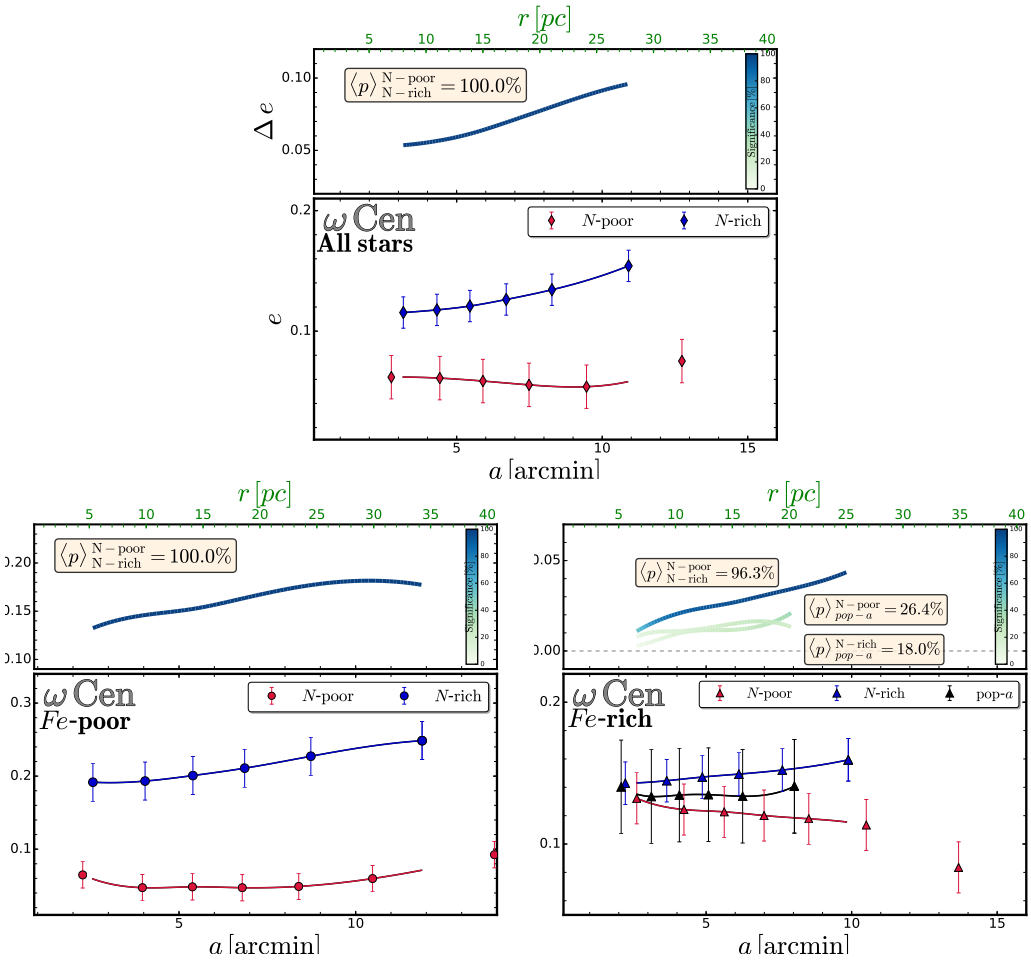

Figure 2.10. *Lower panels.* Ellipticity of N-rich and N-poor stellar populations as a function of the major semi-axis of the best-fit ellipses, a for in the entire sample of analyzed ω Centauri stars (left), among Fe-poor stars (middle) and Fe-rich stars (right). The latter panel also includes population-a stars. *Upper panels.* Absolute values of ellipticity differences inferred from the populations quoted in each panel against a. The level of colors indicate the statistical significance of the difference as indicated by the colorbar.

dle panels of Figure 2.9. Specifically, N-rich Fe-poor stars exhibit more flattened distributions (ellipticity e ~0.20) than N-poor Fe-poor stars, which have $e \sim 0.05$. Qualitatively, the spatial distributions of the Fe-rich sub-populations with different nitrogen abundances follow a similar behaviour as their Fe-poor counterparts, although the ellipticity differences among the various sub-populations are less pronounced. Indeed, as shown in the lower panels of Figure 2.9, N-rich Fe-rich stars have an average ellipticity of $e \sim 0.15$, which is slightly higher than that of N-poor Fe-rich stars ($e \sim 0.12$). The ellipticity difference is significant at the ~2.1 σ-level. On the other hand, population-a stars have, on average, $e \sim 0.13$, and the small ellipticity difference with N-rich Fe-rich and N-poor Fe-rich is not statistically significant.

Overall, Figure 2.9 reveals that the median semi-major axes of the best-fit ellipses of all populations are consistent with each other within one sigma and are almost perpendicular to the global rotation axis determined in Sollima et al. (2019).

For completeness, we plot the ellipticity of the various subpopulations as a function of the major axis of the best-fit ellipse, a, in the bottom panels of Figure 2.10. Upper panels show the absolute value of the ellipticity differences $|\Delta e|$ between the populations quoted in the figures against a. The color scale is indicative of the statistical significance of the difference. All populations are consistent with having constant ellipticity in the analyzed interval of a.

Results on the spatial distributions of the N-poor and N-rich stellar populations of M 22 are illustrated in Figure 2.11. N-rich stars have average ellipticity $e \sim 0.15$ and clearly exhibit a more-flattened distribution than N-poor stars, which have $e \sim 0.05$.

Internal kinematics

The internal kinematics of the stellar populations with different nitrogen abundances and of population-a stars are derived by using the methods described in Section 2.2.1.

The velocity profiles of the entire sample of N-rich and N-poor stars are plotted in the left panels of Figure 2.12 and the corresponding results on the subpopulations of N-poor and N-rich populations among Fe-poor and Fe-rich stars are illustrated in the middle and right panels of Figure 2.12, respectively. The right panels also include the velocity profiles of population-a stars.

A visual inspection of the top-left panels of Figure 2.12 reveals that both N-rich and N-poor stars exhibit significant rotation in the plane of the sky, with $\Delta\mu_{\rm TAN}$ ranging from ~6 km/s towards the cluster core to ~2 km/s in the most-distant regions.

Stellar populations with different nitrogen abundances exhibit radial anisotropic motions between ~1 and 3 half-light radii. Differences in the radial profile of β are present the region with $r/R_{\rm h} \sim 1.5-2.5$, where N-rich stars have more-radially anisotropic motions and between ~3 and 4.5 half-light radii, where N-poor stars are consistent with having isotropic motions while N-rich stars have $\beta \sim -0.2$.

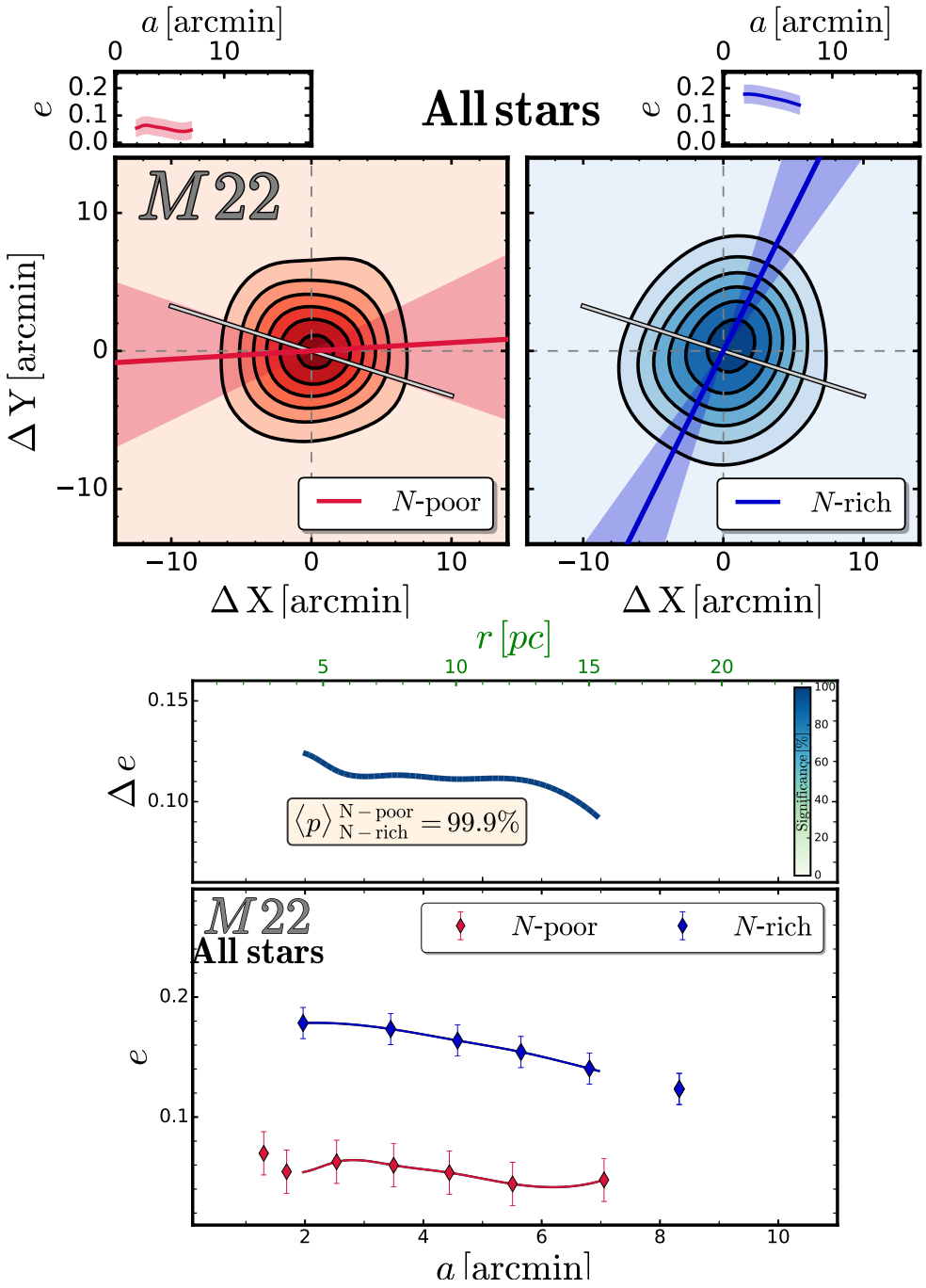

Figure 2.11. *Top panels.* Same as Figure 2.3 and 2.9 for the N-poor (red, left panel) and N-rich (blue, right panel) in M 22. *Bottom panel.* Ellipticity profile as in Figure 2.4 and 2.10.

When we consider the sample of Fe-poor stars alone, we find that N-poor and N-rich stars have similar rotation patterns. In contrast, stellar populations with different nitrogen abundances seem to exhibit different tangential-velocity profiles in the radial annulus between ~ 0.8 and ~ 2.3 half-light radii.

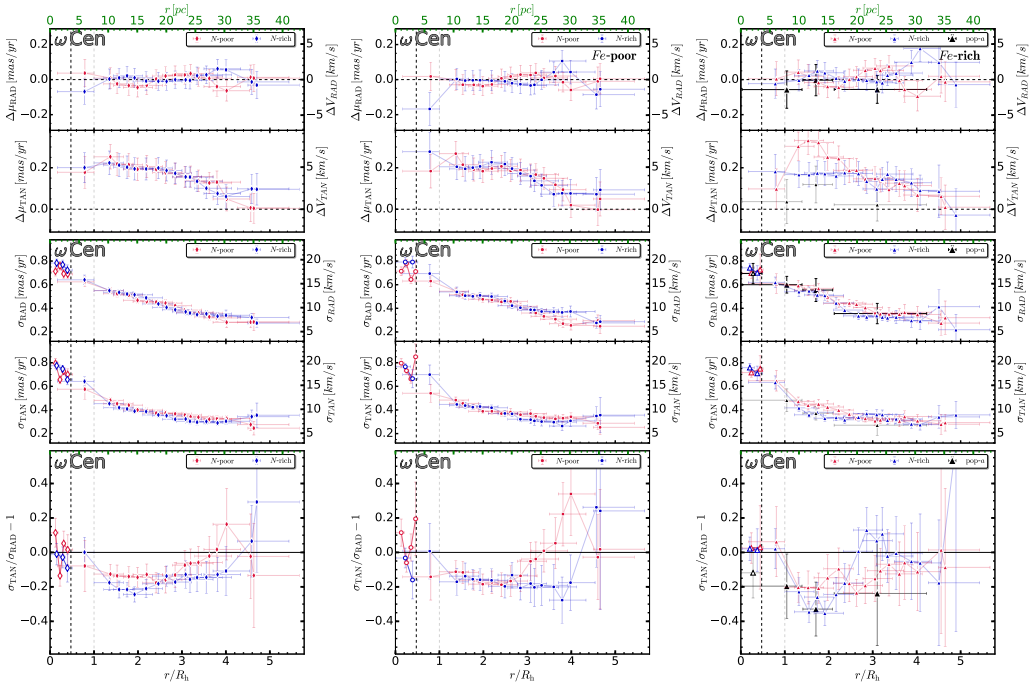

Figure 2.12. From top to bottom: average velocity, velocity dispersion and anisotropy profiles as a function of the distance from the cluster center for N-poor (red dots) and N-rich (blue triangles) stars. Left panels refer to the entire sample of ω Centauri stars, while in the middle and right panels we considered the Fe-poor and Fe-rich populations, respectively. The velocity profiles of population-a stars are plotted with black triangles in the right panels. The black and gray vertical dashed lines highlight the core radius and the half-light radius from Baumgardt & Hilker (2018). The radial quantity is normalized over the half-light radius.

The average values of $\Delta\mu_{\rm TAN}$ for N-poor and N-rich stars, estimated as in Vasiliev (2019a), are 0.27±0.06 and 0.18±0.06, respectively. However, these uncertainties, which account for systematic errors that affect Gaia DR2 proper motions, are upper limits to the true errors on the relative proper motions. Indeed, Gaia DR2 systematic errors depend on stellar colors and positions. Hence, they mostly cancel out when we consider the relative motions of N-rich and N-poor stars that have similar colors and spatial distributions. The average $\Delta\mu_{\rm TAN}$ difference between N-poor and N-rich stars is 0.09±0.03 if we do not consider the contribution of Gaia DR2 systematics. In this case the difference would be significant to the 3σ-level.

To further investigate the rotation of stellar populations with different nitrogen abundances among Fe-rich stars, we plot in Figure 2.13 $\Delta\mu_\alpha cos\delta$ and $\Delta\mu_\delta$ as a function of θ for N-poor Fe-rich and N-rich Fe-rich stars in the two radial bins. We find that the rotation curves of N-poor stars within two half light-radii from the cluster center exhibit higher amplitudes than those of N-rich stars in the same radial bin. The amplitude differences derived from the $\Delta\mu_\alpha cos\delta$ vs. θ and

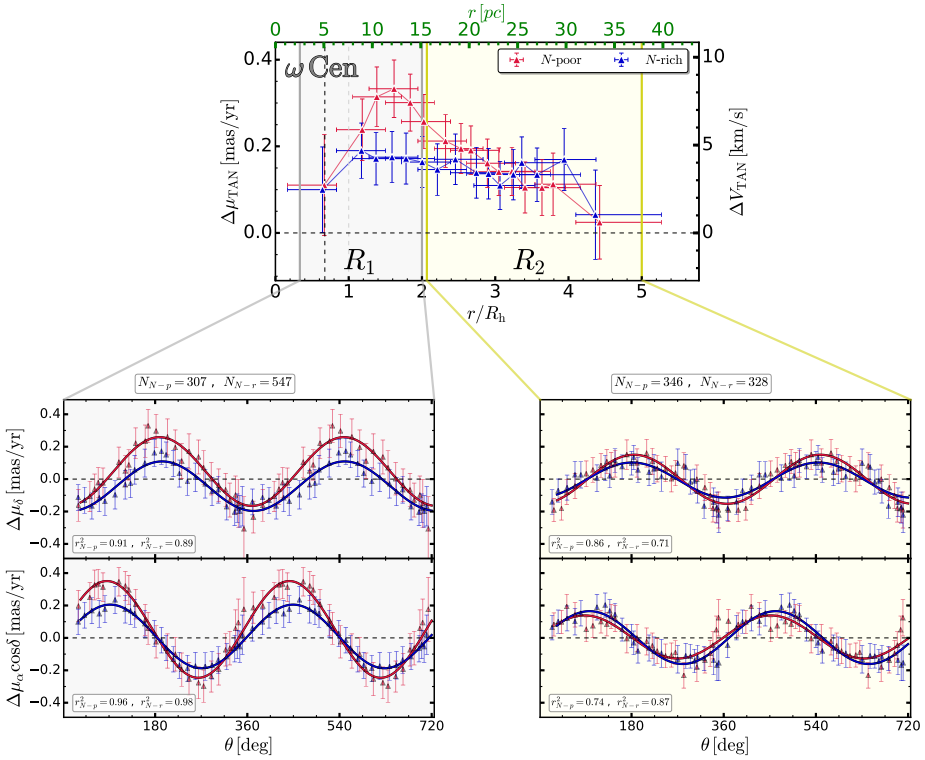

Figure 2.13. Reproduction of the radial profile of $\Delta\mu_{\rm TAN}$ for the N-rich and N-poor groups of Fe-rich stars (top) in ω Cen. In the bottom panels, $\Delta\mu_\alpha \cos\delta$ and $\Delta\mu_\delta$ are plotted as a function of the position angle θ for stars in regions R_1 and R_2 defined in the top panel. The sine functions that provide the best fit with the observations of N-poor and N-rich stars are represented with red and blue lines, respectively.

$\Delta\mu_\delta$ vs. θ planes are significant at 2.4-σ and 2.1-σ, level respectively. Hence, the probability that the amplitude differences observed in both components of proper motions are due to observational errors is smaller than 0.2%. The rotation curves of the two populations are consistent with having the same amplitudes when we consider stars with $r > 2R_{\rm h}$.

2.2.3 Summary and conclusions

We combined Gaia DR2 and *HST* proper motions with multi-band photometry from *HST* and ground-based facilities to investigate the spatial distributions and the internal kinematics of multiple stellar populations in the Type II GCs M 22 and ω Centauri over a wide field of view, from the cluster center up to ~2.5 and ~5.5 half-light radii, respectively.

We first identified stellar populations with different iron abundances along the RGB from differential-reddening corrected CMDs build with appropriate combinations of U, V, I magnitudes (or $m_{\rm F336W}, m_{\rm F606W}, m_{\rm F814W}$ magnitudes, in the

case of *HST* data). Then, we identified and analyzed stellar populations with different nitrogen content. The main results for stellar populations with different metallicities of M 22 can be summarized as follows:

- Fe-poor and Fe-rich stars exhibit the same average proper motions within 1-σ. The same result is true also for stellar populations with different Nitrogen abundance.

- Fe-poor and Fe-rich stars share similar spatial distributions with an average ellipticity, $e \sim 0.1$ (Figure 2.4).

- Both populations exhibit significant rotation in the plane of the sky and their rotation curves are characterized by similar phases and amplitudes (A~2.5 km/s, Figure 2.6). The tangential-velocity profiles of Fe-poor and Fe-rich stars are nearly flat in the analyzed radial interval with an average $\Delta\mu_{\rm TAN} \sim 2.5$ km/s (Figure 2.5).

- Fe-poor and Fe-rich stars share similar velocity-dispersion profiles, with both the radial and tangential component ranging from ~9 to ~6 km/s when moving from the cluster center to a radius of ~2.5 half-light radii. Both populations exhibit isotropic motions (Figure 2.8).

The main findings on the Fe-poor and Fe-rich stars of ω Centauri include:

- The stellar populations with different metallicities share the same motions, thus confirming the conclusions by Anderson & van der Marel (2010); Sanna et al. (2020). Similarly, stellar populations with different N have the same average proper motions.

- The spatial distributions of both stellar populations have similar elliptical shapes with ellipticity, $e \sim 0.06$, and similar directions of the major axes (Figure 2.4).

- The rotation pattern in the plane of the sky is similar for Fe-poor and Fe-rich stars. The tangential-velocity component decreases from ~ 6 km/s at a radial distance of about one half-light radius from the center to ~2 km/s at $r/R_{\rm h} \sim 5$ (Figure 2.5 and 2.6).

- The rotation curves of both populations share similar amplitudes and phases. When we investigate regions with different radial distances from the cluster center, we find that the amplitude of the rotation decreases when moving away from the cluster center (Figure 2.7).

- Both populations exhibit similar velocity-dispersion profiles in the plane of the sky, with the values of radial and tangential velocities ranging from ~18 km/s, in the cluster center, to 7 km/s, at a distance of ~ 5 km/s (Figure 2.8).

- The motions of the stellar populations with different metallicities are isotropic within about one half-light radii from the cluster center and radially anisotropic from ~ 1 up-to $\sim 4\,R_{\rm h}$ (Figure 2.8). The motions become isotropic in the outermost regions.

In addition, we identified two main groups of N-poor and N-rich stars of both ω Centauri and M 22 and studied their spatial distributions and internal kinematics. In the case of ω Centauri we also investigated the population-a, which is composed of the most metal-rich stars of this cluster (e.g. Johnson & Pilachowski, 2010; Marino et al., 2011).
The main results on stellar populations with different nitrogen of ω Centauri can be summarized as follows.

- N-rich stars of ω Centauri exhibit a flatter spatial distribution than N-poor stars. The difference is more pronounced when we consider the sample of metal-poor stars alone, where the N-poor Fe-poor and N-rich Fe-poor sub-populations have average ellipticities of ~0.06 and ~0.22, respectively (Figure 2.10). Population-a stars exhibit higher ellipticity ($e \sim 0.13$) than the bulk of ω Centauri stars, which have $e \sim 0.07$.

- N-poor and N-rich stars of ω Centauri exhibit similar rotation patterns. However, when we consider the Fe-rich population alone, we find that N-rich Fe-rich stars have lower tangential velocities than N-poor Fe-poor stars in the radial interval between ~ 1 and ~ 3 half-light radii (Figure 2.12). In this region, the amplitude of the rotation curve of N-rich Fe-rich stars of ω Centauri seems smaller than that of N-poor Fe-rich stars, but the amplitude difference is significant at ~2.4-sigma and 2.1 level only, when we consider the motions $\Delta\mu_\alpha cos\delta$ vs. θ and $\Delta\mu_\delta$ vs. θ planes, respectively. The conclusion that the amplitude differences are due to observational uncertainties in both components at the same time is smaller than 0.002. Similarly to the group of N-rich Fe-rich stars, population-a seems to exhibit low values of $\Delta\mu_{\rm TAN}$ relative to the N-poor Fe-rich stars [9]

- Both N-rich and N-poor stars of ω Centauri exhibit radially anisotropic motions with some hints for differences between the level of anisotropy of the two populations in the radial interval between 1.5 and 2.5 half-light radii. Between ~3 and 4.5 half-light radii N-poor stars are consistent with isotropic motions while N-rich stars have $\beta \sim -0.2$ (Figure 2.12).

[9] The origin of population-a stars, which exhibit distinct metallicity than the bulk of ω Centauri stars, is still widely debated. Work based on chemical evolution models suggests that it is an extreme case of chemical enrichment (e.g. D'Antona et al., 2016, and references therein). As an alternative, recent work suggest that it could be the product of a merger (Calamida et al., 2020). Specifically, the latter hypothesis would be supported by a strong radial anisotropy of population-a stars, which is a signature of a minor-merger remnant (Hong et al., 2017). Nevertheless, the fact that population-a stars are more centrally concentrated than metal-poor stars (e.g. Bellini et al., 2009) would be a challange for the merging scenario (Gavagnin et al., 2016).

Numerical studies show that tidally-filled stellar systems exhibit isotropic motions in their central regions, as a consequence of the shorter relaxation time and the high stellar encounter rate. Moving toward the middle regions, the system starts to expand due to the relaxation process. Therefore, stars in these regions would exhibit a moderate radially anisotropic motion. Finally, since stars with radial orbits preferentially escape from the system (e.g. Takahashi et al., 1997), the outermost regions are characterized by isotropic motions. On the other hand, tidally underfilling systems do not show isotropic pattern in the outer regions (Vesperini et al., 2014; Tiongco et al., 2016).

Based on N-body simulations of multiple populations in GCs, Tiongco et al. (2019) show that the anisotropy profile of 1G[10] stars evolves as a tidally-filling stellar system, whereas the 2G behaves like a tidally underfilling system (see also Tiongco et al., 2016). Hence, their 1G and 2G stars share similar anisotropy profiles in the inner and middle regions of the clusters but exhibit different trends in the outer regions. The anisotropy profiles of N-poor Fe-poor and N-rich Fe-poor stars (bottom-middle panel of Figure 2.12) are qualitatively consistent with the findings by Tiongco and collaborators. Similar conclusions are drawn by Bellini et al. (2015) in their investigation of the internal kinematics of stellar populations in the GC NGC 2808.

We find that the ellipses that reproduce the distribution of N-rich stars of M 22 have higher ellipticities than those of N-poor stars, in close analogy with what is observed in ω Centauri. This result is qualitatively consistent with the conclusion by Lee (2015), who find that Ca-rich stars of M 22 are more elongated than Ca-poor stars, in the hypothesis that Ca-rich stars are, on average, nitrogen enhanced with respect to the Ca-poor population. N-poor and N-rich stars of M 22 exhibit similar rotation patterns and radially isotropic proper motions. The fact that M 22 has significantly shorter relaxation times than ω Centauri (e.g. Baumgardt & Hilker, 2018), could indicate that M 22 stars are partially mixed and have erased most of the initial dynamical differences between the distinct stellar populations. This possibility could explain why the stellar populations of M 22 share the similar kinematics. However, it is worth noting that our results do not confirm the conclusion by Lee (2015) and Lee (2020) who find metal-rich stars of M 22 rotate faster than metal-poor stars both on the plane of the sky and along the line of sight.
The results are based on the selection of Fe-rich and Fe-poor stars derived from the procedure I of Section 2.2. We repeated the analysis by using the sample of Fe-rich and Fe-poor stars of ω Centauri selected by using procedures II and III of Section 2.2 and confirm all the conclusions of the paper. We conclude that the results are not affected by the criteria adopted to separate stars with different metallicities.

[10] We adopt here the same naming convention used in Tiongco et al. (2019), i.e. 1G and 2G in place of 1P and 2P.

The findings of this paper, together with results from the literature provide constraints on the formation and evolution of multiple populations in Type II GCs. Indeed, the present-day dynamics of stellar populations in clusters where the stars are not fully mixed provide information on the initial conditions of stellar populations in GCs.

In this context, we emphasize that the rotation of stellar populations with different metallicities has been previously studied from radial velocities of RGB stars. In their spectroscopic study of ∼400 stars in ω Centauri, Norris et al. (1997) did not find significant rotation along the line of sight among the most metal-rich stars in their sample (corresponding to ∼20% of the studied stars). In contrast, the metal-poor component clearly exhibits systemic rotation. This result has been challenged by Pancino et al. (2007) who concluded that the metal-poor, metal-intermediate, and metal-rich stars are consistent with having the same rotation patterns based on radial velocities.

Our results on the rotation in the groups of Fe-poor and Fe-rich stars corroborate the evidence that the two main sample of stars with different metallicities share similar rotation patterns both along the line of sight and the plane of the sky. However, the fact that the sample of population-a stars studied in this paper exhibit lower tangential velocities relative to the bulk of ω Centauri stars suggests that the stars of this extreme population, similarly to the other Fe-rich and N-rich stars of ω Centauri, exhibit less pronounced rotation on the plane of the sky than the remaining cluster members, similarly to what has been suggested by Norris et al. (1997) from stellar radial velocities.

The motions on the plane of the sky of ω Centauri stars have been recently studied by using *HST* relative proper motions of stars in a field located ∼17 arcmin south-west of the cluster center (Bellini et al., 2018). The two groups of MS-I and MS-II stars studied by Bellini et al. (2018) can be tentatively associated with the populations of N-poor and N-rich stars analyzed in our paper[11]. Bellini et al. (2018) shows that MS-II stars are significantly more radially anisotropic than MS-I stars, which are consistent with an isotropic velocity distribution. This result is consistent with our finding that at $r/R_{\rm h} \sim 3.5$ the N-rich stars have $\beta \sim -0.2$, while N-poor stars exhibit nearly isotropic motions. Moreover, MS-I stars exhibit excess systemic rotation in the plane of the sky with respect to MS-II stars (Bellini et al., 2018). In this paper, we find that among Fe-rich stars, the rotation curves of the N-poor population exhibit larger amplitudes than those of N-rich stars.

[11] MS-I and MS-II stars have been identified by Milone et al. (2017a) along the entire MS, from the turn off towards the hydrogen-burning limit by using optical and near-infrared *HST* photometry. MS-I stars are consistent with having average [Fe/H]∼ −1.7 and primordial helium content, whereas MS-II stars are, on average, more metal-rich ([Fe/H]∼ −1.4) and have high helium abundance (Y∼0.37–0.40). Both MSs host stellar sub-populations with different metallicities and light-element abundances, with MS-II stars having lower oxygen and higher nitrogen content than MS-I stars. Due to the complexity of ω Centauri, it is not possible to connect the stellar populations analyzed in this paper along the RGB with those identified by Milone et al. (2017a) along the MS. Nevertheless, based on the metallicities and the content of helium and nitrogen, we can associate the bulk of MS-I stars with the N-poor population of this paper, whereas the majority of MS-II stars are the RGB counterparts of the N-rich population.

Hence, both results from this paper and from Bellini and collaborators corroborate the conclusion that stellar populations with different nitrogen abundances exhibit distinct rotation patterns.

A variety of scenarios predict that GCs have experienced a complex formation history and that the multiple stellar populations are a consequence of different star-formation episodes (Renzini et al., 2015, and references therein). According to some of these scenarios, GCs host second stellar generations that formed in high-density subsystems embedded in a more-extended first generation (e.g. Ventura et al., 2001b; D'Ercole et al., 2008; D'Antona et al., 2016; Calura et al., 2019). These scenarios are supported by the evidence that metal-rich and helium-rich stars of ω Centauri, whose half-light relaxation time exceed the Hubble time, are more centrally concentrated than the bulk of cluster stars (e.g. Norris et al., 1996; Sollima et al., 2007; Bellini et al., 2009).

Mastrobuono-Battisti & Perets (2013, 2016) investigated the possibility that the formation of second-generation stars in GCs may occur in flattened and centrally-concentrated disk-like structures. They used N-body simulations to explore the evolution of such stellar disks embedded in first-generation stars and concluded that the signature of the initial configuration can still be observable in the present-day clusters if the relaxation time is long enough. The finding that N-rich stars exhibit elliptical spatial distributions with higher eccentricity than that of N-poor stars, is qualitatively consistent with the possibility that N-rich stars are the second generation of ω Centauri and formed the a disk-like structure.

Based on the chemical composition of the stellar populations of ω Centauri, Marino et al. (2019b) suggested that ω Centauri has first experienced the enrichment in iron and α elements (oxygen) from core-collapse supernovae. This process is followed by the formation of stellar populations from material ejected from more-massive first-generation stars, possibly in the asymptotic-giant branch phase, and processed by p-capture elements. The evidence that the groups of Fe-rich and Fe-poor stars of both ω Centauri and M 22 have similar spatial distributions while N-rich stars are more flattened than N-poor stars is consistent with a scenario where distinct processes are responsible for the enrichment in iron and in p-capture elements, and where the formation of N-rich stellar populations is associated with cooling flow of material in centrally-concentrated disk-like structures.

CHAPTER

3 Multiple Stellar populations in Young star clusters

3.1 Extended Main-Sequence Turn-Off as a common feature of Milky Way Open clusters

This Section is taken from Cordoni et al. (2018).

Abstract

We present photometric analysis of twelve Galactic open clusters and show that the same multiple-population phenomenon observed in Magellanic Clouds (MCs) is present in nearby open clusters. Nearly all the clusters younger than ~2.5 Gyr of both MCs exhibit extended main-sequence turnoffs (eMSTOs) and all the cluster younger than ~700 Myr show broadened/split main sequences (MSs). High-resolution spectroscopy has revealed that these clusters host stars with a large spread in the observed projected rotations.
In addition to rotation, internal age variation is indicated as a possible responsible for the eMSTOs, making these systems the possible young counterparts of globular clusters with multiple populations. Recent work has shown that the eMSTO+broadened MSs are not a peculiarity of MCs clusters. Similar photometric features have been discovered in a few Galactic open clusters, challenging the idea that the color-magnitude diagrams (CMDs) of these systems are similar to single isochrones and opening new windows to explore the eMSTO phenomenon. We exploit photometry+proper motions from Gaia DR2 to investigate the CMDs of open clusters younger than ~1.5 Gyr.
Our analysis suggests that: (i) twelve open clusters show eMSTOs and/or broadened MSs, that cannot be due neither to field contamination, nor binaries; (ii) split/broadened MSs are observed in clusters younger than ~700 Myr, while older objects display only an eMSTO, similarly to MCs clusters; (iii) the eMSTO, if interpreted as a pure age spread, increases with age, following the relation observed

in MCs clusters and demonstrating that rotation is the responsible for this phenomenon.

3.1.1 Introduction

In the past years, work based on high-precision *Hubble Space Telescope* (*HST*) photometry discovered that the color-magnitude diagrams (CMDs) of most star clusters younger than ~2.5 Gyr in the Large and Small Magellanic Cloud (LMC and SMC) are not consistent with simple stellar populations. Specifically, most, if not all, of them exhibit extended main-sequence turnoffs (eMSTOs, e.g. Mackey & Broby Nielsen, 2007b; Glatt et al., 2008; Milone et al., 2009), and clusters younger than ~700 Myr display both eMSTOs and split main sequences (MSs, e.g. Milone et al., 2013, 2015, 2018b; Li et al., 2017; Correnti et al., 2017).
The comparison between the observed and synthetic CMDs from the Geneva database (e.g. Georgy et al., 2014) suggests that split MSs are consistent with two stellar populations with different rotation rates. A group of stars with rotation close to the breakout value ($\omega \sim 0.9\omega_{cr}$), which corresponds to the red MS and includes about two thirds of the total number of MS stars, and a population of slow rotators with $\omega \sim 0$, which populate the blue MS (e.g. D'Antona et al., 2015; Milone et al., 2015, 2016a). On the turn-off region, rapidly and slowly rotating stars distribute on brighter and fainter magnitudes, respectively. Measurements of rotational velocities in MS stars of the LMC cluster NGC 1818 from high-resolution spectra collected with the Very Large Telescope (VLT) has recently provided direct evidence that the red-MS and the blue-MS stars exhibit different rotation rates (Marino et al., 2018a). Similarly, high-resolution Magellan spectra confirm that the bright and the faint MSTO of NGC 1866 are mostly populated by slow and fast rotators, respectively (Dupree et al., 2017).
Although it is now widely accepted that rotation is one of the main driver for the photometric features appearing on the CMDs of young and intermediate-age MC clusters, it might not be able to entirely reproduce the observations. Indeed, as noticed by Milone et al. (2017a), a fraction of eMSTO are consistent with being younger than the bulk of cluster stars. It has been suggested that some clusters have experienced a prolonged star formation, and that age variation, together with rotation is responsible for the eMSTOs (e.g. Goudfrooij et al., 2014, 2017). In this case, the MC clusters could represent the younger counterparts of the old globular clusters with multiple populations (e.g. Conroy & Spergel, 2011; Keller et al., 2011). As an alternative, D'Antona et al. (2017) suggested that the evolution of braked rapidly-rotating stars can mimic an age spread and contribute to the eMSTO.
The recent discovery of eMSTOs in four open clusters, namely NGC 2099, NGC 2360, NGC 2818, and NGC 6705 has challenged the text-book concept that the CMDs of open clusters are proxy of single isochrone and have demonstrated that the eMSTO is not a peculiarity of Magellanic Cloud clusters (Marino et al., 2018b). Spectroscopy of MS stars in NGC 6705 shows that the blue and the red MS are populated by slow and fast rotators, respectively (Marino et al., 2018b). Similarly,

the color and magnitude of eMSTO stars of NGC 2818 and NGC 6705 are connected with their rotational velocity (Bastian et al., 2018; Marino et al., 2018b). These results suggest that rotation plays an important role in shaping eMSTOs and broadened or split MSs in Galactic open clusters, resembling Magellanic Cloud clusters.
In this work we exploit the Gaia data release 2 (DR2 Gaia Collaboration et al., 2018a) to analyze photometry, parallaxes, and proper motions of a large sample of Galactic open clusters younger than ~2 Gyr to investigate the occurrence of the eMSTO in their CMDs. The paper is organized as follows. In Section 3.1.2 we describe the dataset and the data analysis. The CMDs and the investigation of the presence of eMSTO and broadened MSs are discussed in Section 3.1.3. Section 3.1.4 presents a comparison of the data with theoretical models; while Section 3.1.5 is a summary and brief discussion of our results.

3.1.2 Data and data analysis

To unambiguously identify multiple populations along the CMD, if present, we need densely-populated clusters with low differential reddening and negligible contamination from field stars. To do this, we selected all the Galactic open clusters of the new general (NGC), Index (IC), Melotte, and Collinder catalogs that, according to Dias et al. (2002), have E(B−V)<0.35 and host more than 400 cluster members. Moreover, we restrict our analysis to clusters older than 2.5 Gyr, as there is no evidence of eMSTO and split MS in Magellanic Cloud clusters with similar ages. Our sample also includes NGC 6705 (M 11, E(B−V)=0.43), which exceeds our reddening constraint, because previous evidence of eMSTOs and broadened MS has been reported for this cluster (Marino et al., 2018b).
We downloaded Gaia DR2 astrometry, photometry, parallaxes and proper motions of stars within a radial distance from the center of each cluster smaller than 2.5 times the cluster radius provided by Dias et al. (2002) and identified a sample of cluster members by using the following iterative procedure, which is illustrated in Fig. 3.1 for NGC 2099.

- We first analyze the vector-point diagram (VPD) of stellar proper motions, and find that NGC 2099 cluster members are clearly clustered around ($\mu_\alpha\, cos\delta$: μ_δ)~(1.9:−5.6). Hence we draw by eye a circle in the VPD that encloses most cluster members. The stars within the circle are selected to calculate the median values of $\mu_\alpha\, cos\delta$ and μ_δ ($<\mu_\alpha\, cos\delta>$ and $<\mu_\delta>$) and to derive the quantity $\mu_{\rm R} = \sqrt{(\mu_\alpha\, cos\delta - <\mu_\alpha\, cos\delta>)^2 + (\mu_\delta - <\mu_\delta>)^2}$).

- We plotted $G_{\rm RP}$ as a function of $\mu_{\rm R}$ for the selected stars and divided the analyzed magnitude interval with $10.0 < G_{\rm RP} < 17.5$ into bins of 0.5 mag each. For each bin we iterativelly calculated the median value of $\mu_{\rm R}$ ($\mu_{\rm R,med}$) and the corresponding rms (σ) by rejecting all the stars with $\mu_{\rm R} > \mu_{\rm R,med} + 4\cdot\sigma$. The mean magnitudes of each bin are associated to the quantities $\mu_{\rm R,med} + 4\cdot\sigma$ and these points are linearly interpolated to derive the orange

line plotted in the upper-left panel of Fig. 3.1. Stars with deviations from $\mu_{\rm R,med}$ larger than $4 \cdot \sigma$ are excluded from the sample of probable cluster members.

- We plotted $G_{\rm RP}$ as a function of the parallax, π, for the probable cluster members and calculated, for each bin of magnitude defined above, the median parallax $\pi_{\rm med}$ and the corresponding rms, σ, by using the same procedure described for proper motions. The orange lines plotted in the central-upper panel of Fig. 3.1 are derived by adding $\pm 4 \cdot \sigma$ to $\pi_{\rm med}$ and all the stars that lie outside these two lines are excluded from the sample of probable cluster members.

- The selected stars are used to derive improved estimates of $< \mu_\alpha \, cos\delta >$ and $< \mu_\delta >$. This ends one iteration. The procedure required three or four iterations to reach the convergence.

Photometry of cluster members has been corrected for differential reddening by using the method described by Milone et al. (2012a, see their Sec. 1) and illustrated in Fig. 3.2. Briefly, we first defined the reddening direction by using the absorption coefficients in the $G_{\rm BP}$ and $G_{\rm RP}$ bands provided by Casagrande & VandenBerg (2018). Then, we derived the fiducial of MS stars and calculated the color residuals from this fiducial. To estimate the differential reddening suffered by each star in the analyzed field of view, we selected a sample of 35 neighbours formed by bright MS cluster members that are not evident binaries. Our best differential-reddening estimate corresponds to the median of the color residuals, calculated along the reddening line. To derive the corresponding error, we subtracted the median from the residual of each star and calculated the $68.27^{\rm th}$ percentile of the distribution of the corresponding absolute values (σ). We considered the quantity $1.253 \cdot \sigma / \sqrt{35}$ as the uncertainty associated to the differential-reddening.

As an example, we compare in Fig. 3.2 the original CMD of NGC 2099 cluster members (upper-left panel) with the CMD corrected for differential reddening (upper-right panel). We also plot the differential-reddening map for a circular region with radius of 40 arcmin centered on NGC 2099 (bottom left). The bottom-right panel shows the reddening variation as a function of the relative right-ascension distance from the cluster center for stars in six declination intervals.

A visual inspection of the differential-reddening corrected CMDs reveals that at least twelve open clusters, namely IC 2714, Melotte 71, NGC 1245, NGC 1817, NGC 2099, NGC 2360, NGC 2818, NGC 3114, NGC 3532, NGC 5822, and NGC 6705, clearly exhibit multiple sequences in their CMDs. Their CMDs are presented and analyzed in the next section.

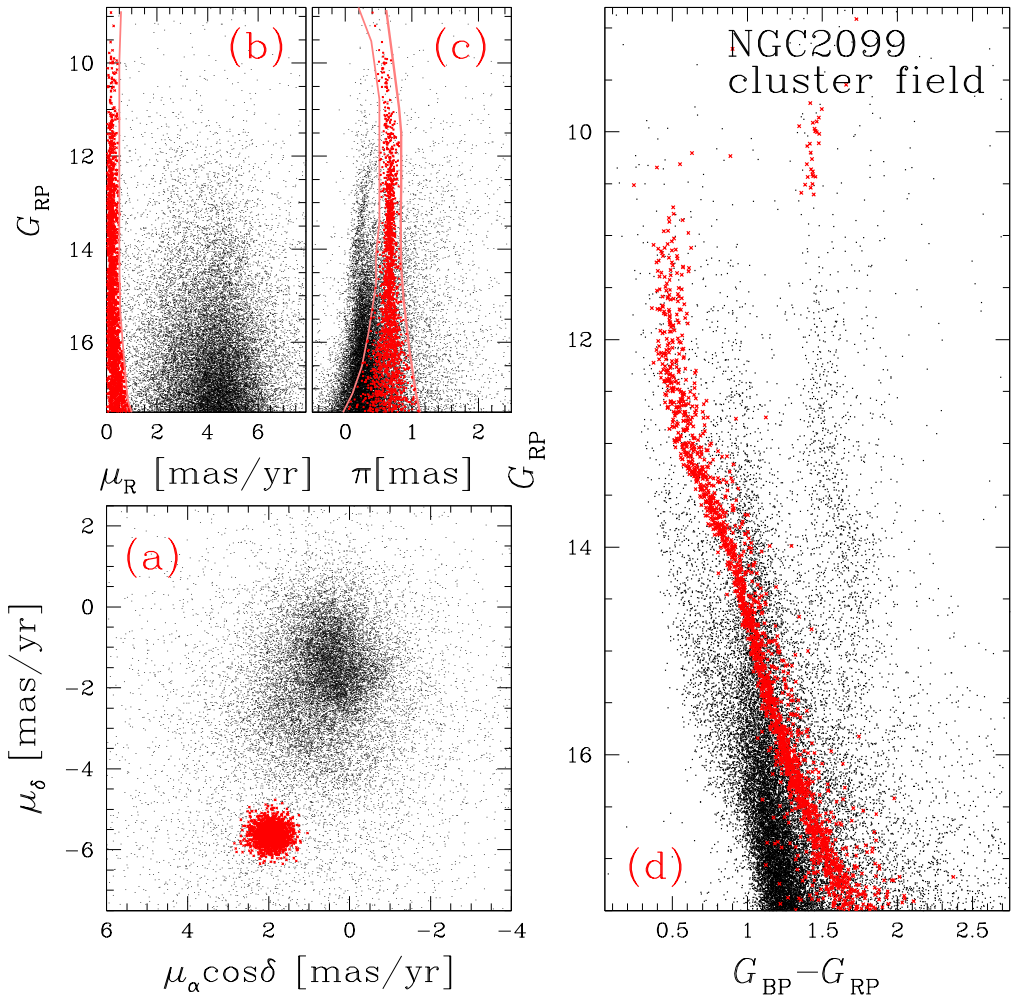

Figure 3.1. This figure illustrates the procedure that we used to select probable members of NGC 2099. The VPD of proper motions for stars in the cluster field is plotted in panel a, while panels b and c show G_{RP} against proper motions and parallaxes, respectively. The red lines are used to separate NGC 2099 members from field stars. The G_{RP} vs. $G_{BP} - G_{RP}$ CMD is illustrated in panel d. Selected cluster members are represented with red symbols. See text for details.

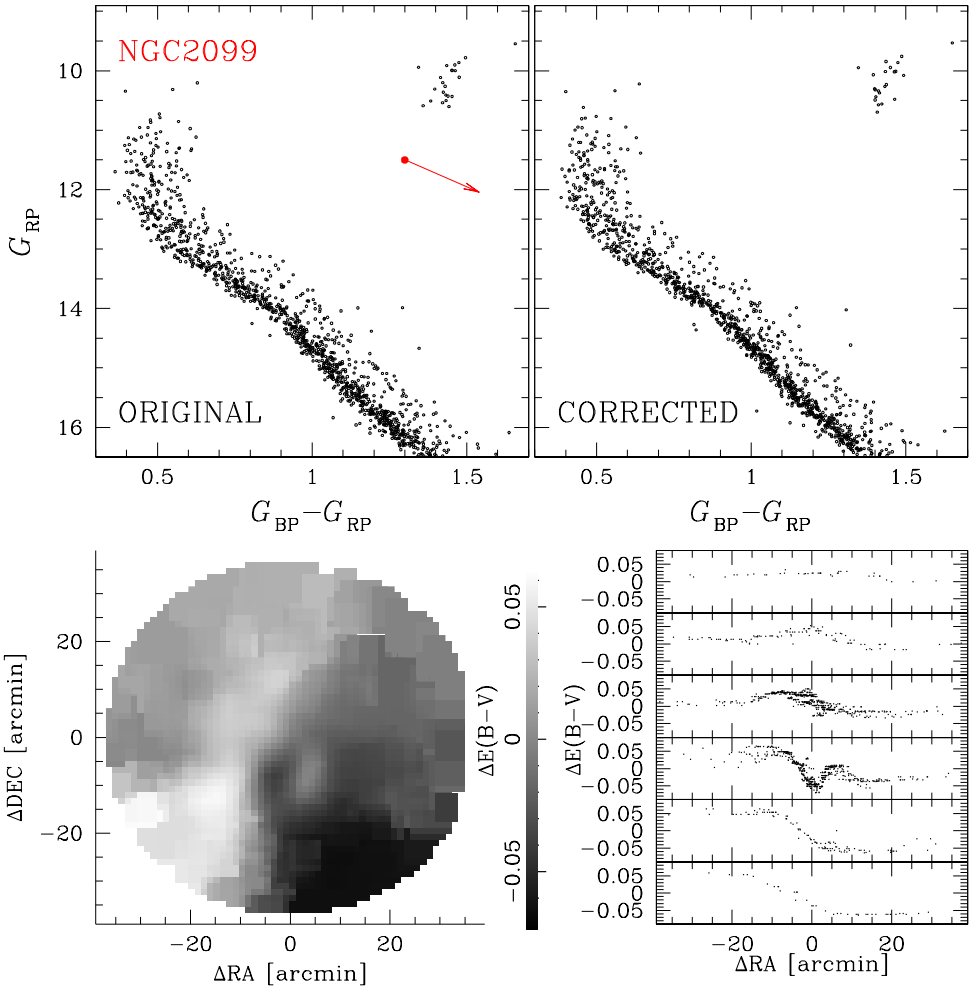

Figure 3.2. *Upper panels.* Comparison of the original CMD of selected cluster members of NGC 2099 (left) with the CMD of the same stars corrected for differential reddening (right). The arrow plotted in the left-panel CMD indicates the reddening vector and corresponds to ΔE(B−V)=0.3 mag. *Lower panels.* Map of differential reddening, centered on NGC 2099. The levels of gray correspond to different E(B−V) values as indicated by the scale on the middle (left). Right panels show E(B−V) as a function of the right-ascension distance from the cluster center for stars in six slices of declination.

3.1.3 Multiple populations along the color-magnitude diagrams

The final CMDs, corrected for differential reddening, of the selected cluster members are plotted in Figs. 3.3– 3.4, where we also represent with red error bars the typical observational uncertainties for stars with different luminosities. A visual inspection of these figures clearly reveals that IC 2714, Melotte 71, NGC 1245, NGC 1817, NGC 2099, NGC 2360, NGC 2818, NGC 3114, NGC 3532, NGC 5822, and NGC 6705 exhibit the eMSTO. Noticeably, the upper MS of NGC 2099, NGC 2287 (M 41), NGC 3114, NGC 3532, and NGC 6705 is broadened, in contrast with the faint MS, which is narrow and well defined. Similarly to what previously observed in MCs clusters, the broadened MS seems to disappear at the luminosity of the MS kink at $T_{\rm eff} \sim 7000$ K, which is a feature of the CMDs that indicates the onset on envelope convection due to the lowering of the adiabatic gradient in the region of partial hydrogen ionization (e.g. D'Antona et al., 2002).

The eMSTOs and the broadened bright MSs are highlighted in the insets of Figs. 3.3–3.4. In the following we demonstrate that they are intrinsic features of the cluster CMDs. To this aim, we investigate the impact of observational uncertainties, residual field-stars contamination and binaries on the appearance of eMSTOs and the broadened MSs on the CMDs.

Specifically, in Sect. 3.1.3 we describe the method used to statistically subtract field stars with cluster-like parallaxes and proper motions from the CMDs of candidate cluster members; in Sect. 3.1.3 we estimate the fraction of binaries in each cluster; and in Sect. 3.1.3 we compare the observations with simulated CMDs that account for both binaries and observational errors.

Field stars

The CMDs shown in Figs. 3.3– 3.4 are mostly populated by cluster members that have been selected on the basis of their parallaxes and proper motions as described in Sect. 3.1.2. To estimate the contamination from those field stars that have proper motions and distances similar to those of cluster members, we applied the procedure illustrated in Fig. 3.5 for NGC 2099.

All the stars plotted in Fig. 3.5 are located in the "reference field", which is a circular annulus with the same area as the cluster field, centered on the cluster and with internal radius corresponding to three times the cluster radius provided by Dias et al. (2002). The VPD of proper motions for stars in the reference field is plotted in Fig. 3.5a; panels b and c show the $G_{\rm RP}$ magnitude as a function of parallax and proper motions, respectively. We plot in each panel the orange lines derived in Fig. 3.1 that are now used to select field stars with cluster-like proper motions and parallaxes, in close analogy with what we did for candidate cluster members. The stars with cluster-like proper motions have been selected according to their position in the diagrams plotted in panels b and c and are represented with aqua crosses in all the panels of 3.5.

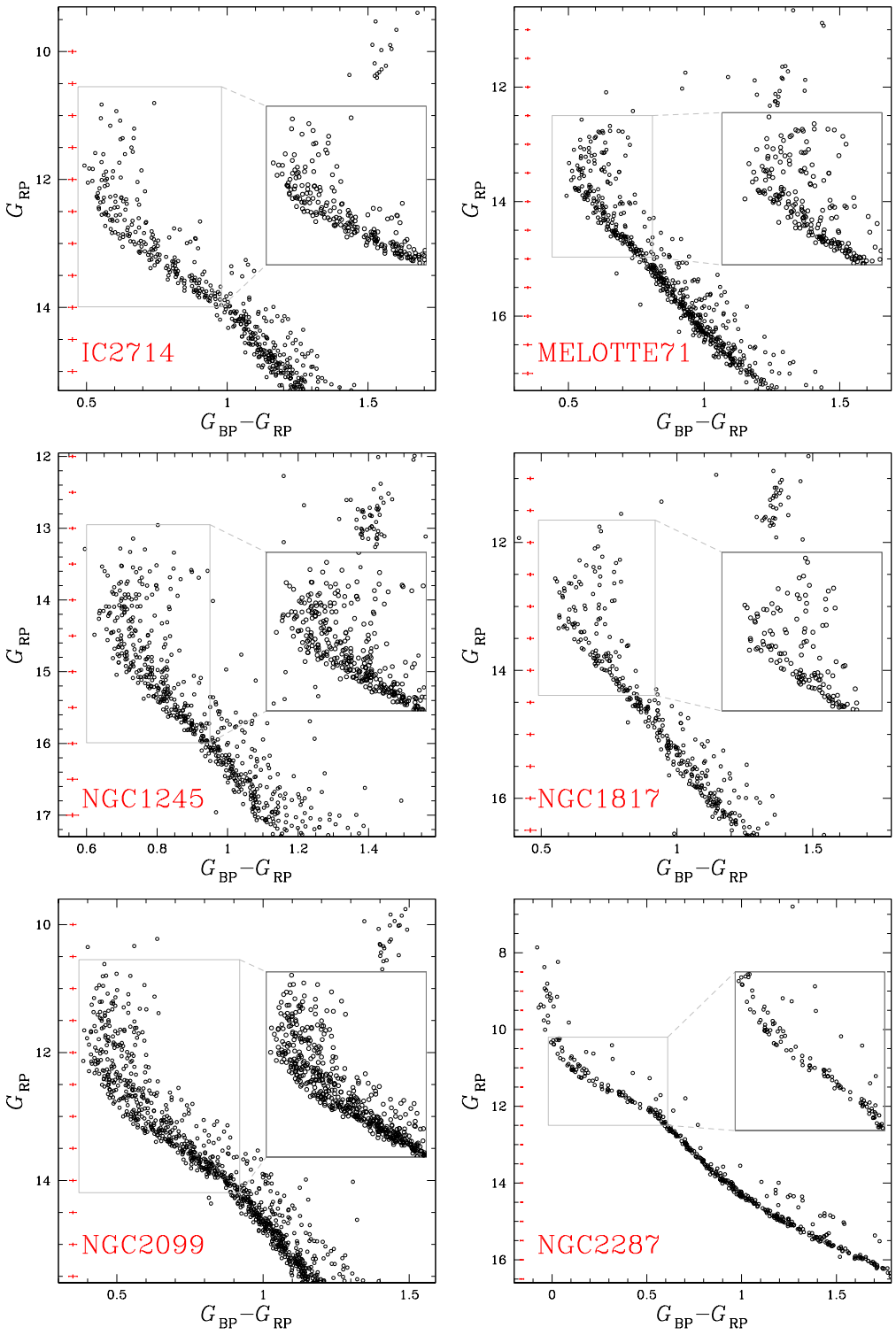

Figure 3.3. G_{RP} vs. $G_{BP} - G_{RP}$ CMDs, corrected for differential reddening, of cluster members for IC 2714, Melotte 71, NGC 1245, NGC 1817, NGC 2099, and NGC 2287. The insets highlight the eMSTO or the broadened MS. Red bars represent typical observational uncertainties.

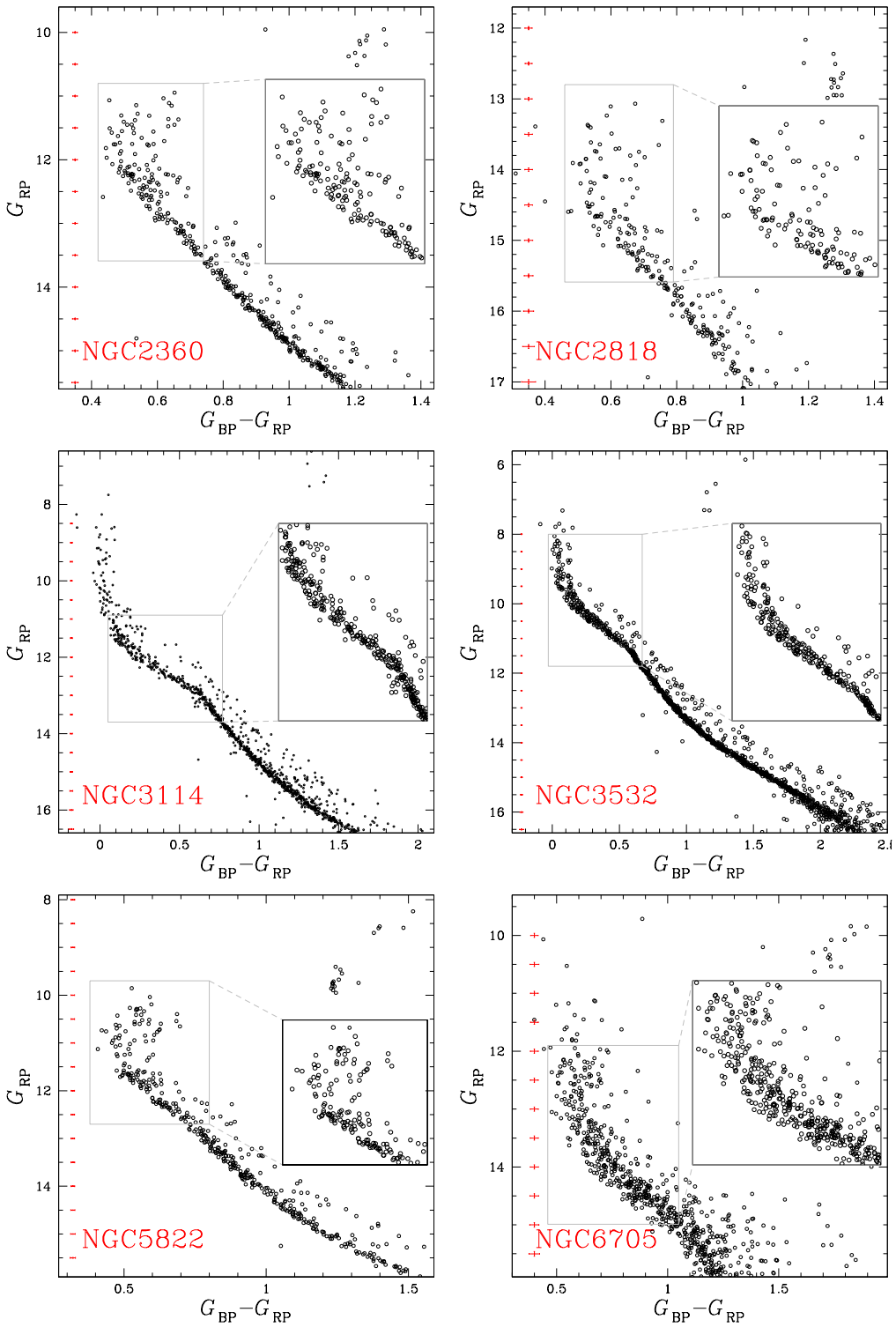

Figure 3.4. As in fig. 3.3 but for NGC 2360, NGC 2818, NGC 3114, NGC 3532, NGC 5822, and NGC 6705.

To statistically subtract the selected field stars from the cluster-field CMD we adopted the same procedure used in our previous papers (e.g. Milone et al., 2009). In a nutshell, we calculated for each selected star (i) in the reference field a distance in the CMD $d_i = \sqrt{k((G^i_{BP,rf} - G^i_{RP,rf}) - (G_{BP,cf} - G_{RP,cf}))^2 + (G^i_{RP,rf} - G_{RP,cf})^2}$ where $G_{BP,rf(cf)}$ and $G_{RP,rf(cf)}$ are the magnitudes of the selected stars in the reference (cluster) field, and $k = 7$ is a constant that accounts for the fact that the color of a star is better constrained than its magnitude (Gallart et al., 2003; Marino et al., 2014). We finally subtracted the stars in the cluster-field CMD with the smallest distance.

Binaries

Unresolved binaries formed by pairs of MS stars are redder and brighter than single MS stars with similar masses while binaries formed by a MSTO star and a MS or a MSTO star are brighter than the corresponding single MSTO stars. In the following, we measure the fraction of MS-MS binary systems of each cluster to estimate the contribution of binaries to the eMSTO and the broadened MS.
To estimate the fraction of unresolved binaries with q>0.7 we used the procedure illustrated in Fig. 3.6 for NGC 2099, which is based on the method by Milone et al. (2012a, 2016a) to characterize binaries in Galactic GCs. We first identified two points along the MS with magnitudes G^{bright}_{RP} and G^{faint}_{RP}, that delimit the MS region where the high-mass binaries are clearly separated from the remaining MS stars and there is no evidence for broadened or split sequences. We then defined two regions in the CMD, namely A and B, that correspond to the gray shaded areas in the CMDs of Fig. 3.6: region A includes all the single stars with $G^{bright}_{RP} < G_{RP} < G^{faint}_{RP}$ and all the binaries with a primary component in the same magnitude interval; region B is the sub-region of A that is populated by binaries with q>0.7 and is represented with dark-gray colors in Fig. 3.6. The reddest line plotted in Fig. 3.6 is the fiducial of equal-mass binaries shifted by four times the observational error in color to the red and the bluest line is the MS fiducial line shifted by four times the error in color to the blue. The fiducial of binaries with q=0.7 is represented by the blue continuous line and is derived by using the mass-luminosity relation inferred from the best-fit isochrone from Marigo et al. (2017). For each cluster, we assumed the metallicity provided by Paunzen et al. (2010), while the adopted values of ages, reddening and distance modulus are those providing the best match between the data and the isochrones and are listed in Table 3.1.
The fraction of binaries is calculated as

$$f^{q>0.7}_{bin} = \frac{N^B_{cl} - N^B_{fi}}{N^A_{cl} - N^A_{fi}} - \frac{N^B_{sim}}{N^A_{sim}} \tag{3.1}$$

where $N^{A,(B)}_{cl}$ is the number of cluster members in the region A (B) of the CMD, $N^{A,(B)}_{fi}$ and $N^{A,(B)}_{sim}$ are the corresponding numbers of field stars with cluster-like proper motions and parallaxes and the number of simulated stars, respectively.

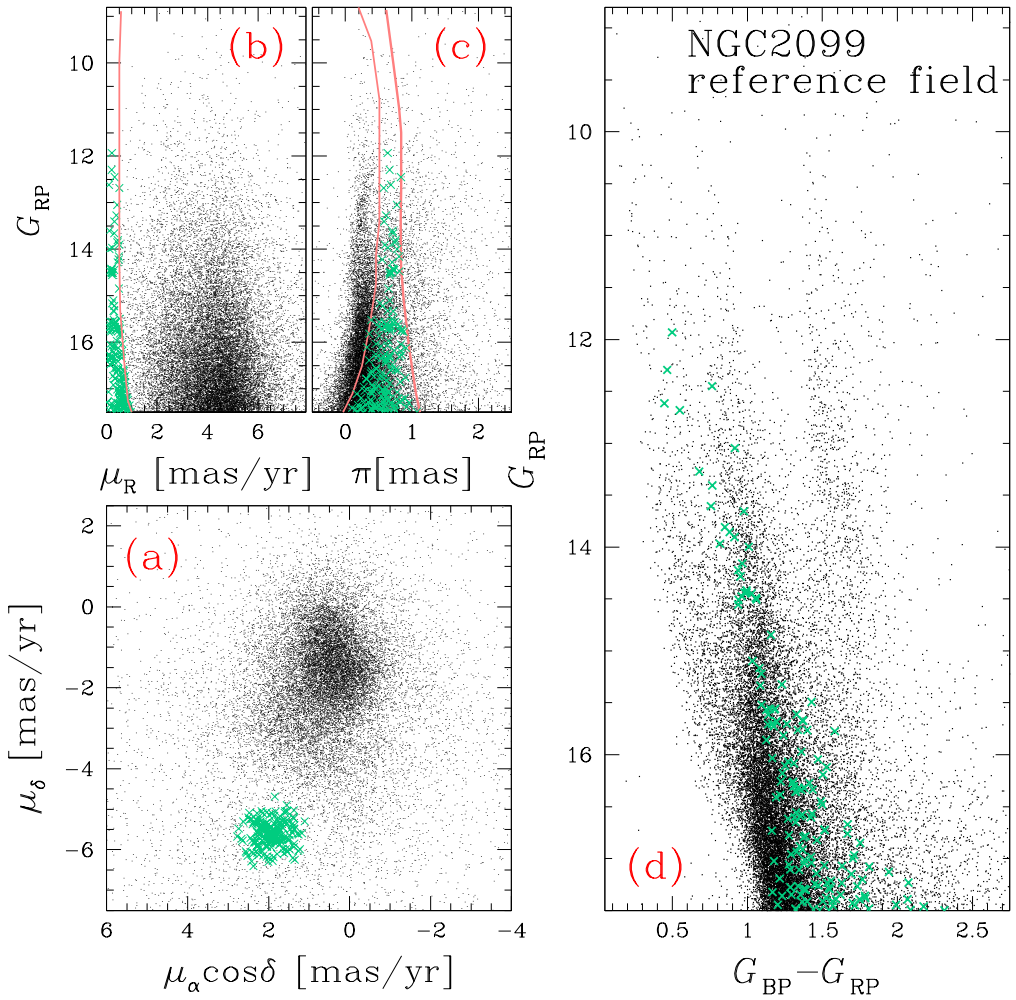

Figure 3.5. This figure illustrates the procedure that we used to identify field stars with similar proper motions and parallaxes as NGC 2099 cluster members. The VPD of proper motions of stars in the "reference field" is plotted in panel a, while panels b and c show G_{RP} as a function of stellar proper motions and parallaxes, respectively. The orange lines defined in Fig. 3.1 are overimposed to the diagrams of panels b and c. The G_{RP} vs. $G_{BP} - G_{RP}$ CMD is illustrated in panel d. Selected field stars are marked with aqua crosses. See text for details.

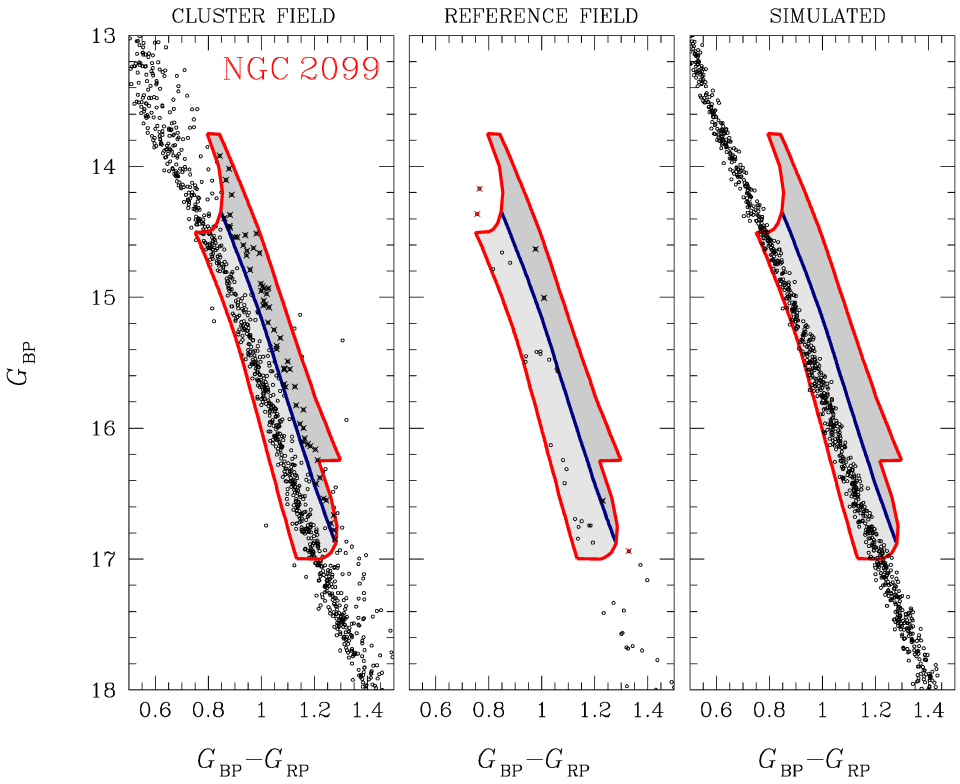

Figure 3.6. G_{BP} vs. $G_{BP} - G_{RP}$ CMD of selected NGC 2099 cluster members in the cluster field (left panel) and CMD of stars with cluster-like proper motions and parallaxes in the reference field (middle panel). Right panel shows the simulated CMD. The shaded areas indicate the region A of the CMD, which is populated single MS stars and by MS-MS binary pairs with a primary component in the mass interval between 1.06 and 1.63 solar masses. The blue lines represent the fiducial lines of binaries with mass ratio, $q = 0.7$. The region B of the CMD, which is populated by binaries with $q \geq 0.7$ (black crosses), is colored dark-gray. See text for details.

The measured fraction of binaries with q> 0.7, $f_{\rm bin}^{\rm q>0.7}$ is used to extrapolate the total fraction of binaries, $f_{\rm bin}^{\rm TOT}$. Specifically, by assuming a flat mass-ratio distribution, as observed among binaries with q> 0.5 of Galactic GCs (Milone et al., 2012a, 2016a), we infer $f_{\rm bin}^{\rm TOT} \sim 3.3 f_{\rm bin}^{\rm q>0.7}$. The total fraction binaries is typically around 0.30 and ranges from ~0.11 for NGC 2287 to ~0.51 for NGC 6705 and is similar to that observed in LMC clusters with similar ages (Milone et al., 2009, see theit Table 2). We thus confirm previous findings that open clusters typically host larger binary fraction than Galactic Globular Clusters (e.g. Sollima et al., 2010).

Simulated CMDs

The obtained total binary fractions, listed in Table 3.1, are used to simulate the CMD of a simple stellar population with the same observational errors, age, metallicity, distance modulus and reddening as inferred from the observations. To do

Cluster	$(m-M)_0$	E(B−V)	Z	Age [Myr]	FWHM [Myr]	$f_{\rm bin}^{\rm q>0.7}$	$f_{\rm bin}^{\rm tot}$
IC 2714	10.60	0.38	0.0205	540	134 ± 57	0.105	0.350
MELOTTE 71	11.60	0.22	0.0095	1220	165 ± 38	0.085	0.283
NGC 1245	12.45	0.29	0.0183	1000	139 ± 21	0.119	0.397
NGC 1817	11.00	0.26	0.0100	1030	165 ± 47	0.083	0.277
NGC 2099	10.90	0.26	0.0300	580	125 ± 21	0.085	0.283
NGC 2287	9.40	0.04	0.0219	280	76 ± 28	0.034	0.113
NGC 2360	10.23	0.16	0.0140	1020	210 ± 35	0.087	0.290
NGC 2818	12.35	0.22	0.0100	1110	160 ± 59	0.088	0.293
NGC 3114	10.05	0.12	0.0209	180	75 ± 31	0.068	0.227
NGC 3532	8.30	0.06	0.0160	430	140 ± 50	0.074	0.247
NGC 5822	9.40	0.11	0.0170	1130	270 ± 52	0.131	0.437
NGC 6705	11.10	0.46	0.0083	570	245 ± 71	0.153	0.510

Table 3.1. Distance modulus, reddening, age, FWHM of the age distribution, fraction of binaries with mass-ratio, q>0.7, and total fraction of binaries inferred in this paper. Cluster metallicities are from Paunzen et al. (2010).

this, we first associated to each star in the observed CMD of cluster member a synthetic star with the same magnitude and the color of the fiducial line. We selected a fraction of single stars equal to $f_{\rm bin}^{\rm TOT}$ and estimated the mass $\mathscr{M}$ of each of them by using the mass-luminosity relation by Marigo et al. (2017). We associated to each selected star a secondary star with a mass $\mathscr{M}_2 = q \cdot \mathscr{M}$ and derived its $G_{\rm RP}$ magnitude from the relations by Marigo and collaborators. The corresponding color has been inferred from the fiducial line. Finally, we summed up the $G_{\rm BP}$ and $G_{\rm RP}$ fluxes of the two components, derived the corresponding magnitudes replaced the original star in the CMD with this binary system, and summed up the observational errors to all the stars of the CMD.
Results are illustrated in Figs. 3.7– 3.9, where we compare for each cluster the CMD of selected cluster members (first column of panels), the CMD with cluster-like proper motions and parallaxes of stars in the reference field (second column), the decontaminated CMD (third column), and the simulated CMDs. A visual inspection of these figures clearly demonstrates that the eMSTOs and the broadened MSs are not due neither to unresolved binaries nor to residual field-star contamination.

3.1.4 Comparison with theory

The eMSTOs of Magellanic-Cloud clusters has been interpreted either as the signature of stellar populations with different ages (e.g. Mackey et al., 2008; Goudfrooij et al., 2011) or as the effect of stellar rotation on a single stellar population (e.g. Bastian & de Mink, 2009; Yang et al., 2013; D'Antona et al., 2016; Marino et al., 2018b). To disentangle between these two possibilities, in this section we com-

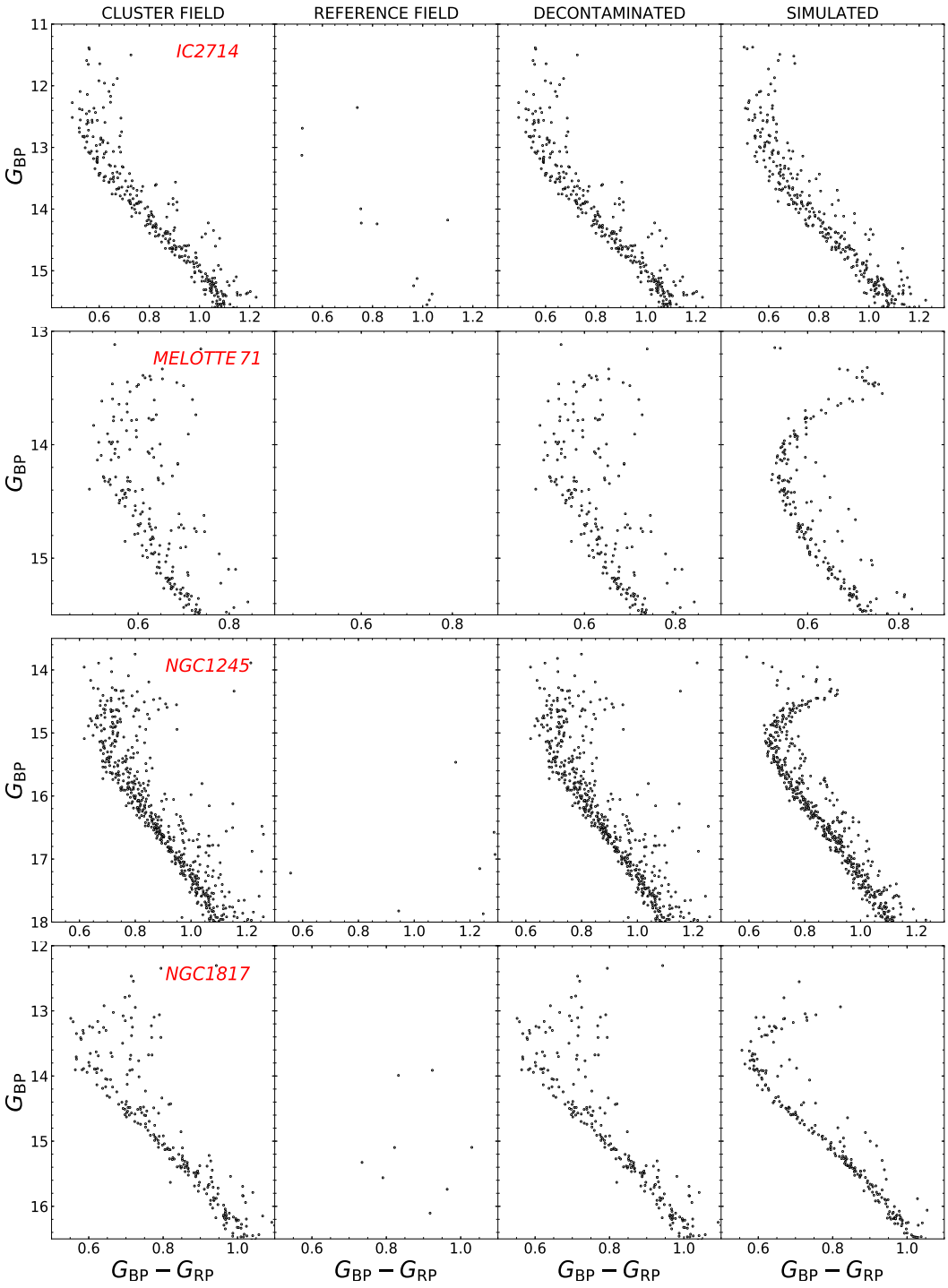

Figure 3.7. From the left to the right. CMD of the selected cluster members in the cluster field for IC 2714, Melotte 71, NGC 1245, and NGC 1817 (first column), CMD of reference-field stars with cluster-like parallaxes and proper motions (second column), CMD of cluster members after the statistical subtraction of field stars with cluster-like parallaxes and proper motions (third column). Simulated CMD (forth column).

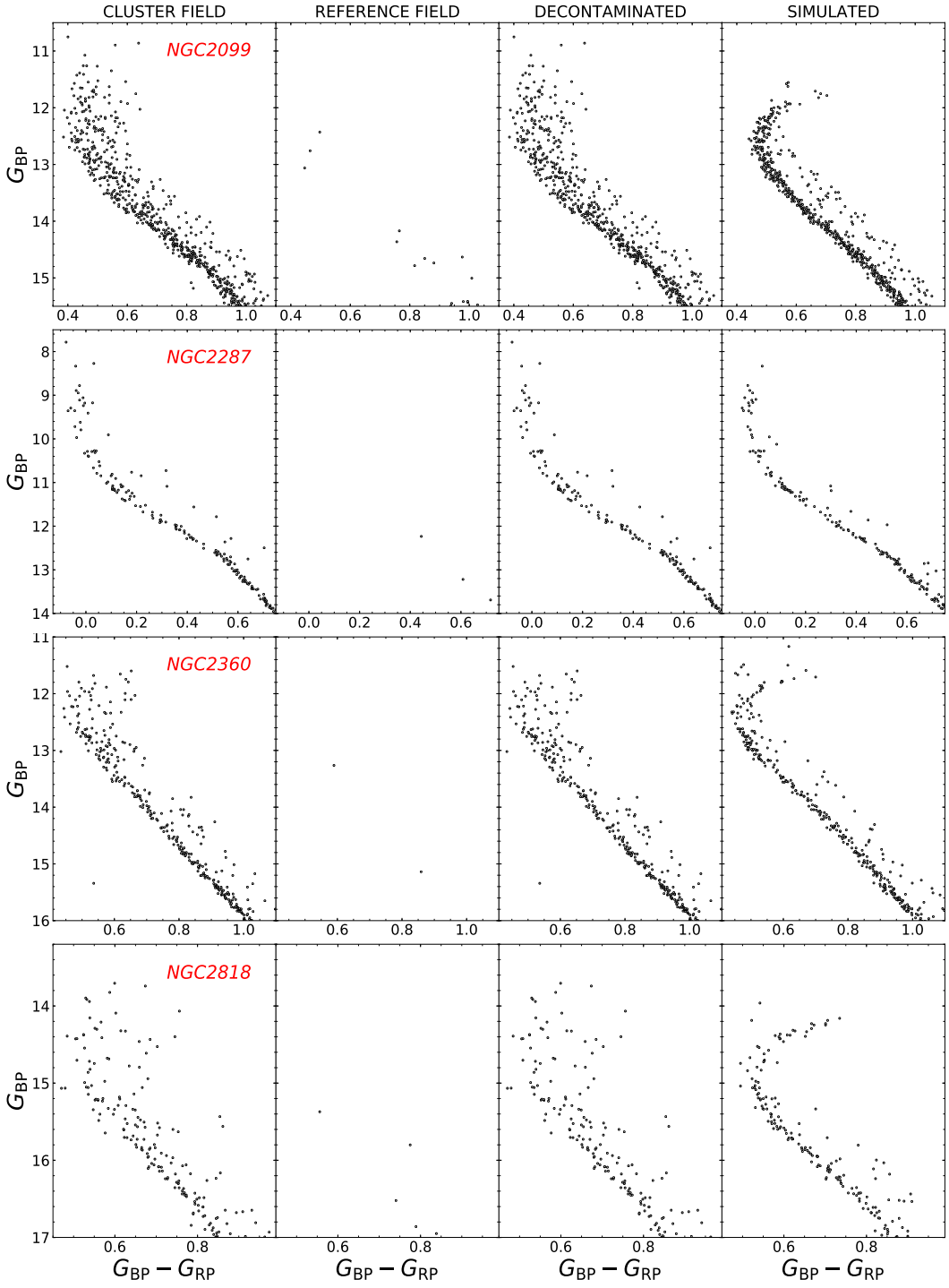

Figure 3.8. As in Fig. 3.7 but for NGC 2099, NGC 2287, NGC 2360 and NGC 2818.

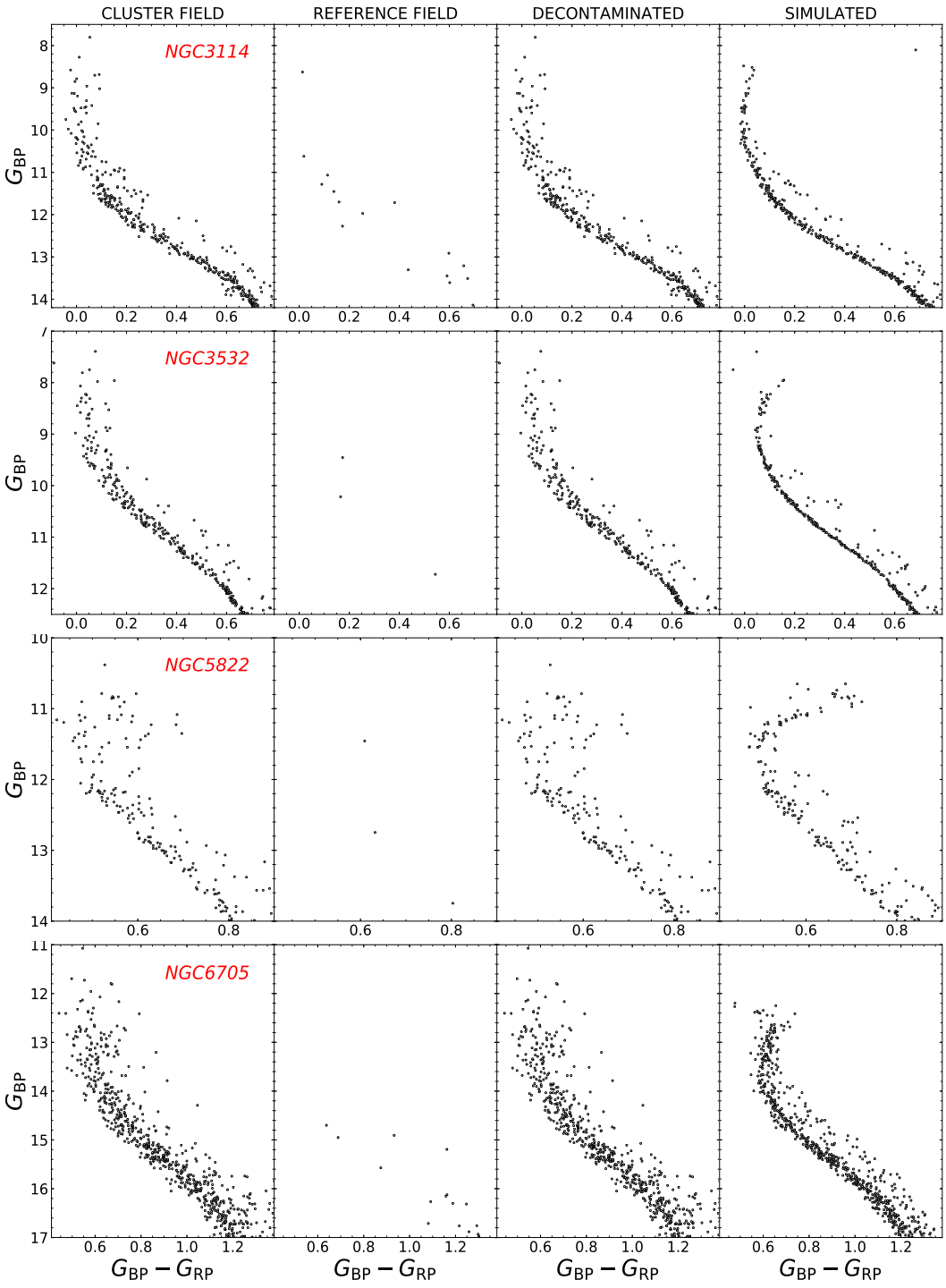

Figure 3.9. As in Fig. 3.7 but for NGC 3114, NGC 3532, NGC 5822 and NGC 6705.

pare the observed CMDs with isochrones of different ages and with simulated CMDs of stars with different rotation rates.

To estimate the age spread, in the hypothesis that the eMSTO is entirely due to a prolonged star formation, we compared the observed CMDs with isochrones by Marigo et al. (2017). The procedure exploited to derive accurate age distributions is illustrated in Fig. 3.10 for NGC 2099, and is similar to what we have used in previous work (e.g. Milone et al., 2015).

In a nutshell, we first derived by hand the parallelepiped plotted in Fig. 3.10 with the criterion of selecting the region around the turn off where the color and magnitude spread due to age variation are clearly distinguishable. Only stars within the parallelepiped are used to infer the age distribution. Then, we overimposed on the CMD a grid of isochrones with the same metallicity and $[\alpha/Fe]$ and ages between 380 and 700 Myr in steps of 10 Myr (grey lines in Fig. 3.10) and derived isochrones separated by 1 Myr by linearly interpolating among these isochrones. We associated to each star the age of the closest isochrone and derived the age distribution shown in the right panel of Fig. 3.10. Finally, we calculated the median age and the absolute value of the difference between the age of each star and the median. We considered the $68.27^{\rm th}$ percentile of the distribution of these absolute values as indicative of the observed age spread, $\sigma_{\rm AGE,obs}$. To estimate the contribution of observational errors on the inferred age spread, we applied the procedure described above to the simulated CMD of a simple population and derived the corresponding age spread, $\sigma_{\rm AGE,sim}$. The intrinsic age spread is estimated as $\sigma_{\rm AGE} = \sqrt{\sigma^2_{\rm AGE,obs} - \sigma^2_{\rm AGE,sim}}$. Uncertainties on $\sigma_{\rm AGE}$ are derived by bootstrapping with replacements performed 1,000 times on both the observed and the simulated age distributions.

Our results are summarized in Table 3.1 where we provide the full width half maximum of the age distribution, FWHM=$2.355 \cdot \sigma_{\rm AGE}$, for each cluster. We find that the FWHM ranges from ∼70 for NGC 3114 to ∼260 Myr for NGC 5822 and correlates with the cluster age as shown in Fig. 3.11, with old clusters having, on average, larger age spread than younger clusters. A similar trend between the age spread inferred from the eMSTO and the cluster age is also present among Magellanic Cloud clusters and is interpreted as the signature of stellar rotation. Indeed, since rotating stars have longer MS lifetime than non-rotating stars with the same age and mass, they would appear younger than coeval non-rotating stars within the same cluster. In this case, if the resulting eMSTO is interpreted as an age spread, the resulting age spread would correlate with the cluster age (Niederhofer et al., 2015; Bastian et al., 2018). On the other hand, in the case of a true age spread we would expect that the amount of age spread does not depend on cluster age, and therefore a correlation would be very unlikely.

To further investigate the effect of rotation on the observed CMDs, we extended the method by Niederhofer and collaborators to Galactic open clusters, and compared the observations with simulated CMDs of coeval stellar populations with different rotation rates based on stellar models from the Geneva database with Z=0.014 and various ages (Mowlavi et al., 2012; Ekström et al., 2012; Georgy et al.,

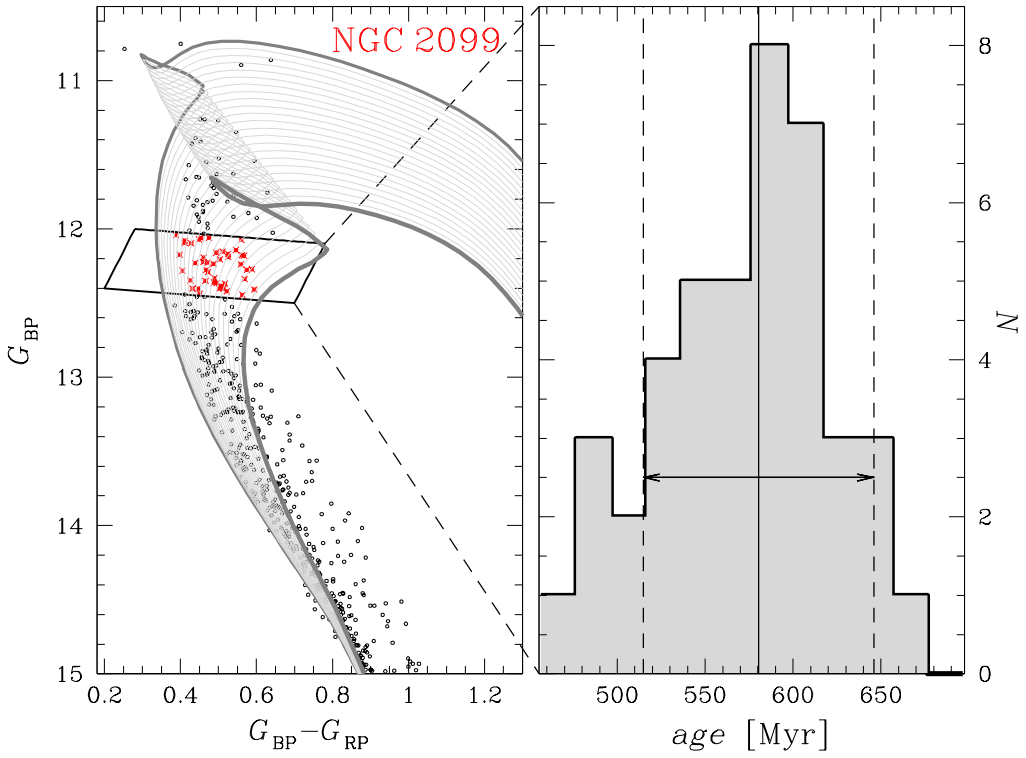

Figure 3.10. *Left Panel.* Grid of isochrones from Marigo et al. (2017) overimposed on the CMD of NGC 2099. The two isochrones represented with dark-tick lines have ages of 380 and 700 Myr, while the thin isochrones are spaced by 10 Myr in age. *Right panel.* Histogram age distribution of the eMSTO stars plotted with red crosses in the left-panel CMD. The median age of these stars is marked with a vertical continuous line, while the two dashed lines have distances of $\pm\sigma$ from the median value.

2014). To simulate the CMDs we first retrieved the synthetic photometry corresponding to the best-fit non-rotating isochrones, and for the isochrones with rotation equal to 0.9 times the breakout value ($\omega = 0.9\omega_{cr}$). These data account for the limb-darkening effect as in Claret (2000), adopt the gravity-darkening model by Espinosa Lara & Rieutord (2011) and assume random distribution for the viewing angle. We transformed the synthetic photometry into the observational plane by adopting the model atmospheres by Castelli & Kurucz (2003) and the transmission curves of the G_{BP} and G_{RP} filters of Gaia. We assumed that one third of stars in the simulated CMD do not rotate, while two thirds of stars have $\omega = 0.9\omega_{cr}$, in close analogy with what is observed in Magellanic Clouds open clusters (e.g. Milone et al., 2018b).

We first applied the procedure above to each synthetic CMD, by assuming that the eMSTO is due to age spread, and derived the FWHM of the age distribution. Results are represented with grey dots in Fig. 3.11. As expected, the age spread increases with the cluster age, in close analogy with what was previously found by

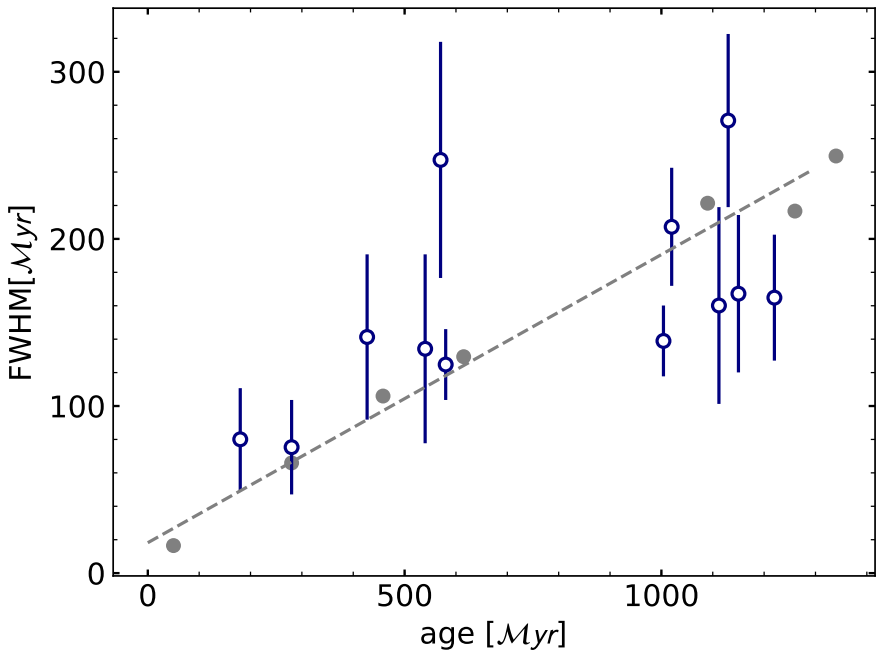

Figure 3.11. Full width half maximum of the age distribution as a function of cluster age. Blue dots with error bars refer to the analyzed clusters. Grey dots are derived from synthetic CMDs of coeval stellar population with different rotation rates. The dashed line is the least-squares best-fit straight line for the gray dots. See text for details.

Niederhofer et al. (2015) in Magellanic Clouds clusters. The fact that the FWHM values derived for synthetic CMDs and for Galactic open clusters follow similar trends against the cluster age suggests that rotation is the main responsible for the observed eMSTOs.

Finally, we compare in Fig. 3.12- 3.13 the CMDs of cluster members (left panels) with simulated CMDs (right panels). Synthetic CMDs are derived from the Geneva database (Georgy et al., 2014) and have metallicity, Z=0.014, and similar age, distance modulus and reddening as those listed in Table 1. Unfortunately, rotating models are not available for stars less massive than ~1.7 $\mathcal{M}_{\odot}$. e note that, while in young clusters like NGC 2287 and NGC 2099 both fast rotators and slow-rotator stars are needed to reproduce the broad MS, the eMSTO of old clusters seems consistent with fast rotators alone. The poor quality of the fit could be due to the modeling of several second-order parameters that characterize the end of the core hydrogen burning phase, including the parametrization of the inclination angle, which strongly affects the stellar luminosity and effective temperature (see D'Antona et al., 2015, for details). Nevertheless, the comparison between data and simulations corroborates the conclusion that stellar rotation is the main responsible for the observed eMSTOs and the broadened MSs.

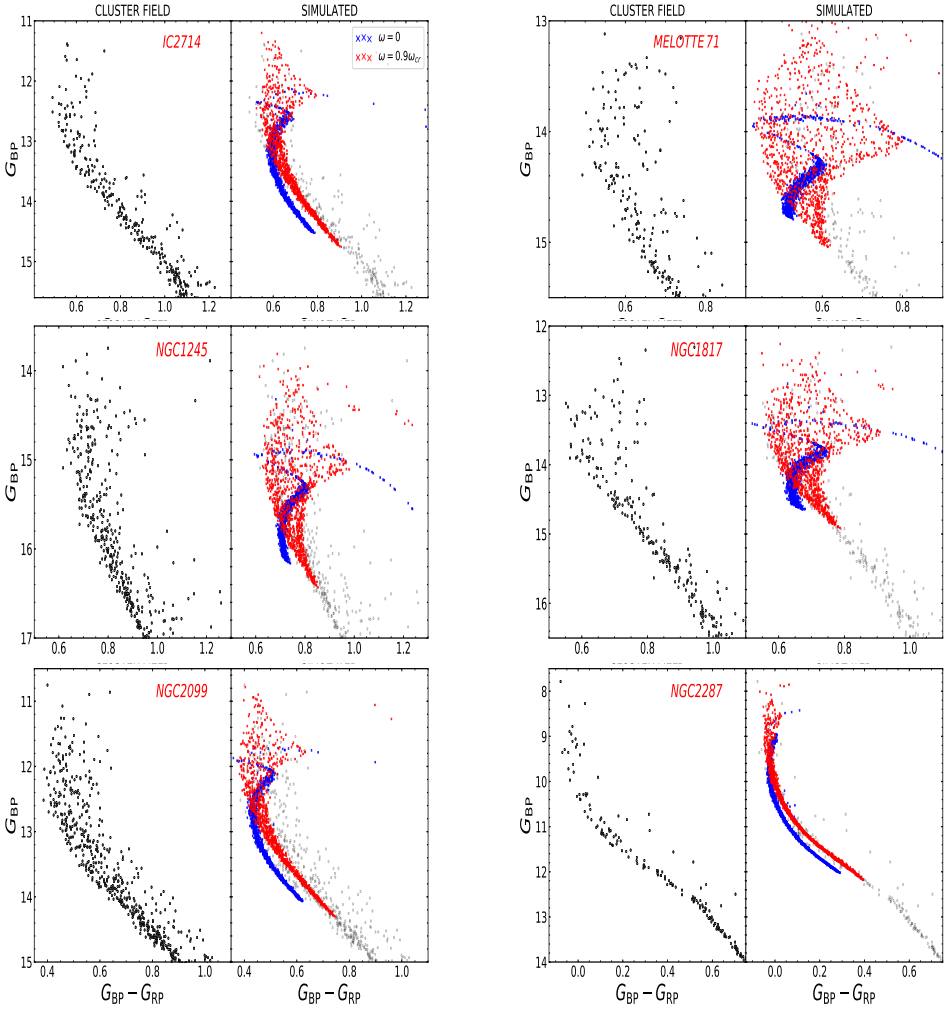

Figure 3.12. *Left panels.* reproduction of the observed CMDs of cluster members of IC 2714, Melotte 71, NGC 1245, NGC 1817, NGC 2099 and NGC 2287. *Right panels.* Comparison of the observed CMDs plotted in the left panels (grey dots) and simulated CMDs of a non rotating stellar population (blue) and of a stellar population with rotation $\omega = 0.9\omega_{\rm cr}$ (red).

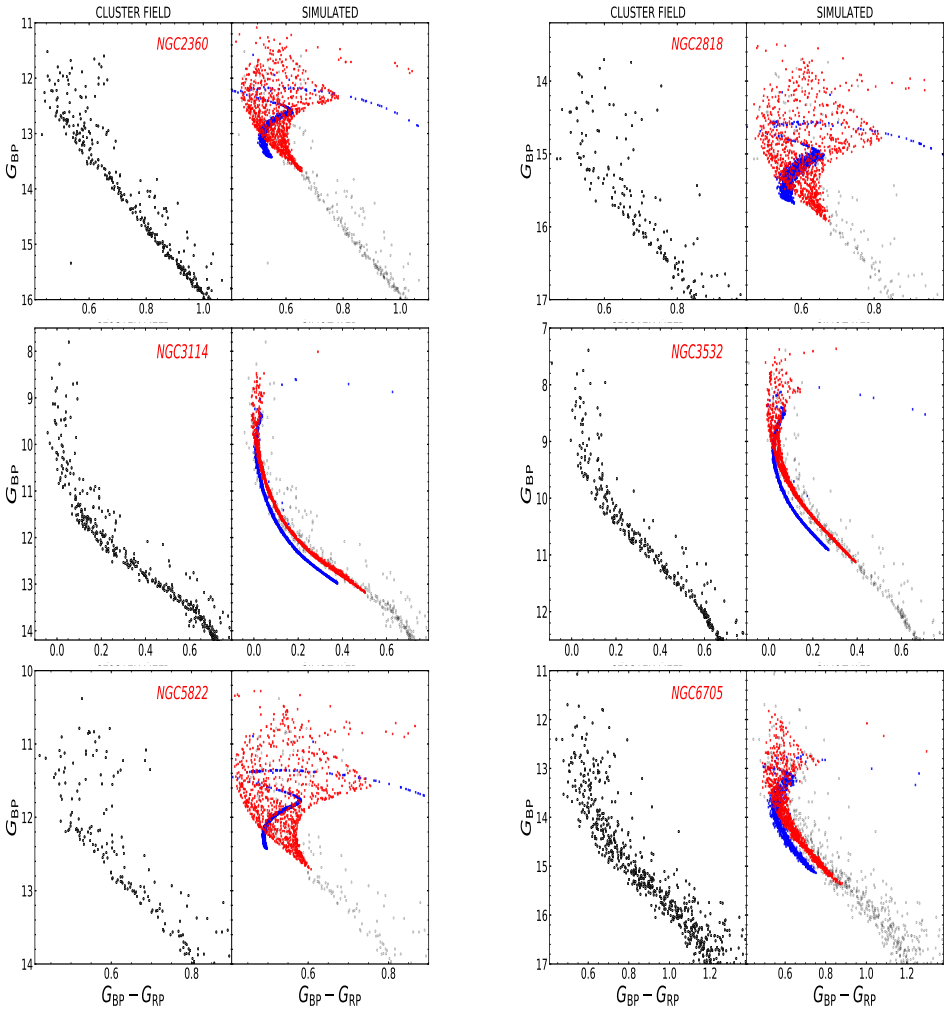

Figure 3.13. As in Fig 3.12 but for NGC 2360, NGC 2818, NGC 3114, NGC 3532, NGC 5822 and NGC 6705

3.1.5 Summary and discussion

We have presented the first analysis of twelve open clusters in the Milky Way in the context of multiple stellar populations. Our results suggest that the multiple photometric sequences observed by Gaia in the CMDs of these nearby objects belong to the same phenomenon present in Magellanic Clouds clusters, and interpreted as due to stellar rotation and/or age spreads.

Since the early discoveries, the eMSTOs have been considered a common feature of the CMDs of LMC and SMC clusters younger than ~2.5 Gyr whereas the CMDs of Galactic open clusters were thought to be similar to simple isochrones. This picture has been challenged by the recent findings of eMSTOs in four Galactic open clusters younger than ~1 Gyr, namely NGC 2099, NGC 2360, NGC 2818, NGC 6705 (Marino et al. 2018; Bastian et al. 2018).

We exploited the Gaia DR2 to analyze the CMDs of twelve Galactic open clusters

younger than ~1.5 Gyr. We carefully separated cluster stars from field stars by using proper motions and parallaxes from Gaia DR2 and corrected the photometry of clusters members for differential reddening. We find that all the analyzed clusters show the eMSTO. In addition, all the clusters younger than ~700 Myr exhibit a broadened upper MS, whereas the bottom of the MS is narrow and well defined. The appearance of certain photometric features depending on age, is similar to that observed in Magellanic Clouds clusters.

We statistically subtracted field stars with cluster-like proper motions and parallaxes from the CMD of candidate cluster stars thus demonstrating that eMSTOs and broadened MSs are not due to residual contamination from field stars. We calculated for each cluster the synthetic photometry of a simple population of stars with the same age, metallicity, binary fraction, and observational errors. The comparison between the observations and the simulated CMDs reveals that the eMSTOs and the broadened MSs are due neither to observational uncertainties nor to unresolved binaries. These facts demonstrate that eMSTOs and broadened MSs are intrinsic features of the CMDs of the analyzed open clusters.

To investigate the physical mechanisms that are responsible for the eMSTO we first compared the CMDs of cluster members with isochrones with different ages. The eMSTOs of the analyzed open clusters are consistent with stellar populations with different ages in close analogy with what has been observed in Magellanic Cloud clusters with similar ages. The FWHM of the age spread ranges from about 70 Myr in the ~150-Myr old cluster NGC 3114 to ~260 Myr in ~ 1.1-Gyr old NGC 5822. Interestingly, the derived age spread correlates with the cluster age, with old clusters having on average larger age spread than young clusters. A similar trend between the FWHM of the age distribution and the cluster age is present among Magellanic-Cloud clusters and is interpreted as an evidence that rotation is the main responsible of the eMSTO. Indeed, in a simple stellar population, fast rotators appear younger than coeval non-rotating stars with the same age.

We compared the CMDs of cluster members with synthetic diagrams derived from Geneva models and find that the eMSTOs and the broadened MSs are consistent with coeval stellar populations with different rotation rates. These findings suggest that rotation is the main responsible for the eMSTOs and the broadened MSs observed in Galactic clusters and corroborate direct spectroscopic evidence that stars with different rotation rates populate the eMSTOs of NGC 6705 and NGC 2818 (Marino et al., 2018b; Bastian et al., 2018) and that the blue and the red MS of NGC 6705 are populated by slow rotators and fast rotators, respectively (Marino et al., 2018b).

Our investigation of 12 Galactic open clusters demonstrates that the eMSTO and the broadened MS are not a peculiarity of Magellanic Cloud star clusters but are ubiquitous features of young Galactic open clusters. Coeval stellar populations with different rotation rates are likely the responsible for the eMSTO and the broadened MS of the analyzed clusters.

3.2 Multiple stellar populations in Magellanic Cloud clusters. Investigating the Turn-On of NGC 1818 to solve the age-spread dilemma.

Abstract

In the past two decades, our knowledge of young star clusters both Galactic and extra-Galactic has dramatically changed. Indeed, the discovery that nearly all star clusters younger than 2Gyr exhibit double/broad Main Sequences (MSs) and extended MS turn offs (eMSTOs) has been a major breakthrough in stellar astrophysics.
The eMSTOs have been first interpreted as the result of prolonged star formation but this conclusion has been challenged by the recent photometric and spectroscopic evidence that stellar rotation also contributes to the eMSTOs. In this work, we introduce a novel approach which exploits the MS Turn-On to disentangle between age spread and rotation. Based on new deep *Hubble Space Telescope* images, we study the ~ 40 Myr-old cluster NGC 1818 in the Large Magellanic Cloud, where the eMSTO is consistent either with an age spread of nearly 30 Myr or with coeval stellar populations with different rotation rates.
We find that the observed luminosity function and the main features of the color-magnitude diagram of NGC 1818 are reproduced by a ~35 Myr-old stellar population with an age spread of ~ 8Myr only. The small age variation inferred from the MS Turn On, which is not affected by stellar rotation, excludes, once and for all, that age spread is the main responsible for the eMSTO of NGC 1818.

3.2.1 Introduction

In the past decades, high-precision *Hubble Space Telescope* (*HST*) photometry revealed that the color-magnitude diagrams (CMDs) of star clusters younger than ~2 Gyr in the Large and Small Magellanic Cloud (LMC and SMC) are not consistent with simple isochrones, but exhibit either bimodal or extended main-sequence turnoffs (eMSTOs, e.g. Mackey & Broby Nielsen, 2007b; Glatt et al., 2008; Milone et al., 2009). More-recently, the same feature has been detected in the color-magnitude diagram of various Galactic open clusters (e.g. Marino et al., 2018a; Cordoni et al., 2018; Bastian et al., 2018).
The eMSTOs have been interpreted as the result of prolonged star formation, thus challenging the long-held notion that star clusters are prototypes of simple stellar populations. Intriguingly, the age spread needed to explain the color broadening of turn off stars is comparable with the age interval that is predicted by some scenarios to form the second stellar generations in ancient globular clusters (GCs). Hence, it has been suggested that Magellanic Cloud clusters with the eMSTO are the young counterparts of GCs with multiple populations and would provide the precious opportunity to investigate the multiple-population

phenomenon a few hundreds million years after the formation (e.g. Keller et al., 2011; Conroy & Spergel, 2011).
Stellar rotation has been proposed as an alternative to explain the eMSTO. Indeed, due to the impact of darkening and rotation-induced mixing on stellar colors and magnitudes, coeval MSTO stars with different rotation rates exhibit different effective temperatures and gravity, thus mimicking an age spread (e.g. Bastian & de Mink, 2009; D'Antona et al., 2015; Georgy et al., 2019). The presence of stars with different rotation rates in Magellanic Cloud clusters is now widely accepted by astronomers and is based on various observational evidences:
i) the discovery that clusters younger than ~ 800Myr exhibit split MSs, which can only be explained by two stellar populations of fast- and slow rotators (Milone et al., 2015, 2018a; Li & Zhao, 2017).
ii) the presence of Be stars among the eMSTOs of young clusters (Keller et al., 2000; Bastian et al., 2017; Marino et al., 2018b; Milone et al., 2018a);
iii) direct spectroscopic evidence that MS and MSTO stars span a wide range of rotation rates (Dupree et al., 2017; Marino et al., 2018b,a).
Nevertheless, it is not clear whether the eMSTOs are entirely due to rotation (D'Antona et al., 2017), or if age variation, in addition to rotation, is needed to reproduce the observations (e.g. Goudfrooij et al., 2017; Milone et al., 2017b).
To disentangle between age and rotation, we introduce a novel approach based on the Turn On point (TOn), which is the point in the CMD where the pre-MS joins the MS (Baume et al., 2003). Indeed, the age of a cluster is equal to the time spent in the pre-MS phase by its most-massive pre-MS stars, thus making the TOn an excellent, and unbiased, indicator of the age of the cluster (Cignoni et al., 2010, 2016). For the first time, we investigate the TOn of NGC 1818 to understand whether this ~ 40 Myr old Large Magellanic Cloud cluster has experienced an extended star-formation history or its eMSTO is entirely due to rotation.
The paper is structured as follows. In Section 3.2.2 we describe the dataset and the data reduction technique. In Section 3.2.3 and 3.2.5 we discuss the data analysis procedure and the results, respectively, while discussion and conclusion are carried out in Section 3.2.6.

3.2.2 Data and Data Reduction

To investigate stellar populations in NGC 1818 we exploit images collected through the F336W, F606W and F814W filters of the Ultraviolet and Visual channel of the Wide-Field Camera 3 (UVIS/WFC3) on board *HST*. The main information on the dataset is provided in Table 3.2.
Stellar photometry and astrometry of stars in a ~2.6-square arcmin field centered on NGC 1818 are derived by using the images corrected for the effects of poor charge transfer efficiency of UVIS/WFC3 (CTE, Anderson & van der Marel, 2010) and the computer program KS2 developed by Jay Anderson (see e.g. Sabbi et al., 2016, for details).
KS2 derives stellar photometry by using two distinct methods both based on the effective Point Spread Functions (Anderson et al., 2008). The first method, which

maximizes the photometric quality of bright stars, measures stars in each exposure, independently. The various flux determinations are then averaged together to get the best estimate of stellar magnitude in each filter. The second method combines the information from all images, by fitting all the pixels in all the exposures. It provides more-robust flux and position estimates of very faint stars. Stellar positions are corrected for geometrical distortion by adopting the solution by (Bellini & Bedin, 2009; Bellini et al., 2011) and photometry has been calibrated by adopting the most-updated zero points provided by the STScI webpage.
Field stars contamination has been accounted for by following the procedure of Milone et al. (2018a).
Finally, we determined the cluster field radius by eye, finding a value consistent with the one determined in Milone et al. (2018a): $R_{\rm cl} = 50$ arcsec.

Artificial stars

In order to determine photometric uncertainties and completeness we performed artificial stars tests as in Anderson et al. (2008). In a nutshell, we created a random simulation of 100,000 stars with the same spatial distribution as the observed stars, distributed along the fiducial line of the observations in the magnitude range $(-5, -14)$, in instrumental magnitudes.
Specifically, for each simulated artificial star, we added the star to each exposure with its flux and position and measured it by following the same method used for real stars. We then considered a star as detected if the input and the output position differ by less than 0.5 pixel and the fluxes by less than 0.75 mag. To infer the photometric uncertainties, which depend on the luminosity of the star, we took the dispersion of the distribution of the difference between the input and the output magnitude in different magnitude bins. The average photometric uncertainties are shown in the right of Figure 3.1
Finally, the completeness level has been determined as the fraction of detected stars over input artificial stars within a specific magnitude bin. Moreover, to account for the different crowding of different fields, we computed the completeness level of the cluster field independently from that of the reference field.
The completeness ranges from ∼100% at a magnitude $m_{\rm F814W} \leq 19$ to ∼20% at $m_{\rm F814W} = 26$. Specifically for a magnitude of $m_{\rm F814W} = 24$ the completeness is roughly 70%.
The observational uncertainties determined through artificial star tests have been used to convolve and compare theoretical simulations with our observations, while the completeness curve has been used to correct the observed LF and account for field contamination.

3.2.3 Color-Magnitude Diagrams of NGC 1818

The CMDs of stars in the cluster field are plotted in Figure 3.1. The $m_{\rm F814W}$ vs. $m_{\rm F606W} - m_{\rm F814W}$ CMD shown in the left panel has been used to estimate the fraction of binaries composed of two MS stars (MS-MS binaries) and to investigate

Table 3.2. Description of the WFC3/UVIS images used in this work.

FILTER	DATE	N×EXPTIME	PROGRAM	PI
F336W	October 29 2015	10s+100s+790s+3×947s	13727	Jason Kalirai
F606W	June 29 2020	724s+2×772s	15945	Giacomo Cordoni
F814W	February 2 2017	90s+666s	14710	Antonino P. Milone
F814W	June 29 2020	810s+2×795s	15945	Giacomo Cordoni

the MS TOn and the pre-MS. Each star of this CMD has been colored according to its completeness value as shown in the color bar. The divergent color map has been chosen with the purpose of highlighting the completeness level of 50%, which corresponds to $m_{\rm F814W} \sim 25.0$. We also represent the fiducial line adopted to generate ASs.
Clearly, the $m_{\rm F814W}$ vs. $m_{\rm F336W} - m_{\rm F814W}$ CMD plotted in the right panel of Figure 3.1 provides a better view of the eMSTO and the split MS than the left-panel CMD. Hence, it will be exploited to investigate the MSTO.

3.2.4 The binary fraction of NGC 1818

To estimate the fraction of MS-MS binaries we used the $m_{\rm F814W}$ vs. $m_{\rm F606W} - m_{\rm F814W}$ CMD and followed the procedure by (Milone et al., 2012a), which has been extended to young open clusters by Cordoni et al. (2018). The main steps are illustrated in Figure 3.2.
To show the distribution of MS-MS binaries in the CMD of NGC 1818 we simulated a simple stellar population composed of binaries alone as shown in the left panel of Figure 3.2.
To do this, we assumed that single stars are distributed along the fiducial line that we derived from the observed cluster-filed CMD. We associated to each point of the fiducial line a value of stellar mass by using the best-fit isochrone from the Padova database (Marigo et al., 2017) and generated pairs of binaries with flat mass-ratio (q) distribution[1]. The best-fit isochrone corresponds to age= 38 Myr, Z=0.006, reddening E(B−V)=0.10 mag and distance modulus, $(m-M)_0$=18.35 mag. Only binary systems with $q > 0.7$ composed of primary stars with $1.3 < \mathscr{M} < 1.9 \mathscr{M}_\odot$ can be clearly distinguished by single MS stars. To estimate their fraction, we defined two regions, A and B, in the CMD plotted in the middle panel of Figure 3.2.
Region A comprises all single stars with masses between 1.3 and 1.9 $\mathscr{M}_\odot$ and all binary systems where the primary component lies in the same mass interval. It is limited by the fiducial line (azure continuous line) blue-shifted by 3 times the color uncertainty, $\sigma_{\rm F606W-F814W}$, and by the fiducial lines of equal-mass binaries (azure dashed line) red-shifted by 3 times $\sigma_{\rm F606W-F814W}$. The bright and faint boundaries of region A are provided by the fiducials composed of binary systems

[1]We define q=$\mathscr{M}1/\mathscr{M}2$, where $\mathscr{M}1$ and $\mathscr{M}2$ are the masses of the two components of the binary system and $\mathscr{M}1 > \mathscr{M}2$

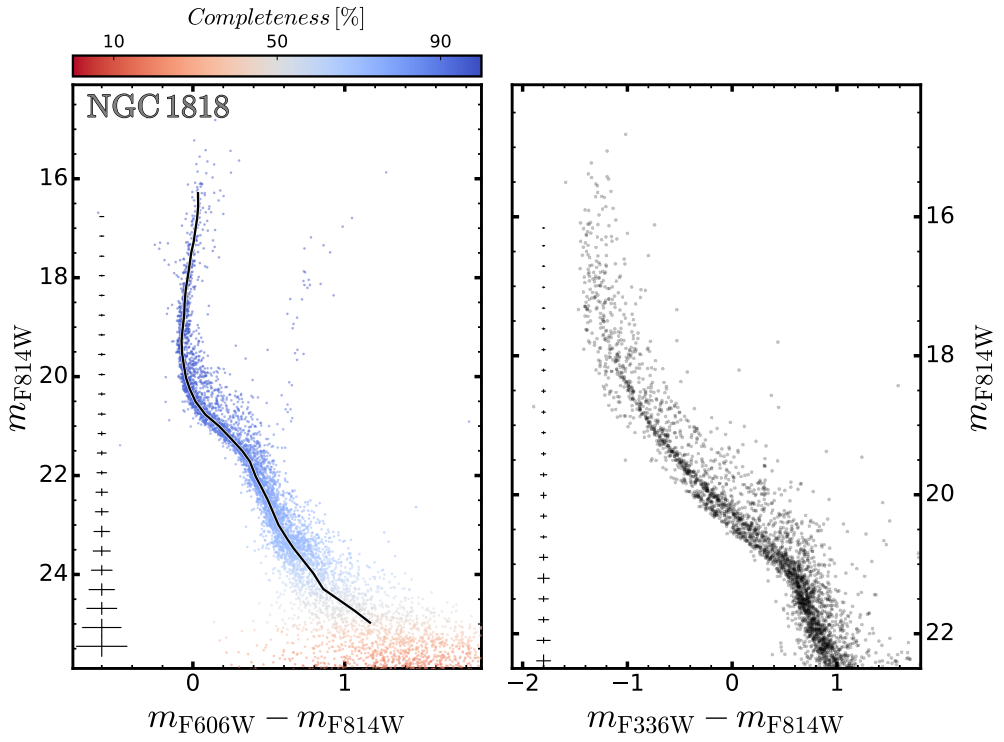

Figure 3.1. *Left panel.* $m_{\rm F814W}$ vs. $m_{\rm F606W} - m_{\rm F814W}$ CMD of stars in the cluster field of NGC 1818. Each star is color coded according to the completeness as shown in the top colorbar. The black solid line represents the fiducial line of MS stars. *Right panel.* $m_{\rm F814W}$ vs. $m_{\rm F336W} - m_{\rm F814W}$ CMD. The error bars plotted on the left of each CMD mark the typical color and magnitude uncertainties inferred from AS tests.

where q ranges from 0 to 1 and the primary star has mass of 1.9 and 1.3 $\mathscr{M}_{\odot}$, respectively. Region B is the portion of region A, redder than the fiducial lines of binaries with mass ratio q=0.7 (blue continuous line). Stars in region B are represented with blue crosses in Figure 3.2, while the remaining stars in region A are colored red. In addition to field stars, region A and B are also populated by field stars as shown in the CMD of reference-field stars (right panel of Figure 3.2). The fraction of binaries with $q > 0.7$ is estimated as

$$f_{\rm bin}^{\rm q>0.7} = \frac{N_{\rm cf}^{\rm B} - N_{\rm rf}^{\rm B}}{N_{\rm cf}^{\rm A} - N_{\rm rf}^{\rm A}} - \frac{N_{\rm AS}^{\rm B}}{N_{\rm AS}^{\rm A}} \tag{3.2}$$

where cf, rf, AS stand for cluster field, reference field and artificial stars, respectively. Artificial stars are used to estimate the fraction of single stars that, due to observational uncertainties, populate region B.
By assuming a flat mass-ratio distribution, as in5ferred for Galactic GCs and $q >$ 0.5 (Milone et al., 2012a, 2016b), we estimate the total fraction of binaries as $f_{\rm bin} \sim$

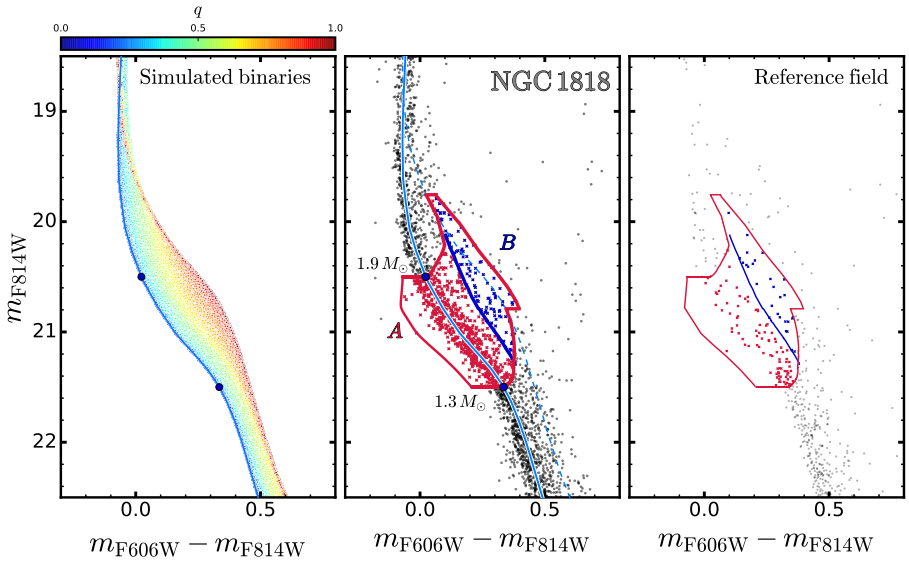

Figure 3.2. *Left panel)* Simulation of a population of 100,000 binaries, with each star color-coded according to its mass ratio, as shown in the top colorbar. *Middle panel)* Unresolved binaries selection process in the $m_{\rm F814W}$ vs. $m_{\rm F606W} - m_{\rm F814W}$ CMD. The azure solid and dashed line represents the MS fiducial line and the MS-MS equal mass binaries fiducial line, respectively. The leftmost solid red line corresponds to the MS fiducial line, shifted by $3\dot{\sigma}$, while the rightmost solid red line is the MS-MS equal mass binaries fiducial line shifted by $3 \cdot \sigma$. Finally, the blue solid line indicates the MS-MS $q = 0.7$ binaries fiducial line, used to select binary stars. The two black dots are the magnitude limits of the binary region, with their mass. *Right panel)* Same as panel a), but for the stars in the reference field. The final unresolved binary fraction has been computed as equation 3.2

$$3.3 \cdot f_{\rm bin}^{q>0.7} = 0.37 \pm 0.05$$

The Luminosity Function

The luminosity function (LF) shown in the right panel of Figure 3.3 has been derived from the left CMD of Figure 3.3. The $m_{\rm F814W}$ band has been chosen in order to maximize the number of well-measured stars fainter than the TOn, whilst having a completeness level larger than 50%.
Specifically, to compute the LF, we adopted a fixed bin width of 0.13 mag and we accounted for incompleteness by weighting each star by the completeness level corresponding to its magnitude. We applied the same procedure to both cluster-field and reference-field stars, and we finally subtracted the latter to the former. The result is represented with a solid black line in the right panel of Figure 3.3.
In order to infer the statistical uncertainties associated to each bin-count, we bootstrapped our sample 1000 times and we determined the dispersion of each

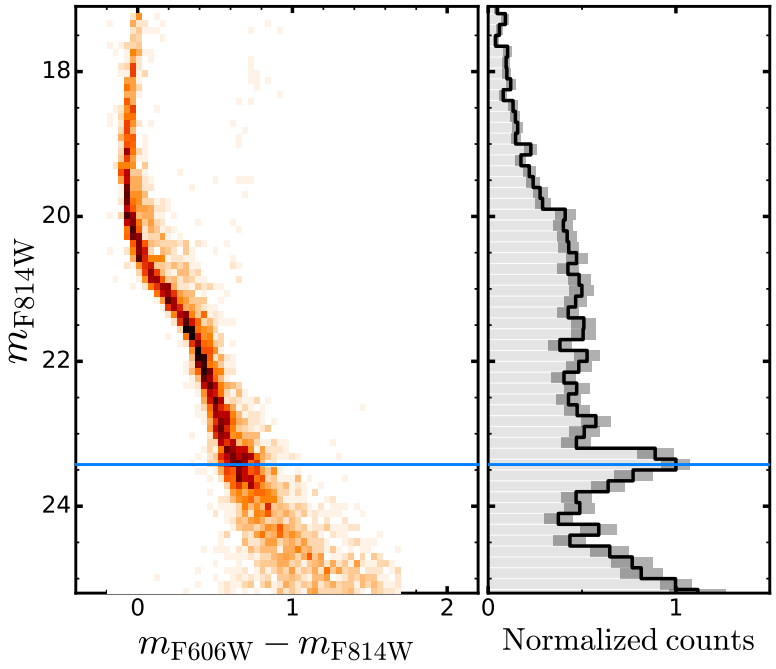

Figure 3.3. *Left panel.* 2-dimensional histogram of the observations, color coded according to the stellar density. *Right panel.* Field- and completeness-corrected observed LF. Dark grey shaded regions represent the observational uncertainties on each bin-count, computed bootstrapping the result as discussed in Section 3.2.4

bin-count distributions. In a nutshell, we re-sampled with replacements 1,000 times the observed CMD, and for each realizations we re-computed the LF. The dark-grey shades in the right panel corresponds to the dispersion of each bin-count distribution. Both the CMD and the LF have been cut at $m_{\rm F814W} = 25.5$ because of the low completeness level that characterize fainter magnitudes.

3.2.5 Age distribution of NGC 1818

In this Section, we investigate the TOff and TOn regions of NGC 1818, separately, to derive independent determinations of age and age distributions.

The Turn Off

In the following, we estimate the age distribution of stars in NGC 1818 by using the region of the CMD around the MS turn off. We exploit high-precision photometry in the F336W and F814W bands, which is the most suitable combination

(Milone et al., 2018a), and assume that the eMSTO is due to internal age variation alone.
The left panel of Figure 3.4 compares the CMD of NGC 1818 with a grid of Padova isochrones (Marigo et al., 2017) that match the color extension of the MSTO. We adopted values of $(m-M)_0 = 18.30$ mag and $E(B-V) = 0.08$ mag for the distance modulus and reddening, respectively, and assumed metallicity Z=0.006. As indicated by the top colorbar, an age span of nearly 100 Myr is required to cover the entirety of the MSTO.

To quantify the age distribution of TOff stars, we used the procedure by (Cordoni et al., 2018, see their Section 4). Briefly, selected all TOff stars brighter than $m_{\rm F814W} = 17.5$ and we interpolated over a set of isochrones, ranging from a minimum age of 10 Myr to a maximum of 110 Myr, with a step of 2 Myr. The result of the interpolation is shown in the top-right panel of Figure 3.4, where each TOff star is color-coded according to the inferred age.
The histogram distribution of stellar ages is represented in the bottom-right panel. It exhibits a prominent peak corresponding to an age of $\sim 35-40$ Myr, and a tail of stars up to ~ 100 Myr. Hints of secondary peaks around ~ 50 Myr and ~ 80 Myr are also present. The median age corresponds to 53 Myr (solid black line) and the age spread is 35 Myr.

The Turn-On

The Turn-On represents the point, along the zero age main-sequence (ZAMS) where pre Main-Sequence (pMS) stars join the MS, and therefore it translates into an over-density of stars detectable in the LF. As discussed in Section 3.2.1, the TOn involves stars with different masses with respect to the TOff region, specifically below $\sim 1\,M_\odot$, and therefore represents an independent clock to determine the age of the cluster. Furthermore, as shown in Figure 3.5, the magnitude of the TOn changes with cluster age, moving to fainter magnitudes for older ages, so that the presence of multiple population would result in the appearance of multiple or broad TOn peaks in the cluster luminosity function.
Specifically, in Figure 3.5 we show the isochrones and LFs of four different stellar populations, from 10 Myr to 80 Myr. The right panels show how the luminosity of the TOn changes of nearly 4 magnitudes in the considered age range, thus being clearly detectable considering the observational uncertainties of the present data-set (shown in Figure 3.1 of Section 3.2.4). Moreover, MIST stellar models (Dotter, 2016), available for two different stellar rotation rates (namely $\omega = 0.0, 0.4\omega_{\rm crit}$, show that stellar rotation does not affect the position of stars in the CMD below the MS knee, i.e. $m_{\rm F814} \sim 21.5$, and therefore the position of the TOn is not sensitive to stellar rotation.

Hence, if the analyzed cluster, i.e. NGC 1818, is composed of a simple stellar population (SSP), its LF would show a single peak corresponding to the TOn magni-

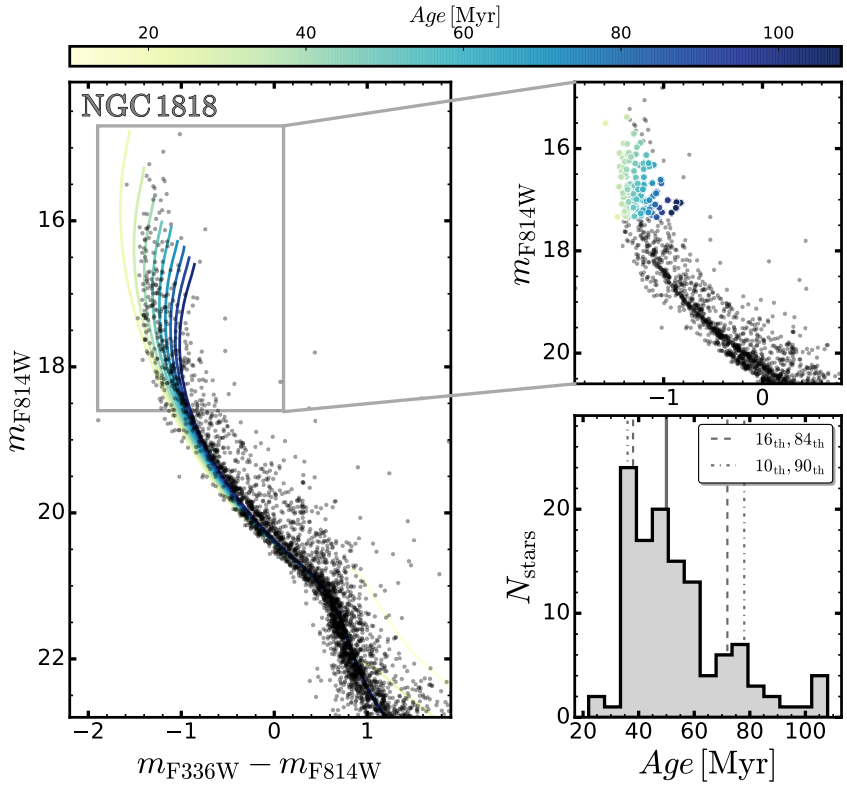

Figure 3.4. *Panel a).* Color-Magnitude Diagram of NGC 1818. The superimposed Padova isochrones range from 10 to 110 Myr, as indicated by the top colorbar. *Panel b)* Zoom of the Turn-Off region, where each Turn-Off stars is color coded according to the inferred age. *Panel c)* Age distribution of Turn-Off stars. The vertical solid line indicates the median age, corresponding to 53 Myr, while dashed line indicate the $10_{\rm th}$ and $90_{\rm th}$ percentile of the distribution.

tude, while, if two or more stellar generations are present, the same number of peaks would appear in the LF.
This approach represents a new and unbiased perspective to shed light on the multiple populations phenomenon in Magellanic Clouds clusters.

To infer the age of NGC 1818 we exploited a similar approach to that described in Cignoni et al. (2016), which is based on the comparison between the observed luminosity function and synthetic CMDs generated from theoretical isochrones.[2] We then performed a χ^2 analysis, allowing for the presence of N different stellar populations with age in the range 10-100 Myr. Specifically, the number N of stellar populations is determined from the adopted time duration of each star formation episode, and from the age range of the simulations. For instance, in the case of a duration of $\Delta t = 2.5$ Myr, the number of simulated stellar popula-

[2] We note that, while they compared both the CMD and the LF, we only exploited the LF in the $m_{\rm F814W}$ band.

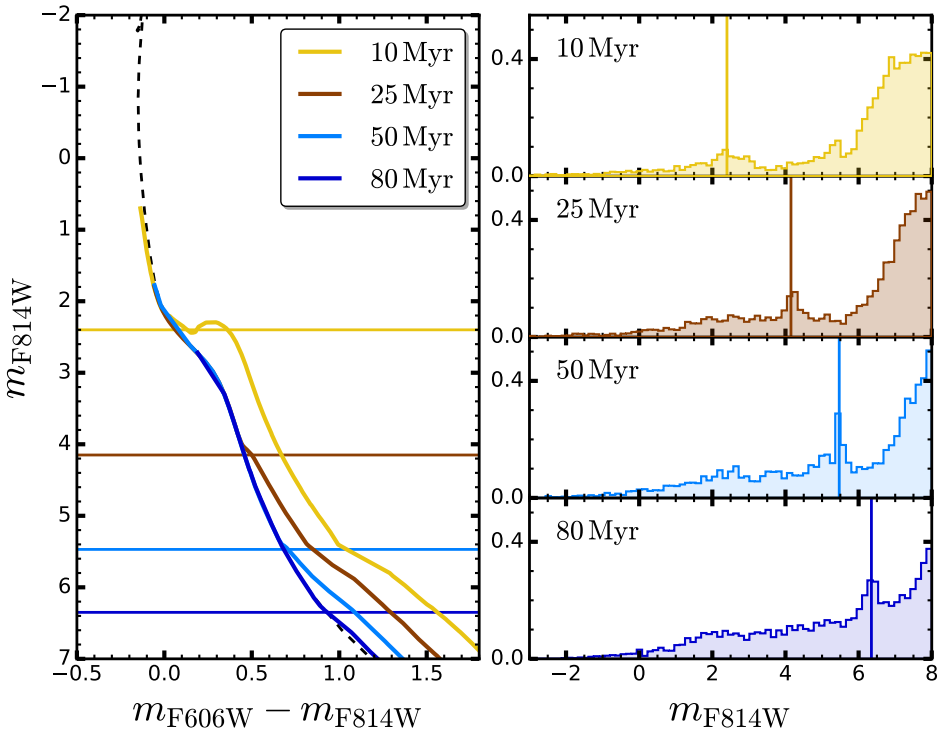

Figure 3.5. Theoretical Padova isochrones for different ages (left panel), from 10 to 80 Myr, as indicated in the top-right legend. The horizontal/vertical lines mark the magnitude of the TOn of each stellar population, visible as a peak in the Luminosity Functions shown in the right panels.

tions is $N = (100-10)/\Delta t = 36$.

We first created a set of synthetic CMDs from the Padova isochrones, adopting a Kroupa (2001) initial mass function (IMF), and a continuos star formation history of $\Delta t = 2.5$ Myr, so that each simulation contains stars with ages within $t_{\rm in}$ and $t_{\rm in} + \Delta t$. We generated a total of $N = 36$ synthetic stellar populations. We then artificially added a population of binary stars corresponding to the observed fraction, determined in Section 3.2.4, and we degraded each simulations according to the observational uncertainties determined from AS tests. Finally, we computed the LF of each simulation and found the combination that best reproduced the observed LF. The best fit has been determined by minimizing the Poissonian χ^2 (Cash, 1979) in Eq. 3.3

$$\chi^2 = \sum_i n_i \ln \frac{n_i}{m_i} - n_i + m_i \tag{3.3}$$

where n_i, m_i are the the bin values of the observed and simulated LFs, while the index i runs over the magnitudes bin. Since we are mainly interested in TOn stars, we selected a magnitude range which includes the TOns of the youngest

and oldest generated stellar populations, excluding those stars for which the completeness fraction goes below 50%, as well as saturated stars ($m_{\rm F814W} < 18$). Specifically, we minimized the χ^2 in a magnitude range between $m_{\rm F814W} = 20.0$ and $m_{\rm F814W} = 25.0$.
To search the parameters space, we used the genetic algorithm from the `geneticalgorithm` Python public library[3], which prevents us from finding local minimum. The output corresponds to an array of $N = 36$ coefficients C_j, between 0 and 1, that indicate the fraction of stars belonging to a given simulated stellar population. Uncertainties are inferred by bootstrapping the results 1,000 times. Briefly, we sampled the observed CMD with replacements 1,000 times, and for each sample we re-performed the fitting of the derived LF, thus obtaining a distribution of 1,000 output coefficients C_j. Figure 3.6 shows the results with the blue LF in the top panel representing the best-fit model, while the shaded area indicates the uncertainties derived with the bootstrap procedure. The bottom panel shows the inferred age distribution of NGC 1818.
A visual inspection of the bottom panel of Figure 3.6 reveals an age distribution clearly peaked at 37.5-40.0 Myr, with a dispersion of nearly 7.5 Myr. Finally, we repeated the same analysis in the case of $\Delta\, t = 0, 5$ Myr[4], finding consistent results.
Such values allows us to correctly estimate the position of the TOn and, thus, the age of the cluster. Finally, the computed stellar counts in each magnitude beans have been corrected accounting for the completeness and field subtracted.

3.2.6 Summary and conclusions

Thirteen years after the early discoveries (Mackey & Broby Nielsen, 2007b), it is widely accepted that the eMSTO is a distinctive feature of star clusters younger than ~ 2 Gyr (Milone et al., 2009, 2018a; Goudfrooij et al., 2017; Cordoni et al., 2018). Despite the strong efforts to explain the eMSTO a comprehensive solution for this phenomenon is still missing.
Some authors suggested that the eMSTO is composed of stars with different ages thus indicating a prolonged star formation (e.g. Mackey et al., 2008; Keller et al., 2011). This scenario has been challenged by the idea that the eMSTO is composed of coeval stars with different rotation rates (e.g. Bastian & de Mink, 2009; D'Antona et al., 2015).
Although stellar populations with different rotation rates have been detected from direct spectroscopic measurements of stellar rotation (e.g. Dupree et al., 2017; Marino et al., 2018a,b), it is still unclear whether rotation can entirely explain the eMSTO (D'Antona et al., 2017) or if some age spread is required to reproduce the color and magnitude broadening of MSTO stars (e.g. Milone et al., 2017b; Goudfrooij et al., 2017).

[3] https://pypi.org/project/geneticalgorithm/
[4] in the case of $\delta\, t = 0$ we simulated stellar populations evenly spaced by 5 Myr

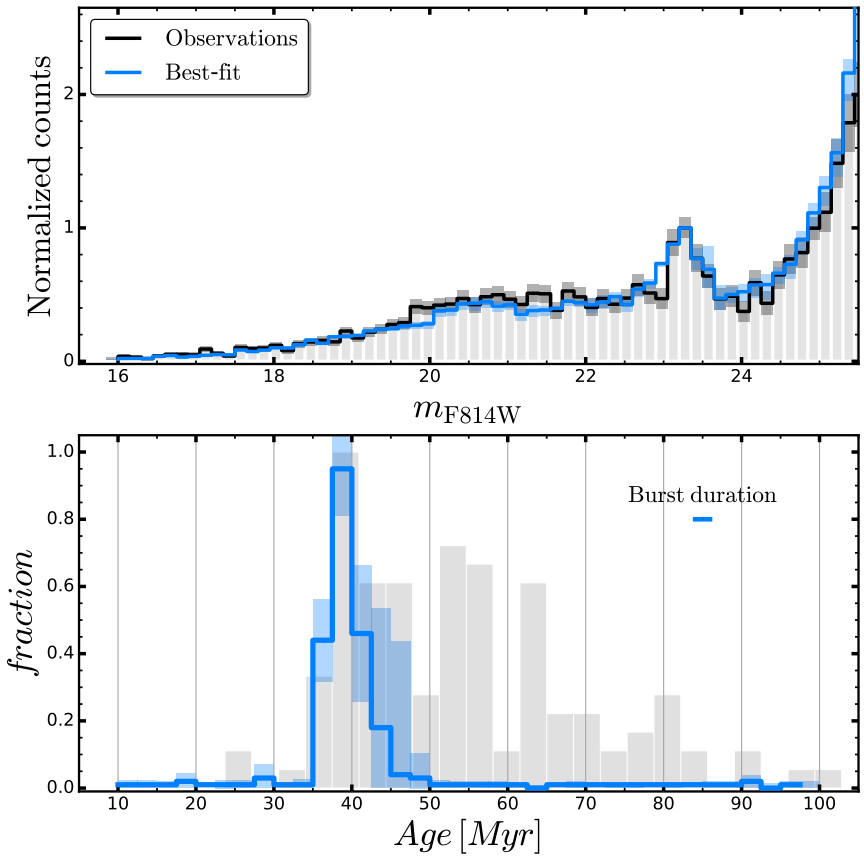

Figure 3.6. *Top panel.* Comparison between the observed LF (black and gray histogram) and the best-fit LF (azure histogram). Only the region between 20.5 and 25 has been considered in the minimization of the χ^2 defined in Eq. 3.3. *Bottom panel.* Age distribution inferred from the Turn-On region (azure histogram), together with the one derived considering Turn-Off stars (shaded grey histogram, discussed in Section 3.2.5). The shaded azure and dark-grey regions are the uncertainties determined by bootstrapping the data.

To shed light on the eMSTO puzzle, we introduced a novel approach and infer cluster age and age spread from the Main Sequence Turn-On. Indeed, the luminosity of the TOn depends on the age of the cluster, moving to fainter magnitudes for increasing cluster ages (e.g. Cignoni et al., 2010, 2016, and Figure 3.5). This is the first time that this formidable chronometer is used in the context of multiple stellar populations.

Based on archive data and new *HST* exposures (GO-15495, P.I. Cordoni), we analyze the TOn and the eMSTO of the ~ 40 Myr-old cluster NGC 1818, in the Large Magellanic Cloud. Previous work on NGC 1818 suggested that its eMSTO is composed of stars with negligible age spread and different rotation rates (D'Antona et al., 2017).

Here we assumed that the eMSTO is entirely due to age spread and derived the

age distribution of NGC 1818 based on the comparison of the CMD of eMSTO stars and Padova isochrones. We find that eMSTO of NGC 1818 is consistent with an age spread of 35 Myr and maximum age variations up to ~100 Myrs.
Then we derived the LF of MS and pre-MS stars and identified, for the first time, the MS turn on of NGC 1818. We compared the observed LFs with a grid of LFs of simulated multiple stellar populations with different ages. The results are consistent with an age dispersion of 8 Myrs. Hence, the MS turn on allowed us to disentangle among age and rotation, thus ruling out the hypothesis that age spread is responsible for the eMSTO of NGC 1818.

CHAPTER

4 Galactic Archaeology through extremely-metal poor stars

4.1 Exploring the Galaxy's halo and very metal-weak thick disk with SkyMapper and Gaia DR2

This Section is taken from Cordoni et al. (2021).

Abstract

In this work we combine spectroscopic information from the *SkyMapper survey for Extremely Metal-Poor stars* and astrometry from Gaia DR2 to investigate the kinematics of a sample of 475 stars with a metallicity range of $-6.5 \leq$ [Fe/H] ≤ -2.05 dex. Exploiting the action map, we identify 16 and 40 stars dynamically consistent with the *Gaia Sausage* and *Gaia Sequoia* accretion events, respectively. The most metal-poor of these candidates have metallicities of [Fe/H] = −3.31 and [Fe/H] = −3.74, respectively, helping to define the low-metallicity tail of the progenitors involved in the accretion events. We also find, consistent with other studies, that ~21% of the sample have orbits that remain confined to within 3 kpc of the Galactic plane, i.e., $|Z_{max}| \leq 3$ kpc. Of particular interest is a sub-sample (~11% of the total) of low $|Z_{max}|$ stars with low eccentricities and prograde motions. The lowest metallicity of these stars has [Fe/H] = –4.30 and the sub-sample is best interpreted as the very low-metallicity tail of the metal-weak thick disk population. The low $|Z_{max}|$, low eccentricity stars with retrograde orbits are likely accreted, while the low $|Z_{max}|$, high eccentricity pro- and retrograde stars are plausibly associated with the *Gaia Sausage* system. We find that a small fraction of our sample (~4% of the total) is likely escaping from the Galaxy, and postulate that these stars have gained energy from gravitational interactions that occur when infalling dwarf galaxies are tidally disrupted.

4.1.1 Introduction

I refer to Section 1.2 for a detailed introduction of the present Section.

In this Chapter I conduct a similar study to those mentioned in Section 1.2 by exploiting the metallicity determinations from the *SkyMapper Survey for extremely metal-poor stars* (see Da Costa et al., 2019), together with Gaia DR2 astrometry (Gaia Collaboration et al., 2018b), to investigate the dynamics of 475 very metal-poor ([Fe/H] < –2) stars in the southern sky. The wide extension in metallicity space, together with the relatively large number of stars, gives us a detailed view of the kinematic properties of these objects. We also consider the potential connection of any of the stars in our sample with the MW accretion events, such as those designated *Gaia Enceladus, Gaia Sausage* and *Gaia Sequoia* that have been recently discovered in large scale analyses of Gaia DR2 data (e.g. Helmi et al., 2018; Belokurov et al., 2018; Myeong et al., 2019; Mackereth et al., 2019). Such a connection has also been pursued in Monty et al. (2020).

This Chapter is organized as follows: in Sections 4.1.2 and 4.1.3 we present the data set and the orbit determination procedure, respectively, while in § 4.1.4 and § 4.1.5 we present and discuss our results. Specifically, in § 4.1.5 we discuss the small number of stars in our sample that appear not to be bound to the Galaxy. The final section (§ 4.1.6) summarizes our findings.

4.1.2 Data

The data set used in this work consists of 475 stars with metallicities ranging from [Fe/H] = −2.08 to [Fe/H] < −6.5 dex. It is composed as follows:

- 114 giant stars with $-6.2 \leq [\mathrm{Fe/H}]_{\mathrm{1D,LTE}} \leq -2.25$ dex. Of these stars 113 come from Yong et al. (in preparation), while the remaining star is the most-iron poor star for which iron has been detected: SMSS J160540.18–144323.1 with $[\mathrm{Fe/H}]_{\mathrm{1D,LTE}} = -6.2 \pm 0.2$ (Nordlander et al., 2019). These stars originate with the extremely metal-poor (EMP) candidates discussed in Da Costa et al. (2019) and all have been observed at high resolution, principally with the MIKE spectrograph (Bernstein et al., 2003) at the 6.5m Magellan (Clay) telescope. We shall refer to these stars as the `HiRes` data set.
- 45 stars observed with the `FEROS` high-resolution spectrograph (Kaufer et al., 1999) at the MPG/ESO 2.2-metre telescope at La Silla. Again, these stars originated from the Da Costa et al. (2019) sample. We removed from the analysis all the stars with [Fe/H] > −2, and the stars in common with `HiRes` data set. The final count of stars belonging to this sub-sample is 38 and we label it as the `FEROS` data set.
- 122 stars from Jacobson et al. (2015) which have $-3.97 \leq [\mathrm{Fe/H}] \leq -1.31$ dex. These stars originated in the SkyMapper commissioning-era survey

(see Da Costa et al., 2019), and were also observed at high-dispersion with the MIKE spectrograph at Magellan. As for the FEROS sample, we removed 7 stars with $[Fe/H]_{1D,LTE} > -2$ and the single star in common with the HiRes data set. However, as discussed in §4.1.3, there appears to be an issue with the radial velocities for the stars observed by Jacobson et al. (2015) during one specific Magellan/MIKE run, namely 2013 May 28 – June 01. As a result, we have removed the stars observed in that run that lack a radial velocity from Gaia DR2 and which had not been already discarded. The final sub-sample used here is then composed of 91 stars and we refer to it as the Jacobson+15 sub-sample.

- 17 stars from Marino et al. (2019a) with metallicity $-3.26 < [Fe/H]_{1D,LTE} < -1.71$ dex. The spectra of these stars were obtained with the Keck HIRES high-resolution spectrograph (Vogt et al., 1994). After the removal of 2 stars present in the Jacobson+15 sub-sample, and 2 stars with $[Fe/H]_{1D,LTE} > -2$, we retain 13 stars. This sub-sample is referred to as the Marino+19 data set.

- 362 giant star candidates from Da Costa et al. (2019) with either $[Fe/H]_{fitter}$[1] < -3.0, or $-3.0 \leq [Fe/H]_{fitter} \leq -2.5$ and $g_{SkyMapper} < 13.7$ mag. The radial velocities from the low-resolution spectra lack sufficient precision for our analysis, so the list of stars was cross-matched with Gaia DR2 to obtain radial velocities. A total of 195 stars were retained after the cross-match. These stars are referred to as the LowRes data set.

- 24 Ultra Metal-Poor giant stars ($[Fe/H] \leq -4$) from Sestito et al. (2019), included to increase the number of UMP stars in the full sample and to provide a consistency check on our procedures. We have specifically selected only known giants from their sample for consistency with the SkyMapper derived samples, which are giant dominated. We refer to Sestito et al. (2019) for a detailed description of the data set but we note it includes the star SMSS J031300.36-670839.3, which has $[Fe/H]_{3D,NLTE} < -6.5$ (Keller et al., 2014; Bessell et al., 2015; Nordlander et al., 2017). This data set is referred to as the Sestito+19 sub-sample.

Unless otherwise noted, the uncertainty in [Fe/H] values derived from high dispersion spectroscopy is taken as ±0.10, while for the stars in the LowRes data set, the uncertainty is ±0.3, and the values are quantized at 0.25 dex intervals. Figure 4.1 then shows the metallicity distribution of each data set, computed using kernel density estimation with a Gaussian kernel and a bandwidth parameter of 0.5; the number of stars belonging to each set is reported in the top-left corner of the panel. Each distribution has been normalized by the number of stars in the sample. Figure 4.1 also shows the distribution for the total sample formed by summing the individual distributions. As is apparent, the sample spans a wide

[1] $[Fe/H]_{fitter}$ is determined from the low-resolution spectra as described in Da Costa et al. (2019).

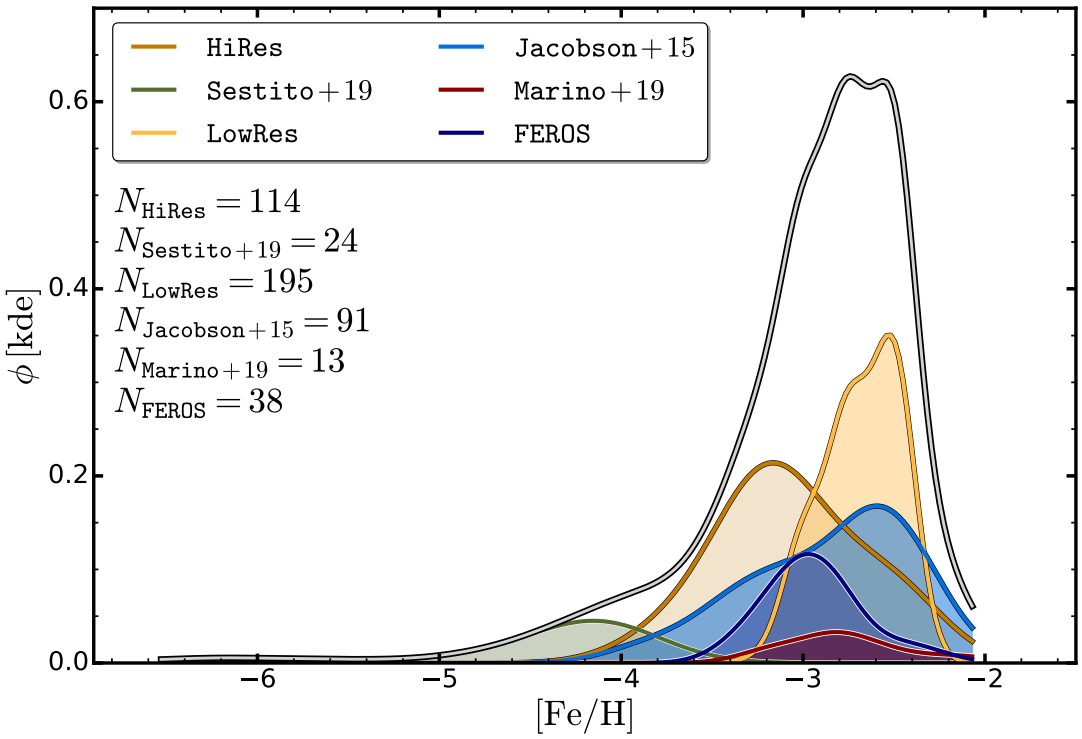

Figure 4.1. Metallicity distributions of the data sets analysed in this work. The six different subsamples are marked with red, orange, blue, dark-red, navy and green. The metallicity distribution of the total sample is shown with the grey-black solid line. Each density distribution (ϕ) has been computed with a Gaussian kernel and renormalized with the total number of stars in the sample for a correct relative visualization.

range in metallicity, with a peak around [Fe/H] ~ -2.8, consistent with the observed metallicity distribution function of the full SkyMapper EMP sample discussed in Da Costa et al. (2019).

Figure 4.2 shows the position of the analyzed stars, both in Galactic latitude and longitude and in the Cartesian Galactocentric reference frame, with each star colour-coded according to its metallicity. Since $\sim$ 90% of the stars come from the SkyMapper survey, the data set is affected by the same selection biases as discussed in Da Costa et al. (2019). Specifically, the SkyMapper survey avoids regions of the sky with significant stellar crowding, while the selection process for candidates restricts the sample to stars with $E(B-V) < 0.25$ mag. The net result is a lack of candidates near the Galactic plane and in the Galactic Bulge (see Figure 4 and Figure 14 in Da Costa et al., 2019) as is evident in the inset in the middle panel of Figure 4.2. Indeed, the majority of the stars lie inside the solar circle in the (X_G, Y_G) plane, although at a variety of heights above and below the plane; the star nearest the Galactic Centre in the sample has a Galactocentric radius of

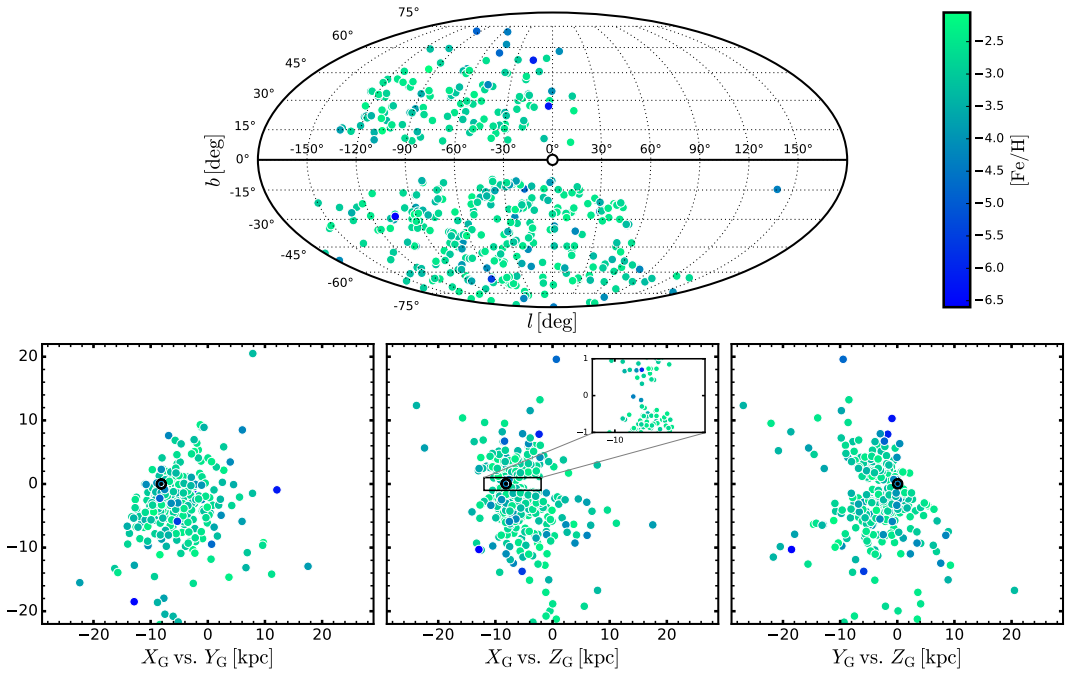

Figure 4.2. *Top panel.* Mollweide projection of the analyzed stars in Galactic coordinates. Each star is colour coded according to its metallicity. *Bottom panels.* Position of the analyzed stars in the Galactocentric Cartesian reference frame using the derived distances as discussed in section 4.1.3. The inset in the middle-bottom panel shows a zoom of the Galactic plane region. In each panel the first named quantity is for the x-axis and the second is for the y-axis. The Sun, marked by the black circle, is at (–8.2, 0.0, 0.02) and the Galactic Centre is at the origin in this co-ordinate system.

1.8 ± 0.8 kpc.

4.1.3 Deriving the kinematics of the sample

To compute the orbit of a star the full 6-dimensional information for the position and velocity is needed. Specifically, we need right ascension (α), declination (δ), distance from the Sun (d), proper motions in right ascension and declination ($\mu_\alpha \cos\delta, \mu_\delta$), and the heliocentric radial velocity (v_r). Gaia DR2 provides the optimal source for these parameters, noting that strictly Gaia provides a measurement of parallax, not distance, and that v_r is only available for the brightest stars. As recently discussed in Bailer-Jones et al. (2018), for example, simply inferring the distance from the parallax measurement alone can lead to unreliable results. To overcome this problem, Bailer-Jones et al. (2018) combined parallax measurements with a realistic prior for the distance as a function of Galactic longitude and latitude, to generate distance estimates.

Sestito et al. (2019) introduced an alternate approach to determining distances that combines the exquisite astrometry and photometry provided by Gaia DR2 with theoretical isochrones in a Bayesian analysis to infer the distance, as well as the physical properties surface gravity (log g) and effective temperature ($T_{\rm eff}$). An advantage of their technique is that it allows the breaking of the potential degeneracy between dwarf and giant star distances at a fixed $T_{\rm eff}$. In our case however, by deliberate choice of the colour-range used to define the underlying sample of low metallicity candidates in the SkyMapper EMP-survey (see Da Costa et al., 2019), our data set consists entirely of giants[2], so that any dwarf/giant distance ambiguity does not arise. It further allows us to exploit the effective temperatures and metallicities of our stars, which are known from either the high-resolution analyses or from the spectrophotometric fits to the low-resolution spectra, to derive absolute magnitudes via the use of red giant branch (RGB) isochrones, particularly for those stars that lack a reliable parallax determination. This approach has the underlying assumption that all the stars lie on the RGB, whereas the distribution of temperatures and gravities in Da Costa et al. (2019) suggests a small fraction (5–10%) of the total sample are red horizontal branch or early-AGB stars. Such stars are more luminous than RGB stars at the same effective temperature and thus the distance determinations based on the RGB locus will be smaller than the true distances. While this will result in some individually incorrect orbital parameters, the overall results are unaffected given the dominance of RGB stars in the sample.
Details of our distance determinations are discussed in the next section, but when we compare our derived distances with those in Sestito et al. (2019) for the stars in common, we find excellent agreement. This is illustrated in Figure 4.3.

Distance determination

Our approach to determining distances for the stars in our sample is twofold. First, for the stars with unreliable Gaia DR2 parallax determinations, which we take here as those with $\sigma_\pi/|\pi| \geq 0.15$, we adopted the following approach, which relies on the assumption that the stars in our sample, being very metal-poor, can be safely assumed to be old (age $\geq$ 10 Gyr)[3]. With this assumption we can then use the known $T_{\rm eff}$ and [Fe/H] values together with RGB isochrones of different metallicity to infer the absolute magnitudes and thus the distance. Specifically, we have used a set of Yonsei-Yale RGB isochrones[4] (Y^2, Demarque et al. (2004)) for an age 12 Gyr, [α/Fe] = +0.3 and metallicities corresponding to [Fe/H] = –3.5, –2.5 and –1.9 to infer the V-band absolute magnitude ($M_{\rm V}$) for each star.

[2]This is verified by the log g values for our stars as determined from the high resolution spectra, where available, or from the spectrophotometric fits to the low-resolution spectra (see Da Costa et al., 2019, for details).

[3]At ages exceeding ~10 Gyr, for a given isochrone set there is very little variation in absolute magnitude with age at fixed metallicity and $T_{\rm eff}$ on the RGB.

[4]These isochrones were adopted for consistency with the analyses in Jacobson et al. (2015); Marino et al. (2019a) and in the `HiRes dataset` (Yong et al. (in preparation), where the isochrones were used to infer surface gravities.

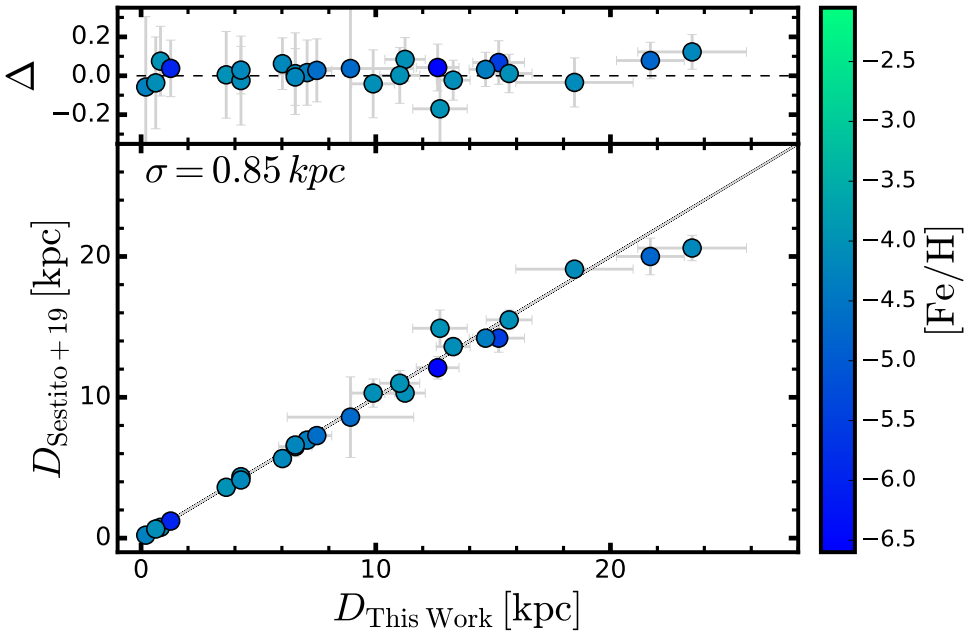

Figure 4.3. *Lower panel:* Comparison between the distance estimates in this work and those from Sestito et al. (2019). The solid line represents the 1:1 relation between the two different estimates. *Upper panel:* the relative differences between our distances and those from Sestito et al. (2019) expressed as ($\Delta = (D_{\mathrm{TW}} - D_{\mathrm{S+19}})/D_{\mathrm{TW}}$). The subscript TW indicates the values from this work. Each star is colour-coded according to its metallicity, as shown by the colour bar.

In practice, to find the absolute magnitude corresponding to a given star's metallicity and T_{eff}, we interpolated in M_{V} across the isochrones at the T_{eff} value. Since the isochrones use visual magnitudes, we first calculated the appropriate V magnitude for each star from the Gaia G values using the coefficients provided by the Gaia documentation[5]. Reddening values from Schlegel et al. (1998) were adopted, corrected according to the recipe in Wolf et al. (2018). For stars with metallicities between −4.5 and −3.5, the (M_{V}) value is a linear extrapolation, while for the small number of stars with [Fe/H] ≤ −4.5, which come primarily from the Sestito et al. (2019) sub-sample, the M_{V} inferred for [Fe/H] = −4.5 was used. The uncertainties in the distances were then determined by assuming an uncertainty of 100 K in T_{eff} and 0.1 dex in metallicity (0.3 dex for stars in `LowRes` subsample) and then propagating these values into the distance determination. Second, for the stars with nominally reliable Gaia DR2 parallax determinations, i.e., those with $\sigma_\pi/|\pi| < 0.15$, we compared the Bailer-Jones et al. (2018) distances with the distances inferred from the RGB isochrones. This is shown in Fig. 4.4. While most stars do scatter about the 1:1 line, there are sizeable differences be-

[5] https://gea.esac.esa.int/archive/documentation/GDR2/Data_processing/chap_cu5pho/sec_cu5pho_calibr/ssec_cu5pho_PhotTransf.html

tween the two estimates for ~25% of the stars, most commonly with the RGB-based distance being larger than the Bailer-Jones et al. (2018) value, indicating that the parallax may have been overestimated, or that the RGB-based distance is incorrect.
We have not sought to investigate the origin of the discrepancy for each individual case, noting that we include uncertainties in $T_{\rm eff}$ and [Fe/H] when estimating the uncertainty in the RGB-based distance. There is, however, a potential systematic uncertainty introduced by RGB isochrone based approach. In particular, as discussed by Joyce & Chaboyer (2018), the location of theoretical RGBs in the Hertzsprung-Russell diagram is sensitive to the adopted value of the mixing length parameter $\alpha_{\rm MLT}$. The value of $\alpha_{\rm MLT}$ employed in any particular isochrone set (e.g., $\alpha_{\rm MLT}$ = 1.7 for the Y^2 isochrones) is usually determined by requiring a fit to the solar values, but, as demonstrated in Joyce & Chaboyer (2018), at low metallicities the location of the RGB computed with a solar-calibrated $\alpha_{\rm MLT}$ is more luminous by ~0.3 mag at a fixed $T_{\rm eff}$ than a comparison with globular cluster RGB observations would suggest: a ~10% smaller value of $\alpha_{\rm MLT}$ is required for consistency with the observations. It is possible therefore that our RGB-based distances are systematically over-estimated, though the comparison shown in Fig. 4.4 suggests that it is not a major effect.
In practice we have adopted the Bailer-Jones et al. (2018) distance and its uncertainty whenever the absolute value of the relative difference ($\Delta = \frac{D_{\rm RGB} - D_{\rm BJ+18}}{D_{\rm RGB}}$) is smaller than 0.35. This is shown as the grey shaded region in Figure 4.4. For the remainder, i.e., for the stars outside the shaded area with $|\Delta| > 0.35$, we adopted the distance inferred from RGB isochrones. Overall, this results in the use of the RGB isochrone distance for 357 stars, while for the remaining 118 the Bailer-Jones et al. (2018) distance is employed[6].
The largest (heliocentric) distance of the stars in our sample is the RGB-based distance of ~ 35 kpc for the high-luminosity giant ($\log g \approx 0.3$) SMSS J004037.55–515025.1, which has [Fe/H] = –3.83 and is in the `Jacobson+15` sub-sample. The smallest is the Bailer-Jones et al. (2018) distance of 0.21 kpc for the sub-giant BD+44 493 ($\log g \approx 3.2$ and [Fe/H] = –4.30) from the `Sestito+19` sub-sample. Overall, the median heliocentric distance for the entire sample is ~ 5 kpc, with a median ~ 7 kpc for RGB-based distances, and a median of ~ 3 kpc for Bailer-Jones et al. (2018) distances.

Orbital properties

To compute the orbital parameters we used the full 6-dimensional information on the position and velocity for each star. Gaia DR2 provides coordinates and proper motions, while the distances have been obtained as discussed in the previous section. Radial velocities come from the high-dispersion spectra, when available, and from Gaia DR2 for the `LowRes` sample.

[6]We have checked that the kinematics for the stars where we have adopted the Bailer-Jones et al. (2018) distance are not significantly altered if instead the RGB distance is assumed. This is not surprising as for these stars the Bailer-Jones et al. (2018) and RGB distances are consistent.

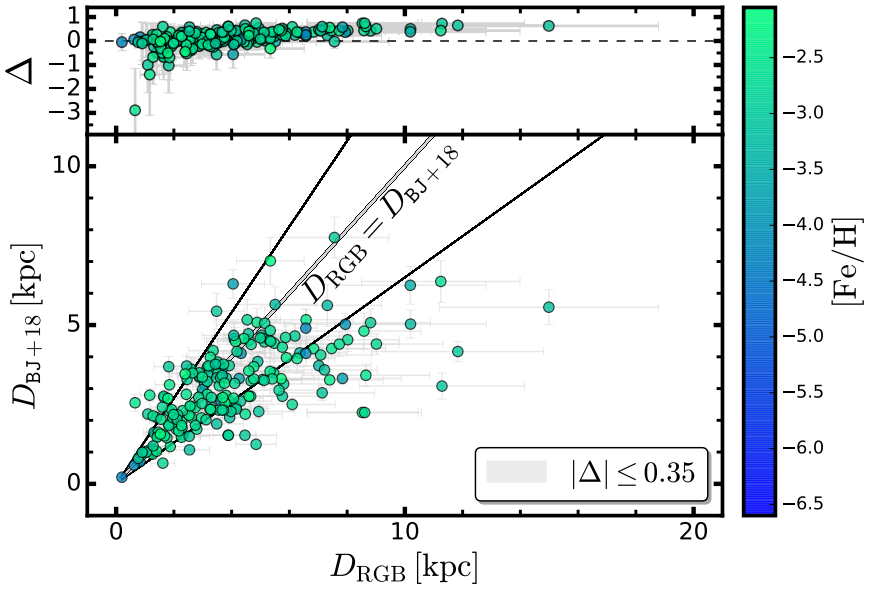

Figure 4.4. Comparison between the distance determined in this work and the distance inferred in Bailer-Jones et al. (2018) for the 195 stars with $\sigma_\pi/|\pi| < 0.15$. Each star is colour coded according to its metallicity, as shown in the right colour-bar. The grey shaded region within the black solid lines encloses stars with $|\Delta| \leq 0.35$, for which we adopted the Bailer-Jones distances. The top panel shows the relative differences between distances inferred through RGB isochrones and distances from Bailer-Jones et al. (2018) ($\Delta = (D_{\rm RGB} - D_{\rm BJ+18})/D_{\rm RGB}$)

We note that there are a number of the stars with radial velocities from the high-dispersion spectra that also have radial velocities from Gaia DR2, and this allows us to check for anything unusual or unexpected. As mentioned in §4.1.2, in this comparison process we discovered an anomaly in the Jacobson et al. (2015) radial velocities for a particular Magellan/MIKE run. In that run 32 stars were observed of which 8 also have radial velocities from Gaia DR2. The comparison for these 8 stars shows extreme disagreement for 7 stars, with values of the difference V_r(J+15) – V_r(Gaia DR2) ranging from –400 to +415 km s^{-1}. We are at a loss to explain the origin of the disagreements[7] and have consequently excluded from the analysis the stars from this run that lack Gaia DR2 radial velocities, while using the Gaia DR2 radial velocities in the kinematic calculations for the remaining 7 stars that have [Fe/H] ≤ –2.0 dex. We stress that such large disagreements are seen only for this one observing run in the `Jacobson+15` sample, the radial velocities from other runs are very consistent with Gaia DR2 values when available. This is also the case for the stars in the `HiRes` and `FEROS` samples. Overall, for the 41 stars with radial velocities from our high-dispersion spectra and from

[7] It is important to recall that Gaia DR2 velocities were not available at the time the Jacobson et al. (2015) results were published, so the velocity anomalies would not have been apparent.

Gaia DR2, the velocities agree well with a mean difference, in the sense of our velocities minus Gaia, of 1.7 $\mathrm{km\,s^{-1}}$ and a standard deviation of 5.5 $\mathrm{km\,s^{-1}}$. This agreement indicates that any systematic uncertainties in the radial velocity determinations are very minor compared to other contributors to uncertainties in the orbit determinations. We have always used the radial velocity and the corresponding uncertainty from the high dispersion spectra when available; the Gaia radial velocities and their uncertainties were utilized only when there was no alternative.

The kinematics of our sample of metal-poor stars have been determined using the GALPY[8] Python package (Bovy, 2015). The orbit of each star was obtained by direct integration backward and forward in time for 2 Gyrs.This choice relies on the assumption that such a timescale is shorter than any significant variation in the Galactic potential

We adopted the potential identified as the best candidate among the ones studied in McMillan (2017)[9]. Briefly, it consists of an axisymmetric model with a bulge, thin, thick and gaseous disks, and a Navarro-Frenk-White (Navarro et al., 1996) dark matter halo. The heliocentric distances derived in the previous section have been converted to distances from the Galactic Centre (GC) in the GALPY routine, specifying the galactocentric position of the Sun as $(X, Y, Z) = (-8.21, 0, 0.0208)$ kpc, and its circular speed as $v_0 = 232.8\,\mathrm{km\,s^{-1}}$. Both quantities are taken from McMillan (2017).

For each star we determined the apogalacticon and perigalacticon (D_{apo}, D_{peri}) of the orbit, the maximum vertical excursion from the Galactic plane (Z_{max}), the eccentricity $\left(e = \frac{D_{\mathrm{apo}} - D_{\mathrm{peri}}}{D_{\mathrm{apo}} + D_{\mathrm{peri}}}\right)$, the energy ($E$), the three actions ($J_{\mathrm{R}}$, J_ϕ, J_{Z})[10] and the velocity components U, V, W in the frame of the local standard of rest (LSR). As have others (e.g. Myeong et al., 2018), we emphasize that action space is the ideal plane in which to evaluate large samples of MW stars to identify and study possible sub-structures and debris from accretion events. The reason is that the actions are nearly conserved under the hypothesis that the potential is smoothly evolving (Binney & Spergel, 1984).

The uncertainties associated with the derived orbital parameters are determined by sampling the Probability Distribution Functions (PDFs) of the observed values. In particular, we drew 500 random realizations of the distance and velocity components and, for each realization, recomputed the orbital parameters assuming Gaussian distributions with means and dispersions equal to the observed values and their uncertainties. In particular, the uncertainties in the two proper motion components ($\mu_\alpha \cos\delta$, μ_δ) were drawn from a bivariate Gaussian taking into consideration the full covariance as defined in Equation 4.1, following

[8] http://github.com/jobovy/galpy

[9] We note that our adopted potential is different from that used in Sestito et al. (2019).

[10] See Binney (2012) for a description of these variables. In particular, the azimuthal action J_ϕ corresponds to the vertical angular momentum L_Z for an axisymmetric potential, as is the case here. In the following we will therefore refer to the azimuthal action in place of the vertical angular momentum. We also adopted the Stäckel fudge method to calculate the actions as implemented in GALPY.

the Gaia DR2 documentation.

$$cov = \begin{pmatrix} \sigma^2_{\mu_\alpha} & \sigma_{\mu_\alpha} \cdot \sigma_{\mu_\delta} \cdot corr(\mu_\alpha, \mu_\alpha) \\ \sigma_{\mu_\alpha} \cdot \sigma_{\mu_\delta} \cdot corr(\mu_\alpha, \mu_\alpha) & \sigma^2_{\mu_\delta} \end{pmatrix} \quad (4.1)$$

The uncertainties on the orbital parameters have then been determined by propagating the 16th and 84th percentiles of the resulting parameter distributions.
As examples, we consider the two most iron-poor stars known: SMSS J031300.36–670839.3 (Keller et al., 2014; Bessell et al., 2015) and SMSS J160540.18–144323.1 (Nordlander et al., 2019). For the former we find an "outer-halo" orbit with $e = 0.70 \pm 0.05$, $D_{\rm peri} = 6.5 \pm 2.0$, $D_{\rm apo} = 36.6 \pm 9.8$ and $|Z_{\rm max}| = 34.2 \pm 9.2$ kpc. These parameters are in good agreement with those listed in Sestito et al. (2019). For the latter star, however, we determine an extreme "outer-halo" orbit that may in fact be unbound as the derived energy E is close to zero. The inferred parameters are $e = 0.93$, $D_{\rm peri} = 6.5 \pm 2.0$, $D_{\rm apo} \approx 423$ and $|Z_{\rm max}| \approx 327$ kpc; the latter two quantities are quite uncertain.
As discussed in detail in §4.1.5, SMSS J160540.18–144323.1 is, in fact, one of a small number of stars (30 out of 475) for which we find apparent apogalacticon distances larger than the Milky Way virial radius, i.e., larger than ~250 kpc. For such stars, a substantial fraction of the 500 random realizations resulted in unbound orbits (i.e., $D_{\rm apo} = \infty$), thus potentially biasing both the medians and the uncertainties derived from the orbital parameter distributions. The uncertainties for these specific stars are considered in more detail in §4.1.5.
As an independent check on the uncertainties and on the role of the adopted potential, we can compare our orbit parameters with those listed in Sestito et al. (2019, see their Table 4) for the 24 Ultra Metal-Poor stars in common. The agreement is generally excellent. Specifically, defining Δ as the difference between our values and those of Sestito et al. (2019) normalized by our values, then for the 24 stars we find median Δ values of 0.04, 0.03, 0.03 and 0.08 for $D_{\rm apo}$, $D_{\rm peri}$, J_ϕ and E, respectively, noting that for the energy comparison we have taken into account the different solar energy used here to that in the Sestito et al. (2019) study.

4.1.4 Results

The physical properties and the computed orbital parameters of the first 10 stars are listed in Tables 4.1 and 4.2 while the complete tables are available with the online supplementary material. For Table 4.1 the columns are, respectively, an index number, the Gaia DR2 and SkyMapper or other IDs, the on-sky location in degrees, the parallax and its uncertainty from Gaia DR2, the adopted distance and its uncertainty, a flag indicating whether the distance is from the RGB isochrones (value=0), or from Bailer-Jones et al. (2018) (value=1), the proper motions from Gaia DR2 and their uncertainties, the heliocentric radial velocity and its uncertainty, log $T_{\rm eff}$ and its uncertainty, the abundance [Fe/H], the reddening, and the data set from which the star originates. Similarly for Table 4.2, the columns are the index number (as for Table 4.1), the eccentricity and its uncertainty, the apo- and peri-galactic distances, the maximum deviation from the Galactic plane, the

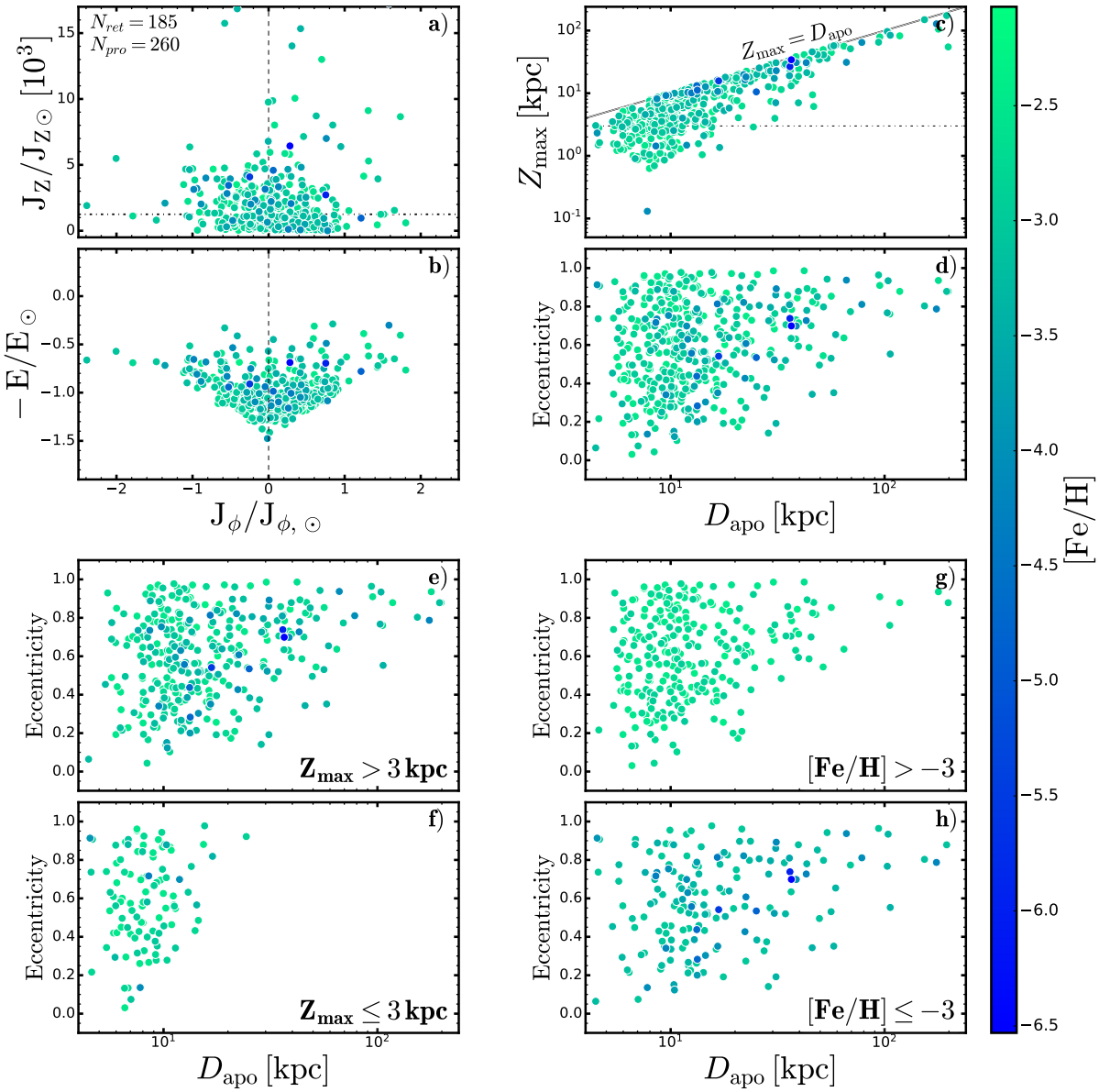

Figure 4.5. Orbital parameters for the stars with $D_{apo} \leq 250$ kpc. *Panels a) and b):* Vertical action (J_Z [km s^{-1}]) and energy (E [km^2 s^{-2}]) as a function of the azimuthal action (i.e. the vertical component of the angular momentum, J_ϕ [km s^{-1}]). All quantities have been normalized by the solar values. The horizontal dashed-dotted line in panel a) indicates $J_Z/J_{Z,\odot} = 1.25 \times 10^3$. *Panels c) and d):* Maximum altitude from the MW plane ($|Z_{max}|$ [kpc]) and eccentricity plotted as a function of the apogalactic (D_{apo} [kpc]) distance. Note that since $|Z_{max}|$ cannot exceed D_{apo}, the region above the 1:1 line in panel c) is forbidden. The horizontal dashed-dotted line in panel c) marks Z_{max} = 3 kpc. *Panels e) and f):* as for panels c) and d) but split by $|Z_{max}|$. *Panels g) and h):* as for panels c) and d) but split by metallicity [Fe/H].

actions (J_R, J_ϕ, J_Z), the energy, and the U, V and W velocity components in the LSR frame.

Figure 4.5 shows the inferred orbital parameters for all the stars with $D_{apo} \leq 250$ kpc, with each star colour-coded according to its metallicity, as shown in the right colour-bar. In particular, panels a) and b) show the vertical action (J_Z [kpc km s^{-1}]), indicative of the vertical excursion of the star, and the orbital energy (E [km^2 s^{-2}])[11], as a function of the azimuthal action (J_ϕ [kpc km s^{-1}])[12]. The quantities have been normalized by the solar values computed for the `McMillan2017` potential employed here: $J_{\phi,\odot} = 2014.24$ kpc km s^{-1}, $J_{Z,\odot} = 0.302$ kpc km s^{-1} and $E_\odot = -153507.15$ km^2 s^{-2}. We note that if we adopt the `MWPotential2014` employed by Sestito et al. (2019), and include the increased dark matter halo mass, we obtain solar values similar to those in that work. Retrograde orbits are characterised by a negative value of J_ϕ, while prograde orbits have a positive J_ϕ. We find that overall ~ 42% (185/445) of our stars with $D_{apo} \leq 250$ kpc exhibit retrograde orbits, and note that the selection of the stars for inclusion in our sample should not have any bias as regards prograde or retrograde orbits.

Regarding the uncertainties in the derived orbital quantities, these are listed for each individual star in Table 4.2, but as examples, we find that for stars with $D_{apo} \leq 20$ kpc, the median errors in D_{apo}, D_{peri}, $|Z_{max}|$ and e are 0.9 kpc, 0.6 kpc, 1.0 kpc and 0.08, respectively. These increase to 11.6 kpc, 1.7 kpc, 7.7 kpc and 0.08 for stars with $20 \leq D_{apo} \leq 50$ kpc, respectively, and to 56.4 kpc, 2.7 kpc, 52.0 kpc and 0.09 for stars with $50 \leq D_{apo} \leq 250$ kpc.

In panels c) and d) we show the maximum height ($|Z_{max}|$ [kpc]) and eccentricity e as function of the apogalatic distance (D_{apo} [kpc]). A preliminary inspection of panels a) and c) reveals that, despite the low metallicity of the stars in the sample, we detect a significant number of stars with small vertical excursion, in agreement with Sestito et al. (2019, 2020b) and Di Matteo et al. (2020). In particular, if we follow Sestito et al. (2020b) and adopt $J_Z/J_{Zsun} < 1.25 \times 10^3$, shown as the dotted horizontal line in panel a), to characterize orbits that are confined to the disk, then ~50% of our sample meets this definition. Similarly, if we follow Sestito et al. (2019) in using $|Z_{max}| = 3$ kpc (horizontal dashed-dotted line in panel c) of Figure 4.5) to discriminate between "disk-like" and "halo-like" orbits, we find that 102, or ~21%, of the stars in our sample meet this criterion, i.e., have orbits that do not deviate far from the Galactic plane. Further, panel d) suggests that, while stars with $D_{apo} \lesssim 25$ kpc have an approximately uniform distribution in eccentricity, highly eccentric ($e \gtrsim 0.5$) orbits are favoured for stars with $D_{apo} \gtrsim 25$ kpc, while panels c) and f) show that there is an apparent dearth of stars with low values of $|Z_{max}|$ beyond $D_{apo} \approx 30$ kpc. These apparent effects are most probably a consequence of the criteria adopted to select SkyMapper EMP candidates, as stars with low $|Z_{max}|$ and large D_{apo} aren't likely to meet the apparent magnitude cut that underlies the sample ($g_{skymapper} < 16$ for the `HiRes` stars

[11] The energy is multiplied by −1 to maintain the canonical "V"-shape.

[12] The azimuthal action corresponds to the vertical angular momentum L_Z for an axisymmetric potential as is used here.

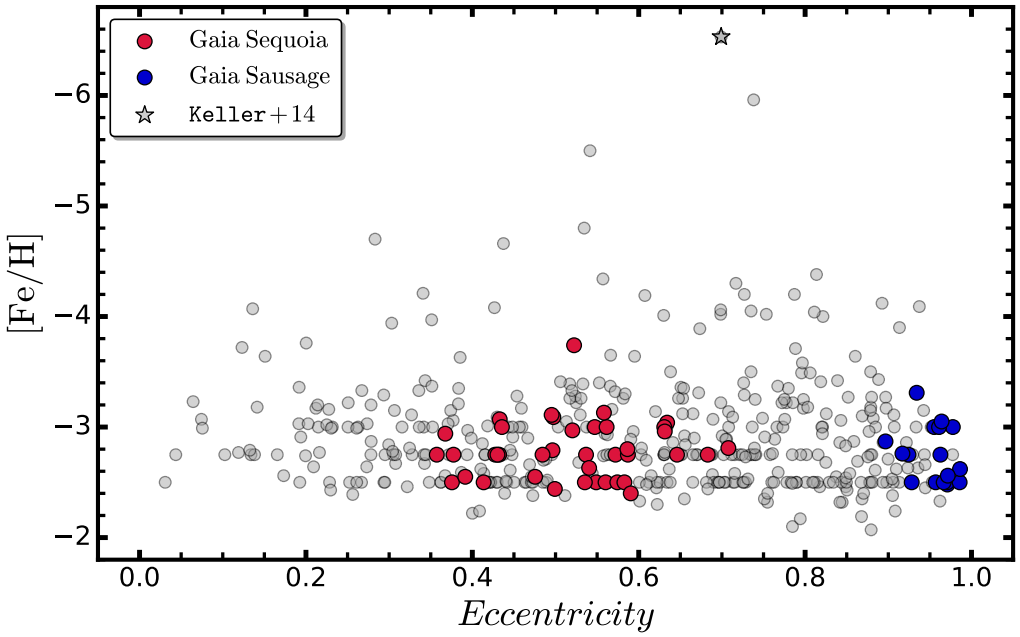

Figure 4.6. [Fe/H] vs. e for the stars with $D_{\rm apo} < 250$ kpc. *Gaia Sausage* and *Gaia Sequoia* candidates are shown with blue and red circles, respectively. The Keller star (Keller et al., 2014; Nordlander et al., 2017) is shown as a grey star indicating the upper limit on the abundance.

and $g_{\rm skymapper} < 13.7$ for the `LowRes` stars). In particular, the bottom-middle and bottom-right panels of Figure 4.2 show that stars with $|Z| \leq 3$ kpc and Galactocentric distances beyond 10-15 kpc are rare in our sample.

The two bottom left panels again show the eccentricity versus the apogalactic distance, but separately for stars with $|Z_{\rm max}|$ in excess of 3 kpc (panel e) and those with $|Z_{\rm max}|$ less than this value (panel f). Similarly, the two bottom right panels also show eccentricity versus the apogalactic distance but this time the sample is split by metallicity: stars with [Fe/H] > -3 are shown in panel g) while the more metal-poor stars are shown in panel h). The similarity of panels g) and h) show that there is no obvious dependence of the kinematics on metallicity, at least for this sample of metal-poor stars.

To more clearly illustrate this point, we show in Figure 4.6 a plot of [Fe/H] against e, the orbital eccentricity. Diagrams of this nature have long played an important role in discussions of the formation of the Galaxy. For example, in their classic paper, Eggen et al. (1962) argued on the basis of an apparent correlation between ultra-violet excess (an indicator of [Fe/H]) and orbital eccentricity, that the proto-Galaxy collapsed rapidly to a planar structure with a timescale of only a few $\times 10^8$ years. Specifically, in their sample of stars, those with [Fe/H] less than –1.5, approximately, all had $e \geq 0.6$ (Eggen et al., 1962). Norris et al. (1985) challenged the rapid collapse interpretation arguing that the lack of low-e metal-poor stars was a result of a kinematic bias in the selection of the Eggen et al. (1962) sample. Instead, using a sample selected without any kinematic bias, Norris et al.

Table 4.1. Observed properties of the first ten stars in our sample. The columns are: a numeral index, Gaia DR2 and SkyMapper or other IDs, coordinates, parallax and uncertainty, distance and uncertainty, a flag for distance method (0=RGB interpolation, 1=Bailer-Jones et al. (2018)), proper motions and uncertainties, radial velocity and uncertainty, $\log T_{\rm eff}$ and uncertainty, [Fe/H], E(B-V) and origin data set as discussed in Section 4.1.2. The complete table is available electronically.

Index	Gaia DR2	SMSS J	α	δ	π	σ_π	D	σ_D	FLAG	μ_α	μ_δ	σ_{μ_α}	σ_{μ_δ}	$v_{\rm r}$	$\sigma_{v_{\rm r}}$	$log\,T_{\rm eff}$	$\sigma_{\log T_{\rm eff}}$	[Fe/H]	E(B−V)	Dataset$_{\rm id}$
			deg	deg	mas	mas	kpc	kpc		mas/yr	mas/yr	mas/yr	mas/yr	km s^{-1}	km s^{-1}	K	K	dex	mag	
1	2398202677437168384	230525.31-213807.0	346.3555462	-21.6353089	0.272750	0.049314	2.46	0.65	0	-1.142	-15.056	0.066	0.067	-15.7	0.4	3.708	0.009	-3.26	0.027	HiRes
2	2406023396270909440	232121.57-160505.4	350.3399235	-16.0848819	0.418462	0.036657	1.10	0.20	0	17.161	3.631	0.069	0.054	-39.1	1.0	3.736	0.008	-2.87	0.022	HiRes
3	2541284393302759296	001604.23-024105.0	4.0177235	-2.6848020	0.282214	0.046544	2.98	0.78	0	13.561	-9.876	0.093	0.055	49.3	1.2	3.705	0.009	-3.14	0.031	HiRes
4	2623363791014198656	224145.62-064643.0	340.4401074	-6.7786758	0.030874	0.031151	12.07	3.06	0	1.853	-2.861	0.053	0.048	-201.6	5.0	3.681	0.009	-3.16	0.029	HiRes
5	2666382767566459264	214716.16-081546.9	326.8173947	-8.2630725	0.499372	0.031415	3.48	0.93	0	1.497	-37.651	0.057	0.049	-12.3	0.3	3.708	0.009	-3.17	0.037	HiRes
6	2909324470226028800	053721.56-244251.5	84.3398617	-24.7143189	0.016537	0.027294	9.91	2.69	0	2.367	0.329	0.036	0.047	231.2	5.8	3.710	0.008	-3.50	0.021	HiRes
7	3064362275530429312	081627.99-055913.3	124.1166115	-5.9870501	0.176978	0.028682	7.47	1.92	0	-0.403	-1.921	0.048	0.032	159.8	4.0	3.688	0.009	-3.37	0.063	HiRes
8	3064545859613457536	081112.13-054237.7	122.8005492	-5.7104991	0.098921	0.047035	21.76	5.71	0	0.245	-2.879	0.075	0.066	121.0	3.0	3.686	0.009	-3.74	0.038	HiRes
9	3458991567268745728	120218.07-400934.9	180.5752523	-40.1597114	0.266276	0.035374	3.29	0.39	1	11.765	-2.682	0.040	0.029	-17.6	0.4	3.746	0.008	-2.89	0.090	HiRes
10	3473880535256883328	120638.24-291441.1	181.6593108	-29.2447637	0.257289	0.024364	3.41	0.28	1	-0.576	-2.246	0.031	0.016	58.1	1.5	3.708	0.009	-3.06	0.052	HiRes

(1985) showed that metal-poor stars with relatively low orbital eccentricities exist, a population they identified as a metal-weak component of the thick-disk. The Norris et al. (1985) result was confirmed and strengthened by Beers et al. (2014, see their Fig. 10) who showed that for stars with [Fe/H] ≤ –1.5 there is no correlation between orbital eccentricity and metallicity: stars can be found with e values between ~0.1 and 1. Our results in Figure 4.6 extend the lack of any correlation to substantially lower metallicities than those in Beers et al. (2014), where there were only a few stars at or below [Fe/H] = –2.5 and none below –3.0 dex. We discuss the implications of the existence of extremely metal-poor stars with low eccentricities (and low $|Z_{\rm max}|$) in §4.1.5. Figure 4.6 also shows the location of candidate members of the *Gaia Sausage* and *Gaia Sequoia* accretion events. The identification and properties of these stars are discussed in detail in §4.1.5.

Finally, as noted above, we find that 30 stars from the full sample have apparent $D_{\rm apo}$ values larger than 250 kpc, i.e., larger than the virial radius of the Milky Way. The majority of these stars possess energies that are consistent with, or larger than, zero and they likely have unbound orbits. These stars will be discussed in more detail in §4.1.5 but we note again that they are not plotted in the panels of Fig. 4.5 or in Fig. 4.6.

4.1.5 Discussion

In the following sub-sections we discuss in detail the results for the 475 very metal-poor stars analyzed. We will focus specifically on three key aspects. The first is the relation between the stars in our sample and the recently described remnants of the postulated *Gaia Sequoia* and *Gaia Sausage* accretion events (Belokurov et al., 2018; Myeong et al., 2019). For the sake of this analysis, following the hypothesis of Belokurov et al. (2018) and Myeong et al. (2019), we assume that these accretion events are distinct, but see Helmi et al. (2018) for an alternative

Table 4.2. Derived orbital properties for the first ten stars in our sample. The columns are: numeral index; eccentricity; apo- and peri-perigalacticon distances; maximum height; orbital actions; orbital energy; U, V, W velocities and orbit type (Halo, Disk, Sequoia, Sausage, Unbound). Each numerical quantity is followed by upper and lower uncertainties. The complete table is available electronically.

index	Eccentricity	D_{apo} kpc	D_{peri} kpc	Z_{max} kpc	J_R kpc·km s^{-1}	J_ϕ kpc·km s^{-1}	J_Z kpc·km s^{-1}	Energy kpc·km^2 s^{-2}	U km s^{-1}	V km s^{-1}	W km s^{-1}	Orbit type
1	$0.58^{+0.17}_{-0.20}$	$8.4^{+0.3}_{-0.2}$	$2.2^{+1.4}_{-0.9}$	$2.4^{+1.0}_{-0.8}$	$295.5^{+137.9}_{-138.6}$	$690.9^{+360.1}_{-287.7}$	$96.8^{+55.2}_{-45.0}$	-176530^{+2662}_{-634}	$86.7^{+22.1}_{-25.4}$	$-147.8^{+48.3}_{-42.4}$	$3.9^{+5.6}_{-4.8}$	Disk
2	$0.28^{+0.05}_{-0.06}$	$10.4^{+0.5}_{-0.6}$	$5.9^{+0.5}_{-0.3}$	$1.4^{+0.3}_{-0.3}$	$104.6^{+44.7}_{-43.7}$	$1698.7^{+51.1}_{-44.4}$	$33.6^{+9.0}_{-8.9}$	-156666^{+938}_{-697}	$-83.8^{+19.3}_{-15.6}$	$-16.0^{+3.4}_{-2.8}$	$16.6^{+6.0}_{-4.9}$	Disk
3	$0.71^{+0.17}_{-0.28}$	$11.2^{+1.7}_{-1.3}$	$1.9^{+2.0}_{-1.1}$	$6.3^{+2.7}_{-2.6}$	$540.3^{+227.7}_{-319.5}$	$456.2^{+582.2}_{-522.2}$	$298.2^{+127.1}_{-128.8}$	-162656^{+6212}_{-2240}	$-91.6^{+30.5}_{-26.4}$	$-165.6^{+62.1}_{-52.5}$	$-121.1^{+25.5}_{-22.9}$	Halo
4	$0.57^{+0.12}_{-0.08}$	$12.7^{+3.0}_{-2.0}$	$3.5^{+1.2}_{-1.1}$	$10.8^{+1.8}_{-0.5}$	$460.7^{+84.5}_{-87.2}$	$-494.8^{+319.1}_{-292.1}$	$715.3^{+204.8}_{-79.9}$	-154330^{+10450}_{-7291}	$-63.8^{+4.9}_{-6.4}$	$-253.2^{+39.1}_{-44.3}$	$58.4^{+28.2}_{-33.3}$	Halo
5	$0.80^{+0.14}_{-0.17}$	$51.8^{+98.8}_{-23.2}$	$5.8^{+0.4}_{-2.5}$	$41.0^{+81.7}_{-18.7}$	$2937.5^{+19134394.1}_{-2646.9}$	$-1367.7^{+748.7}_{-431.8}$	$1187.9^{+661.6}_{-563.7}$	-92378^{+86287}_{-63565}	$245.3^{+65.1}_{-75.1}$	$-515.5^{+163.7}_{-141.5}$	$-225.7^{+75.8}_{-66.0}$	Halo
6	$0.64^{+0.02}_{-0.03}$	$18.8^{+3.4}_{-2.9}$	$4.1^{+1.2}_{-0.6}$	$5.8^{+6.4}_{-2.7}$	$764.6^{+72.7}_{-104.6}$	$1488.5^{+149.5}_{-186.2}$	$153.8^{+311.1}_{-78.2}$	-136232^{+9007}_{-8547}	$-141.8^{+6.1}_{-5.4}$	$-194.3^{+16.4}_{-16.7}$	$2.2^{+31.7}_{-28.1}$	Halo
7	$0.57^{+0.06}_{-0.05}$	$14.3^{+1.8}_{-1.6}$	$4.0^{+0.1}_{-0.2}$	$2.1^{+0.7}_{-0.4}$	$489.9^{+151.6}_{-109.4}$	$1451.1^{+39.9}_{-42.1}$	$35.8^{+9.8}_{-4.3}$	-148391^{+4764}_{-5055}	$-60.9^{+8.3}_{-8.8}$	$-146.4^{+10.6}_{-12.2}$	$6.0^{+11.8}_{-12.8}$	Disk
8	$0.52^{+0.30}_{-0.24}$	$30.5^{+13.4}_{-7.4}$	$9.6^{+14.8}_{-6.9}$	$17.2^{+6.5}_{-6.0}$	$882.5^{+568.7}_{-462.6}$	$-2744.0^{+2195.0}_{-3106.5}$	$632.8^{+453.9}_{-383.4}$	$-110197^{+23747}_{-18420}$	$109.1^{+50.3}_{-49.6}$	$-280.2^{+56.9}_{-58.2}$	$-84.2^{+33.3}_{-37.4}$	Sequoia
9	$0.76^{+0.06}_{-0.06}$	$30.7^{+6.1}_{-4.4}$	$4.1^{+0.4}_{-0.5}$	$4.0^{+2.1}_{-1.3}$	$1649.8^{+566.7}_{-404.9}$	$1830.3^{+96.3}_{-125.6}$	$55.5^{+17.5}_{-12.8}$	-114866^{+7743}_{-6481}	$178.5^{+22.7}_{-20.3}$	$99.1^{+9.3}_{-8.6}$	$-2.5^{+0.7}_{-0.7}$	Halo
10	$0.38^{+0.03}_{-0.02}$	$9.1^{+0.1}_{-0.1}$	$4.1^{+0.2}_{-0.2}$	$2.4^{+0.2}_{-0.2}$	$159.9^{+20.5}_{-17.4}$	$1198.2^{+38.8}_{-45.3}$	$82.4^{+11.6}_{-9.5}$	-166959^{+229}_{-216}	$34.7^{+1.0}_{-0.7}$	$-52.8^{+2.1}_{-2.3}$	$7.0^{+2.9}_{-3.0}$	Disk

view, particularly of *Gaia Enceladus* as a single ancient major merger event. The purpose of our work, however, is not to discern between the scenarios proposed to explain these structures in the Galactic halo, but rather to investigate their very low-metallicity content. The second key point is the analysis of low-metallicity stars with disk-like orbital properties that likely have a fundamental role in contributing to the understanding of the formation and evolution the MW's disk. Finally, we discuss the properties and potential origin of the stars in our sample that are either loosely bound or not bound to the Galaxy.

Gaia Sausage and *Gaia Sequoia* candidate members

The exquisite data provided by Gaia DR2 has recently revealed the trace of at least two early major accretion events in the history of our Galaxy, referred to as *Gaia Sausage* and *Gaia Sequoia* (Helmi et al., 2018; Belokurov et al., 2018; Mackereth et al., 2019; Myeong et al., 2019; Koppelman et al., 2019). These discoveries are a direct consequence of the development of computational techniques and resources capable of processing very large data sets.

Here we exploit the action-space classification provided in Myeong et al. (2019, their Figure 9) to identify possible members of these accretion features within our sample of low-metallicity stars. Monty et al. (2020) have adopted a similar approach finding possible members of these systems with metallicities as low as [Fe/H] = −3.6 dex. The number, abundances and abundance ratios of these stars could provide important information on the early evolution of the progenitors of the two accretion events.

The top-left panel of Figure 4.7 shows the action map $(J_Z - J_R)/J_{tot}$ vs. J_ϕ/J_{tot} with J_{tot} being the sum of the absolute value of the three actions ($J_{tot} = J_R + J_Z + |J_\phi|$). Following the classification in Myeong et al. (2019), we highlight the loci of the

Sequoia and *Sausage* accretion events with red and blue rectangles, respectively. We find that out of the 475 analyzed stars, 16 stars are kinematically coincident with the *Sausage* accretion event, while 40 stars are candidate *Sequoia* members. As expected from their definition and the action map (Helmi et al., 2018; Belokurov et al., 2018; Myeong et al., 2019; Yuan et al., 2020), the latter are characterized by mildly eccentric ($e \sim 0.5$) retrograde orbits, while the former have highly eccentric orbits ($e \sim 0.9$). Appendix 4.1.8 shows some typical orbits for stars identified as possible *Gaia Sequoia* and *Gaia Sausage* members.

We remind the reader that our membership identification follows the criteria introduced in Myeong et al. (2019), and is thus entirely based on the dynamics through the use of the action map. We stress that this approach does not allow for any "background" population that may be present in these regions of the action map. Consequently, we cannot straightforwardly assume that all the stars in our sample that are dynamically coincident with the *Sequoia*/*Sausage* accretion events actually belong to such remnants. In Appendix 4.1.7 we have attempted to perform a more accurate analysis through the use of a clustering algorithm approach. Briefly, the clustering analysis of our very metal-poor sample does provide independent evidence for the existence of groupings consistent with the *Sequoia* (group 6) and *Sausage* (group 8) dynamical definitions, though there are also indications that our *Sequoia* and *Sausage* samples, as defined in Fig. 4.7, are potentially contaminated by a "background" population that might be as much as $\sim$ 50% and ~35%, respectively. These background estimates are determined by exploiting the clustering analysis groupings discussed in Appendix 4.1.7, and the numbers of stars within the *Gaia Sequoia* and *Gaia Sausage* loci.

Panels b), c), d) and e) of Figure 4.7 show a detailed analysis of stars identified as candidate *Sequoia*, shown in red, and *Sausage* members, shown in blue. In panel c) we note that, by construction, *Sausage* stars are characterized by more radial orbits, although at low J_R, some candidate *Sequoia* stars seem to share the similar values of J_R as *Sausage* stars. The Toomre diagram in panel d) shows that both groups are consistent with halo dynamics, and again we note that there is some degree of overlap between the two groups of stars. As regards panel b), which shows the energy versus azimuthal action, *Sausage* candidates show the distinctive vertical distribution, indicative of almost null azimuthal angular momentum, while *Sequoia* stars are clearly highly retrograde, as expected. Comparing panel b) with Koppelman et al. (2019, their Figure 2) we note that our accreted candidates span a wider range in energy. However, we note that the definition of *Sequoia* and *Sausage* parameters differs from work to work. Indeed, Yuan et al. (2020) identifies *Sausage* members that lie well outside the selection box of Myeong et al. (2019) and the energy range of Koppelman et al. (2019). For the sake of our analysis, we choose to be consistent with the Myeong et al. (2019) classification, although we stress again that a number of the candidates may not actually belong to the remnants of the accretion events.

As regards abundances, we find that the most metal-poor star in our sample that is a candidate member of *Sequoia* (SMSS J081112.13-054237.7) has a metallicity of [Fe/H] = −3.74, while the most metal-poor *Sausage* candidate (SMSS J172604.29-

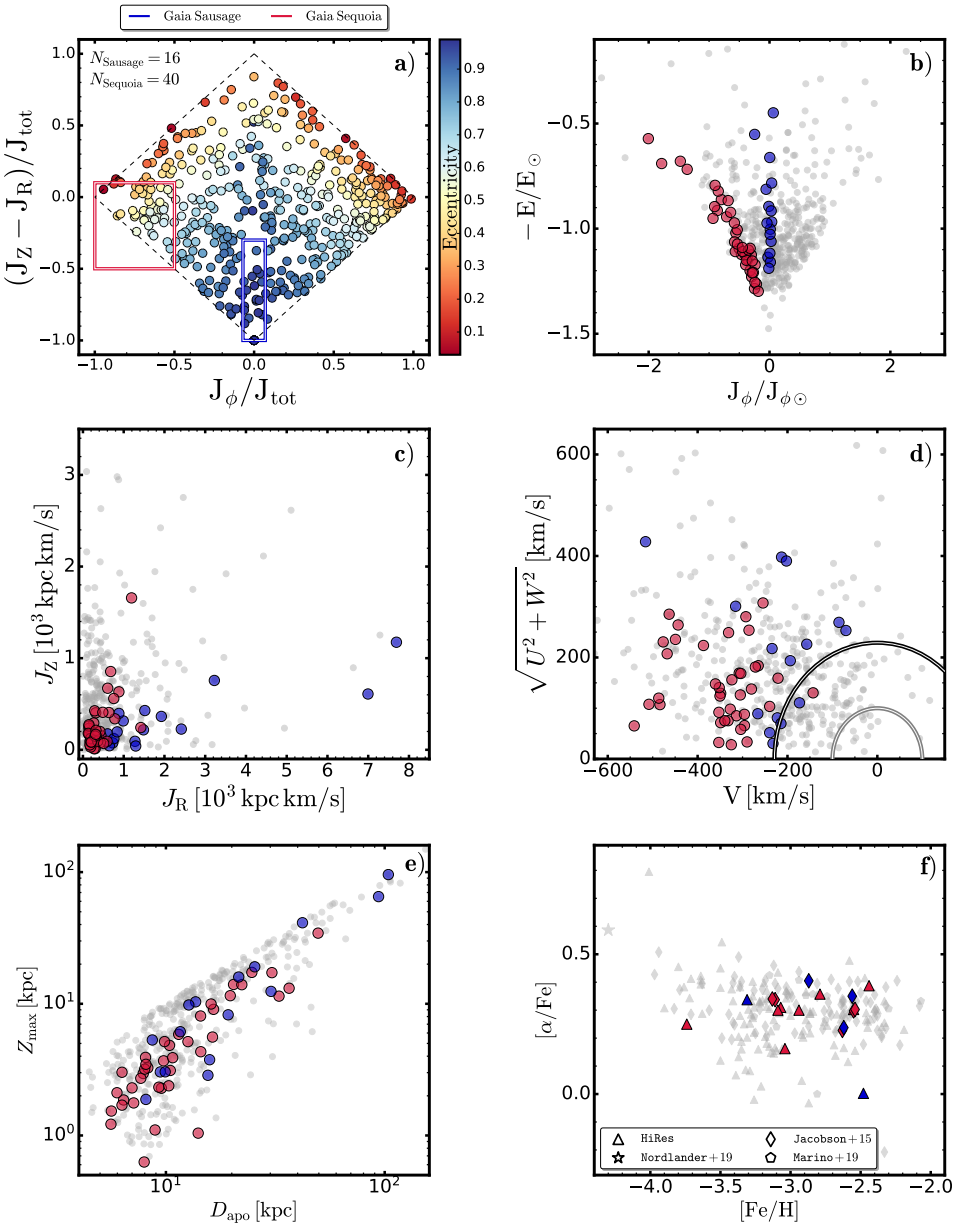

Figure 4.7. *Panel a)* Action map for all the stars in our sample. The red and blue boxes identify the *Gaia Sequoia* and *Gaia Sausage* loci, as determined in Myeong et al. (2019). Each star is colour coded according to its eccentricity. *Panel b)* Energy (E) against azimuthal action (J_ϕ) normalized by the solar values. Red and blue circles represent *Sequoia* and *Sausage* candidate members, respectively, while grey small points mark stars outside of the selection boxes in the action map. *Panel c) and d)* Vertical action (J_Z) against radial action (J_R) and Toomre diagram, respectively. The solid lines in panel d) show circular velocities of 100 and 239 km s^{-1}. *Panel e)* Maximum altitude ($Z_{\rm max}$) against apogalacticon distance ($D_{\rm apo}$). *Panel f)* Chemical abundances for all the stars in the `HiRes`, `Jacobson+15` and `Marino+19` samples, shown in grey shaded triangles, diamonds and pentagons, respectively. The star SMSS J160540.18–144323.1 (Nordlander et al., 2019), shown with a star-like symbol, is arbitrarily put at [Fe/H] = −4.3 for plotting purposes as it is much more metal-poor than any of the other stars plotted. *Gaia Sausage* and *Gaia Sequoia* member candidates are marked with blue and red symbols, respectively. The values of [α/Fe] have been computed as the mean of [Ca/Fe], [Mg/Fe], [TiI/Fe] and [TiII/Fe], whenever available.

590656.1) has [Fe/H] = −3.31 dex. Both stars come from the `HiRes` sample so that the abundance uncertainty is of order 0.1 (excluding any systematic uncertainties such as those arising from the neglect of 3D/NLTE effects). These values are quite consistent with the results of Monty et al. (2020). In that work, which uses dwarf stars, the lowest metallicity star plausibly associated with *Sequoia*, G082–023, has [Fe/H] = −3.59±0.10 while the most metal-poor star plausibly associated with *Sausage*, G064–012, has [Fe/H] = −3.55 ± 0.10 (Monty et al., 2020).
Finally, for the stars in the `HiRes`, `Jacobson+15` and `Marino+19` samples, we are able to investigate the chemical patterns of the likely accreted stars. Panel f) of Figure 4.7 shows [α/Fe] vs. [Fe/H] for the 218 stars for which [α/Fe] values are available. Specifically, [α/Fe] is computed as the unweighted mean of [Mg/Fe], [Ca/Fe], [TiI/Fe] and [TiII/Fe] where available[13]. The star SMSS J160540.18–144323.1 (Nordlander et al., 2019) has been arbitrarily plotted at a metallicity of [Fe/H]=–4.3 since otherwise it would be the only star with [Fe/H]<–5 in the panel. A visual inspection reveals that, with the single exception of SMSS J111201.72-221207.7, all the *Sequoia* and *Sausage* candidates are α-enhanced, and no other trend is evident. Specifically, in our sample of very metal-poor *Sequoia* and *Sausage* candidates, we see no evidence for a "knee" in the ([α/Fe], [Fe/H]) relation. The metallicity of the knee marks the abundance where [α/Fe] begins to decrease with increasing [Fe/H] as the nucleosynthetic contributions from SNe Ia become increasingly important. Our result, however, is not inconsistent with the results of Matsuno et al. (2019) and Monty et al. (2020) who find evidence of the presence of a knee at higher abundances than any of the *Sequoia* and *Sausage* candidates plotted in Fig. 4.7. For example, Monty et al. (2020) indicate that the knee in *Sequoia* is at [Fe/H] ≈ –2 while that for *Gaia Sausage* is at [Fe/H] ≈ –1.6, values significantly more metal-rich than any of the candidates in Fig. 4.7.

A very metal-weak component in the Thick Disk?

It has recently been shown (Sestito et al., 2019, 2020b; Di Matteo et al., 2020; Venn et al., 2020) that, in contrast to the commonly accepted view, a significant fraction (∼ 20%) of very low-metallicity stars resides in the MW disk rather than in the halo. Here we find a similar result: for the stars in our sample 102 out of 475 (∼ 21 %) exhibit disk-like dynamics in having orbits that are confined to within 3 kpc of the plane of the Milky Way.
The straightforward conclusion would be to propose these stars as supporting the existence of an extension to yet lower metallicities of the proposed Metal-Weak Thick-Disk (e.g., Chiba & Beers, 2000). However, a detailed analysis is required to discern the origin of these stars. Specifically, it is of key importance to understand if they are indeed disk-like stars, or if they are, for example, halo stars whose orbital plane happens to lie in the MW disk.

[13]We note that while detailed abundances, including those for neutron-capture elements, have been published for the `Jacobson+15` and `Marino+19` samples, this not the case for the `HiRes` sample (Yong et al., 2021). Consequently, we refrain from investigating other element ratios.

We therefore explore a number of orbital parameters to shed light on the nature of these stars. Specifically, Sales et al. (2009, and references therein) have shown how the orbital eccentricity can be used to probe the formation scenario of the Milky Way thick disk. Furthermore, as mentioned in the previous sections, the actions, and in particular the azimuthal action, provide important clues for the origin of a star. Here we couple these two orbital properties to disentangle the origin of the very low-metallicity stars residing in the MW disk.

As noted above, we classify as "disk" stars those with $|Z_{\rm max}| \leq 3$ kpc. This choice is made on the basis of the following considerations. First, Li & Zhao (2017) find that the (exponential) scale height of the MW thick disk is $z_0 = 0.9 \pm 0.1$ kpc; it then follows that the vast majority of the thick disk population should be found within ~3 scale heights, i.e., within $|Z_{\rm max}| = 3$ kpc.

Second, Figure 4.8 shows the eccentricity distribution for different values of the maximum vertical excursion, from 2 kpc to 8 kpc. For each panel, the yellow histogram (designated as "disk") shows the distribution of stars within N kpc, with $N = \{2, 3, 4, 5, 8\}$, while the grey shaded histogram (designated as "halo") represents stars with $|Z_{\rm max}| > N$ kpc. As is evident from the figure, for heights above the plane exceeding 3 kpc, i.e., panels c), d) and e), the eccentricity distributions for the stars above and below the cut-off height become increasingly similar. On the other hand, for a cutoff value of $|Z_{\rm max}| = 3$ kpc, an apparent difference is present in the sense the e-distribution for the low $|Z_{\rm max}|$ stars has a possible excess of intermediate eccentricity stars together with a possible narrow surfeit of stars with $e \approx 0.85$, which is also evident in panel a). However, application of both Kolmogorov-Smirnoff and Anderson-Darling tests (see, e.g. Scholz & Stephens, 1987) to compare the "disk" and "halo" distributions in panel b) revealed that the apparent differences are not statistically significant. Nonetheless, we adopt $|Z_{\rm max}| = 3$ kpc as the value of $|Z_{\rm max}|$ to discriminate between predominantly disk and predominantly halo populations. For completeness, we also note that if we choose $|Z_{\rm max}|$ cutoff values of 2.5 or 4 kpc and repeat the analysis discussed below, the outcomes are essentially unaltered.

Finally, the third reason for adopting a value of $|Z_{\rm max}| = 3$ kpc for the disk-like population is that it is consistent with Sestito et al. (2019, 2020b), allowing our results to be directly compared with theirs.

Looking again in detail at panel b) in Figure 4.8, we can see that the eccentricity distribution of the disk-like stars hints at the presence of two main groups. The first group has a relatively broad distribution peaking at $e \approx 0.55$ while the second population has a narrower distribution centred at $e \approx 0.85$. This interpretation is confirmed by the application of Gaussian Mixture Modeling to the e-distribution for the stars with $|Z_{\rm max}| \leq 3$ kpc, a process that does not require any choice as regards histogram bin size. The best-fit is for two Gaussians, one centred at $e = 0.52$ containing 80% of the population and with a standard deviation of 0.14. The second Gaussian is centred at $e = 0.89$ with a narrow σ of 0.03. The two Gaussians are overplotted with blue thick lines in panel b) of Fig. 4.8. We shall refer to these two groups as the "low-eccentricity" and "high-eccentricity" populations, respectively, and adopt $e = 0.75$ as the eccentricity to separate them.

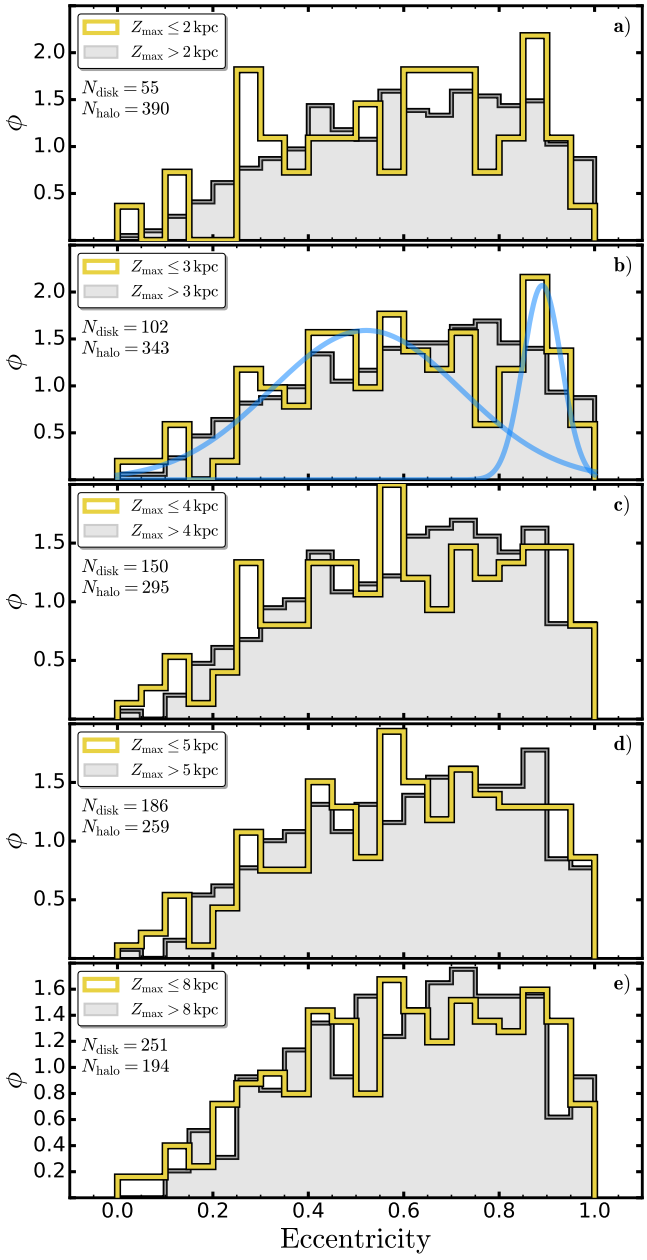

Figure 4.8. Eccentricity distribution of disk-like stars and halo-like stars for different choice of the cutoff $|Z_{max}|$, from 2 kpc, panel a), to 8 kpc, panel e). In each panel, the eccentricity distribution for stars within $|Z_{max}| \leq N$ kpc is shown with the yellow histogram, while stars with $|Z_{max}| > N$ kpc are indicated by the grey shaded histogram. Stars with $D_{apo} > 250$ kpc are not considered. Panel b) also shows, as blue continuous curves, the outcome of applying Gaussian mixture modeling to the set of e-values for the disk-like stars, i.e., without any binning.

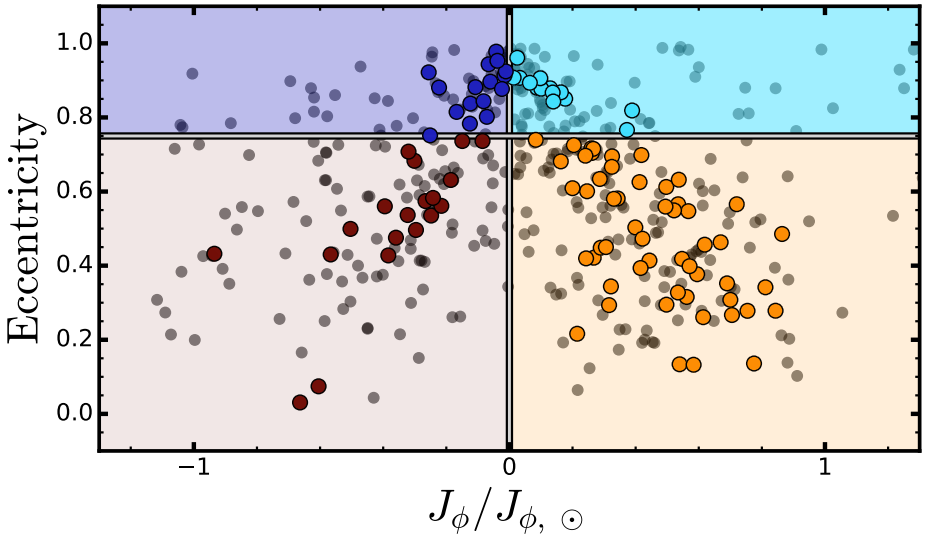

Figure 4.9. Eccentricity vs. azimuthal actions for all the stars in our sample (grey dots). Coloured filled points are for stars with $Z_{\rm max} \leq 3\,$kpc. Specifically, stars on retrograde orbits with eccentricity greater and lower than 0.75 are marked with dark-blue and dark-red circles, respectively. Prograde stars with eccentricity greater and lower than 0.75 are indicated with azure and orange circles.

We now employ J_ϕ to identify the motion of the disk stars as either prograde or retrograde. This is shown in Figure 4.9, where we mark retrograde high-e and low-e population stars with dark-blue and dark-red points, respectively, while prograde high-e and low-e group stars are indicated by azure and orange circles.[14] Overall we find 72 low-e stars (53 prograde and 19 retrograde) and 30 high-e stars (15 prograde and 15 retrograde).
We then analyzed the orbital parameters of each of these sub-groups of disk-star candidates. The results are shown in Figure 4.10. The distributions shown in panels a) – j) are kernel density distributions computed by adopting a Gaussian kernel with a fixed value of 0.4 for the bandwidth scaling parameter, while the top three panels show the action map, the Toomre diagram, and the E vs. J_ϕ plot, respectively. The disk candidates are marked with different colours, as defined in Figure 4.9.

Low-eccentricity stars

In panel a) of Figure 4.10, it is interesting to see that the eccentricity distributions of the prograde and retrograde high-e groups are almost identical, while, conversely, there are hints of a difference in the corresponding distributions for the low-e stars. Specifically, the prograde low-e stars (orange line) have a broader

[14] The colours are chosen consistently with the colour bar in Figure 4.7, so that high eccentricity stars are identified by blue-ish colours, while red-ish colours indicate low eccentricity stars.

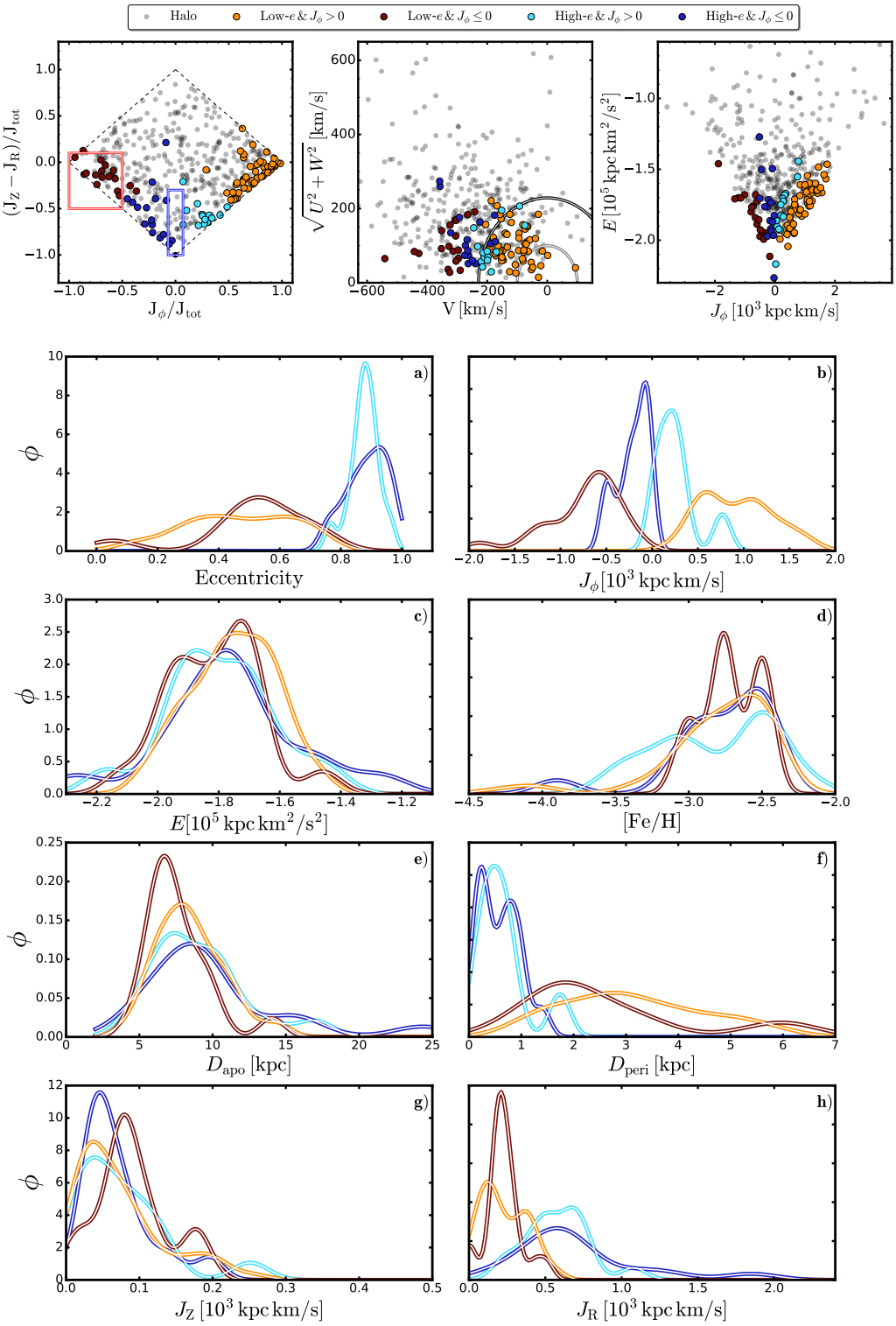

Figure 4.10. *Top panels.* Action map, Toomre diagram and energy vs. angular momentum for the stars with $|Z_{max}| \leq 3$ kpc. The colours are the same as illustrated in Figure 4.9. *Panels a) - h).* Kernel density function of the orbital parameters of the identified four groups of disk stars.

distribution while the retrograde low-e stars (red line) have a narrower distribution peaking at $e \sim 0.5$-0.6. Together these e-distributions are quite consistent with the theoretical results in Sales et al. (2009), particularly as regards the e-distributions in the top-left panel of their Figure 3 (Sales et al., 2009). In that context the retrograde low-e stars can be interpreted as an accreted population, while the prograde low-e stars are likely "in-situ", i.e., born within the thick-disk of the Galaxy.

To support this interpretation we consider again the action map, here shown in the upper-left of Figure 4.10 with the $|Z_{\rm max}| \leq 3$ kpc stars identified. It is evident from this panel that the majority of the retrograde low-e stars fall within the locus defining the *Gaia Sequoia* accretion event, consistent with these stars having an accretion origin. Comparing the corresponding panels in Figures 4.7 and 4.10 for the Toomre diagram and the Energy (E) against azimuthal action (J_ϕ) diagram, respectively, confirms the connection.

Regarding the prograde low-e stars, a substantial number of these fall in the region of the Toomre diagram usually restricted to disk stars; their rotation velocities lag that of the Sun by relatively small amounts, less than 100 km s^{-1} in some cases. We therefore conclude that the prograde low-e stars define a *very metal-weak* component to the Galaxy's thick disk. This conclusion is supported by the eccentricity distribution of the stars, which agrees well with the eccentricity distributions for (more metal-rich) thick-disk stars shown in Li & Zhao (2017, their Figure 12 and 14).

These 53 low-e, low $Z_{\rm max}$ prograde stars represent $\sim$ 11% of our total sample. Of these 53, 6 are included in the high-dispersion data sets and the [α/Fe] versus [Fe/H] for these stars is shown in Figure 4.11. Four of the 19 low-e, low $Z_{\rm max}$ retrograde stars are also included on the plot along with the remainder of the stars in the high-dispersion data sets. For completeness as regards the [Fe/H] distributions of the samples, we also show in the upper part of the figure the [Fe/H] values for the remainder of the prograde and retrograde low-e, low $Z_{\rm max}$ samples. Detailed abundance information, such as [α/Fe], is not available for these stars that arise from the `LowRes` sample. Further, in order to avoid any potential systematic effects, we have chosen not to plot the [α/Fe] values for the 3 low-e, low $Z_{\rm max}$ `Sestito+19` sample stars in Figure 4.11. The stars are BD+44 493 ([Fe/H] = –4.30), 2MASS J18082002-5104378 ([Fe/H] = –4.07) and LAMOST J125346.09+075343.1 ([Fe/H] = –4.02) and all 3 have prograde orbits. The [Fe/H] values for these stars are taken from Table 1 of Sestito et al. (2019).

It is evident from the figure that, though the sample is very limited, the four retrograde low-e stars show no obvious difference in location in this plane from the remainder of the (halo dominated) sample with high-dispersion abundance analyses. The location of the six prograde low-e stars, however, is intriguing despite the small numbers. It appears that the mean [α/Fe] for these stars is lower than that for the full sample by perhaps 0.15, and two of the stars, namely SMSS J230525.31-213807.0 which has [Fe/H] = –3.26 and which is also known as HE 2302-2154a, and SMSS J232121.57-160505.4 ([Fe/H] = –2.87, HE 2318-1621), are among the small number (of order a dozen in total) that have [α/Fe] < 0.1 in

the high-dispersion samples. Such α-poor stars, also referred to as "Fe-enhanced" stars (e.g. Cayrel et al., 2004; Yong et al., 2013; Jacobson et al., 2015), may reflect formation from gas enriched in SNe Ia nucleosynthetic products that, if valid, may have implications for the epoch at which these stars settled into, or formed in, the thick disk (see also Sestito et al., 2019, 2020b; Di Matteo et al., 2020). However, we consider further discussion of the element abundance distributions in these stars beyond the scope of the present paper.

The overall [Fe/H] distribution of the retrograde and prograde stars as inferred from Figure 4.11 is similar to that for the full sample. The star with the lowest combination of metallicity and eccentricity in our sample of prograde, low $Z_{\rm max}$ stars is SMSS J190836.24–401623.5 that has [Fe/H] = –3.29 ± 0.10 and for which we find e = 0.29 and a high V velocity of –21 km s^{-1}. We also note that the orbital parameters derived here for the UMP star 2MASS J1808002–5104378, which is included in our `Sestito+19` data set, are very similar to those found in Sestito et al. (2019). Specifically we find for this star e = 0.13 and V = –29 km s^{-1}, while Sestito et al. (2019) list values of 0.09 and –45 km s^{-1}, respectively. Moreover, as noted by Sestito et al. (2019), the "Caffau-star" (Caffau et al., 2011), which is an apparently carbon normal (i.e., [C/Fe] < 0.7) dwarf (and therefore not included in our sample) with [Fe/H] ≈ –5.0, and which is the star with the lowest total metal abundance known to date, is a further example of an ultra-low metallicity star with a disk-like orbit. Sestito et al. (2019) determine that this star has a prograde orbit with e = 0.12 that is confined to the Galactic plane, and which has a high V velocity of –24 km s^{-1}. We agree with the suggestion of Sestito et al. (2019) that these stars may have formed in a gas-rich "building-blocks" of the proto-MW disk. The origin of these stars is also discussed within the context of the theoretical simulations presented in Sestito et al. (2020a). The simulations reveal the ubiquitous presence of populations of low-metallicity stars confined to the disk-plane. In particular, the simulations show that the prograde planar population is accreted during the assembly phase of the disk, consistent with our interpretation and that of Sestito et al. (2019).

Panels b)-h) of Figure 4.10 show the kernel density distributions of the other orbital parameters. These distributions do not exhibit clear differences between prograde and retrograde low-e stars, with the possible exception of $D_{\rm apo}$, in panel e), and $D_{\rm peri}$, in panel f), which mimic the differences in the eccentricity distribution evident in panel a).

We conclude that the low $Z_{\rm max}$ prograde and retrograde low-e stars likely have different origins, with the former possibly being formed *in-situ* in the Galaxy's thick disk while the latter are likely accreted from disrupted Milky Way satellites. Whether these latter stars belong to the *Sequoia* main remnant, or its higher-energy tails (Thamnos 1 and 2, Koppelman et al., 2019) is beyond the scope of the present work, although, as panel a) of Figure 4.10 shows, most fall within the region defining *Sequoia* stars.

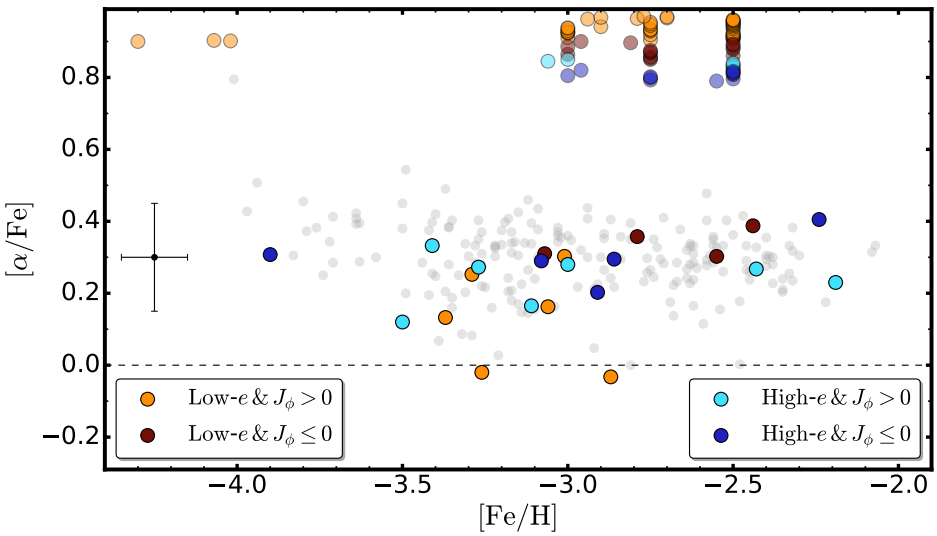

Figure 4.11. [α/Fe] vs. [Fe/H] for the stars in the `HiRes`, `Jacobson+15` and `Marino+19` samples. Low-e, low-$Z_{\rm max}$ prograde and retrograde stars are marked with orange and dark-red points, respectively, while high-e, low-$Z_{\rm max}$ prograde and retrograde stars are shown with azure and dark-blue colours. Stars from the `LowRes` sample, for which only [Fe/H] values are available, are arbitrarily placed between [α/Fe]=0.79 and [α/Fe]=0.95 on the y-axis. This is to allow an assessment of the [Fe/H] distributions of the samples. The (non-physical) range of [α/Fe] values is needed to separate the points as the [Fe/H] values in the `LowRes` sample are generally quantized at 0.25 dex values. This also applies to the 3 orange points with [Fe/H] $\leq$ –4.0 that are from the `Sestito+19` dataset. For the stars with high dispersion spectroscopic abundances, the typical uncertainty in [Fe/H] is ±0.1 dex and ±0.15 dex in [α/Fe], as indicated by the black point on the left side. For the stars from the `LowRes` sample the typical uncertainty in [Fe/H] is ±0.3 dex. The dashed line indicates [α/Fe] = 0.

High-eccentricity stars

The interpretation of the 30 low $Z_{\rm max}$, high-e stars in our sample is less straightforward, since, as the panels of Figure 4.10 reveal, nearly all their orbital parameters show similar distributions for the prograde and retrograde stars, with the only exception being the azimuthal action (by construction). We note first that the only mechanism able to explain, at least qualitatively, the occurrence of disk stars with high-eccentricity orbits, is the heating mechanism discussed in Sales et al. (2009, e.g., Figure 3). Some of the stars in this sub-sample could therefore be disk stars heated by accretion events. Alternatively, some could simply be halo stars that happen to have orbital planes that lie close to the Milky Way disk plane. However, even though these high-e stars do not satisfy the *Gaia Sausage* Myeong et al. (2019) membership criteria, we find that many qualitatively share its typical orbital properties: high-eccentricity, low or no angular momentum, small Galac-

tic pericenters, Galactic apocenters as great as ~ 20-25 kpc and strong radial motions. We therefore argue that at least some stars could be associated with the *Sausage* accretion event. In support of this conjecture, we note that they are consistent with the Yuan et al. (2020) classification for *Gaia Sausage* stars, both in the action map locus, and in the energy regime.
Myeong et al. (2019) suggest that the *Sausage* accretion event was an almost head-on collision with the Milky Way. Such an event generates orbits with small perigalacticons that are strongly radial, eccentric, and with roughly equal numbers of prograde and retrograde stars. These are the properties that we see for our low $Z_{\rm max}$, high-e stars and it therefore seems reasonable to conclude that many of our low $Z_{\rm max}$, high-e stars have their origin in the *Sausage* accretion event.
For seven of the 15 prograde high-e, low $Z_{\rm max}$ stars, detailed abundances are available from our high-dispersion data sets. The [α/Fe] abundance ratios are shown as a function of [Fe/H] in Figure 4.11. The corresponding data for 5 of the 15 retrograde stars are also shown in the figure. The [Fe/H] values for the remainder of the stars in these groups are shown across the top of the plot. The numbers of stars with high-dispersion analyses in both high-e, low $Z_{\rm max}$ sub-samples are small, but there does not appear to be any obvious difference between them and the distribution of the full sample.

The candidate unbound stars

As introduced in Section 4.1.4, we find 30 stars with potentially unbound orbits, defined by having an apparent $D_{\rm apo} \geq 250$ kpc[15]. One star, HE 0020–1741, comes from our subset of the `Sestito+19` sample. Sestito et al. (2019) list $D_{\rm apo} \approx 296$ kpc for this star, the largest value in their determinations, while in the Mackereth & Bovy (2018) catalogue[16] the star is classified as unbound in accord with our result. The remaining 29 stars are from the SkyMapper samples.
To test the sensitivity of the results to the adopted potential we investigated the orbits of these stars using a different choice of the potential, namely the `GALPY` *MWPotential2014*. The calculations reveal that all 30 stars again have $D_{\rm apo} >$ 250 kpc. In addition, for this choice of potential, we find that the star SMSS J044419.01–111851.2 may also be unbound; it is on a loosely bound orbit in the `McMillan2017` potential with an apogalacticon distance of ~ 200 kpc.
In order to shed light on the nature of these stars we have investigated the distributions of the 500 random realizations of the orbits, together with the corresponding orbital parameters, such as the apparent apo/peri-galacticon distance ratio ($D_{\rm apo}/D_{\rm peri}$), the energy (E) and the azimuthal action (J_ϕ). Panels a) – d) of Figure 4.12 show the information for the 30 potentially unbound stars.
Since the direct orbit integration for the observed positions and velocities resulted in unbound orbits (apparent $D_{\rm apo} > 250$ kpc), it would be incorrect to

[15] For a genuine unbound orbit $D_{\rm apo} = \infty$. The term "apparent $D_{\rm apo}$" employed here for the potentially unbound stars represents the Galactocentric radius at either the –2 Gyr or +2 Gyr endpoint of the orbit integration, whichever is larger.

[16] `https://vizier.u-strasbg.fr/viz-bin/VizieR?-source=I/348`

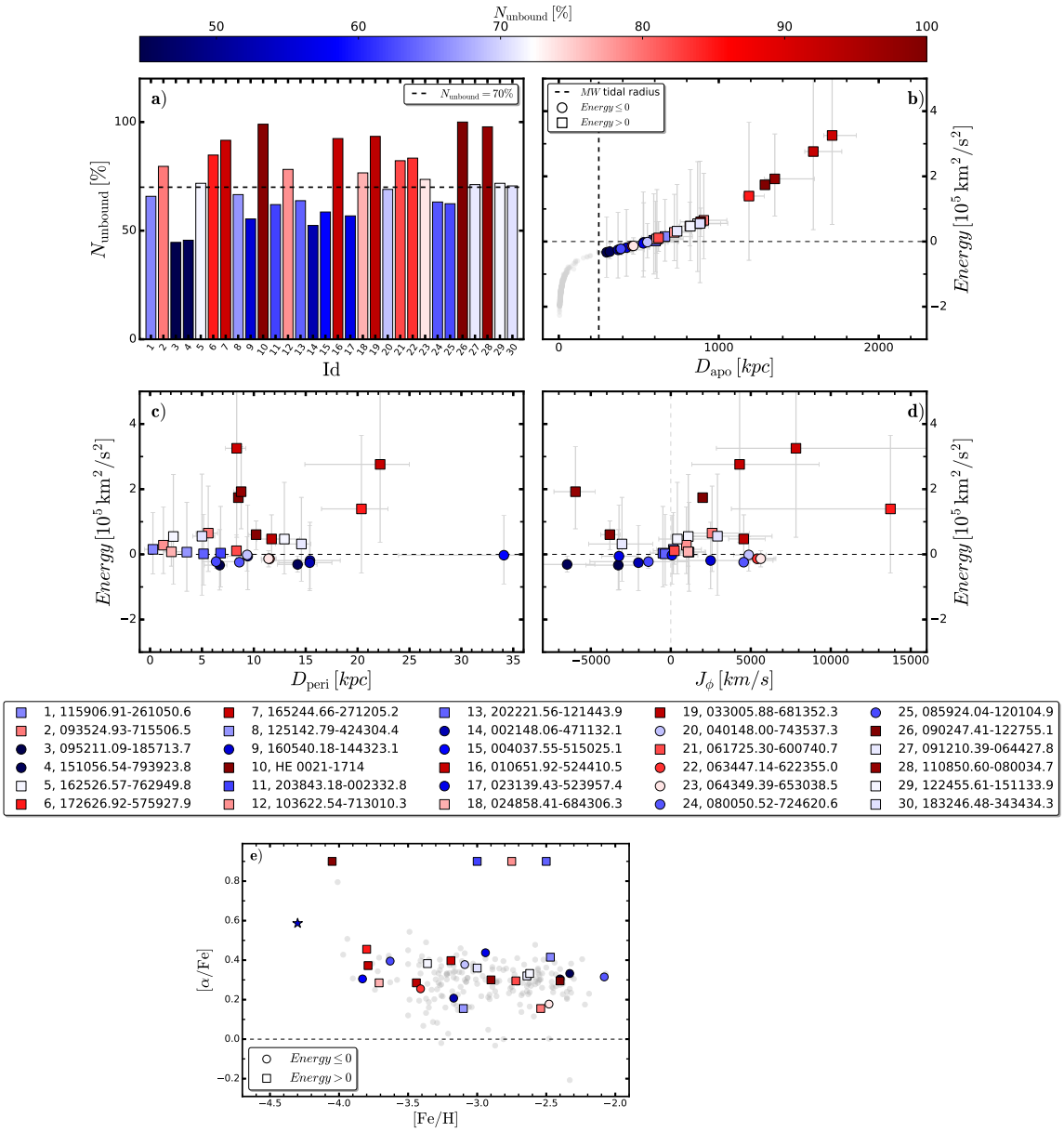

Figure 4.12. *Panel a).* Barplot of the percentage of unbound realizations for the 35 stars with apparent $D_{\rm apo} \geq 250$ kpc. The names of the stars are listed in the panel below panels c) and d). Each bar is colour-coded according to the percentage of $N_{\rm unbound}$, as shown in the top colour bar. *Panel b).* Energy against apparent apogalacticon distance. Filled circles indicate stars with negative energy, while filled squares mark those with positive energy. The black vertical dashed line marks the Milky Way tidal radius (250 kpc), while the stars with $D_{\rm apo} < 250$ kpc are shown as grey shaded points. *Panel c)* and *Panel d)* show the Energy against the perigalacticon distance ($D_{\rm peri}$) and the Energy against the azimuthal action (J_ϕ). Individual error bars are shown in panels b), c) and d). *Panel e).* [α/Fe] vs. [Fe/H] for the candidate unbound stars that occur in the `HiRes`, `Jacobson+15` and `Marino+19` samples. As in Fig. 4.7, the star SMSS J160540.18–144323.2 (Nordlander et al., 2019) is shown with a star-like symbol placed at [Fe/H]=–4.3. As for the other panels, filled circles indicate stars with negative energy, while filled squares mark those with positive energy. The remainder of the stars in our high-dispersion samples are shown as light-grey circles. The metallicity estimates for the 4 stars not in our high dispersion samples are plotted at the top of the panel.

adopt the uncertainties as defined in Section 4.1.3 for all parameters. Specifically, for these stars we opt not to give uncertainties for the apparent $D_{\rm apo}$, e, $Z_{\rm max}$ and $J_{\rm R}$ values since the medians for the 500 realizations and the "observed" values, i.e., the values from the observed properties, differ significantly. On the other hand, for the remaining orbital parameters, namely $D_{\rm peri}$, E, J_ϕ, $J_{\rm Z}$, and the U, V, W velocities, the median values are consistent with the observed ones, and therefore we compute the uncertainties in these quantities as before, from the difference between the 16$^{\rm th}$ and the 84$^{\rm th}$ percentile of the PDFs.
Panel a) of Figure 4.12 shows the fraction of unbound realizations for each star. Each bar is colour-coded according to its percentage, from a minimum of 42.6% for SMSS J095211.09–185713.7 (number 3 in the identification panel in the Figure 4.12) to a maximum of 100% for SMSS J090247.41–122755.1 (#26). White- and reddish colour tones indicate stars with a fraction of unbound orbits greater than 70%, which we take as a conservative value to identify likely unbound stars. Blueish colours represent stars with a lower unbound fraction. A visual inspection of panel b) reveals that nearly all stars with $N_{\rm unbound} > 70\%$ exhibit positive energies, thus confirming that they are likely to be escaping from the Galaxy. Overall, we find that 17 stars have $N_{\rm unbound} > 70\%$, and of these 15 have $E > 0$ (the two stars with $N_{\rm unbound} > 70\%$ but $E \leq 0$ are numbers 22 and 23 in Figure 4.12). Panel b) also shows that four stars (numbers 1, 8, 11, 13) have a positive energy, but with $N_{\rm unbound}$ slightly below 70%. We consider these stars as also likely unbound, bringing the total number of candidate unbound stars to 21, or 4.4% of the total sample. We note in particular that aside from HE 0020–1741 (#10), three further stars in our set of 21 unbound candidates are also classified as unbound in the Mackereth & Bovy (2018) catalogue. These are the bright r-process element enhanced star SMSS J203843.18–002332.8 (#11, RAVE J203843.2–002333, Placco et al., 2017), together with SMSS J183246.48–343434.3 (#30) and SMSS J202221.56–121443.9 (#13). On the other hand, one of our stars, SMSS J103622.54-713010.3 (#12), has a bound orbit in the Mackereth & Bovy (2018) catalogue. There are no stars in common with the list of 20 'clean' high-velocity star candidates with unbound probability exceeding 70% in Marchetti et al. (2019).
The remaining nine stars have negative (bound) energies, although the values are consistent with zero within their uncertainties. Their classification is thus uncertain as they could be unbound or on loosely bound orbits. None are found in the Mackereth & Bovy (2018) catalogue.
We now speculate as to the origin of these stars, proposing three possible physical mechanisms that could provide each star with sufficient energy to escape the Galaxy.

- A star in a close binary can be expelled from the Galactic Centre via an interaction with the central black hole. The clearest example of this process is the star S5-HVS1 discussed in Koposov et al. (2020).

- A star can acquire high velocity (of order of the binary's pre-SNe explosion orbital velocity) from being in a binary when the companion explodes as a supernova (e.g., Eldridge et al., 2011).

- A star can acquire energy as part of a gravitational interaction involving the merger of a dwarf galaxy with the Milky Way (e.g., Abadi et al., 2009).

For the first mechanism to happen, the star has to have an origin close to the Galactic Centre, which means that its $D_{\rm peri}$ should be near zero. However, as panel c) of Figure 4.12 shows, only one star (SMSS J115906.91–261050.6, #1, $D_{\rm peri}$ = 0.26 kpc) has a perigalacticon distance within 1 kpc of the Galactic Centre, while the remainder of the candidates have $D_{\rm peri} > 1$ kpc. This suggests that the first possibility is unlikely, particularly when it is recognised that all the stars in the sample are giants and therefore unlikely to be in a sufficiently compact binary.
The second mechanism also seems unlikely because the unbound stars are all giants with, as a consequence, relatively large stellar radii. As a result, the separation between the components of any pre-SNe binary containing the star is unlikely to be sufficiently small that the orbital velocity, which underlies the "kick velocity" provided when the companion becomes a SNe, would be sufficiently high that the liberated star is no longer bound to the Galaxy. Furthermore, at least for those stars where high dispersion spectra are available, there is no evidence of any "pollution" from the SNe event.
This leaves us with the third possible origin, which is plausible given that it is generally accepted that the formation of the Galactic halo is driven by the accretion and tidal disruption of dwarf galaxies (e.g., the recent discovery of remnants of accretion events: Helmi et al., 2018; Belokurov et al., 2018; Koppelman et al., 2019; Myeong et al., 2019). Specifically, we postulate that our set of unbound stars originated in the outskirts of dwarf galaxies that were accreted by the Milky Way, gaining energy from the gravitational interaction that resulted in the disruption of the dwarfs. Given the relatively low metallicities of the unbound stars, which range from –4 (or less) to –2 in [Fe/H] (see the lowermost panel of Fig. 4.12), we speculate that the disrupted systems were relatively low-mass, low-metallicity systems.In this context, we note that 16 out of 21 stars have prograde orbits, while 5 have negative J_ϕ and thus a retrograde orbit. This likely indicates that multiple accretion events may be involved. However, it is necessary to keep in mind that the timescale for an unbound star to reach the virial radius from the inner regions of the Galaxy is $\sim$ 1 Gyr. Consequently, the gravitational interactions that generated the unbound stars in our sample likely occurred relatively recently, which may argue against the proposed "origin in accretion events" scenario. Detailed evaluation of the orbits of the unbound stars, individually and collectively, is required to assess the situation and to investigate their origins(s). The metallicities of other candidate unbound stars, such as those in Marchetti et al. (2019) will also provide important input (e.g., Hawkins & Wyse, 2018).
We note also that there is a fourth possibility, that uncertainties in the analysis lead to incorrect orbital parameters. For example, if the distance to the star used in calculating the orbit were overestimated, this could result in unbound or nearly-bound status. This is the likely explanation for the discrepancy concerning the star SMSS J103622.54–713010.3 (unbound here, bound in the Mackereth & Bovy (2018) catalogue) as our adopted distance is more than a factor of two

larger than the Bailer-Jones et al. (2018) distance. The availability of improved parallaxes and stellar parameters from the forthcoming Gaia EDR3 and DR3 releases will help alleviate these discrepancies. As another possibility, we note that the total mass of the Galaxy may in fact be larger than that used in our modeling. If this is the case then, although on high-energy orbits, the stars would remain bound (e.g., Monari et al., 2018; Fritz et al., 2020).
Panel e) of Figure 4.12 shows the [α/Fe] vs. [Fe/H] relation for 26 of the 30 candidate unbound stars that are in our high-dispersion samples, together with the values for the remainder of the stars from the high dispersion samples. The estimates of [Fe/H] for the remaining 4 stars, from the `LowRes` data set, are shown at the top of the panel. It is evident from this panel that candidate unbound stars are not distinguished from the full sample as regards the overall metallicity distribution or the [α/Fe] distribution.

4.1.6 Summary and conclusions

In this work we have analyzed a sample of 475 very metal-poor giant stars, most of which have originated from the SkyMapper search for the most metal-poor stars in our Galaxy (Da Costa et al., 2019). The data set covers a metallicity range of almost five dex ($-6.5 <$ [Fe/H] ≤ -2), and together with the relatively large number of stars, makes it ideal to investigate the kinematics, and ultimately the origin, of these very rare and important objects together with the implications for the formation of the Milky Way.
We first exploited the action map for our sample together with the classification criteria of Myeong et al. (2019) to identify candidate members of the *Gaia Sausage* and *Gaia Sequoia* accretion events. We find 16 stars dynamically consistent with *Gaia Sausage* and 40 with *Gaia Sequoia*. While we cannot be certain all candidates are in fact associated with these entities, the lowest metallicities ([Fe/H] = –3.31 for *Gaia Sausage* and –3.74 for *Gaia Sequoia*) are quite consistent with the findings of Monty et al. (2020). With a single exception, all our candidate *Gaia Sausage* and *Gaia Sequoia* stars for which we have high-dispersion spectra are α-rich, similar to the general halo population. This is again consistent with the results of Monty et al. (2020).
The recent work of Sestito et al. (2019, 2020b), Di Matteo et al. (2020) and Venn et al. (2020) has revealed an unexpected significant population of very low-metallicity stars residing in the plane of the Galaxy. We find a similar result in that ~ 21 % of the stars in our sample have orbits that remain confined to within 3 kpc of the Galactic plane. Moreover, these stars show a different eccentricity distribution compared to the stars with larger $|Z_{\rm max}|$ values, pointing towards a different origin and/or evolution compared to the (halo dominated) bulk of the sample.
Our detailed analysis of these low $|Z_{\rm max}|$ stars reveals four sub-populations as regards orbit eccentricity and prograde or retrograde motion. Of particular interest are the stars with relatively low eccentricities ($e < 0.75$, median ≈ 0.5) and prograde velocities. These stars, which make up ~ 11% of the total sample, have metallicities at least as low as [Fe/H] = –4.3 and are best interpreted as reveal-

ing the existence of a very low-metallicity tail to the Galaxy's metal-weak thick disk population (e.g. Chiba & Beers, 2000). On the other hand, the low-e retrograde stars that have $|Z_{\rm max}| \leq 3$ kpc ($\sim$ 4% of the sample) are most likely an accreted population. We also find a population ($\sim$ 6% of the sample) of low $|Z_{\rm max}|$ stars that have high eccentricity orbits (median $\approx$ 0.88) with small pericenters and which are split equally between prograde and retrograde motion. It seems likely that many of these stars might be associated with the *Gaia Sausage* accretion event (Myeong et al., 2019; Yuan et al., 2020; Koppelman et al., 2019). With the possible exception of the low-e, low $|Z_{\rm max}|$ prograde stars that may have a somewhat lower mean [α/Fe] abundance ratio, none of the four sub-populations with low $|Z_{\rm max}|$ are distinguished, as regards [α/Fe] or [Fe/H], from the full set of stars for which high-dispersion based analyses are available.
Finally, we find that a small fraction of our sample (21 stars, $\sim$ 4.4%) are likely to be escaping from the Galaxy, i.e., are on orbits that are not bound. The [Fe/H] and [α/Fe] distributions of these stars are not distinguished from those for the full sample; for example, their metallicities are spread from –4 (or less) to –2 in [Fe/H]. Our preferred interpretation for these stars is that they have acquired sufficient energy to escape from the Galaxy via the gravitational interaction that occurs when infalling dwarf galaxies are tidally disrupted by the Milky Way.

Data availability

The data underlying this article are available in the article and in its online supplementary material.

4.1.7 Clustering analysis

As an alternative approach, we analyzed our sample of stars exploiting the `scikit-learn` Spectral clustering algorithm (Pedregosa et al., 2011). This analysis has the advantage of being almost completely independent from our choices (i.e., limiting $|Z_{\rm max}|$, prograde/retrogade etc.), while on the other hand has the limitations of being a "blind" analysis. Specifically, in order for the result to be trustworthy, we should have knowledge of how the selection biases (e.g., bright stars in the solar neighbourhood, uncrowded stellar environments and the other effects discussed in Da Costa et al. (2019)) propagate into the cluster choices. Unfortunately, it is not possible to quantify these biases.
Nonetheless, we believe that it is worth exploring this fully independent classification approach. The clustering has been performed in the 4-dimensional space with the three actions and the eccentricity ($J_{\rm R}$, J_ϕ, $J_{\rm Z}$, e) with the following input parameters: `affinity=nearest_neighbors` and `assign_labels=discretize`.
Figure 4.13 shows the results of the clustering analysis. In the top three panels we show the same top three panels as for Figure 4.10 but now for the 8 identified clusters. We note that group # 1 (red markers with coordinates $(0,-1)$ in the action map) is the group of unbound stars, and therefore is not investigated fur-

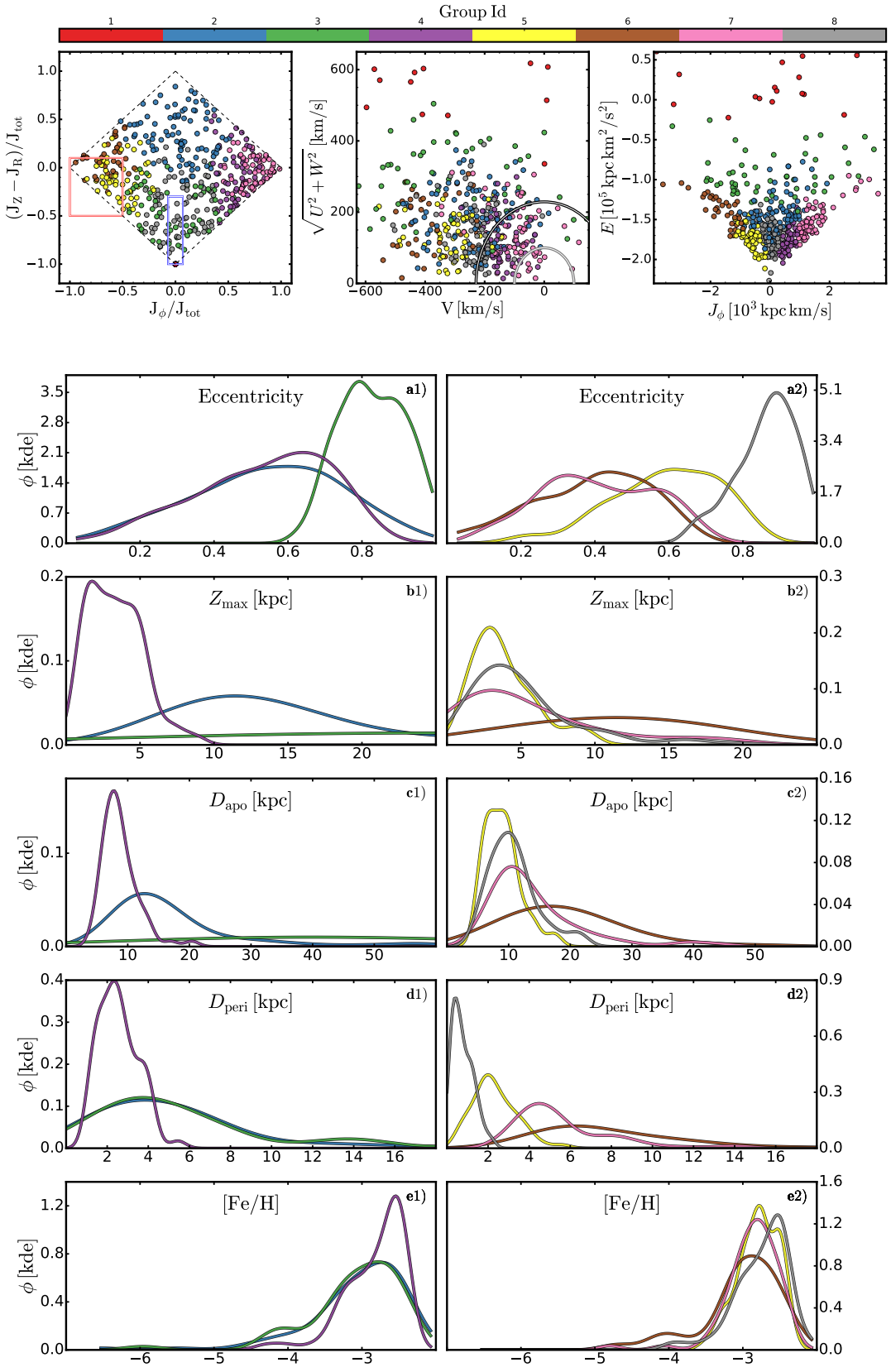

Figure 4.13. *Top row.* Same as the top row Figure 4.10 except stars are colour-coded by group. The group colours are identified at the top of the panels. *Panels a1)-e2).* Kernel density distributions of the computed orbital parameters for the groups identified by the clustering algorithm. In the panels with suffix 1 we represent the distributions for groups 2 to 4, while panels with suffix 2 show groups 5-8. The kernel density estimates of the orbital parameters for group 1 (G1) are not shown for scaling reasons.

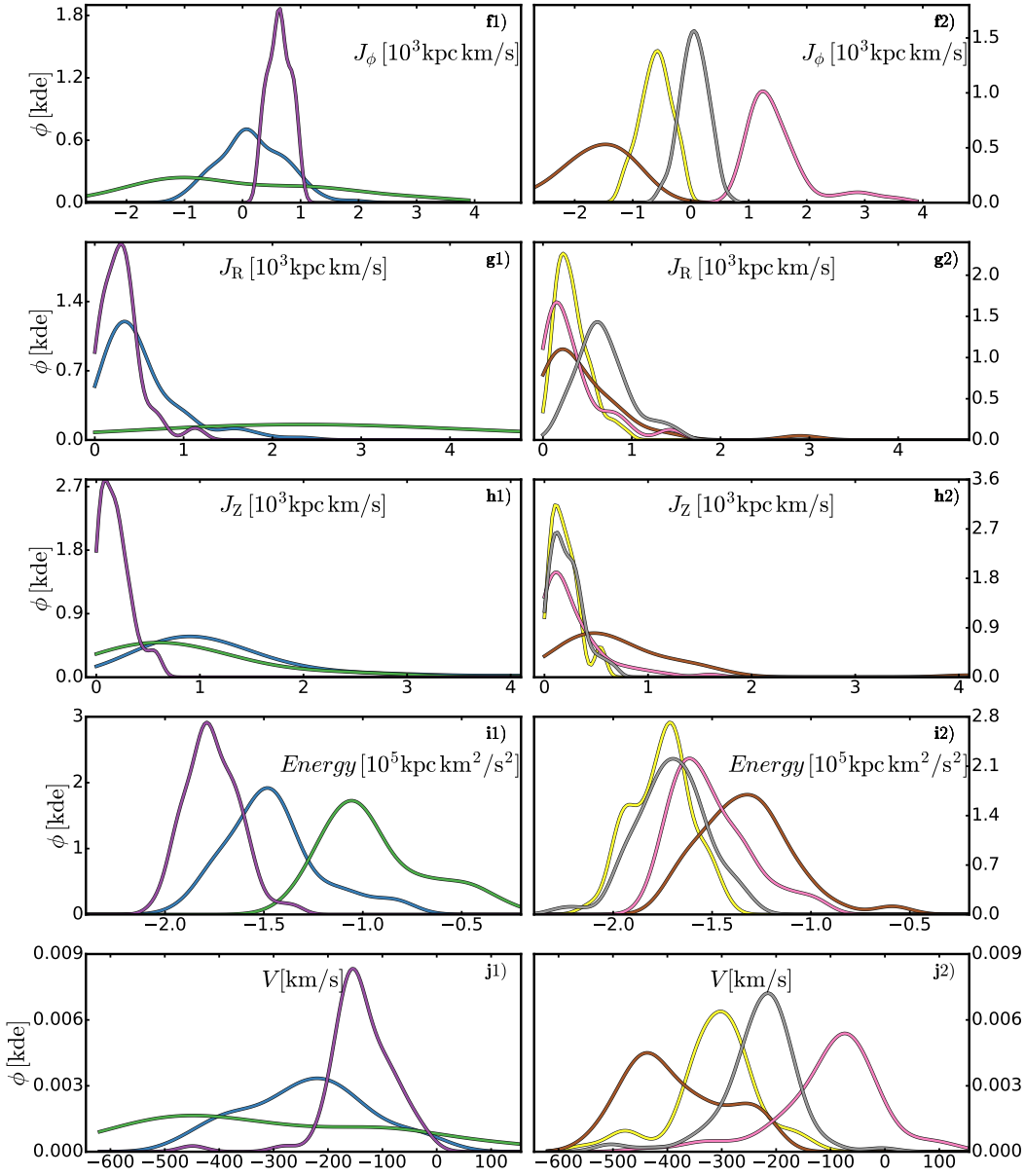

Figure 4.14. *Panels f1)-j2).* Same as panels a1)-e2) of Figure 4.13.

ther in the lower panels[17]. Panels a1)–e2) in Figure 4.13 and panels f1) to j2) in Figure 4.14 then show the kernel density distributions of different orbital parameters for each sub-group, with groups 2–4 in the left panels and groups 5–8 in the right panels. A comparison of Figures 4.13 and 4.14 with Figure 4.10 suggests the following.

- group # 1 (G1, red markers, 28 stars) is composed of stars with energies consistent or greater than 0, visible in the top-right panel of Figure 4.13. These stars have apparent apogalacticon distances larger than the Milky Way virial radius, i.e., 250 kpc. They are characterized by large values of the radial action, J_R, which translates in $J_\phi/J_{tot} \sim 0$ and $(J_Z - J_R)/J_{tot} \sim -1$. Overall, we find that 28 stars are grouped in G1. All of these stars are in the sub-sample discussed in Section 4.1.5, although two stars in the Section 4.1.5 sub-sample, namely SMSS J095211.09–185713.7 and SMSS J002148.06–471132.1, are not classified as G1 stars, despite having apparent D_{apo} larger than 250 kpc. These two stars have negative (bound) energies and are classified by the clustering algorithm in Group #7 (pink points), which is composed of stars on loosely bound orbits. There is therefore essentially no discrepancy between the sub-sample discussed in Section 4.1.5 and the high-energy G1 stars identified by the clustering algorithm. We do not show the kernel density distributions of these stars in the subsequent panels for scaling reasons.

- group # 2 (G2, blue markers, 93 stars) are a combination of prograde and retrograde halo stars. We note that they span quite a wide energy range, but we find difficult to draw further conclusions. Presumably this group is made up of a mixture of in-situ and accreted halo stars.

- group # 3 (G3, green markers, 54 stars) is a mixture of prograde and retrograde stars on loosely bound orbits, that venture far from the Galactic plane.

- group # 4 (G4, purple markers, 61 stars) partially overlaps with low-e stars in all three of the top-panels of Figure 4.10. Furthermore, their eccentricity distribution peaks at $e \sim 0.4 - 0.6$, while most of them remain roughly confined within 5 kpc of the Galactic plane and 20 kpc from the Galactic centre. A possible interpretation would be to consider these stars as thick-disk stars. This hypothesis is also supported by the Toomre diagram in the top center panel of of Figure 4.13, where purple stars occupy a locus typical of thick-disk stars. By the comparison with Figure 4.10 we find a partial match of this group with the low-e prograde population (orange points), identified as candidate very metal-weak thick disk stars.

- group # 5 (G5, yellow markers, 53 stars) partially shares the location of the low-e and retrograde population (red dots in Figure 4.10) as well as partially

[17] For scaling reason some group #1 stars are not shown in the top three panels of Figure 4.13.

overlapping with the locus of the Sequoia remnants identified in Myeong et al. (2019). The eccentricity distribution peaks at about $e \sim 0.6$, and they are confined to the inner halo ($D_{\rm apo} \leq 10\,$kpc). Panel b1) of Figure 4.13 shows that $\sim 80\%$ of these stars are confined within 5 kpc from the Galactic plane. Most of them don't orbit further than 10 kpc from the Galactic centre. Comparing then the top-right panels of Figure 4.13 with Koppelman et al. (2019, bottom-right panel of their Figure 2), we see that G5 stars have a higher energy (in absolute values) than *Gaia Sequoia* stars, while their energy and their angular momentum suggest a possible association with the Thamnos 1/2 groups (Koppelman et al., 2019).

- group # 6 (G6, brown markers, 37 stars) is composed of stars with very retrograde and mildly-eccentric orbits that venture far from the Galactic plane and from the Galactic centre, with $Z_{\rm max}$ and $D_{\rm apo}$ peaking at ~15-20 kpc. These stars have energies that range from ~ -1 to ~ -1.7 [$10^5\,$kpc$\cdot$km$^2\,$s^{-2}]. This group is consistent with the identification of the *Gaia Sequoia* remnants in Koppelman et al. (2019).

- group # 7 (G7, pink markers, 67 stars) partially overlaps with G4 both in the action map and in the Toomre diagram, while it is well-defined in the Energy vs. J_ϕ-plane. Panel a2) of Figure 4.13 shows that the eccentrity distribution of these stars is double peaked, with the first peak at $e \sim 0.3$ and a second one at $e \sim 0.6$. Given the distribution of $D_{\rm apo}$ and $Z_{\rm max}$ it would seem that these stars are a mixture of halo and thick-disk stars, with lower binding energies than their G4 counterparts. As for G4, we note that there is a clear overlap between this group and the low-e prograde stars shown in Figure 4.10.

- group # 8 (G8, grey markers, 82 stars) share roughly the same location of the high-e both retrograde and prograde population (azure and navy dots in Figure 4.10) in all top three panels of Figure 4.13. Furthermore, the distribution of their orbital parameters nearly overlaps with those of the combined high-e prograde and retrograde populations. Their energy and angular momentum agrees with the *Gaia Sausage* definition in Yuan et al. (2020). We find particularly interesting the pericenter/apocenter distributions, whose analysis suggest that most of these stars move back and forth from the Galactic centre to the Galactic outskirts, always remaining within few kpc from the Galactic plane (~60% these stars are indeed confined within 5 kpc from the plane). Given the observed orbital properties, and in particular the perigalacticon distances as low as ~1 kpc, we speculate that such a remnant can be formed via a "head-on" accretion event, as in the *Sausage* progenitor (Myeong et al., 2019).

It is clear that the two different analyses (discussed here and in Section 4.1.5) reach qualitatively the same conclusions. First, we find solid evidence for the existence of a very metal-weak component in the Galactic thick disk. Further, from

the analysis of the orbital actions and by means of the action map, we have identified possible members of the *Gaia Sequoia* and *Gaia Sausage* accretion events. The analysis also suggests that the low $|Z_{max}|$, high-e population that is composed of stars with both prograde and retrograde orbits, may also be associated with the *Gaia Sausage* event. Both analyses also identify a consistent set of candidates that are likely not bound to the Galaxy.

4.1.8 Example orbits

In the following we show four typical orbits of Halo, very metal-weak thick disk, *Sequoia* and *Sausage* stars within our sample. Each orbit is colour coded according to the integration time, while the white dot represents the current position in the Galactocentric cartesian reference frame. As discussed in Section 4.1.3, each orbit has been integrated in a `McMillan2017` potential (McMillan, 2017) backward and forward in time for 2 Gyr. The actions have been computed with the Stäckel fudge method implemented in `GALPY`.

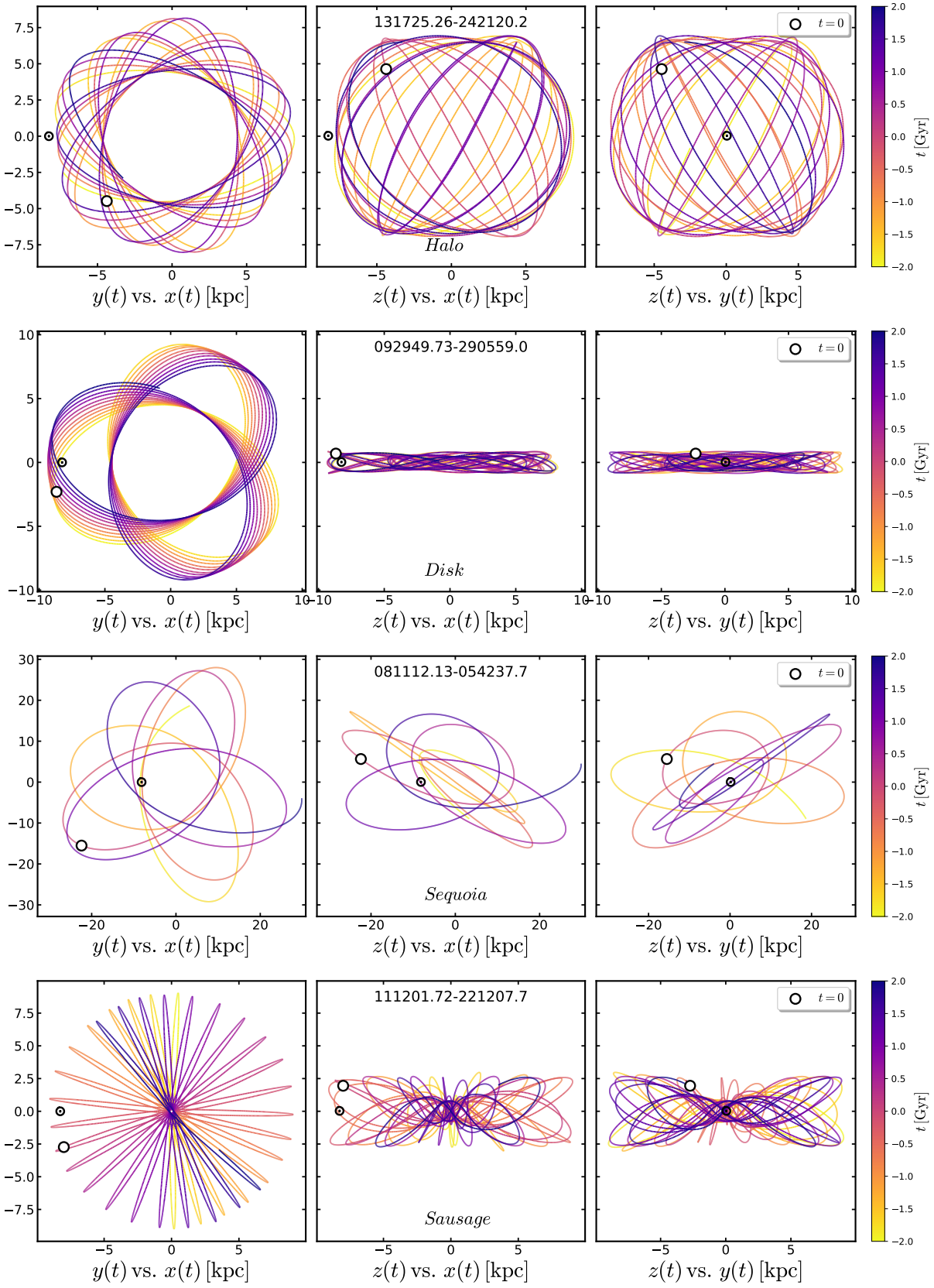

Figure 4.15. From top to bottom: typical orbit in the Galactocentric cartesian frame for examples of Halo, very metal-weak thick disk, *Sausage* and *Sequoia* stars, respectively. Each orbit is colour coded according to the integration time, and the white point indicates the current position of the star. The position of the Sun is indicated by the circled dot. Note that the orbit for the *Sequoia* star shown in the third row is much larger than for the other three stars.

CHAPTER

5 Conclusions

Galactic Archaeology is a vast field which aims at the understanding of the physical processes that lead to the formation of our Galaxy, and, more in general, of the early Universe, through the study of stellar fossils. Moreover, the oldest structures in the Milky Way provide priceless clues into its formation process. Specifically, among the oldest objects in our Universe, in my project I focused on the study of old Galactic Globular clusters and the first generations of stars.

Once considered the prototype of simple stellar populations, old Galactic GCs are now known to harbour multiple stellar populations. In my *Ph.D.* I have undertaken the study of Multiple Stellar Populations in Galactic and extra-galactic star clusters by means of ground- and space-based facilities, like the Very Large Telescope (VLT), the Hubble Space Telescope (HST) and the Gaia satellite.
Despite the huge efforts of the astronomical community, the origin of multiple stellar populations in Galactic GCs remains concealed. Hence, new data and new perspectives are required in order to solve this fascinating yet enigmatic puzzle. In the present thesis I address this conundrum from two independent perspectives: the internal dynamics of multiple stellar populations in old GCs, and multiple populations in young clusters.
Indeed, recent work demonstrated that the internal dynamics of stars belonging to different stellar populations can provide crucial insights into the formation of such stellar populations (Vesperini et al., 2013; Mastrobuono-Battisti & Perets, 2016; Hénault-Brunet et al., 2015). Specifically, in the framework provided by multi-generations scenarios, discussed in Section 1.1, second generations of stars would form in the innermost regions of the cluster in a more centrally concentrated environment, thus affecting the internal dynamics of such stars. These differences in the initial configuration and dynamics may then be retained by cluster stars, being detectable in their present day dynamics. In light of this, the outskirts of star clusters, characterized by longer relaxation times, represent the perfect environment to investigate the kinematics of multiple stellar populations

seeking dynamical and morphological differences.
So, evidence of the presence, or lack thereof, of any difference in the internal kinematics and/or spatial distribution would provide strong constraints for the existing scenarios, favouring the multi-generations models in the first case.

In the context of old Galactic Globular clusters I analysed, for the first time, the spatial distribution and internal dynamics of Multiple Stellar Populations in a sample of 7 type-I (Cordoni et al., 2020a) and 2 type-II (Cordoni et al., 2020b) globulars. To investigate the whole cluster region, we exploited the exquisite astrometry and proper motions measurements provided by Gaia Data Release 2 (DR2 Gaia Collaboration et al., 2018a) and HST, coupled with space- and ground-based photometry (Stetson et al., 2019).
Among type-I GCs, my study reveals the presence of significant differences, in terms of both kinematics and morphology, among multiple stellar populations in NGC 0104 and NGC 5904. On the other hand, the remaining clusters, namely NGC 0288, NGC 6121, NGC 6254, NGC 6752 and NGC 6838, are consistent with the presence of multiple stellar populations sharing the same internal dynamics. Such results are consistent with the criterion introduced in Hénault-Brunet et al. (2015). Indeed, according to Henault-Brunet and collaborators, multiple populations are expected to be not fully mixed if the mass of the host cluster exceeds the threshold expressed in Equation 5.1

$$M_{\rm threshold} = 10^5 M_\odot \cdot \left(\frac{4\,{\rm kpc}}{R_{\rm G}} \right) \tag{5.1}$$

where $R_{\rm G}$ indicates the Galactocentric radius of the clusters. Remarkably, the results in Section 2.1 are qualitatively consistent with such criterion.
As discussed in Section 1.1, Type-II GCs show internal variations in metallicity and in elements associated to *s* processes (e.g. Yong & Grundahl, 2008; Da Costa et al., 2009; Yong et al., 2014; Marino et al., 2015; Johnson et al., 2015; Marino et al., 2019b). In Section 2.2 I extended the analysis carried out in Section 2.1 to 2 clusters belonging to this class, namely ω Centauri and M 22. In this work, I coupled ground- and space-based photometry to study the dynamical and morphological properties of multiple stellar populations from the innermost region of the cluster to the outskirts. Moreover, the exquisite photometry provided by HST observations, allowed us to separate multiple stellar populations based on both their heavy- and light-elements content.
My analysis revealed that, while Fe-poor and Fe-rich stars share the same morphology and internal dynamics in both clusters, N-poor and N-rich stars exhibit significant differences in terms of both spatial distribution and kinematics. Specifically, N-poor rich stars consistently show a more flat and elliptical distribution in the plane of the sky. We refer to Section 2.2.3 for a detailed discussion of these findings. Overall, the results in Section 2.2 suggest that the formation of N-rich stellar populations is likely associated with the cooling flow of material in centrally concentrated structures, while the enrichment in iron and in p-capture elements is the result of different physical processes.

Finally, the findings in Section 2.1 and Section 2.2 constitute important clues into the formation of multiple stellar populations in old Galactic Globular clusters, providing new observational constraints for all future scenarios and theoretical works.

On the other hand, while numerous studies are attempting to address the origin of multiple stellar populations focusing on ancient GCs, young Magellanic Clouds GCs provide the perfect environment to investigate multiple stellar populations in their early life. Specifically, Milone et al. (2009, and series) confirmed that multiple populations are a common feature among Magellanic Clouds GCs younger than 2 Gyr.
In my master thesis I analyzed a sample 27 Magellanic Clouds clusters with ages ranging from few tens of Myr to nearly 2 Gyr, investigating the phenomenon of extended Main-Sequence Turn-On and split/broad Main-Sequences. While my results definitively imputed stellar rotation as the main driver of the peculiar features observed in the color-magnitude diagrams of these objects, they revealed that the presence of an age spread of a few tens of Myr could still be needed in order to match the observations. The same conclusion is discussed in Milone et al. (2016a) and D'Antona et al. (2017) where a younger stellar population is required to reproduce the brighter region of the Turn-Off.
Further increasing the complexity of this puzzle, Gaia DR2 provided evidence of extended Main-Sequence Turn-Offs and split/broad Main-Sequences in young Galactic Open clusters (OCs). In Section 3.1 I show that, as in Magellanic Clouds clusters, eMSTOs and split MSs are a common features of young Galactic OCs, affirming the central role of stellar rotation.
So, while rotation correctly reproduce the observations of both young MCs clusters and Galactic OCs, the degeneracy between age and rotation in the Turn-Off region does not allow to exclude residual age differences.
To finally disentangle the role of stellar rotation and age in the shaping of the CMDs, I proposed a new approach exploiting deep HST observations of the 40 Myr clusters NGC 1818, collected as part of GO 15495 of which I am Principal Investigator. Such method relies on the relation between the Main-Sequence Turn-On, i.e. the point along the Zero-Age Main-Sequence where pre-MS stars join the MS, and the age of the stellar population. Remarkably, while the MS Turn-Off exhibits a strong degeneracy between age and stellar rotation, the luminosity of the MS Turn-On is poorly affected by rotation, while being strongly dependent on the age. Hence, the use of such feature allows us to break the degeneracy and shed light on the nature of multiple stellar populations in young Magellanic Clouds clusters.
My work, discussed in detail in 3.2 reveals that NGC 1818, with an age of ~ 37 Myr, has undergone one single star formation episodes which lasted, at most, 8 Myr. Such results exclude the presence of large age differences, initially postulated to explain the observed CMDs. Moreover, as Milone et al. (2018a) found no evidence of correlation between the properties of multiple stellar population in young GCs and the mass of the host cluster, we can speculate that the results

obtained for the low mass cluster NGC 1818 can be generalized to other more massive Magellanic Clouds clusters.
In a broader context, the negligible age spreads in the very young Large Magellanic Cloud cluster NGC 1818 indicates that multiple stellar populations in this young systems are formed from coeval stars. Furthermore, if young Magellanic Clouds clusters are indeed the younger counterpart of ancient Galactic GCs, then, this would exclude multi-generations scenarios. As an alternative scenario, multiple stellar populations in GCs and extendend Main-Sequence Turn-Offs and split MSs are different phenomena.

The results presented in Section 3.1 and Section 3.2 seems to suggest that the multipopulation phenomenon observed in young star clusters is likely linked to the age of the cluster, i.e. to evolutionary effects that affect stars in that particular age range.

In the context of Galactic Archaeology, the scientific motive underlying my research is the understanding of the formation of Globular Clusters, and more in general, the comprehension of their role in the building up of our Galaxy. Therefore, the final goal is to shed light on the formation process of our Galaxy and its sub-components. In this framework, much information can be gained through the study of the first generations of stars, i.e. population-III stars and their progeny, commonly referred to as Extremely to Ultra Metal-Poor stars. As a matter of fact, being as old as the Milky Way itself, the dynamics of these stars provide a fundamental window on our infant Galaxy, shedding light on its formation.
During my *Ph.D.* I conducted a detailed kinematical study of 475 Very Metal-Poor stars, i.e. stars with [Fe/H] < -2, collected as part of the SkyMapper Survey for Extremely Metal-Poor stars (Da Costa et al., 2019). By deriving the orbits of these stars, and exploiting thei orbital properties, I investigated the association of these stars with the recently discovered remnants of past accretion events, namely the *Gaia Sausage* and the *Gaia Sequoia*, confirming the existence of very metal-poor tail of these groups of stars suggested in Monty et al. (2020). Moreover, my revealed that nealy 21% of the stars are confined within 3 kpc from the Galactic plane, consistently with the recent findings in Sestito et al. (2019); Di Matteo et al. (2020); Sestito et al. (2020b). A detailed kinematical analysis of the orbital properties of these stars revealed that 53 stars exhibit orbital properties consistent with stars belonging to the Milky way thick disc, thus demonstrating the existence of the very low metallicity tail of the Galaxy's metal-weak thick disc (Chiba & Beers, 2000). This result is apparently inconsistent with the commonly accepted view of the formation of the Milky Way, where the Thick disc represents the youngest component of the Galaxy, having formed later than the Halo and the Bulge. On the other hand, the presence of these stars in the Galactic thick disc seems to point in a different direction, and a number of different hypothesis has been proposed. Specifically, as discussed in Sestito et al. (2019) it could be that these stars were accreted from small satellites once the MW disk had already formed, or they could represent low metallicity stars formed in the gas-rich building-blocks that

came together to form the main body of the Galaxy's disk. As a result, the history of the MW disk must have been sufficiently quiescent that old metal-poor stars were able to retain their disk-like orbits to the present-day.

Bibliography

Abadi M. G., Navarro J. F., Steinmetz M., 2009, ApJ, 691, L63

Aguado D. S., et al., 2019, MNRAS, 490, 2241

Anderson J., King I. R., 2003, AJ, 126, 772

Anderson J., van der Marel R. P., 2010, ApJ, 710, 1032

Anderson J., et al., 2008, AJ, 135, 2055

Bailer-Jones C. A. L., et al., 2018, AJ, 156, 58

Bastian N., de Mink S. E., 2009, MNRAS, 398, L11

Bastian N., et al., 2013, MNRAS, 436, 2398

Bastian N., et al., 2017, MNRAS, 465, 4795

Bastian N., et al., 2018, MNRAS, 480, 3739

Baume G., et al., 2003, A&A, 402, 549

Baume G., et al., 2007, MNRAS, 375, 1077

Baumgardt H., Hilker M., 2018, MNRAS, 478, 1520

Beers T. C., Christlieb N., 2005, ARA&A, 43, 531

Beers T. C., Preston G. W., Shectman S. A., 1992, AJ, 103, 1987

Beers T. C., et al., 2014, ApJ, 794, 58

Bekki K., Freeman K. C., 2003, MNRAS, 346, L11

Bellazzini M., et al., 2008, AJ, 136, 1147

Bellazzini M., et al., 2012, A&A, 538, A18

Bellini A., Bedin L. R., 2009, PASP, 121, 1419

Bellini A., et al., 2009, A&A, 493, 959

Bellini A., Anderson J., Bedin L. R., 2011, PASP, 123, 622

Bellini A., et al., 2015, ApJl, 810, L13

Bellini A., et al., 2018, ApJ, 853, 86

Belokurov V., et al., 2018, MNRAS, 478, 611

Bernstein R., et al., 2003, in Iye M., Moorwood A. F. M., eds, Society of Photo-Optical Instrumentation Engineers (SPIE) Conference Series Vol. 4841, Instrument Design and Performance for Optical/Infrared Ground-based Telescopes. pp 1694–1704, doi:10.1117/12.461502

Bertelli G., et al., 2003, AJ, 125, 770

Bessell M. S., et al., 2015, ApJ, 806, L16

Bianchini P., et al., 2018, MNRAS, 481, 2125

Bianchini P., Ibata R., Famaey B., 2019, ApJl, 887, L12

Binney J., 2012, MNRAS, 426, 1328

Binney J., Spergel D., 1984, MNRAS, 206, 159

Bland-Hawthorn J., Gerhard O., 2016, ARA&A, 54, 529

Bovy J., 2015, ApJS, 216, 29

Brook C. B., et al., 2007, ApJ, 661, 10

Caffau E., et al., 2011, Nature, 477, 67

Calamida A., et al., 2020, ApJ, 891, 167

Calura F., et al., 2019, MNRAS, 489, 3269

Carretta E., et al., 2009, A&A, 505, 117

Cash W., 1979, Parameter estimation in astronomy through application of the likelihood ratio., 228: 939–947

Castelli F., Kurucz R. L., 2003, in Piskunov N., Weiss W. W., Gray D. F., eds, Proceedings of the International Astronomical Union, IAU Symposium Vol. 210, Modelling of Stellar Atmospheres. p. A20 (arXiv:astro-ph/0405087)

Cayrel R., et al., 2004, A&A, 416, 1117

Chiba M., Beers T. C., 2000, AJ, 119, 2843

Christlieb N., et al., 2008, A&A, 484, 721

Cignoni M., et al., 2010, ApJ, 712, L63

Cignoni M., et al., 2016, ApJ, 833, 154

Claret A., 2000, A&A, 363, 1081

Conroy C., Spergel D. N., 2011, ApJ, 726, 36

Cordero M. J., et al., 2014, ApJ, 780, 94

Cordoni G., et al., 2018, ApJ, 869, 139

Cordoni G., et al., 2019, A two orbits proposal to solve the age spread dilemma in young Magellanic Clouds clusters, HST Proposal

Cordoni G., et al., 2020a, ApJ, 889, 18

Cordoni G., et al., 2020b, ApJ, 898, 147

Cordoni G., et al., 2021, MNRAS, 503, 2539

Correnti M., et al., 2017, MNRAS, 467, 3628

Cottrell P., Da Costa G., 1981, ApJ, 245, L79

Cui X.-Q., et al., 2012, Research in Astronomy and Astrophysics, 12, 1197

D'Antona F., et al., 2002, ApJ, 564, L93

D'Antona F., et al., 2015, MNRAS, 453, 2637

D'Antona F., et al., 2016, MNRAS, 458, 2122

D'Antona F., et al., 2017, Nature Astronomy, 1, 0186

D'Ercole A., et al., 2008, MNRAS, 391, 825

D'Ercole A., et al., 2010a, MNRAS, 407, 854

D'Ercole A., et al., 2010b, MNRAS, 407, 854

Da Costa G. S., Marino A. F., 2011, Pasa, 28, 28

Da Costa G. S., et al., 2009, ApJ, 705, 1481

Da Costa G. S., et al., 2019, MNRAS, 489, 5900

De Mink S., et al., 2009, A&A, 507, L1

Decressin T., et al., 2007a, A&A, 464, 1029

Decressin T., Charbonnel C., Meynet G., 2007b, A&A, 475, 859

Demarque P., et al., 2004, ApJS, 155, 667

Denissenkov P. A., Hartwick F., 2013, Monthly Notices of the Royal Astronomical Society: Letters, 437, L21

Denissenkov P. A., Hartwick F. D. A., 2014, MNRAS, 437, L21

Denissenkov P., et al., 2015, MNRAS, 448, 3314

Di Matteo P., et al., 2020, A&A, 636, A115

Dias W. S., et al., 2002, A&A, 389, 871

Dotter A., 2016, ApJS, 222, 8

Dupree A. K., et al., 2017, ApJ, 846, L1

D'Antona F., et al., 2017, Nature Astronomy, 1, 0186

Eggen O. J., Lynden-Bell D., Sandage A. R., 1962, ApJ, 136, 748

Ekström S., et al., 2012, A&A, 537, A146

El-Badry K., et al., 2018, MNRAS, 480, 652

Eldridge J. J., Langer N., Tout C. A., 2011, MNRAS, 414, 3501

Espinosa Lara F., Rieutord M., 2011, A&A, 533, A43

Frebel A., Norris J. E., 2015, ARA&A, 53, 631

Fritz T. K., et al., 2020, MNRAS, 494, 5178

Gaia Collaboration et al., 2016, A&A, 595, A2

Gaia Collaboration et al., 2018a, A&A, 616, A1

Gaia Collaboration et al., 2018b, A&A, 616, A1

Gaia Collaboration et al., 2018c, A&A, 616, A12

Gaia Collaboration et al., 2021, A&A, 649, A1

Gallart C., et al., 2003, AJ, 125, 742

Gavagnin E., Mapelli M., Lake G., 2016, MNRAS, 461, 1276

Georgy C., et al., 2014, A&A, 566, A21

Georgy C., et al., 2019, A&A, 622, A66

Gieles M., et al., 2018, MNRAS, 478, 2461

Glantz S. A., Slinker B. K., Neilands T., 1990, Inc., New York

Glatt K., et al., 2008, AJ, 136, 1703

Goudfrooij P., et al., 2011, ApJ, 737, 3

Goudfrooij P., et al., 2014, ApJ, 797, 35

Goudfrooij P., Girardi L., Correnti M., 2017, ApJ, 846, 22

Halir R., Flusser J., 1998, Numerically Stable Direct Least Squares Fitting Of Ellipses

Harris W. E., 1996, AJ, 112, 1487

Hawkins K., Wyse R. F. G., 2018, MNRAS, 481, 1028

Helmi A., et al., 2018, Nature, 563, 85

Hénault-Brunet V., et al., 2015, MNRAS, 450, 1164

Hong J., et al., 2017, MNRAS, 472, 67

Jacobson H. R., et al., 2015, ApJ, 807, 171

Johnson C. I., Pilachowski C. A., 2010, ApJ, 722, 1373

Johnson C. I., et al., 2015, AJ, 150, 63

Joyce M., Chaboyer B., 2018, ApJ, 856, 10

Kamann S., et al., 2018, MNRAS, 473, 5591

Kaufer A., et al., 1999, The Messenger, 95, 8

Keller S. C., Bessell M. S., Da Costa G. S., 2000, AJ, 119, 1748

Keller S. C., Mackey A. D., Da Costa G. S., 2011, ApJ, 731, 22

Keller S. C., et al., 2014, Nature, 506, 463

King I. R., 1966, AJ, 71, 64

Koposov S. E., et al., 2020, MNRAS, 491, 2465

Koppelman H. H., et al., 2019, A&A, 631, L9

Krause M., et al., 2013, A&A, 552, A121

Kroupa P., 2001, MNRAS, 322, 231

Landolt A. U., 1992, AJ, 104, 340

Lanzoni B., et al., 2018, ApJ, 861, 16

Lee J.-W., 2015, ApJs, 219, 7

Lee J.-W., 2017, ApJ, 844, 77

Lee J.-W., 2020, ApJl, 888, L6

Lee Y. W., et al., 1999, Nature, 402, 55

Li C., Zhao G., 2017, ApJ, 850, 25

Li C., et al., 2017, ApJ, 844, 119

Li C., et al., 2018, ApJ, 860, 53

Libralato M., et al., 2018, ApJ, 861, 99

Libralato M., et al., 2019, ApJ, 873, 109

Lindegren L., et al., 2018, A&A, 616, A2

Mackereth J. T., Bovy J., 2018, PASP, 130, 114501

Mackereth J. T., et al., 2019, MNRAS, 482, 3426

Mackey A. D., Broby Nielsen P., 2007b, MNRAS, 379, 151

Mackey A., Broby Nielsen P., 2007a, MNRAS, 379, 151

Mackey A. D., et al., 2008, ApJ, 681, L17

Mackey A. D., et al., 2013, ApJ, 762, 65

Majewski S. R., et al., 2017, AJ, 154, 94

Marchetti T., Rossi E. M., Brown A. G. A., 2019, MNRAS, 490, 157

Marigo P., et al., 2017, ApJ, 835, 77

Marino A., et al., 2008, A&A, 490, 625

Marino A. F., et al., 2009, A&A, 505, 1099

Marino A. F., et al., 2010, in Charbonnel C., et al., eds, Proceedings of the International Astronomical Union, IAU Symposium, Vol. 268, Light Elements in the Universe. pp 183–184 (arXiv:1001.1500), doi:10.1017/S1743921310004096

Marino A. F., et al., 2011, A&A, 532, A8

Marino A. F., et al., 2014, MNRAS, 442, 3044

Marino A. F., et al., 2015, MNRAS, 450, 815

Marino A. F., et al., 2016, MNRAS, 459, 610

Marino A. F., et al., 2017, ApJ, 843, 66

Marino A. F., et al., 2018a, AJ, 156, 116

Marino A. F., et al., 2018b, ApJ, 863, L33

Marino A. F., et al., 2019a, MNRAS, 485, 5153

Marino A. F., et al., 2019b, MNRAS, 487, 3815

Martocchia S., et al., 2018, MNRAS

Mastrobuono-Battisti A., Perets H. B., 2013, ApJ, 779, 85

Mastrobuono-Battisti A., Perets H. B., 2016, ApJ, 823, 61

Matsuno T., Aoki W., Suda T., 2019, ApJ, 874, L35

McMillan P. J., 2017, MNRAS, 465, 76

Milone A. P., et al., 2008, ApJ, 673, 241

Milone A. P., et al., 2009, A&A, 497, 755

Milone A. P., et al., 2012a, A&A, 540, A16

Milone A. P., et al., 2012b, ApJ, 744, 58

Milone A. P., et al., 2013, A&A, 555, A143

Milone A. P., et al., 2015, ApJ, 808, 51

Milone A. P., et al., 2016a, MNRAS, 455, 3009

Milone A. P., et al., 2016b, MNRAS, 458, 4368

Milone A. P., et al., 2017a, MNRAS, 464, 3636

Milone A. P., et al., 2017b, MNRAS, 465, 4363

Milone A. P., et al., 2018a, MNRAS, 477, 2640

Milone A. P., et al., 2018b, MNRAS, 479, 5005

Milone A. P., et al., 2020, MNRAS, 491, 515

Monari G., et al., 2018, A&A, 616, L9

Monelli M., et al., 2013, MNRAS, 431, 2126

Monty S., et al., 2020, MNRAS, 497, 1236

Morrison H. L., Flynn C., Freeman K. C., 1990, AJ, 100, 1191

Mowlavi N., et al., 2012, A&A, 541, A41

Mucciarelli A., et al., 2011, MNRAS, 413, 837

Myeong G. C., et al., 2018, ApJ, 856, L26

Myeong G. C., et al., 2019, MNRAS, 488, 1235

Navarro J. F., Frenk C. S., White S. D. M., 1996, ApJ, 462, 563

Niederhofer F., et al., 2015, MNRAS, 453, 2070

Nordlander T., et al., 2017, A&A, 597, A6

Nordlander T., et al., 2019, MNRAS, 488, L109

Norris J., Bessell M. S., Pickles A. J., 1985, ApJS, 58, 463

Norris J. E., Freeman K. C., Mighell K. J., 1996, ApJ, 462, 241

Norris J. E., et al., 1997, ApJl, 487, L187

Pancino E., et al., 2000, ApJl, 534, L83

Pancino E., et al., 2007, ApJ, 661, L155

Paunzen E., et al., 2010, A&A, 517, A32

Pedregosa F., et al., 2011, Journal of Machine Learning Research, 12, 2825

Piotto G., et al., 2012, ApJ, 760, 39

Placco V. M., et al., 2017, ApJ, 844, 18

Renzini A., et al., 2015, MNRAS, 454, 4197

Richer H. B., et al., 2013, ApJ, 771, L15

Sabbi E., et al., 2016, ApJs, 222, 11

Sales L. V., et al., 2009, MNRAS, 400, L61

Sanna N., et al., 2020, A&A, 637, A46

Schlegel D. J., Finkbeiner D. P., Davis M., 1998, ApJ, 500, 525

Scholz F. W., Stephens M. A., 1987, Journal of the American Statistical Association, 82, 918

Sestito F., et al., 2019, MNRAS, 484, 2166

Sestito F., et al., 2020a, arXiv e-prints, p. 2009.14207

Sestito F., et al., 2020b, MNRAS, 497, L7

Silverman B. W., 1986, Density estimation for statistics and data analysis

Sollima A., 2021, MNRAS, 502, 1974

Sollima A., et al., 2007, ApJ, 654, 915

Sollima A., et al., 2010, MNRAS, 401, 577

Sollima A., Baumgardt H., Hilker M., 2019, MNRAS, 485, 1460

Starkenburg E., et al., 2017, MNRAS, 471, 2587

Stetson P. B., 2005, PASP, 117, 563

Stetson P. B., et al., 2019, MNRAS, 485, 3042

Takahashi K., Lee H. M., Inagaki S., 1997, MNRAS, 292, 331

Tiongco M. A., Vesperini E., Varri A. L., 2016, MNRAS, 455, 3693

Tiongco M. A., Vesperini E., Varri A. L., 2019, MNRAS, 487, 5535

Tumlinson J., 2010, ApJ, 708, 1398

Vasiliev E., 2019a, MNRAS, 484, 2832

Vasiliev E., 2019b, MNRAS, 489, 623

Venn K. A., et al., 2020, MNRAS, 492, 3241

Ventura P., et al., 2001a, The Astrophysical Journal Letters, 550, L65

Ventura P., et al., 2001b, ApJ, 550, L65

Vesperini E., et al., 2013, MNRAS, 429, 1913

Vesperini E., et al., 2014, MNRAS, 443, L79

Vesperini E., et al., 2018, MNRAS, 476, 2731

Vesperini E., et al., 2021, MNRAS, 502, 4290

Vogt S. S., et al., 1994, in Crawford D. L., Craine E. R., eds, Society of Photo-Optical Instrumentation Engineers (SPIE) Conference Series Vol. 2198, Instrumentation in Astronomy VIII. p. 362, doi:10.1117/12.176725

Wand M., Ripley B., Ripley M. B., 2015, Package 'KernSmooth'

White S. D. M., Springel V., 2000, in Weiss A., Abel T. G., Hill V., eds, The First Stars. p. 327 (arXiv:astro-ph/9911378), doi:10.1007/10719504_62

Wolf C., et al., 2018, PASA, 35, e024

Yang W., et al., 2013, ApJ, 776, 112

Yanny B., et al., 2009, AJ, 137, 4377

Yong D., Grundahl F., 2008, ApJl, 672, L29

Yong D., Carney B. W., de Almeida M. L. T., 2005, AJ, 130, 597

Yong D., et al., 2013, ApJ, 762, 26

Yong D., et al., 2014, MNRAS, 441, 3396

Yong D., et al., 2021, MNRAS, 507, 4102

York D. G., et al., 2000, AJ, 120, 1579

Yuan Z., et al., 2020, ApJ, 891, 39

Zhao G., et al., 2012, Research in Astronomy and Astrophysics, 12, 723

de Mink S. E., et al., 2009, A&A, 507, L1

van de Ven G., et al., 2006, A&A, 445, 513